

TECHNISCHE UNIVERSITÄT MÜNCHEN

Fakultät für Medizin

Institut für diagnostische und interventionelle Radiologie

# Gradient-Echo-Based Multi-Parametric Mapping in Magnetic Resonance Imaging for Measuring Trabecular Bone Density in Osteoporosis

Maximilian Nikolaus Diefenbach

Vollständiger Abdruck der von der Fakultät für Medizin der Technischen Universität München zur Erlangung des akademischen Grades eines

Doktor der Naturwissenschaften (Dr. rer. nat.)

genehmigten Dissertation.

Vorsitzender: Prof. Dr. Wolfgang Weber  
Prüfer der Dissertation: 1. Prof. Dr. Dimitrios C. Karampinos  
2. Prof. Dr. Axel Haase  
3. Prof. Dr. Frederik B. Laun

Die Dissertation wurde am 20.01.2020 bei der Technischen Universität München eingereicht und durch die Fakultät für Medizin am 14.07.2020 angenommen.

# Abstract

Osteoporosis is a prevalent disease characterized by trabecular bone loss and increased bone fracture risk at proximal skeletal sites leading to reduced individual quality-of-life for patients and major socioeconomic costs in health care. There is a strong clinical significance for osteoporosis screening, however, current methods are invasive and limited in diagnostic precision and fracture risk prediction. Magnetic Resonance Imaging (MRI) is a non-invasive methodology able to measure many quantitative parameters, which directly correlate with fundamental tissue properties and are candidates for Magnetic Resonance (MR) biomarkers in several diseases.

The purpose of this work is to develop an MRI-based methodology feasible in clinical settings that can quantitatively measure trabecular bone density to enable the study of new MR biomarker candidates for accurate and non-invasive osteoporosis screening.

A multi-step parameter estimation scheme was developed, which uses Quantitative Susceptibility Mapping (QSM) to detect changes in bone content exploiting the diamagnetic susceptibility of bone tissue. The normally MRI-invisible bone at the standard echo times in the employed time-interleaved monopolar multi-gradient echo sequence is indirectly measured through susceptibility-induced phase changes in surrounding tissues. Potentially confounding phase changes due to the chemical shifts in fatty tissues, present in and around major osteoporosis sites, is accounted for by preceded Water–Fat Imaging (WFI) techniques. Susceptibility-induced phase changes are thereby separated from fat-shift-induced phase changes before phase information is inverted to spatial susceptibility distributions.

The present cumulative doctoral thesis compiles three journal publications that together develop the complete MRI-based methodology to perform quantitative multi-parameter mapping in the human body combining WFI and QSM.

The first journal publication develops a method to initialize the field map parameter in water–fat separation algorithms by demodulation of several magnetic field contributions from multi-echo data. The demodulation of the inhomogeneities of the main magnetic field, the shim field, an object-based field and a residual linear field before water–fat separation was shown to significantly reduce water–fat swaps, which also ensures accurate field mapping needed for QSM in the body.

The second journal publication established a framework for generalized parameter estimation and corresponding noise-performance analysis in multi-echo MR signal models of multiple chemical species. The generalized formulation of the signal model Jacobian via novel input matrices is able to describe the whole class of signal models described by a weighted sum of complex exponentials with phases linear in the echo time. The method was validated by numerical simulations and against known signal models from WFI literature. The framework allows parameter estimation besides WFI and was the

basis for QSM field mapping outside the brain.

The third journal publication applied the simultaneous estimation of fat fraction,  $R_2^*$  and susceptibility in trabecularized yellow bone marrow of the calcaneus to measure trabecular bone density in healthy volunteers and osteoporosis patients. In regions of different trabecular bone density, mean susceptibility values, reconstructed with three different assumptions on the spatial distribution, were compared to  $R_2^*$  values, Computed Tomography (CT) attenuation, and Bone-Volume-to-Total-Volume (BV/TV) ratios estimated from high-resolution MRI. QSM showed good sensitivity on BV/TV visually and in quantitative Region-of-Interest (ROI) analysis, which was also verified in numerical simulations of simplified trabecular bone models. The article demonstrates the clinical feasibility of trabecular bone QSM for osteoporosis screening.

# Contents

<b>Abstract</b>	<b>2</b>
<b>List of included journal publications</b>	<b>6</b>
<b>List of Related Journal Publications</b>	<b>7</b>
Shared-First-Authored Journal Publications . . . . .	7
Co-authored Journal Publications . . . . .	7
First-Authored Conference Abstracts . . . . .	8
Co-authored Conference Abstracts . . . . .	10
<b>1 Introduction</b>	<b>14</b>
1.1 Significance And Purpose . . . . .	15
1.2 Thesis Structure . . . . .	16
<b>2 Background Theory</b>	<b>17</b>
2.1 Basics of Magnetic Resonance Imaging . . . . .	17
2.1.1 MR Signal Generation . . . . .	17
2.1.2 MR Signal Localization and Acquisition . . . . .	23
2.1.3 Magnetic Resonance Image Reconstruction . . . . .	27
2.2 Encoding of Physical Properties . . . . .	30
2.2.1 Intra-Voxel Dephasing . . . . .	31
2.2.2 Chemical Shift . . . . .	32
2.2.3 Susceptibility-Induced Phase Accumulation . . . . .	33
2.3 MR Parameter Estimation . . . . .	35
2.3.1 Water–Fat Imaging . . . . .	35
2.3.2 Quantitative Susceptibility Mapping . . . . .	39
<b>3 Comprising Journal Publications</b>	<b>47</b>
3.1 Compliance with Ethical Standards . . . . .	47
3.2 Journal Publication I: Improving Chemical Shift Encoding-Based Water– Fat Separation based on a Detailed Consideration of Magnetic Field Con- tributions . . . . .	47
3.2.1 Abstract . . . . .	47
3.2.2 Author Contribution . . . . .	48
3.2.3 Original Article . . . . .	48
3.3 Journal Publication II: Generalized Parameter Estimation in Multi-Echo Gradient-Echo-Based Chemical Species Separation . . . . .	64
3.3.1 Abstract . . . . .	64

*Contents*

3.3.2	Author Contribution . . . . .	64
3.3.3	Original Article . . . . .	65
3.4	Journal Publication III: On the Sensitivity of Quantitative Susceptibility Mapping for Measuring Trabecular Bone Density . . . . .	90
3.4.1	Abstract . . . . .	90
3.4.2	Author Contribution . . . . .	91
3.4.3	Original Article . . . . .	91
<b>4</b>	<b>Discussion</b>	<b>108</b>
4.1	Review of Existing Literature . . . . .	108
4.1.1	Water–Fat Imaging . . . . .	108
4.1.2	Quantitative Susceptibility Mapping . . . . .	110
4.1.3	Magnetic Resonance Imaging in Osteoporosis . . . . .	112
4.2	Present work . . . . .	113
4.2.1	Novelty . . . . .	113
4.2.2	Impact . . . . .	114
4.2.3	Limitations . . . . .	115
4.3	Perspectives . . . . .	116
	<b>Bibliography</b>	<b>118</b>
	<b>List of Figures</b>	<b>134</b>
	<b>List of Acronyms</b>	<b>135</b>
	<b>List of Symbols</b>	<b>137</b>
	<b>Acknowledgments</b>	<b>139</b>

## List of Included Journal Publications

- [JF1] **M. N. Diefenbach**, S. Ruschke, H. Eggers, J. Meineke, E. J. Rummeny, D. C. Karampinos. “Improving Chemical Shift Encoding-Based Water–Fat Separation Based on a Detailed Consideration of Magnetic Field Contributions”. In: *Magnetic Resonance in Medicine* 80.3 (2018), pp. 990–1004. URL: <https://doi.org/10.1002/mrm.27097>.
- [JF2] **M. N. Diefenbach**, C. Liu, D. C. Karampinos. “Generalized Parameter Estimation and Optimal Experimental Design in Multi-Echo Gradient-Echo-Based Chemical Species Separation”. In: *Quantitative Imaging in Medicine and Surgery* (2020). Ahead of print.
- [JF3] **M. N. Diefenbach**, J. Meineke, S. Ruschke, T. Baum, A. Gersing, D. C. Karampinos. “On the Sensitivity of Quantitative Susceptibility Mapping for Measuring Trabecular Bone Density”. In: *Magnetic Resonance in Medicine* (2018). URL: <https://doi.org/10.1002/mrm.27531>.

# List of Related Journal Publications

## Shared-First-Authored Journal Publications

- [JS1] D. Franz\*, **M. N. Diefenbach\***, F. Treibel, D. Weidlich, J. Syväri, S. Ruschke, M. Wu, C. Holzapfel, T. Drabsch, T. Baum, H. Eggers, E. J. Rummeny, H. Hauner, D. C. Karampinos. “Differentiating Supraclavicular from Gluteal Adipose Tissue Based on Simultaneous PDFFF and T2\* Mapping Using a 20-echo Gradient-Echo Acquisition”. In: *Journal of Magnetic Resonance Imaging* 50.2 (2019), pp. 424–434. URL: <https://doi.org/10.1002/jmri.26661>.

## Co-authored Journal Publications

- [JC1] T. Baum, A. Rohrmeier, J. Syväri, **M. N. Diefenbach**, D. Franz, M. Dieckmeyer, A. Scharr, H. Hauner, S. Ruschke, J. S. Kirschke, D. C. Karampinos. “Anatomical Variation of Age-Related Changes in Vertebral Bone Marrow Composition Using Chemical Shift Encoding-Based Water–Fat Magnetic Resonance Imaging”. In: *Frontiers in Endocrinology* 9 (2018). URL: <https://doi.org/10.3389/fendo.2018.00141>.
- [JC2] E. Burian, A. Rohrmeier, S. Schlaeger, M. Dieckmeyer, **M. N. Diefenbach**, J. Syväri, E. Klupp, D. Weidlich, C. Zimmer, E. J. Rummeny, D. C. Karampinos, J. S. Kirschke, T. Baum. “Lumbar Muscle and Vertebral Bodies Segmentation of Chemical Shift Encoding-Based Water–Fat MRI: the Reference Database Myosegmentum Spine”. In: *BMC Musculoskeletal Disorders* 20.1 (2019), p. 152. URL: <https://doi.org/10.1186/s12891-019-2528-x>.
- [JC3] E. Burian, K. Subburaj, M. R. K. Mookiah, A. Rohrmeier, D. M. Hedderich, M. Dieckmeyer, **M. N. Diefenbach**, S. Ruschke, E. J. Rummeny, C. Zimmer, J. S. Kirschke, D. C. Karampinos, T. Baum. “Texture Analysis of Vertebral Bone Marrow Using Chemical Shift Encoding-Based Water–Fat MRI: a Feasibility Study”. In: *Osteoporosis International* 30.6 (2019), pp. 1265–1274. URL: <https://doi.org/10.1007/s00198-019-04924-9>.
- [JC4] C. Cordes, T. Baum, M. Dieckmeyer, S. Ruschke, **M. N. Diefenbach**, H. Hauner, J. S. Kirschke, D. C. Karampinos. “MR-Based Assessment of Bone Marrow Fat in Osteoporosis, Diabetes, and Obesity”. In: *Frontiers in Endocrinology* 7 (2016). URL: <https://doi.org/10.3389/fendo.2016.00074>.

- [JC5] D. C. Karampinos, S. Ruschke, M. Dieckmeyer, **M. Diefenbach**, D. Franz, A. S. Gersing, R. Krug, T. Baum. “Quantitative MRI and Spectroscopy of Bone Marrow”. In: *Journal of Magnetic Resonance Imaging* 47.2 (2017), pp. 332–353. URL: <https://doi.org/10.1002/jmri.25769>.
- [JC6] E. Klupp, B. Cervantes, S. Schlaeger, S. Inhuber, F. Kreuzpointer, A. Schwirtz, A. Rohrmeier, M. Dieckmeyer, D. M. Hedderich, **M. N. Diefenbach**, F. Freitag, E. J. Rummeny, C. Zimmer, J. S. Kirschke, D. C. Karampinos, T. Baum. “Paraspinal Muscle DTI Metrics Predict Muscle Strength”. In: *Journal of Magnetic Resonance Imaging* nil.nil (2019), jmri.26679. URL: <https://doi.org/10.1002/jmri.26679>.
- [JC7] S. Ruschke, H. Eggers, H. Kooijman, **M. N. Diefenbach**, T. Baum, A. Haase, E. J. Rummeny, H. H. Hu, D. C. Karampinos. “Correction of Phase Errors in Quantitative Water–Fat Imaging Using a Monopolar Time-Interleaved Multi-Echo Gradient Echo Sequence”. In: *Magnetic Resonance in Medicine* 78.3 (2016), pp. 984–996. URL: <https://doi.org/10.1002/mrm.26485>.
- [JC8] S. Ruschke, **M. N. Diefenbach**, D. Franz, T. Baum, D. C. Karampinos. “Molecular in Vivo Imaging of Bone Marrow Adipose Tissue”. In: *Current Molecular Biology Reports* 4.2 (2018), pp. 25–33. URL: <https://doi.org/10.1007/s40610-018-0092-z>.
- [JC9] N. Sollmann, M. Dieckmeyer, S. Schlaeger, A. Rohrmeier, J. Syaeri, **M. N. Diefenbach**, D. Weidlich, S. Ruschke, E. Klupp, D. Franz, E. J. Rummeny, C. Zimmer, J. S. Kirschke, D. C. Karampinos, T. Baum. “Associations Between Lumbar Vertebral Bone Marrow and Paraspinal Muscle Fat Compositions-An Investigation By Chemical Shift Encoding-Based Water–Fat MRI”. In: *Frontiers in Endocrinology* 9 (2018). URL: <https://doi.org/10.3389/fendo.2018.00563>.
- [JC10] A. S. Gersing, J. Boddien, J. Neumann, **M. N. Diefenbach**, S. Kronthaler, D. Pfeiffer, C. Knebel, T. Baum, B. J. Schwaiger, A. Hock, E. J. Rummeny, K. Woertler, D. C. Karampinos. “Accelerating Anatomical 2d Turbo Spin Echo Imaging of the Ankle Using Compressed Sensing”. In: *European Journal of Radiology* 118 (2019), pp. 277–284. URL: <https://doi.org/10.1016/j.ejrad.2019.06.006>.

## First-Authored Conference Abstracts

- [CF1] **M. N. Diefenbach**, S. Ruschke, H. Kooijman, A. T. Van, E. J. Rummeny, A. Haase, D. C. Karampinos. “Improving Chemical Shift-Encoded Water–Fat Separation Based On A Detailed Consideration Of Magnetic Field Contributions”. In: *Proceedings 24. Annual Meeting International Society for Magnetic Resonance in Medicine*. Vol. 24. Oral presentation, Magna Cum Laude Merit Award. Singapore: <http://archive.ismrm.org/2016/0576.html>, 2016, p. 0576.

- [CF2] **M. N. Diefenbach**, A. T. Van, J. Meineke, H. Kooijman, A. Haase, E. J. Rummeny, J. S. Kirschke, T. Baum, D. C. Karampinos. “On the Feasibility of Quantitative Susceptibility Mapping For Trabecular Bone Volume Density Mapping at 3 T”. In: *Proceedings 24. Annual Meeting International Society for Magnetic Resonance in Medicine*. Vol. 24. Oral presentation, Magna Cum Laude Merit Award. Singapore: <http://archive.ismrm.org/2016/0677.html>, 2016, p. 0677.
- [CF3] **M. N. Diefenbach**, J. Meineke, P. Foehr, S. Ruschke, T. Baum, J. S. Kirschke, A. Hock, H. Kooijman, E. J. Rummeny, D. C. Karampinos. “Simultaneous R2\* and Quantitative Susceptibility Mapping of Trabecularized Yellow Bone Marrow: Initial Results in the Calcaneus”. In: *Proceedings 25. Annual Meeting International Society for Magnetic Resonance in Medicine*. Vol. 25. Oral presentation, Magna Cum Laude Merit Award. Honolulu, Hawaii: <http://archive.ismrm.org/2017/0850.html>, 2017, p. 0850.
- [CF4] **M. N. Diefenbach**, S. Ruschke, D. C. Karampinos. “A Generalized Formulation for Parameter Estimation in MR Signals of Multiple Chemical Species”. In: *Proceedings 25. Annual Meeting International Society for Magnetic Resonance in Medicine*. Vol. 25. Electronic poster presentation. Honolulu, Hawaii: <http://archive.ismrm.org/2017/5181.html>, 2017, p. 5181.
- [CF5] **M. N. Diefenbach**, A. Van, J. Meineke, A. Scharr, J. S. Kirschke, A. Gersing, T. Baum, B. Schwaiger, D. C. Karampinos. “Vertebral Column Quantitative Susceptibility Mapping using Joint Background Field Removal and Dipole Inversion”. In: *Proceedings 26. Annual Meeting International Society for Magnetic Resonance in Medicine*. Vol. 26. Oral presentation, Magna Cum Laude Merit Award. Paris, France: <http://archive.ismrm.org/2018/0191.html>, 2018, p. 0191.
- [CF6] **M. N. Diefenbach**, A. Van, J. Meineke, J. S. Kirschke, B. Schwaiger, T. Baum, A. Gersing, D. C. Karampinos. “On the Sensitivity of Bone Marrow Magnetic Susceptibility and R2\* on Trabecular Bone Microstructure”. In: *Proceedings 26. Annual Meeting International Society for Magnetic Resonance in Medicine*. Vol. 26. Power pitch + Electronic poster presentation. Paris, France: <http://archive.ismrm.org/2018/0533.html>, 2018, p. 0533.
- [CF7] **M. N. Diefenbach**, F. Treibel, D. Franz, J. Syväri, S. Ruschke, H. Eggers, D. C. Karampinos. “Technical Challenges in Measuring Adipose Tissue T2\*”. In: *Proceedings 26. Annual Meeting International Society for Magnetic Resonance in Medicine*. Vol. 26. Electronic poster presentation. Paris, France: <http://archive.ismrm.org/2018/5612.html>, 2018, p. 5612.
- [CF8] **M. N. Diefenbach**, C. Böhm, J. Meineke, C. Liu, D. C. Karampinos. “One-Dimensional k-Space Metrics on Cone Surfaces for Quantitative Susceptibility Mapping”. In: *Proceedings 27. Annual Meeting International Society for Magnetic Resonance in Medicine*. Vol. 27. Oral presentation, Magna Cum Laude

Merit Award. Montreal, Canada: <https://cds.ismrm.org/protected/19MPresentations/abstracts/0322.html>, 2019, p. 0322.

- [CF9] **M. N. Diefenbach**, A. T. Van, J. Meineke, H. Kooijman, A. Haase, E. J. Rummeny, J. S. Kirschke, T. Baum, D. C. Karampinos. “Quantitative Susceptibility Mapping of Trabecular Bone in the Distal Tibia”. In: *International Workshop on MRI Phase Contrast & Quantitative Susceptibility Mapping*. Vol. 4. Traditional poster presentation. Vienna, Austria: <http://www.neuroimaging.at/qsm2016/>, 2016, p. 52.

## Co-authored Conference Abstracts

- [CC1] T. Baum, A. Rohrmeier, J. Syväri, **M. N. Diefenbach**, D. Franz, M. Dieckmeyer, A. Scharr, H. Hauner, S. Ruschke, J. S. Kirschke, D. C. Karampinos. “Anatomical Variation of Age-Related Changes in Vertebral Bone Marrow Composition using Chemical Shift Encoding-Based Water–Fat MRI”. In: *Proceedings 26. Annual Meeting International Society for Magnetic Resonance in Medicine*. Vol. 26. Paris, France: <http://archive.ismrm.org/2018/1243.html>, 2018, p. 1243.
- [CC2] C. Böhm, **M. N. Diefenbach**, J. Meineke, A. Haase, D. C. Karampinos. “Improved Body Quantitative Susceptibility Mapping by Using a Variable-Layer Single-Min-Cut Graph-Cut Algorithm for Field-Mapping”. In: *Proceedings 27. Annual Meeting International Society for Magnetic Resonance in Medicine*. Vol. 27. Power Pitch, Magna Cum Laude Merit Award. Montreal, Canada: <https://index.mirasmart.com/ISM2019/PDFfiles/0693.html>, 2019, p. 0693.
- [CC3] C. Böhm, **M. N. Diefenbach**, A. Haase, D. C. Karampinos. “Accelerated Single-Min-Cut Graph-Cut Algorithm Using a Variable-Layer Graph Construction Improves Field-Mapping in Water–Fat Regions”. In: *Proceedings 27. Annual Meeting International Society for Magnetic Resonance in Medicine*. Vol. 27. Digital Poster. Montreal, Canada: <https://index.mirasmart.com/ISM2019/PDFfiles/4007.html>, 2019, p. 4007.
- [CC4] W. Chen, B. Jiang, **M. N. Diefenbach**, D. Liang, D. Karampinos. “Separation of Water and Fat during Spin-Lock Magnetic Resonance Imaging with Multifrequency Fat Spectrum Modeling”. In: *Proceedings 27. Annual Meeting International Society for Magnetic Resonance in Medicine*. Vol. 27. Digital Poster. Montreal, Canada: <https://index.mirasmart.com/ISM2019/PDFfiles/4008.html>, 2019, p. 4008.

- [CC5] D. Franz, D. Weidlich, J. Syväri, **M. N. Diefenbach**, C. Holzapfel, T. Drabsch, T. Baum, H. Eggers, E. J. Rummeny, H. Hauner, D. C. Karampinos. “The Presence of Brown Adipose Tissue is Associated with Thyroid Function in Subjects with Low and Normal BMI”. In: *Proceedings 26. Annual Meeting International Society for Magnetic Resonance in Medicine*. Vol. 26. Oral presentation. Paris, France: <http://archive.ismrm.org/2018/1266.html>, 2018, p. 1266.
- [CC6] D. Franz, **M. N. Diefenbach**, J. Syväri, D. Weidlich, E. J. Rummeny, H. Hauner, S. Ruschke, D. C. Karampinos. “Differentiating supraclavicular from gluteal adipose tissue based on simultaneous PDFFF and T2\* mapping using a twenty-echo gradient echo acquisition”. In: *Proceedings 26. Annual Meeting International Society for Magnetic Resonance in Medicine*. Vol. 26. Traditional poster presentation. Paris, France: <http://archive.ismrm.org/2018/2498.html>, 2018, p. 2498.
- [CC7] S. Kronthaler, **M. N. Diefenbach**, S. Ruschke, J. Meineke, H. Eggers, P. Boernert, D. Karampinos. “Time Interleaved Multi-Gradient-Echo Imaging with UTE and Non-UTE Sampling for Simultaneous PDFFF, T2\* and Magnetic Susceptibility Mapping of Cortical Bone”. In: *Proceedings 26. Annual Meeting International Society for Magnetic Resonance in Medicine*. Vol. 26. Electronic poster presentation. Paris, France: <http://archive.ismrm.org/2018/5157.html>, 2018, p. 5157.
- [CC8] S. Ruschke, D. Weidlich, **M. N. Diefenbach**, H. Eggers, H. Kooijman, H. H. Hu, E. J. Rummeny, A. Haase, J. S. Kirschke, T. Baum, D. C. Karampinos. “Simultaneous T2, T2’ and PDFFF Mapping in the Spine using an Adiabatic T2-Prepared Time-Interleaved Multi-Echo Gradient Echo Acquisition”. In: *Proceedings 24. Annual Meeting International Society for Magnetic Resonance in Medicine*. Vol. 24. Oral presentation, Magna Cum Laude Merit Award. Singapore: <http://archive.ismrm.org/2016/0568.html>, 2016, p. 0568.
- [CC9] S. Ruschke, D. Weidlich, **M. N. Diefenbach**, H. Eggers, H. Kooijman, H. H. Hu, E. J. Rummeny, A. Haase, J. S. Kirschke, T. Baum, D. C. Karampinos. “Simultaneous T2, T2’ and PDFFF Mapping in the Spine using an Adiabatic T2-Prepared Time-Interleaved Multi-Echo Gradient Echo Acquisition”. In: *ISMRM Workshop on Data Sampling and Image Reconstruction*. Poster presentation. Sedona, Arizona, USA, 2016, p. 36.
- [CC10] A. T. Van, **M. N. Diefenbach**, J. Meineke, H. Kooijman, A. Haase, D. C. Karampinos. “Background Field Removal in the Presence of Subcutaneous Fat in Body QSM”. In: *International Workshop on MRI Phase Contrast & Quantitative Susceptibility Mapping*. Vol. 4. Poster presentation. Vienna, Austria: <http://www.neuroimaging.at/qsm2016/>, 2016, p. 11.
- [CC11] D. Weidlich, **M. N. Diefenbach**, S. Schlaeger, A. Hock, S. Ruschke, D. C. Karampinos. “In-Vivo Water T2 Mapping in Tissues Containing Water and Fat using a T2-Prepared 3D Dixon TSE Sequence and a Pre-Calibrated Fat Spectrum Model”. In: *Proceedings 26. Annual Meeting International Society for*

## Contents

*Magnetic Resonance in Medicine*. Vol. 26. Paris, France: <http://archive.ismrm.org/2018/4223.html>, 2018, p. 4223.

- [CC12] A. Rohrmeier, J. Syväri, M. Diefenbach, D. Franz, S. Ruschke, M. Dieckmeyer, J. S. Kirschke, D. C. Karampinos, T. Baum. “Vertebral Bone Marrow Composition: Assessment of Age and Gender Dependency using Chemical Shift Encoding-Based Water–Fat MRI”. In: Vienna, Austria, 2018, B–0441.
- [CC13] E. Burian, K. Subburaj, M. R. K. Mookiah, A. Rohrmeier, M. Dieckmeyer, M. N. Diefenbach, S. Ruschke, E. J. Rummeny, C. Zimmer, J. S. Kirschke, D. C. Karampinos, T. Baum. “Texture Analysis of Vertebral Bone Marrow using Chemical Shift Encoding-Based Water–Fat MRI - a Feasibility Study”. In: Lille, France, 2018.
- [CC14] N. Sollmann, M. Dieckmeyer, S. Schlaeger, R. Rohrmeier, J. Syvaeri, M. N. Diefenbach, D. Weidlich, S. Ruschke, E. Klupp, D. Franz, E. J. Rummeny, C. Zimmer, J. S. Kirschke, D. C. Karampinos, T. Baum. “Associations Between Lumbar Vertebral Bone Marrow and Paraspinal Muscle Fat Compositions-an Investigation by Chemical Shift Encoding-Based Water–Fat MRI”. In: Lille, France, 2018.
- [CC15] C. Zoellner, S. Kronthaler, C. Boehm, S. Ruschke, M. Diefenbach, D. Franz, D. C. Karampinos. “Fat Deblurring in Golden Angle Radial Stack-of-Stars Multi-Echo Gradient Echo for Navigator-Gated High-Resolution Water–Fat Imaging”. In: Singapore, 2019.
- [CC16] D. Franz, L. Patzelt, J. Syväri, C. Zöllner, M. N. Diefenbach, R. Braren, U. Nitsche, O. Prokopchuk, E. J. Rummeny, D. C. Karampinos. “Psoas Volume and PDFFF in Cancer Patients: Dynamics and Association with Severity of Cachexia Progression”. In: Singapore, 2019, p. 23.
- [CC17] M. N. Diefenbach, C. Liu, D. C. Karampinos. “Extending the Signal Models of the ISMRM Fat–Water Toolbox: Generalized Parameter Estimation in Multi-Echo Gradient-Echo-Based Chemical Species Separation”. In: Singapore, 2019, p. 18.
- [CC18] C. Böhm, M. N. Diefenbach, J. Meineke, A. Haase, D. C. Karampinos. “Improved Body Quantitative Susceptibility Mapping by using a Variable-Layer Single-Min-Cut Graph-Cut Algorithm for Field-Mapping”. In: Seoul, Korea, 2019.
- [CC19] C. Böhm, M. N. Diefenbach, J. Meineke, A. Haase, D. C. Karampinos. “Fusion of Susceptibility Maps in k-Space based on One-Dimensional Error Metrics on Field-Map Data Improves QSM”. In: Seoul, Korea, 2019.
- [CC20] C. Böhm, M. N. Diefenbach, J. Meineke, A. Haase, D. C. Karampinos. “Estimating Magnetic Susceptibility within a Hollow Cylinder and its Implications in Body QSM”. In: Seoul, Korea, 2019.

*Contents*

- [CC21] C. Zoellner, S. Kronthaler, C. Boehm, S. Ruschke, **M. Diefenbach**, D. Franz, A. Hock, G. M. Beck, J. M. Peeters, D. C. Karampinos. “Fat Deblurring in Golden Angle Radial Stack-Of-Stars Multi-Echo Gradient Echo for Navigator-Gated High-Resolution Water–Fat Imaging”. In: Rotterdam, Netherlands, 2019.

# 1 Introduction

A major interest in MRI is the development of quantitative imaging techniques. Quantitative Magnetic Resonance Imaging (qMRI) tries to obtain exact voxel values in MRI source or post-processed images independent of hardware or experimental situations and only sensitive to physiological tissue properties. qMRI measurements can therefore enable patient specific diagnosis and treatment monitoring towards personalized medicine and open novel possibilities for longitudinal investigations of pathologies.

In the past decade, many qMRI methodologies were developed exploiting all types of fundamental contrast mechanisms to derive clinically valuable biomarkers. Techniques using thermalization of tissue magnetization or spin diffusion as contrast mechanisms, such as MR-relaxometry or Diffusion-Weighted Imaging, are primarily based on measuring changes in the MR signal magnitude. Methods using tissue electromagnetism or spin motion to produce MR contrasts, like MR Spectroscopy or Flow Imaging, additionally incorporate the phase information of the MR signal to gain information about the underlying tissue.

Among the tissue properties that are encoded in both the magnitude and the phase of the MR signal is the magnetic susceptibility. Tissues with different magnetic susceptibility locally distort the magnetic field in an MRI scanner resulting in phase changes in the signal. In the past, these susceptibility effects have been studied based on susceptibility-induced intravoxel dephasing that leads to a signal magnitude  $R_2^*$ -decay in the commonly used gradient-echo imaging. However,  $R_2^*$ -mapping does not necessarily depict the inherent tissue susceptibility at a certain location as the susceptibility-induced field distortions are the sum of contributions from all surrounding magnetic susceptibility sources. To uncover the true local susceptibility, the phase of the signal has to be incorporated.

QSM is an emergent MR technique using the MR phase information from gradient-echo data to directly reconstruct spatial susceptibility distribution [1]. QSM was initially developed and is primarily used for neurological research applications in the brain and consists of three conceptual steps [2]: *i*) estimation of the magnetic field inside the scanner, *ii*) removal of field contributions not originating from susceptibility sources inside a defined ROI, and *iii*) solving a field-to-susceptibility inverse problem.

When applying QSM outside the brain, especially the first field mapping step needs to be adapted to the presence of multiple MR resonances compared to brain QSM, where the assumption of single water proton resonances is sufficient. In the body where fat is abundant in many tissues, chemical shifts in the resonance frequencies of the fat molecule lead to nonlinear MR phase evolutions. Leaving them unaccounted for, such nonlinear MR phase contributions from chemical shifts would confoundingly propagate into the later QSM steps. The field mapping step in body QSM therefore uses water-fat separation techniques to differentiate phase contributions due to chemical shifts from

susceptibility-induced field contributions enabling an accurate treatment of the MR phase evolution.

For unconfounded field maps, QSM theoretically results in three-dimensional tomographic maps that yield the average magnetic susceptibility per voxel independent of field-strength and voxel volume [2]. QSM can thereby measure and differentiate voxels primarily containing diamagnetic tissues from voxels with primarily para- and ferromagnetic content. The susceptibility of human bone tissue is diamagnetic and has a lower than the susceptibility of water and therefore most soft-tissues [3]. In standard gradient-echo MRI with longer echo times, thicker cortical bone structures do not directly emit detectable MR signal as the apparent transverse relaxation rate of bone is very large,  $R_2^* \sim 2500 \text{ s}^{-1}$  [4], and the generated magnetization in cortical bone decays to quickly. However, voxels containing fine networks of trabecular bone show MR signal due to the surrounding bone marrow. In theory, the voxel-averaged scalar magnetic susceptibility of the trabecularized bone marrow scales linearly with the ratio of BV/TV according to Wiedeman’s additivity law, which states that a mixture of different susceptibility constituents exerts a bulk magnetic susceptibility, which is the sum of each proportionate susceptibility component in the mixture [5]. Voxels of trabecularized bone marrow emit detectable MR signals, which hold phase information about the averaged susceptibility inside the voxel. Body QSM of trabecularized bone marrow is therefore a candidate to indirectly measure normally MR-invisible trabecular bone structures through their indirect bulk susceptibility effect on the surrounding bone marrow. Hence, accurate trabecular bone QSM could enable the non-invasive assessment of trabecular bone density and thereby the detection of trabecular bone loss, which is one of the most important pathological changes in osteoporosis.

## 1.1 Significance And Purpose

Osteoporosis is defined as the condition of low bone mineral mass and density leading to a weakening of bones, which is the most common cause of broken bone among the elderly population. Especially the loss of trabecular bone in osteoporosis patients leads to large increase in fracture risk primarily occurring in the spine and the hip. Fractures in trabecular bone due to osteoporotic bone loss greatly reduce individual quality-of-life, correlate with mortality and pose a great economic burden on health care systems. In the US, one in three post-menopausal women is estimated to experience bone fractures due to decreased bone densities [6]. In the EU the estimated prevalence of osteoporosis in men and women is around 35 % [7]. There is medicamentous treatment for osteoporosis, if the disease is diagnosed early [8]. However, due to the lacking precision of current Bone Mineral Density (BMD) measurements, early diagnosis of osteoporosis remains challenging [9].

Bone imaging in radiology is clinically highly significant for the detection of trabecular bone thinning and loss and to predict fracture risk in patients with osteoporosis [10]. Current gold-standard methods for osteoporosis imaging are however invasive as they are based on the application of ionizing radiation. Non-invasive high-resolution MR

trabecular bone imaging is challenging due to the necessary long scan times prone to motion artefacts. With the loss of diamagnetic bone mineral density in osteoporosis, the bulk magnetic susceptibility in trabecular bone regions decreases. The accompanied change in the geometry of the trabecular network also affects the MR signal decay [11]. Furthermore, it has been shown that trabecular bone loss is correlated with the increase of bone marrow fat content in the cavities of the trabecular bone network [12]. These three types of pathological tissue changes—decrease of susceptibility, change of transverse relaxation rates and increase of bone marrow fat fraction—are technically measurable by non-invasive MRI without the need for high-resolution scanning.

**Therefore the purpose of this work is to test the central hypothesis, whether the development of a trabecular bone MRI methodology based on multi-parameter mapping is possible, clinically feasible and sensitive enough to measure changes in trabecular bone density for osteoporosis screening.**

### 1.2 Thesis Structure

The present cumulative thesis is structured in the three following parts.

The first part summarizes background theory about MR physics, MRI reconstruction, and parameter estimation theory.

The second part lists the comprised journal publications in separate sections together with publication information and the main author's research contribution.

The third part contextualizes the work with respect to previous studies in literature, discusses results and indicates further research perspectives.

## 2 Background Theory

In the following sections we introduce the basic concepts of the methodologies employed and developed for this thesis. The focus lies on the introduction of notation for the later chapters; in depth derivations can be found in most standard MRI textbooks and the cited references. The chapter tries to cover the full spectrum of physical, mathematical, and algorithmic concepts to explain the methods from this thesis' comprising journal publications.

First, we briefly summarize the basic steps in general MRI experiments from the generation of MR signals, over their spatial localization to the main concept in MRI reconstruction.

Second, we show how tissue properties are encoded into MR images in standard multi-echo MRI acquisitions.

Third, the employed MR parameter estimation techniques in WFI and QSM are explained.

### 2.1 Basics of Magnetic Resonance Imaging

This chapter describes the basic principles of magnetic resonance imaging, from the generation of MR signals in a spin ensemble over the method of signal localization by spatial encoding to the reconstruction of images.

#### 2.1.1 MR Signal Generation

To generate an MR signal in MRI, the quantum mechanical spin of protons—mostly as hydrogen nuclei in water molecules in the human body—is exploited.

In the classical picture of a rotating proton with angular momentum  $\mathbf{J}$ , its electromagnetic charge distribution creates a magnetic dipole moment  $\boldsymbol{\mu} = \gamma\mathbf{J}$ , whose magnitude is determined by the proton's spin quantum number  $I = 1/2$  via  $|\mathbf{J}| = \hbar\sqrt{I(I+1)}$ , where  $\gamma$  is the proton's gyromagnetic ratio and  $\hbar$  is the reduced Planck constant. In a volume element of human tissue, there is an abundance of protons, whose associated dipole moments accumulate to a magnetization vector  $\mathbf{M} = \sum_{i=1}^N \boldsymbol{\mu}_i$ . In the absence of an external magnetic field the net magnetization averages out as the dipole moments are generally randomly oriented and cancel each other to  $|\mathbf{M}| = 0$ . In an MRI experiment, a strong static external magnetic field  $\mathbf{H}_0 = H_0\hat{\mathbf{z}}$  is applied to the object inside the MRI scanner, leading to Zeeman splitting of the protons' energy levels  $E_{\pm} = \boldsymbol{\mu}\mathbf{H}_0 = m_I\hbar\gamma H_0$  in the contained spin ensemble, where  $m_I = -I, -I+1, \dots, I = \pm 1/2$  is the magnetic quantum number of the proton. According to the Boltzmann distribution the lower energy level is occupied by a few more ( $\sim \exp((E_+ - E_-)/k_B T)$ ) protons with  $\mu_z = -\hbar\gamma H_0/2$ ,

## 2 Background Theory

which collectively contribute to an observable net magnetization  $M_{\parallel} > 0$  collinear to the main magnetic field  $\mathbf{H}_0$ . In the plane perpendicular to  $\mathbf{H}_0$ , the spins precess due to the exerted torque  $\boldsymbol{\tau} = \boldsymbol{\mu} \times \mathbf{H}_0$  with the Lamor frequency  $\omega_0 = -\gamma H_0$  equally canceling any transverse net magnetization component  $M_{\perp} = 0$ . At thermal equilibrium the magnetization is therefore  $\mathbf{M}_0 \sim H_0 \hat{\mathbf{z}}$ . This bulk magnetization in MRI can in general be treated classically as the number of protons that contribute is large ( $N > 10^{23}$ ).

The dynamics of the net magnetization vector  $\mathbf{M}$  in an external magnetic field  $\mathbf{H}$  is governed by the classical Bloch equation,

$$\frac{\partial \mathbf{M}(t)}{\partial t} = \gamma \mathbf{M}(t) \times \mathbf{H}(t) - R_2 M_x(t) \hat{\mathbf{x}} - R_2 M_y(t) \hat{\mathbf{y}} + R_1 (M_0 - M_z(t)) \hat{\mathbf{z}}, \quad (2.1)$$

where dissipative effects in the spin ensemble towards the equilibrium magnetization  $M_0 \hat{\mathbf{z}}$  are phenomenologically modeled by the two constants  $R_1$  and  $R_2$ . On top of the static magnetic field, a sinusoidally time-varying magnetic field  $|\mathbf{H}_1| = 2H_1 \cos(\Omega t + \phi)$  with  $H_1 \ll H_0$  is applied orthogonal to  $\mathbf{H}_0$ . When considering a reference frame rotating around  $\mathbf{H}_0$  with the same angular frequency  $\Omega$  as  $\mathbf{H}_1(t)$ , the effective field in this frame of reference becomes time-independent

$$\mathbf{H}_e = [H_1 \cos \phi, H_1 \sin \phi, H_0 - \Omega/\gamma]^T,$$

with arbitrary phase  $\phi$  in the transverse plane with respect to  $\hat{\mathbf{x}}$ . The Bloch equation for the magnetization  $\mathbf{M}'$  in the rotating frame of reference can then be written as

$$\frac{\partial \mathbf{M}'(t)}{\partial t} = -\boldsymbol{\Gamma} \mathbf{M}'(t) + R_1 \mathbf{M}_0, \quad (2.2)$$

where the matrix notation of the cross product in (2.1) was used for the definition of the time-independent matrix

$$\boldsymbol{\Gamma} = \begin{pmatrix} R_2 & \omega_3 & -\omega_2 \\ -\omega_3 & R_2 & \omega_1 \\ \omega_2 & -\omega_1 & R_1 \end{pmatrix}, \quad (2.3)$$

with  $\omega_i, i = 1, 2, 3$  being the components of the effective Lamor precession  $\boldsymbol{\omega}_e = -\gamma \mathbf{H}_e$  of the magnetization  $\mathbf{M}$  due to the (time-independent) torque  $\mathbf{M} \times \gamma \mathbf{H}_e$ . As can be seen from (2.2) by setting  $d\mathbf{M}'/dt = 0$ , the magnetization approaches a steady state  $\mathbf{M}'_{ss} = R_1 \boldsymbol{\Gamma}^{-1} \mathbf{M}_0$ . Dropping the prime and redefining  $\mathbf{M}$  as the magnetization in the rotating frame, the formal solution to the Bloch equation (2.2) is given by

$$\begin{aligned} \mathbf{M}(t) &= e^{-\boldsymbol{\Gamma}t} \mathbf{M}(0) + (1 - e^{-\boldsymbol{\Gamma}t}) \mathbf{M}_{ss} \\ &= e^{-\boldsymbol{\Gamma}t} [\mathbf{M}(0) - \mathbf{M}_{ss}] + \mathbf{M}_{ss}. \end{aligned}$$

Unlike often stated in MRI textbooks, the Bloch equation does have a general solution obtained by proper evaluation of the propagator  $\exp(-\boldsymbol{\Gamma}t)$ . Here, we briefly sketch the general evaluation of the matrix exponential  $\exp(-\boldsymbol{\Gamma}t)$ , a complete treatment can be found in Reference [13]. As will be shown, the general solution can be reduced to

## 2 Background Theory

finding the roots of a third order polynomial with components depending on the physical parameters  $R_1, R_2, \omega_e$ . Without giving the general solution, we immediately apply some simplifying assumptions on the applied field  $\mathbf{H}_1(t)$  that are often fulfilled in most MRI scenarios and are valid for all standard experiments performed for this thesis.

To calculate the matrix exponential  $\exp(-\mathbf{\Gamma}t)$ , one can employ its inverse Laplace transform. Similar to the well known Laplace transform  $\mathcal{L}$  of the term  $(s - a)^{-1}$  being  $\exp(at)$  for constant  $a$ , the propagator can be written as

$$e^{-\mathbf{\Gamma}t} = \mathcal{L}^{-1}\left[(s\mathbb{1} + \mathbf{\Gamma})^{-1}\right],$$

with the identity matrix  $\mathbb{1}$ . The inverse Laplace transform  $f(t)$  for a function  $F(s)$  can be calculated by the complex Bromwich integral

$$f(t) = \mathcal{L}^{-1}[F(s)](t) = \frac{1}{2\pi i} \lim_{T \rightarrow \infty} \int_{\kappa - iT}^{\kappa + iT} F(s) e^{st} ds, \quad (2.5)$$

where the real constant  $\kappa$  is chosen greater than the real part of any singularities of  $F(s)$  and the contour is closed to the left of  $\kappa$  such that it encloses all singularities. The complex integral can then be solved with Cauchy's residue theorem

$$\oint_{\gamma} g(s) ds = 2\pi i \sum_{c_n} \text{Res}(g, c_n), \quad (2.6)$$

where the residue of a complex function  $f(z)$  at its poles  $c_n$  of order  $n$  can be calculated by

$$\text{Res}(g, c_n) = \frac{1}{(n-1)!} \lim_{s \rightarrow c_n} \frac{d^{n-1}}{ds^{n-1}} ((s - c_n)^n g(s)). \quad (2.7)$$

For  $F(s) = (s\mathbb{1} + \mathbf{\Gamma})^{-1} = \mathbf{A}^{-1}$  in (2.5), the inverse  $\mathbf{A}^{-1}$  can be computed by Cramer's rule,  $\mathbf{A}^{-1} = \text{adj } \mathbf{A} / \det \mathbf{A}$ , as the quotient of the adjugate  $\text{adj } \mathbf{A}$  and the determinant  $\det \mathbf{A}$  of the matrix  $\mathbf{A} = s\mathbb{1} + \mathbf{\Gamma}$ . The function  $g(s)$  in (2.6) and (2.7) is

$$g(s) = F(s) e^{st} = (s\mathbb{1} + \mathbf{\Gamma})^{-1} e^{st} = \frac{\text{adj}(s\mathbb{1} + \mathbf{\Gamma})}{\det(s\mathbb{1} + \mathbf{\Gamma})} e^{st},$$

and the evaluated matrix exponential  $\exp(-\mathbf{\Gamma}t)$ , the propagator for the general Bloch equation (2.2), can finally be written as

$$e^{-\mathbf{\Gamma}t} = \sum_{c_n} \text{Res}(g(s), c_n) = \sum_{c_n} \text{Res}\left(\frac{\text{adj}(s\mathbb{1} + \mathbf{\Gamma})}{p(s)} e^{st}, c_n\right), \quad (2.8)$$

where  $c_n$  are the roots of  $g(s)$  and  $p(s) = \det(s\mathbb{1} + \mathbf{\Gamma})$  is the characteristic polynomial of the matrix  $-\mathbf{\Gamma}$ .  $p(s)$  is of order 3 and has in general three, possibly degenerate roots, one real and two complex, that can be computed e.g. by Vieta's formula. What is left for the general solution of the Bloch equation is to find the poles of  $g(s)$  and compute its residue at these points using (2.7). The sum of those residue holds the propagator (2.8).

## 2 Background Theory

A full expansion of the propagator in terms of all initial physical parameters  $R_1, R_2, \mathbf{H}_1$  is given in [13]. As such a rigorous mathematical treatment needs to characterize the poles of  $g(s)$  by distinguishing different cases of possible degenerated roots of the polynomial  $p(s)$ , the generality quickly leads to possibly complicated and nonintuitive relations of the results to the initial physical parameters.

Here, we show, based on the general solution of the Bloch equation ((2.8) and (2.2)), the solution in a practical MRI experiment by choosing a specific form of the applied field  $\mathbf{H}_1$  allowing for some simplifying assumptions. In MRI this second magnetic field is called a pulse and is typically of the form

$$\mathbf{H}_e \rightarrow \mathbf{H}_1(t) \Pi\left(\frac{t - \tau_p/2}{\tau_p}\right),$$

where  $\Pi(t)$  is the boxcar function that is 1 in the interval  $[-1/2, 1/2]$  and 0 otherwise. The pulse is only active during a short duration, which is typically much smaller than the inverse physical parameter relaxation parameter,  $\tau \ll 1/R_1, 1/R_2$  such that the assumption  $R_1, R_2 \rightarrow 0$  is valid. On this time scale the Bloch equation simplifies to

$$\mathbf{M}(t) = e^{-\mathbf{\Gamma}t} \mathbf{M}(0), \quad \text{with} \quad \mathbf{\Gamma} = \begin{pmatrix} 0 & \omega_3 & -\omega_2 \\ -\omega_3 & 0 & \omega_1 \\ \omega_2 & -\omega_1 & 0 \end{pmatrix}. \quad (2.9)$$

The (characteristic) polynomial in (2.8) is

$$p(s) = \det(s\mathbf{1} - \mathbf{\Gamma}) = s(s - i\omega_e)(s + i\omega_e),$$

which has the three distinct non-degenerate roots  $s_0 = 0, s_{\pm} = \pm i\omega_e$ . The adjugate of  $(s\mathbf{1} + \mathbf{\Gamma})$  can also be easily computed and conveniently written as

$$\text{adj}(s\mathbf{1} - \mathbf{\Gamma})_{ij} = s^2 \delta_{ij} - s \sum_k \epsilon_{ijk} \omega_k + \omega_i \omega_j,$$

where  $\epsilon_{ijk}$  denotes the Levi-Civita symbols, which is 1 for cyclic,  $-1$  for anticyclic permutations of the indices and 0 otherwise, which also corresponds to

$$\text{adj}(s\mathbf{1} - \mathbf{\Gamma}) = s^2 \mathbf{1} - s\mathbf{\Gamma} + \omega_e \mathbf{1} + \mathbf{\Gamma}^2, \quad (2.10)$$

verifiable by simple matrix multiplication. As the adjugate is not further factorizable, the roots of the  $p(s)$ ,  $\{s_0, s_{\pm}\}$ , are also the three simple poles of the function

$$g(s) = \frac{\text{adj}(s\mathbf{1} + \mathbf{\Gamma})}{p(s)} e^{st}.$$

Therefore, the propagator can readily be evaluated by the sum

$$e^{-\mathbf{\Gamma}t} = \sum_i \frac{\text{adj}(s_i \mathbf{1} + \mathbf{\Gamma})}{\prod_{j \neq i} (s_j - s_i)} e^{s_i t}, \quad (2.11)$$

## 2 Background Theory

which derives the final result by inserting the adjugate (2.10), and the poles  $s_i = s_0, s_{\pm}$  into (2.11):

$$\begin{aligned}
e^{-\mathbf{\Gamma}t} &= \frac{\omega_e \mathbb{1} + \mathbf{\Gamma}^2}{\omega_e^2} \\
&\quad + \frac{-\omega_e^2 \mathbb{1} - i\omega_e \mathbf{\Gamma} + \omega_e \mathbb{1} + \mathbf{\Gamma}^2}{-2\omega_e^2} e^{i\omega_e t} \\
&\quad + \frac{\omega_e^2 \mathbb{1} + i\omega_e \mathbf{\Gamma} - \omega_e \mathbb{1} + \mathbf{\Gamma}^2}{2\omega_e^2} e^{i\omega_e t} \\
&= \frac{1}{\omega_e} (\omega_e \mathbb{1} + \mathbf{\Gamma}^2 - \text{Re}\{(-\omega_e^2 \mathbb{1} - i\omega_e \mathbf{\Gamma} + \omega_e \mathbb{1} + \mathbf{\Gamma}^2) e^{i\omega_e t}\}) \\
&= \mathbb{1} - \frac{\mathbf{\Gamma}}{\omega_e} \sin(\omega_e t) + \left(\frac{\mathbf{\Gamma}}{\omega_e}\right)^2 (1 - \cos(\omega_e t))
\end{aligned}$$

The final result,

$$e^{-\mathbf{\Gamma}t} = \mathbb{1} - \frac{\mathbf{\Gamma}}{\omega_e} \sin \omega_e t + \left(\frac{\mathbf{\Gamma}}{\omega_e}\right)^2 (1 - \cos \omega_e t), \quad (2.12)$$

describes a rotation of the magnetization vector around the axis  $\boldsymbol{\omega}_e$ , and can be written in the familiar form of a general rotation matrix

$$e^{-\mathbf{\Gamma}t} = \mathbf{R}(\alpha, \phi, \theta) = \mathbf{R}_z(-\phi) \mathbf{R}_y(-\theta) \mathbf{R}_z(-\omega_e t) \mathbf{R}_y(\theta) \mathbf{R}_z(\phi),$$

upon definition of the angles as  $\alpha = -\omega_e t$ ,  $\cos \phi = \omega_1 / \sqrt{\omega_1^2 + \omega_2^2}$ ,  $\sin \phi = \omega_2 / \sqrt{\omega_1^2 + \omega_2^2}$ ,  $\cos \theta = \omega_3 / \omega_e$ ,  $\sin \theta = \sqrt{\omega_1^2 + \omega_2^2} / \omega_e$ , with the standard rotation matrices (2.13),

$$\begin{aligned}
\mathbf{R}_{x'}(\phi) &= \begin{bmatrix} 1 & 0 & 0 \\ 0 & c_\phi & s_\phi \\ 0 & -s_\phi & c_\phi \end{bmatrix} & \mathbf{R}_{y'}(\phi) &= \begin{bmatrix} c_\phi & 0 & -s_\phi \\ 0 & 1 & 0 \\ s_\phi & 0 & c_\phi \end{bmatrix} & \mathbf{R}_{z'}(\phi) &= \begin{bmatrix} c_\phi & s_\phi & 0 \\ -s_\phi & c_\phi & 0 \\ 0 & 0 & 1 \end{bmatrix} \\
s_\phi &\equiv \sin \phi, & c_\phi &\equiv \cos \phi,
\end{aligned}$$

for the rotations around the axes  $\hat{\mathbf{x}}', \hat{\mathbf{y}}', \hat{\mathbf{z}}'$  of the rotating frame of reference. By identifying the initial matrix  $\mathbf{\Gamma}$  from (2.3) as the cross product matrix composed of the generators of rotation of the SO(3) group, the result for the propagator of the MR pulse (2.12) can directly be verified to be the correct description of the rotating magnetization vector. The solution to the Bloch equation (2.9) (in the rotating frame of reference) is therefore

$$\mathbf{M}(t) = \mathbf{R}(\alpha(t), \phi, \theta) \mathbf{M}(0), \quad t \in [0, \tau_p]. \quad (2.13)$$

The solution for the Bloch equation of an applied pulse (2.13) has the advantage that it describes not only resonant but also off-resonant pulse excitation, depending on the choice of the applied pulse  $\mathbf{H}_e$  and therefore  $\boldsymbol{\omega}_e$ . In a typical MRI experiment, after the

## 2 Background Theory

pulse duration  $\tau_p$ ,  $\tau_p < t$ , the magnetization vector is again left in a static magnetic field, which then obeys the Bloch equation

$$\frac{\partial \mathbf{M}(t)}{\partial t} = -\mathbf{\Gamma} \mathbf{M}(t) + R_1 \mathbf{M}_0, \quad \tau_p < t \quad (2.14a)$$

$$\mathbf{\Gamma} = \begin{pmatrix} R_2 & -\omega_3 & 0 \\ \omega_3 & R_2 & 0 \\ 0 & 0 & R_1 \end{pmatrix}. \quad (2.14b)$$

The general method of solving the Bloch equation presented above is again applicable for (2.14) but leads to a cubic characteristic polynomial that is not easily factorizable as in the case of the pulse excitation with neglected exponential relaxation before. Therefore, we proceed by simplifying the propagator  $\exp(-\mathbf{\Gamma}t)$  via decomposing  $\mathbf{\Gamma}$  into the two commuting matrices

$$\mathbf{\Gamma} = \mathbf{D} + \mathbf{Z} = \begin{pmatrix} R_2 & & \\ & R_2 & \\ & & R_1 \end{pmatrix} + \begin{pmatrix} 0 & -\omega_3 & \\ \omega_3 & 0 & \\ & & 0 \end{pmatrix}, \quad \mathbf{D}\mathbf{Z} - \mathbf{Z}\mathbf{D} = 0,$$

omitting all further zero matrix entries. Note that the zero commutator allows to factorize  $\exp(-\mathbf{\Gamma}t) = \exp(-\mathbf{D}t) \exp(-\mathbf{Z}t)$ . While the matrix exponential of the diagonal matrix  $\mathbf{D}$  is trivially evaluated to

$$e^{-\mathbf{D}t} = \begin{pmatrix} e^{-R_2 t} & & \\ & e^{-R_2 t} & \\ & & e^{-R_1 t} \end{pmatrix} = \mathbf{E}(t),$$

this time, we immediately identify  $\mathbf{Z} = -\omega_3 \mathbf{L}_z$  as the generator of rotation around  $\hat{\mathbf{z}}$ , which directly yields

$$e^{-\mathbf{Z}t} = e^{\omega_3 t \mathbf{L}_z} = \mathbf{R}_z(\omega_3 t).$$

The solution to the Bloch equation (2.14) is therefore

$$\begin{aligned} \mathbf{M}(t) &= \mathbf{R}_z(\vartheta(t)) [\mathbf{E}(t) \mathbf{M}(\tau_p) + (\mathbb{1} - \mathbf{E}(t)) \mathbf{M}_{\text{ss}}] \\ &= \mathbf{R}_z(\vartheta(t)) [\mathbf{E}(t) \mathbf{R}(\alpha(\tau_p), \phi, \theta) \mathbf{M}(0) + (\mathbb{1} - \mathbf{E}(t)) \mathbf{M}_{\text{ss}}], \end{aligned} \quad (2.15)$$

where we defined  $\vartheta(t) = \omega_3 t$  and used the fact that  $\mathbf{E}(t)$  and  $\mathbf{R}_z$  commute.

According to (2.16), the steady-state is given by

$$\mathbf{M}_{\text{ss}} = R_1 \mathbf{\Gamma}^{-1} \mathbf{M}_0 = R_1 (\mathbf{D} + \mathbf{Z})^{-1} \mathbf{M}_0 \hat{\mathbf{z}} = M_0 \hat{\mathbf{z}}, \quad (2.16)$$

which is invariant under  $\mathbf{R}_z$  and therefore

$$\mathbf{M}(t) = \mathbf{R}_z(\vartheta(t)) [\mathbf{E}(t) \mathbf{R}(\alpha(\tau_p), \phi, \theta) \mathbf{M}(0)] + (1 - e^{-R_1 t}) M_0 \hat{\mathbf{z}}.$$

## 2 Background Theory

For an instantaneous on-resonant pulse (short  $\tau_p$ ,  $\Omega = -\gamma H_0 = \omega_0$ ) in the transverse  $xy$ -plane ( $\theta = 0$ ), one can easily deduce the textbook result for the magnetization vector in the laboratory frame:

$$\begin{aligned} M_{xy}(t) &= M_x(t) + iM_y(t) \\ &= M_{xy}(\tau_p)e^{i\omega_0 t}e^{-R_2 t} \\ M_z(t) &= (1 - e^{-R_1 t})M_0 + e^{-R_1 t}M_z(\tau_p), \end{aligned}$$

where the magnetization immediately after the pulse  $\mathbf{H}_1$  with flip angle  $\alpha = \gamma H_1 \tau_p$  is

$$\mathbf{M}(\tau_p) = \mathbf{R}_{\alpha, \phi} \mathbf{M}(0) = \mathbf{R}_z(\phi) \mathbf{R}_x(\alpha) \mathbf{R}_z(-\phi) \mathbf{M}_0.$$

The solution to the Bloch equation (2.15) describes the basic sequence in a typical MRI experiment, where the bulk magnetization created by the main magnetic field  $\mathbf{H}_0$  is first excited by a pulse  $\mathbf{H}_1$ , which tilts the magnetization away from the  $z$ -axis. The transverse magnetization component  $M_{xy}$  then precesses around the main magnetic field accompanied by a relaxation towards the steady state.

Due to first principles in electrodynamics, the precessing transverse magnetization emits a radio frequency signal, circularly polarized about the  $z$ -axis. This signal  $S(t)$  is proportional to the transverse magnetization and detectable via electromagnetic induction into receiver coils inside the MRI scanner. The MR signal can be made dependent on many physical tissue parameters, e.g. by choosing the pulse duration  $\tau_p$  or the exact timings of the acquisition windows of the receiver coil and therefore holds a rich amount of information which can finally be used to produce a wealth of different image contrasts.

Generally, the magnetization vector is not homogeneous throughout the imaged object in the scanner due to different physical electromagnetic tissue properties and as the number of spins contributing to the bulk magnetization is large,  $M_{xy}(t)$  is therefore better described by the integral

$$S(t) \sim M_{xy}(t) = \int_V m(\mathbf{r}, t) d\mathbf{r}, \quad (2.17)$$

of the time-dependent magnetization density  $m(\mathbf{r}, t)$  over the volume  $V$  inside the scanner. As MRI attempts to visualize the spatial distribution of the magnetization density, after the signal generation by the excitation pulse, the spatial information needs to be directly encoded in the MR signal in order to localize the magnetization contributions from each rasterized locations inside the scanner.

### 2.1.2 MR Signal Localization and Acquisition

To be able to reconstruct an MR image from the generated MR signal, spatial information needs to be encoded into  $S(t) \sim M_{xy}(t)$  to localize tissue contrast information to pixel or voxel values. The fundamental idea of modern MRI is to superimpose additional magnetic gradient fields, which vary linearly in space, on top of the main magnetic field  $\mathbf{H}_0$ .

## 2 Background Theory

By applying these gradient fields  $\mathbf{G}(t)\mathbf{r}$  over a time range  $-\tau/2 \leq t \leq \tau/2$  after the pulse ( $t < \tau_p$ ), the local precession frequency of the transverse magnetization  $M_{xy}$  also varies linearly in space. The gradient fields create a location-dependent linear phase dispersion over time, which is detected by a receiver coil via the previously mentioned electromagnetic induction. The receiver coil system measures the time domain signal and demodulates the spatially constant precession term  $\exp(-i\omega_0 t)$  to

$$S'(t) = S(t)e^{-i\omega_0 t} \sim \int_V m(\mathbf{r}, t) \exp\left(-i\gamma \left(\int_0^t \mathbf{G}(t) dt\right) \mathbf{r}\right) d\mathbf{r}. \quad (2.18)$$

By defining the variable

$$\mathbf{k}(t) = -\gamma \int_{t-\tau/2}^{t+\tau/2} \mathbf{G}(t) dt, \quad (2.19)$$

and assuming the acquisition window, the time duration  $[-\tau/2, \tau/2]$ , to be also small compared to the inverse relaxation rates,  $\tau \ll 1/R_1, 1/R_2$ , it is evident that the signal (2.18) resembles the three-dimensional Fourier transform of the magnetization density. This relation is stated in the important "Imaging Equation"

$$S'(\mathbf{k}) \sim \int_V m(\mathbf{r}, t) e^{-2\pi i \mathbf{k} \mathbf{r}} d\mathbf{r} = \mathcal{F}\{m(\mathbf{r}, t)\}. \quad (2.20)$$

The signal  $S'(t)$  can therefore be viewed as acquired by the MRI scanner in the Fourier or  $k$ -space domain along the trajectory  $\mathbf{k} = \mathbf{k}(t)$ . The localization information is effectively encoded by the frequency  $\mathbf{k}$ , which is known through the applied gradient fields with their so-called waveforms  $\mathbf{G}(t) = [G_x(t), G_y(t), G_z(t)]^T$  by the definition (2.19). The applied waveforms always lead to a phase dispersion of the magnetic spins, which contribute to the magnetization vector in each voxel. This phase dispersion leads to a specific precession frequency  $\mathbf{k}$  per voxel at  $\mathbf{r} = [x, y, z]^T$  and therefore connects acquired samples in  $k$ -space with corresponding spatial locations in image-space. This signal encoding by the applied waveforms is the important intermediate step to later reconstruct the generated MR signal to images.

In general, MRI gives a large freedom in designing the gradient waveforms, which define the MRI acquisition scheme and the trajectory on which the MR signal is sampled in  $k$ -space. The most basic MR experiment is the so-called Free Induction Decay (FID), where the MR signal after a solitary excitation pulse is sampled with a constant gradient waveform, the so-called read-out gradient. Figure 2.1 shows the FID signal created by this simple MR acquisition scheme in a so-called pulse diagram, visualizing the timing of Radio Frequency (RF) or gradient magnetic fields from left to right.

The signal evolution of the transverse magnetization density per voxel in the FID experiment is given by

$$s(\mathbf{r}, t) = m(\mathbf{r}, t) \exp(-2\pi i \mathbf{G} t \mathbf{r}), \quad (2.21)$$

which is not symmetric over the acquisition window, and does not follow an even function in the time domain. Therefore, its Fourier transform—the "spectrum" of the magnetization density  $m(\mathbf{r}, t)$ —has a real absorption mode and an imaginary dispersion mode [14].

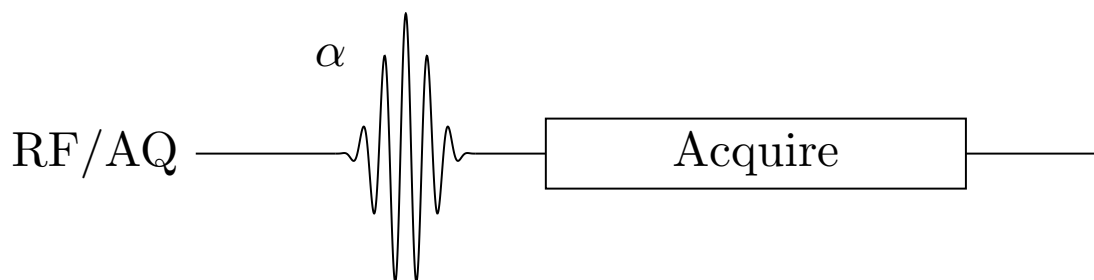


Figure 2.1: Schematic pulse diagram of a basic FID MR experiment.

Due to the finite dispersion mode, the acquired signal (2.20) for an FID is undesirably phase-shifted and requires a phase-correction to recover a purely real absorption line for a later image reconstruction of the magnetization density signal (2.21). To overcome the requirement of a phase-correction step for each trajectory in  $k$ -space in an MRI experiment, one chooses an acquisition scheme in which the signal per voxel (2.21) is ideally an odd function over the time duration of the acquisition scheme, such that its Fourier transform has directly only a pure absorption line and a phase-correction as for the FID is not needed.

There are two prominent MR acquisition schemes that form a symmetric "echo" signal over the read-out gradient duration, called the Spin Echo (SE) sequence and the Gradient Echo (GRE) sequence.

In a SE sequence (Figure 2.2), the FID signal after the single excitation pulse is not directly sampled by the read-out gradient, but a second  $180^\circ$  inversion pulse is played out at the time  $t = TE/2$ . The inversion pulse reverses the dispersion due to microscopic field inhomogeneities, which are always present in practical experimental conditions. Therefore, the reversible signal decay of the FID refocuses after the inversion pulse to the initial signal up to the factor  $\exp(-R_2TE)$ , which manifest the formation of the "spin echo" at  $t = TE$ , after which the signal decays again [15]. Sampling the signal symmetrically around the so-called echo-time  $TE$  leads to the desired symmetry of the signal dynamic over the acquisition window, where the signal follows and even function in time.

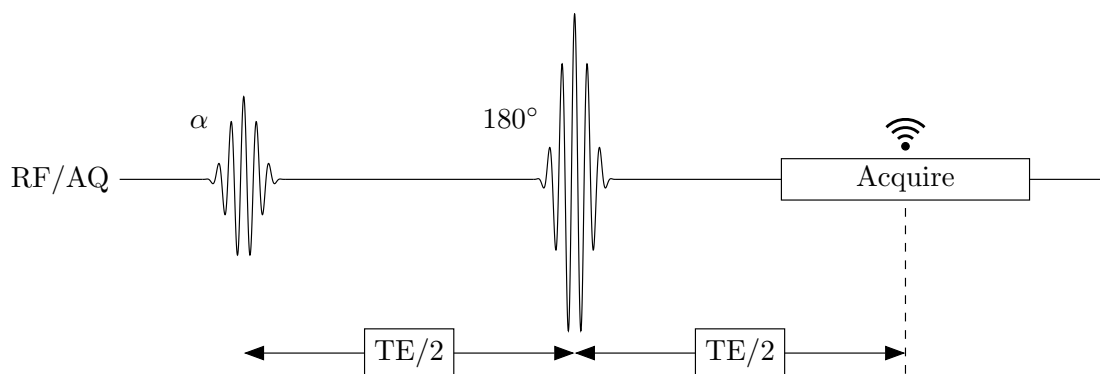


Figure 2.2: Schematic pulse diagram of a basic SE sequence.

## 2 Background Theory

In a GRE sequence (Figure 2.3), in addition to the dispersion due to microscopic field inhomogeneities, the MR signal created by the excitation pulse is deliberately dephased by a dephasing gradient of different polarity and half the duration of the read-out gradient. A so-called "gradient echo" is then formed after the first half of the acquisition window, which defines the echo time TE in a GRE sequence [16]. In contrast to the spin echo, the gradient echo is ideally refocused up to  $s(\mathbf{r}, t) \exp(-R_2^*TE)$ , where  $R_2^*$  is an effective transverse relaxation constant different from  $R_2$  as only the dispersion part from the dephasing gradient is rephased and not the reversible decay from the microscopic field inhomogeneities, which are present in any practical MR experiment. The apparent  $R_2^*$ -relaxation is further discussed in Section 2.2.1.

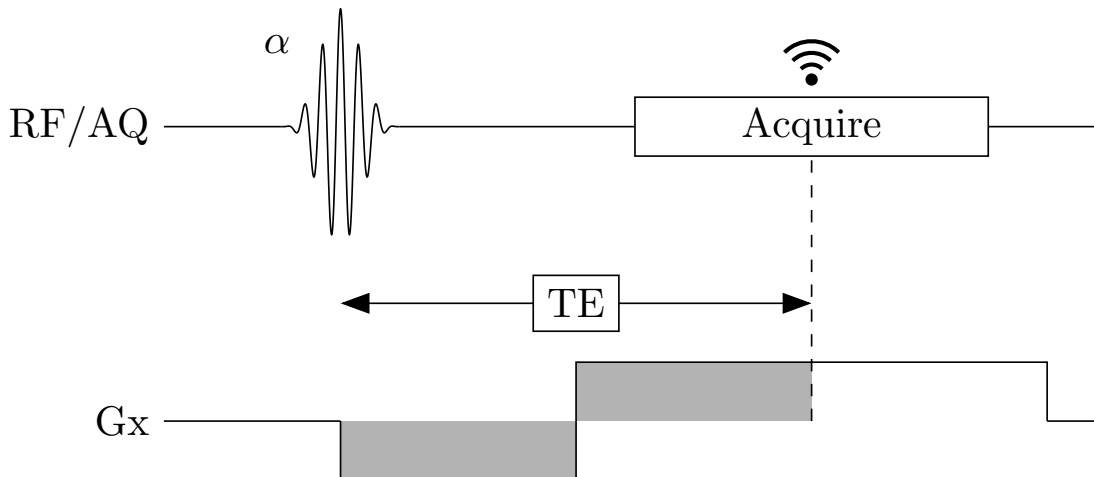


Figure 2.3: Schematic pulse diagram of a basic GRE sequence.

In both types of echo formations, SE and GRE, the read-out gradient symmetrically sampling the echo is only able to encode signal along an one-dimensional line in  $k$ -space. The above pulse sequence diagrams are therefore understood as building blocks of the full pulse sequence played out during the entire MR experiments. To traverse the full  $k$ -space the entire sequence in the diagrams from excitation pulse to the latest gradient plus eventual waiting times—defining the so-called TR—needs to be repeated with a varied gradient waveform to sample along a different one-dimensional  $k$ -space trajectory until enough  $k$ -space volume is sampled to later be able to reconstruct a full image.

In addition to the type of echo preparation and the number of subsequent echoes acquired, the full MR acquisition scheme is also defined by the geometry of the sampling trajectories. Trajectories distinguish between Cartesian or non-Cartesian  $k$ -space lines in two or three dimensional space. For gradient waveforms defining only two dimensional trajectories in  $k$ -space, the third dimension needs to be encoded by an initial slice-selective excitation in each TR, which can be achieved by a constant gradient in the slice dimension played out during the excitation pulse. For both, 3D and 2D, trajectories, a Cartesian read-out is most common in standard clinical MRI practice. In Cartesian sequences, the gradient waveforms define a Cartesian grid on which the created signal

is sampled. In non-Cartesian read-outs, the trajectories describe  $k$ -space lines off the Cartesian grid, which enables more time-efficient MR signal acquisitions, but require more complex subsequent image reconstruction techniques. In the next section we show the basic ideas of Cartesian MR image reconstruction.

### 2.1.3 Magnetic Resonance Image Reconstruction

The aim of MR image reconstruction is to spatially resolve the acquired MR signal  $s(\mathbf{r}, t)$  (2.21) and thereby visualize the transverse magnetization component  $m(\mathbf{r}, t)$  2.17 in a stack of two dimensional images.

As previously mentioned already, the main idea in modern MRI reconstruction is to identify the localized, spatially encoded, MR signal  $S'(\mathbf{k})$  (2.20) as the forward Fourier transform of the magnetization density  $m(\mathbf{r}, t)$ .

This association allows to describe effects on the signal due to the experimental setup, such as hardware realizations and possible perturbations, in terms of mathematical properties of the Fourier transforms and thereby explain possible resulting image properties.

We focus on the simple case of Cartesian MR acquisition schemes, which were exclusively used for this work, but the  $k$ -space concepts also apply to non-Cartesian MR acquisitions in which the sampled  $k$ -space trajectories are necessarily resampled to the rectilinear Cartesian grid in an extra post-processing step either via so-called gridding [17] or Nonlinear Fast Fourier Transformation (NUFFT) [18].

Formally inverting the Imaging Equation (2.20) to recover the spatially resolved magnetization density as

$$m(\mathbf{r}, t) \sim \int_V S'(\mathbf{k}) e^{2\pi i \mathbf{k} \mathbf{r}} d\mathbf{k} = \mathcal{F}^{-1}\{S'(\mathbf{k})\} \quad (2.22)$$

shows how the inverse three-dimensional Fourier transform allows the conversion from the acquired  $k$ -space data to localized information in image-space. However, the relation of the Fourier transform (2.22) is not directly applicable, because in the MR data acquisition and reconstruction, the signal is not analogous and therefore not continuous. The signal and with it the recovered spatial distribution of the magnetization density are both subject to discretization. In fact, two different discretization steps happen in an MRI experiment: the digitalization of the MR signal by an Analog-to-Digital (A2D) converter connected to the receiver coil(s) during the acquisition and the discretization in the reconstruction to map the spatial domain onto two-dimensional pixels or three-dimensional voxels. We briefly show the mathematical structure of these finite sampling steps, where it suffices to focus on only the one-dimensional case, as the Fourier transform is fully separable across the different spatial dimensions. Without loss of generality the three-dimensional case is a straightforward replication of the one-dimensional case in the remaining dimensions.

The sampling of the MR signal on Cartesian trajectories by the A2D converter effectively introduces two terms into the Imaging Equation (2.20). First, the finite duration

## 2 Background Theory

of the acquisition window introduces a truncation by the windowing or boxcar function

$$\Pi(k) = \begin{cases} 1 & \text{for } k_{\min} \leq k \leq k_{\max}, \\ 0 & \text{otherwise.} \end{cases} \quad (2.23)$$

Second, during the acquisition window the A2D converter samples the localized MR signal described by multiplication with the sampling function

$$u(k) = \Delta k \sum_{n=-\infty}^{\infty} \delta(k - n\Delta k). \quad (2.24)$$

Inserting the physically motivated functions (2.23) and (2.24), which describe the finite sampling of the MR signal into the (one-dimensional) Imaging Equation (2.20), writes

$$m'(x) = \int_{-\infty}^{\infty} S'(k) e^{2\pi i k x} u(k) \Pi(k) dk \quad (2.25)$$

where we changed the symbol from  $m(\mathbf{r}, t)$  to  $m'(x)$  because of the one-dimensionality and as the finite sampling always violates complete data-consistency to a certain extent. The real magnetization density is only to be recovered up to a truncation error due to the finite  $k$ -space volume resembled by  $\Pi(k)$ . The effect of the finite sampling from the A2D converter on the reconstruction  $m'(x)$  is described by the product of the two terms  $\Pi(k)u(k)$  and (2.25) results in

$$m'(x) = \Delta k \sum_{p=-n}^{n-1} S'(p\Delta k) e^{2\pi i p \Delta k x}, \quad (2.26)$$

where the  $k$ -space dimension was discretized as  $-n\Delta k \leq k < n\Delta k$  with  $N = 2n \in \mathbb{N}$  equidistant samples. From (2.26) it is evident that the sampled spin density  $m'(x)$  is periodic in regular intervals of

$$L = 1/\Delta k, \quad (2.27)$$

which defines the Field-of-View (FOV) in image-space. The finite sampling of the spatial dimension  $x$  to a discretized image-space is described by multiplication of (2.26) with the same sampling function  $u(x) = \Delta x \sum_{q=-n'}^{n'-1} \delta(x - q\Delta x)$  where  $-n'\Delta x \leq x < n'\Delta x$ :

$$\Delta x \sum_{q=-n'}^{n'-1} m'(x) \delta(x - q\Delta x) = \Delta x \Delta k \sum_{q=-n'}^{n'-1} \sum_{p=-n}^{n-1} S'(p\Delta k) e^{2\pi i p \Delta k x} \delta(x - q\Delta x) \quad (2.28)$$

The resolution  $\Delta x$  is defined by the number of voxels,  $N' = 2n' \in \mathbb{N}$ , and the FOV as

$$\Delta x = L/N'. \quad (2.29)$$

## 2 Background Theory

Imposing that the number of discrete  $k$ -space samples being equal the number of voxels in image-space,  $N = N'$ , combines (2.27) and (2.29) to

$$\Delta x \Delta k = 1/N,$$

whose substitution in (2.28) finally results in the reconstructed (one-dimensional) image of the spin density distribution

$$m'(q\Delta x) = \Delta k \sum_{p=-N/2}^{N/2-1} S'(p\Delta k) e^{2\pi i p q / N}. \quad (2.30)$$

Equation (2.30) shows how the two discretized quantities—the sampled  $k$ -space data,  $S'(p\Delta k)$  and the voxel values for the spin density,  $m'(q\Delta x)$ —form a Discrete Fourier Transform (DFT) pair. The computationally efficient method of Fast Fourier Transformation (FFT) can therefore be used to implement the DFT and reconstruct the sampled  $k$ -space data as an image [19].

The derived equations (2.20), (2.26), and (2.30) give the basis for understanding many image properties in MRI. For example, the effect of undersampling  $k$ -space can be seen from Equation (2.26). If the FOV (2.27) is smaller than the length of the imaging object, denoted by  $A$ , the Nyquist sampling criterion,  $A \leq L$ , is violated, causing the infamous effect of aliasing. Similarly, effects causing Gibbs ringing or image blurring can be understood from the truncation (2.23) or other additional functions in  $k$ -space and their Fourier transforms. Therein, the concept of MR data acquisition in  $k$ -space proves very helpful and shows the unavoidable trade-offs in an MRI experiment. Obviously, the more sampling points are acquired, the better the image that can be reconstructed. However, as each  $k$ -space sample needs to be spatially encoded onto the generated MR signal, the pulse sequence block describing the read-out might need to be repeated resulting in a longer scan time. Typically the whole pulse sequence cannot be directly speeded up as limiting physical constraints, either related to the hardware or medical safety, do always apply. For example, a too large power transmission by RF coils increases body temperature and fast switching gradient fields—if the gradient hardware allows them—can induce peripheral nerve stimulation, both effects to be avoided for obvious safety demands. Consequently, there is always an inherent trade-off in MRI of scan time versus image quality.

Increasing the speed of MRI is therefore an important topic of both ongoing and past MRI research efforts. The importance of fast MRI led to the development of several novel MRI acquisition schemes successful in decreasing the MR acquisition time with limited image quality reduction and therewith increased time efficiency and patient comfort. Most important are the advances in "Parallel Imaging" and more recently "Compressed Sensing".

Parallel Imaging takes advantage of multiple coils for receiving the MR signal [20]. The spatial sensitivity of the different surface-coils arranged in one so-called array can be used to complement the spatial encoding procedure using gradient waveforms. Using the signal strength in the different receiver coils as localization information, only a

fraction of the time-consuming phase-encoding repetitions need to be performed, which directly saves scan time. There are two basic types to perform parallel imaging and the corresponding image reconstruction of multi-coil MR signals. The two types differ on whether the under-sampled signal is first complemented in  $k$ -space, like in the GeneRALized Autocalibrating Partial Parallel Acquisition (GRAPPA) approach [21], or the aliased Fourier transform in image-space is unfolded using image-space sensitivity information, like in the SENSitivity Encoding (SENSE) approach [22]. More recent parallel imaging techniques also combine the two principles, like in Eigenvector-based Self-consistent Parallel Imaging Reconstruction from Arbitrary  $k$ -Space (ESPIRIT) [23].

Compressed Sensing also allows to heavily under-sample the MR  $k$ -space data to achieve large scan time savings. Instead of relying on multiple receiver coils, a Compressed Sensing method uses the sparsity property of MR images [24]. Greyscale MR images are often compressible with a large reduction factor exploiting the fact that in a certain domain, the information content of the MR images can be represented by only a few coefficients. Some MR images (e.g. flow images in MR angiography) are already sparse in the standard pixel domain (image-space) but typical examples of domains where MR images show a large degree of sparsity are the wavelet or gradient domain. Using recent advances in mathematics and image reconstruction theory [25, 26] use the fact that pseudo-randomly under-sampled  $k$ -space acquisitions lead to noise-like aliasing artefacts in image-space reconstructions. Those noise-like artefacts can then be removed by non-linear non-Cartesian reconstruction algorithms using regularization terms that promote a low number of representing coefficients in the corresponding sparsifying domain to denoise the image similar to other denoising algorithms in standard image processing.

In this present work, Compressed Sensing was not used but we partly made use of the SENSE method. Results of reconstruction methods typically focus on the quality of magnitude images and little is known on how Parallel Imaging methods or Compressed Sensing affects the phase of the reconstructed images and therefore any subsequent quantitative parameter estimations techniques. In our applications however, the phase information was of major interest. We consequently did not perform any  $k$ -space under-sampling even though all our scans were performed with multi-array receiver coils. To combine the multi-coil data, we only performed SENSE unfolding, which did not lead to any scan time reduction but resulted in high quality phase data without any confounding effects from under-sampling.

This chapter concludes the overview of background theory of MRI physics from MR signal generation to reconstructed MR images. In the next sections we briefly give an overview of the encoding of more physically relevant properties onto the MR signal to be able to later estimate quantitative parameter maps from reconstructed images.

## 2.2 Encoding of Physical Properties

The treatment to derive the MR signal (2.21) and the subsequently reconstructed image (2.30) in the previous Section 2.1 followed the time evolution of the net magnetization of an ensemble of protons. However, in human tissue these protons are always bound in

## 2 Background Theory

molecules and therefore surrounded by an electron cloud defining the protons' chemical environment. Electron clouds are subject to polarization by the main magnetic field and therefore generate their own magnetic field based on the magnetic susceptibility of the molecule. The polarization of electrons during an MRI experiment gives rise to three important effects: intravoxel-dephasing, the chemical shift, and phase accumulation over time due to bulk-susceptibility [3].

### 2.2.1 Intra-Voxel Dephasing

The magnetization density (2.17) can be expanded in frequency space into isochromats—ensembles of spins that precess with the same precession frequency. In a homogeneous static magnetic field in the absence of field inhomogeneities, all spins precess with the same angular frequency about  $\mathbf{H}_0$ . The magnetization density can therefore be written as

$$m(\mathbf{r}, t) = \int_{-\infty}^{\infty} m(\omega) e^{-i\omega(\mathbf{r})t} e^{-R_2(\mathbf{r})t} d\omega \quad (2.31a)$$

$$m(\omega) = \sum_{n=1}^N \mu_{xy_n}(\tau_p) \delta(\omega_0 - \omega_n), \quad (2.31b)$$

where  $\mu_{xy} = \mu_x + i\mu_y$  is the transverse component of a single spin. In this case all spins are in the same isochromat and precess with the Larmor frequency  $\omega_0$ . In a real MRI experiment however, there are always magnetic field inhomogeneities  $\Delta\mathbf{H}(\mathbf{r})$  of various sources present. Due to the main magnetic field in MRI,  $H_0\hat{\mathbf{z}}$ , being much stronger than any transverse components, one can assume the field inhomogeneities to only have a noticeable effect along the  $z$ -axis such that  $\Delta\mathbf{H}(\mathbf{r}) \approx \Delta H(\mathbf{r})\hat{\mathbf{z}}$ . These field inhomogeneities are typically assumed to follow a Lorentzian distribution and therefore lead to a distribution of precession frequencies in the spin ensemble, which is also of Lorentzian shape [27]:

$$m'(\omega) = \sum_{n=1}^N \mu_{xy_n}(\tau_p) \frac{(\gamma\Delta H(\mathbf{r}))^2}{(\gamma\Delta H(\mathbf{r}))^2 + (\omega - \omega_0)^2}$$

The magnetization distribution  $m'(\mathbf{r}, t)$  in the presence of field inhomogeneities thus writes [28]

$$m'(\mathbf{r}, t) = \int_{-\infty}^{\infty} \sum_{n=1}^N \mu_{xy_n}(\tau_p) \frac{(\gamma\Delta H(\mathbf{r}))^2}{(\gamma\Delta H(\mathbf{r}))^2 + (\omega - \omega_0)^2} e^{-i\omega(\mathbf{r})t} e^{-R_2(\mathbf{r})t} d\omega \quad (2.32a)$$

$$= \sum_{n=1}^N \mu_{xy_n}(\tau_p) e^{-i\omega_0 t} e^{-R_2 t} e^{-\gamma\Delta H(\mathbf{r})t}, \quad (2.32b)$$

where the relaxation terms can be combined by defining the effective transverse relaxation rate

$$R_2^* = R_2 + \gamma\Delta H = R_2 + R_2'.$$

## 2 Background Theory

The MR signal evolution in a more realistic situation including microscopic field inhomogeneities therefore effectively decays as

$$S'(t) \sim \int_V m(\mathbf{r}, t) e^{-i\omega_0 t} e^{-R_2^* t} d\mathbf{r}, \quad (2.33)$$

with the decay rate  $R_2^*$  describing irreversible signal decay by  $R_2$  due to the inherent thermalization and a reversible dephasing leading to the effective relaxation by  $R_2'$ . In a pure GRE sequence the two effects are not separable and subsequent echo signals in a multi-echo acquisition decay by  $\exp(-R_2^* \text{TE})$ . In comparison, in a SE sequence the refocusing pulses are able to refocus the dephasing due to the microscopic field inhomogeneities and subsequent spin echoes therefore decay by  $\exp(-R_2 \text{TE})$ . In both sequence types, assuming a different distribution of field inhomogeneities and resulting frequencies distributions, the relaxation behavior deviates from a simple mono-exponential decay.

The  $R_2^*$  value localized to a voxel holds information on the intra-voxel dephasing due to possible large external magnetic fields or a broad distribution of internal frequencies as it is created for example by the presence of small magnetic particles like contrast agents, natural iron depositions or microscopic highly concave structures like blood vessels or trabecular bone structures. To gain  $R_2^*$ -information about such tissues, the signal dynamics (2.33) needs to be sampled over multiple echoes either in multi-echo sequences, where additional echoes are formed in the same TR, multi-acquisition sequences, where the whole TR is repeated with a shifted read-out, or a combination of both [29]. The effective decay of the signal magnitude over echo times then encodes voxelwise information on the value of  $R_2^*$ .

### 2.2.2 Chemical Shift

Besides intra-voxel dephasing, the electron cloud polarization can lead to an additional effect on the signal dynamics. For observer protons inside a molecule, the field created by the polarized electron cloud is known as the demagnetization field [30], which is dependent on the chemical surrounding and the local geometry of the proton's location inside the molecule (electron configuration, angle and length of chemical bonds between nuclei, etc.). According to Lenz's law [31], the demagnetization field is opposed to the polarizing field, the main magnetic field  $\mathbf{H}_0$  in MRI. Protons in a specific chemical environment, a so-called chemical species denoted by subscript  $p$ , therefore experience a reduced field strength and precess with a specific Larmor precession frequency defined by their shielding constant  $\delta_p$ :

$$\omega_p = -\gamma H_0 (1 - \sigma_p) = \omega_0 (1 + \delta_p)$$

By convention the chemical shift in MRI (and magnetic resonance spectroscopy) is often given in units of the deshielding constant  $\delta_p$  [32]. Compared to water, most molecules in human tissue have a higher electron density and therefore a negative deshielding constant with respect to the assumed center frequency  $\omega_0$  tuned to the protons in water molecules. In body MRI the most important molecules, due to their large chemical shifts,

## 2 Background Theory

are lipids present in fatty tissue. These fat molecules hold a number of different chemical species, each with its own specific chemical shift. The most abundant chemical species in a fat molecule is the methylene group in fatty acid with its specific chemical shift of  $\delta_{CH_2} = -1.3$  ppm. When uncounted for, the presence of main fat peak with its large chemical shifts explain the infamous chemical-shift artifacts [27] in reconstructed MR images. In the signal equation (2.33) the presence of a single chemical species denoted  $p$  adds an additional magnetic field term to the precession of an observer proton:

$$S(t) \sim \int_V m(\mathbf{r}, t) \exp(-i\omega_0(1 + \delta_p)t) d\mathbf{r},$$

The factor  $\omega_0\delta_p$  leads to a modulation of the periodic precession of the magnetization around the main magnetic field with frequency  $\omega_0$ . Therefore, the dynamics of the signal  $S(t)$  over multiple echoes also effectively encodes the presence of species  $p$  in the modulated frequency of the signal phase. In Section 2.3.1, the signal evolution over echoes is given for the presence of multiple species, where the same concept of multi-echo imaging is needed to estimate properties of chemical species per voxel.

### 2.2.3 Susceptibility-Induced Phase Accumulation

Polarized electron clouds not only lead to the creation of the demagnetization field and consequent chemical shifts inside the molecules, but the same polarization mechanisms [3] also lead to dipolar magnetic fields outside of a polarized molecule, which affects observer protons in its surrounding. The unit dipolar field of a single magnetic dipole  $\mathbf{m}_{\mathbf{r}'}$  located at position  $\mathbf{r}'$  evaluated at location  $\mathbf{r}$  is given by

$$\mathbf{B}_m(\mathbf{r} - \mathbf{r}') = \frac{\mu_0(3(\mathbf{m}_{\mathbf{r}'} \cdot \hat{\mathbf{r}})\hat{\mathbf{r}} - \mathbf{m}_{\mathbf{r}'})}{4\pi|\mathbf{r} - \mathbf{r}'|^3} + \frac{2}{3}\mu_0\mathbf{m}_{\mathbf{r}'}\delta^3(|\mathbf{r} - \mathbf{r}'|), \quad (2.34)$$

where  $\hat{\mathbf{r}}$  is the unit vector in the direction of  $\mathbf{r} - \mathbf{r}'$  [14]. The magnetic field an observer proton at location  $\mathbf{r}$  experiences in an MRI scanner is the sum of the field contributions from all surrounding dipole fields: To derive the effective susceptibility-induced mean-field equations for an ensemble of dipole moments, technically one needs mathematically elaborate spatio-temporal averaging and the separation of far and near field contributions followed by a mathematical concept called the Lorentz correction connected to the theoretically important second term in (2.34) [33]. Without going in the necessary detail for a rigorous treatment, we just motivate the further derivation of the main equations, which are important for the explanation of the effects of the susceptibility-induced field and refer to [28] and [34] for in-depth mathematical descriptions. Heuristically stating the ad hoc equation for the susceptibility-induced field as

$$\mathbf{B}(\mathbf{r}) = \mu_0 \int_V \sum_{\mathbf{r}' \in V} \left[ \frac{3(\hat{\mathbf{r}} \cdot \mathbf{m}_{\mathbf{r}'})\hat{\mathbf{r}} - \mathbf{m}_{\mathbf{r}'}}{4\pi|\mathbf{r} - \mathbf{r}'|^3} + \frac{2}{3}\mathbf{m}_{\mathbf{r}'}\delta^3(|\mathbf{r} - \mathbf{r}'|) \right] d^3\mathbf{r}' \quad (2.35)$$

the ensemble of magnetic dipoles can be connected to the bulk magnetization vector as " $\sum_{\mathbf{r} \in V} \mathbf{m}_{\mathbf{r}} = \mathbf{M}(\mathbf{r})$ ". Furthermore, to derive effective mean-field equations, the volume

## 2 Background Theory

$V$  in (2.35) is virtually separated into the volume  $V'$  in which distant interactions between dipole momenta and observer spins take place on long ranges and the Lorentz volume in which near field interaction are taken into account, here incorporated into  $\mathbf{B}_{\text{near}}$ . There is a freedom to choose the size and geometry of the Lorentz volume, as it is merely a mathematical construct, however it needs to be chosen in such a way that in the inside of the volume, the contribution from the distant outside dipoles can be treated as a mean-field from an continuous outside medium. After such manipulations, not taken out here, Equation (2.35) can be written as

$$\mathbf{B}(\mathbf{r}) = \mu_0 \int_{V'} \left[ \frac{3(\hat{\mathbf{r}} \cdot \mathbf{M}(\mathbf{r}'))\hat{\mathbf{r}} - \mathbf{M}(\mathbf{r}')}{4\pi|\mathbf{r} - \mathbf{r}'|^3} \right] d^3\mathbf{r}' + \mathbf{B}_{\text{near}}(\mathbf{r}).$$

In MRI it is typically assumed that the magnetic dipole moments in a small volume element are randomly distributed, as we already made use of in Section 2.1.1. In this case, the near field term vanishes and by a proper choice of the Lorentz volume, which is still macroscopically small enough that its separation from  $V$  results in a much smaller total volume  $V'$ . Furthermore, the bulk magnetization vector in thermal equilibrium is given by

$$\mathbf{M}(\mathbf{r}) = \chi(\mathbf{r})\mathbf{H}_0$$

and, as we have seen in Section 2.1.1, the static main magnetic field  $\mathbf{H}_0(\mathbf{r}) = H_0\hat{\mathbf{z}}$ . With the  $z$ -component dominating the polarization due to the strong main magnetic field, the transverse equilibrium magnetization can again be neglected and the created susceptibility-induced additional field is given by

$$\begin{aligned} B_z(\mathbf{r}) &= \mu_0 H_0 \int_V \left[ \hat{\mathbf{z}}^T \frac{3(\hat{\mathbf{r}} \cdot \hat{\mathbf{z}})\hat{\mathbf{r}} - \hat{\mathbf{z}}}{4\pi|\mathbf{r} - \mathbf{r}'|^3} \chi(\mathbf{r}') \right] d^3\mathbf{r}' \\ &= \mu_0 H_0 \int_V \left[ \frac{3\cos^2\theta - 1}{4\pi|\mathbf{r} - \mathbf{r}'|^3} \chi(\mathbf{r}') \right] d^3\mathbf{r}', \end{aligned}$$

where  $\theta$  is the azimuthal angle between the  $z$ -axis and the  $xy$ -plane. By defining the unit dipole kernel

$$d(\mathbf{r}) = \begin{cases} 0 & \text{for } |\mathbf{r}| = 0 \\ \frac{3\cos^2\theta - 1}{4\pi|\mathbf{r}|^3} & \text{otherwise,} \end{cases} \quad (2.37)$$

the susceptibility-induced field can be written as the convolution

$$B_z(\mathbf{r}) = (d * \chi)(\mathbf{r}), \quad (2.38)$$

which is the basic equation for QSM [2]. In MR experiments the (unidirectional) demagnetization field (2.38) created by the bulk-susceptibility of the imaging object is superimposed on the main magnetic field and the total magnetic field inside an MR scanner is therefore

$$\mathbf{H}(\mathbf{r}) = \mathbf{H}_0 + \mathbf{B}_\chi(\mathbf{r}),$$

## 2 Background Theory

where the susceptibility-induced part is described via (2.38) as  $\mathbf{B}_\chi = B_z \hat{\mathbf{z}}$ . Thus, the signal evolution in MRI follows

$$S(t) \int_V m(\mathbf{r}, t) e^{i\gamma(H_0 + B_\chi)t} e^{-R_2^* t}, \quad (2.39)$$

where we introduce the notation  $B_\chi = |\mathbf{B}_\chi| = B_z$ . Equation (2.39) shows how the susceptibility-induced field contribution  $B_\chi$  leads to a phase accumulation in the complex MR signal, where for the static field the phase increase depends linearly on the echo time.

Typically, a clinical MR scanner has a system of dedicated gradient coils to produce the so-called shim field, which attempts to compensate the susceptibility-induced field contribution during the MRI sequence. Before the actual MR sequence, a sequence module is inserted, which measures line shapes in a whole volume MR Spectroscopy experiment or the spatial phase evolution in a fast low-resolution prescan. Based on these measurements, current strengths for the shim gradient coils are calculated so that the superposition of their created spherical harmonic field oppose and ideally cancel the susceptibility-induced field. The journal publication shows how the shim field can be introduced into a multi-echo parameter estimation of the magnetic field map.

### 2.3 MR Parameter Estimation

After the reconstruction of MRI images and their dynamics that encode the tissue parameters of interest, the task of MR parameter estimation techniques is to extract quantitative voxel value estimates of such parameters. This thesis primarily employed parameter estimation for quantitative WFI and QSM, which are described in the next two sections.

#### 2.3.1 Water–Fat Imaging

As stated in Section 2.2.2, the presence of chemical species is encoded in the MR signal evolution. In body MRI the most important chemical species are lipids that have a number of hydrogen atoms bound at different locations inside fatty acid molecules each with their own specific resonance due their different chemical environment. The different chemical environments of the protons in the lipid molecule lead to different peaks in the lipid's MR spectrum. WFI uses acquisitions of multiple echos at increasing echo times to estimate the "contributions of the fat peaks" to the MR signal, yielding important biomarkers like e.g. the proton-density fat fraction and other specific parameters in fatty tissues like  $R_2^*$ . The time evolution of the complex MR signal inside a single voxel,  $s_n \equiv s(t_n)$ , can be written in general as

$$s_n = \sum_{p=1}^P \varrho_p e^{i\phi_p} e^{(i\omega_p - r_p) t_n}, \quad (2.40)$$

where the contribution to the signal from fat peak  $p = 1, \dots, P$  is characterized by its magnitude  $\varrho_p$ , phase after the RF-excitation (at  $t = 0$ )  $\phi_p$ , resonance frequency  $\omega_p$  and transverse relaxation rate  $r_p$ .

## 2 Background Theory

Since the estimation of the whole set of model parameters  $\{\varrho_p, \phi_p, \omega_p, r_p\}$ ,  $p = 1, \dots, P$  in (2.40) would require an impractical amount of echoes  $s_n$ , it is necessary to reduce the number of parameters on the right hand side of (2.40). A typical example in WFI is the reduction of (2.40) to the widely used multi-peak single- $R_2^*$  model by fixing the chemical-shifts of all  $p \in 2, \dots, 10$  fat peaks—assuming the first peak  $p = 1$  corresponds to the water peak—to a priori values normally obtained from MR spectroscopy by setting  $\omega_m = \omega_1 + \delta\omega_p$ ,  $p \in 2, \dots, P$ . Furthermore, all peaks, including water are assumed to decay with the same relaxation time  $R_2^*$ , which finally yields

$$\begin{aligned}\hat{s}_n &= (W + c_n F) e^{(i2\pi f_B - r_2^*)t_n}, \\ c_n &= \sum_{p=1}^P a_p e^{i2\pi\delta f_p t_n}, \quad \text{with} \quad \sum_{p=1}^P a_p = 1,\end{aligned}\tag{2.41}$$

where we substituted  $W = \rho_1 \exp(i\phi_1)$  and  $f_B = \omega_1/2\pi$  for the water peak and  $F\alpha_p = \varrho_p \exp(i\phi_p)$ ,  $p \in \{1, \dots, P\}$  for the fat peaks.

The signal model given by equation (2.41) describes the signal in a single observation at acquired echo time  $t_n$ . The definition of the following model matrix [35, 36]

$$\mathbf{A}(f_B, R_2^*) = \text{diag} \left[ e^{(i2\pi f_B - R_2^*)t_1}, \dots, e^{(i2\pi f_B - R_2^*)t_n} \right] \begin{pmatrix} 1 & \sum_{p=1}^P \alpha_p e^{i2\pi\delta f_p t_1} \\ \vdots & \vdots \\ 1 & \sum_{p=1}^P \alpha_p e^{i2\pi\delta f_p t_n} \end{pmatrix}, \tag{2.42}$$

allows to write the signal model in the multi-observation matrix formulation

$$\hat{\mathbf{s}} = [s_1, \dots, s_n]^\top = \mathbf{A}(f_B, R_2^*)[W, F]^\top. \tag{2.43}$$

The least-squares parameter estimation problem is then stated as

$$W, F, f_B, R_2^* = \arg \min_{W', F', f'_B, R_2^{*'}} \|\mathbf{s} - \hat{\mathbf{s}}(W', F', f'_B, R_2^{*'})\|_2^2. \tag{2.44}$$

By means of the Variable Projection (VARPRO) [37] the linear parameters in (2.44) can be substituted by

$$[W, F]^\top = \mathbf{A}^+(f_B, R_2^*)\hat{\mathbf{s}}, \tag{2.45}$$

where  $\mathbf{A}^+$  is the Moore-Penrose pseudo-inverse of matrix (2.42), resulting in the optimization

$$f_B, R_2^* = \arg \min_{f'_B, R_2^{*'}} \|(1 - \mathbf{A}\mathbf{A}^+)\hat{\mathbf{s}}\|^2, \tag{2.46}$$

which only minimizes the nonlinear parameters  $f_B, R_2^*$  in the signal model (2.41) as the linear parameters  $W$  and  $F$  are determined by (2.45). The VARPRO minimization problem (2.46) specific to the single- $R_2^*$  was generalized to the broader class of weighted sums of complex exponentials with phase terms linearly varying in the echo time [38]

## 2 Background Theory

and can in general be solved by standard nonlinear fitting but faces three important challenges:

First, the field map parameter  $f_B$  is subject to phase wrapping and its value can only be determined up to modulo  $2\pi$ . In standard WFI primarily interested in the other model parameters, a wrapped field map is not important, but in cases where further processing of the field map is needed—as for QSM described in the next section—the wrapping needs to be taken into account.

Second, and also connected to the complex exponential with the time-dependent argument scaled by the field map parameter, the least-squares cost function (2.46) is non-convex in the field map parameter. The nonlinearity of the field map parameter often leads to the occurrence of multiple local minima of the cost function that can correspond to unphysical parameter combinations. A convergence of the field map to such local minima can lead to the infamous water–fat swaps, where the water and the fat signal in a voxel are assigned the wrong way [39]. Iterative nonlinear optimization schemes therefore require an initialization of the field map close to the true parameter value to ensure convergence to the global minimum. Finding a good initialization of the field map often necessitates the incorporation of additional information to the single-voxel minimization problem (2.46). In Section 3.2, we developed a method to add prior knowledge from several field map contributions to the problem. Another common approach is to incorporate neighborhood information of each voxel and set up a global cost function for all voxels similar to

$$f_B, R_2^* = \arg \min_{f'_B, R_2^{*'}} \sum_{\mathbf{r}} \left[ \left\| (1 - \mathbf{A}(f'_B, R_2^{*'})) \mathbf{A}^+(f'_B, R_2^{*'}) \mathbf{s} \right\| + \sum_{\mathbf{r}' \in \mathcal{N}(\mathbf{r})} U(|f'_B(\mathbf{r}) - f'_B(\mathbf{r}')|^2) \right], \quad (2.47)$$

where the least-squares terms for all voxels are summed up and an "interaction term"  $U$  between each voxel (at discrete location  $\mathbf{r}$ ) and its neighborhood voxels at  $\mathbf{r}' \in \mathcal{N}(\mathbf{r})$  is added. Such global minimization problems can successfully be solved with graph cut algorithms [40], first demonstrated for WFI in [41] and further developed and employed in specific applications in [42, 43, 44]. A refined single-iteration graph cut algorithm for WFI field map initialization was also developed in [45, 46, 47] yielding optimal swap-free water–fat parameter estimates and simultaneously unwrapped and unsmoothed field maps for further processing.

The third challenge in solving (2.46) (or the first term in the global estimation (2.47)) is the noise propagation in the optimization, which depends on the echo time selections in combination with the physical tissue parameters. At certain unfavorable combinations of echo times and model parameters, the noise in the input data  $\mathbf{s}$  amplifies in the parameter estimates, which renders them useless for later diagnostic purposes. It is therefore important to choose well-suited echo times for the expected tissue parameters to optimally design the experiment before the data acquisition. The standard method for such an optimal experimental design in terms of echo time selection and model parameters is the Cramér-Rao analysis [48, 49], based on the computation of the Fisher Information Matrix (FIM) [50] for the chosen signal model. The FIM is defined as the expectation

## 2 Background Theory

value ( $\mathbb{E}[\dots]$ ) of the second derivative of the log-likelihood  $\ln \mathcal{L}$ :

$$\mathbf{I}_{kl} = \mathbb{E} \left[ \frac{\partial}{\partial \beta_l} \frac{\partial}{\partial \beta_k} \ln \mathcal{L} \right],$$

where the likelihood  $\mathcal{L}$  in the case of additive white Gaussian noise with variance  $\sigma^2$  follows

$$\mathcal{L} \sim \exp \left( -\frac{1}{2\sigma^2} \|\mathbf{s} - \mathbf{A}\boldsymbol{\varrho}\|_2^2 \right), \boldsymbol{\varrho} = [W, F]^\top$$

In general, the FIM is then given by

$$\mathbf{I} = \frac{1}{\sigma^2} \text{Re} \left\{ \mathbf{J}^\dagger \mathbf{J} \right\}, \quad (2.48)$$

where  $\mathbf{J}$  is the Jacobian of the chosen signal model [51]. In the case of the widely used single- $R_2^*$  signal model (2.41), the Jacobian, which defines the FIM by (2.48), is

$$\mathbf{J} = \left[ \frac{\partial \hat{\mathbf{s}}}{\partial |W|}, \frac{\partial \hat{\mathbf{s}}}{\partial |F|}, \frac{\partial \hat{\mathbf{s}}}{\partial \angle W}, \frac{\partial \hat{\mathbf{s}}}{\partial \angle F}, \frac{\partial \hat{\mathbf{s}}}{\partial f_B}, \frac{\partial \hat{\mathbf{s}}}{\partial R_2^*} \right].$$

The Cramér-Rao Lower Bound (CRLB), which gives the theoretically minimal variances (Var) of the parameter estimates [51], is defined as the

$$\text{CRLB} = \text{diag} \mathbf{I}^{-1} = [\text{Var} |W|, \text{Var} |F|, \text{Var} \angle W, \text{Var} \angle F, \text{Var} f_B, \text{Var} R_2^*]^\top.$$

Minimizing the CRLB model parameters of interest and/or different echo samplings can be used for optimal design [52] of the experimentally selected echo times. In the journal publication [38] from Section 3.3, we also generalized the Cramér-Rao noise performance analysis to a broad class of signal models by formulation of a model-agnostic Jacobian.

With the Cramér-Rao analysis for the scenario of WFI, where phase unwrapping of the field map parameter is not of major importance, the above challenges of field map initialization and echo time selection optimal with respect to the Signal-to-Noise ratio (SNR) can be adequately addressed. After successful WFI parameter estimation, clinically important radiological biomarkers can then be collected and determined, like e.g. tissue  $R_2^*$  or the Proton Density Fat Fraction (PDFF), which is computed in a magnitude discrimination method [53] as

$$\text{PDFF} = \begin{cases} 1 - \frac{|W|}{|W+F|} & \text{for } |W| > |F| \\ \frac{|F|}{|W+F|} & \text{for } |W| \leq |F|, \end{cases}$$

which is generally more noise robust against phase errors in the input images than simply computing the PDFF as  $|F|/|W| + |F|$ . WFI and our proposed generalized chemical-species separation can be seen and is mathematically equivalent to the field mapping step in QSM in the body, where the presence of fat needs to be addressed.

### 2.3.2 Quantitative Susceptibility Mapping

QSM reconstructs tissue susceptibility from complex GRE data and is formally comprised of three algorithmic steps to extract spatial information about the underlying magnetic susceptibility distribution of the imaging objects: i) Magnetic-field mapping, ii) Background Field Removal (BFR), iii) Field-to-Susceptibility Dipole Inversion (DI). In the following sections we briefly describe the key ideas of each of these algorithmic steps.

#### Magnetic-Field Mapping

Starting from complex multi-gradient-echo MR images, the first step in QSM is the estimation of the magnetic field inside the MR scanner during the scan. For a simple one-component MR signal model with only on-resonant water protons as the only chemical species present, the signal phase evolution  $\phi(t)$  is directly proportional to the field map  $f_B$  as

$$s(t) = M(t) \exp(i\phi(t)), \quad \phi(t) = 2\pi f_B t. \quad (2.49)$$

In tissues containing water-fat mixtures, the magnetic field mapping step needs to account for the presence of different chemical species as those lead to superimposed modulations on the signal evolution. The water-fat separation algorithm described in the previous Section 2.3.1 can be used to accurately estimate the field map value for each voxel, which is automatically corrected for the modulations due to different involved chemical shifts.

However, analogous to the original MR phase being available only via the phasor  $\exp(i\phi(t))$  of the complex image signal (2.49), the argument of the phasor  $\exp(i2\pi f_B t)$  in the water-fat signal model (2.41) is also subject to phase wrapping and consequently its value  $\phi = 2\pi f_B t$  is also only ambiguously defined up to modulo  $2\pi$ . The wrapped phase value  $\phi_{\text{wr}}$  underlies the principal (unwrapped phase) value  $\phi_{\text{unwr}}$  carrying an unknown multiple of  $2\pi$ :

$$\phi_{\text{wr}} = \phi_{\text{unwr}} + n2\pi, \quad \phi_{\text{wr}} \in (-\pi, \pi], \quad n \in \mathbb{Z}$$

There are several proposed algorithms for phase unwrapping [54], which try to find the correct multiple  $2\pi n$  and subtract it from the wrapped phase to obtain an unwrapped phase map without unphysical discontinuities. A common fast algorithm to unwrap the field map term  $\phi_{\text{wr}} = 2\pi f_B t$  is based on the following identity [55]

$$\nabla^2 \phi_{\text{unwr}} = \text{Im} \left\{ \frac{\nabla^2 e^{i\phi_{\text{wr}}}}{e^{i\phi_{\text{wr}}}} \right\} = \cos \phi_{\text{wr}} \nabla^2 \sin \phi_{\text{wr}} - \sin \phi_{\text{wr}} \nabla^2 \cos \phi_{\text{wr}}.$$

The Laplacian unwrapping method [56] inverts the Laplacian operator and computes

$$\phi_{\text{unwr}} = \nabla^{-2} [\cos \phi_{\text{wr}} \nabla^2 \sin \phi_{\text{wr}} - \sin \phi_{\text{wr}} \nabla^2 \cos \phi_{\text{wr}}].$$

The unwrapped field map is finally given by

$$f_B = \phi_{\text{unwr}} / 2\pi t,$$

as it was computed in the journal publication [57] in Section 3.4. The field map  $f_B$  is then input for the subsequent QSM step removing background field contributions.

### Background Field Removal

The measured magnetic field  $f_B$  in a certain ROI is a combination of different contributions from susceptibility sources inside the ROI and long-ranged field perturbation from sources outside the ROI, since the whole imaging object is magnetized through the main magnetic field and the susceptibility-induced magnetic fields generally extend through the whole imaging FOV. A large contribution from outside the FOV is often created by the large susceptibility difference ( $\approx 9$  ppm) between soft tissue and air. In typical MRI scans with limited FOVs not covering the whole object inside the MRI scanner, these air-tissue boundaries lie outside the FOV, but have field map contributions ranging inside the ROI. Typical susceptibility differences inside the imaging object are in the sub-ppm range and their magnetic fields are therefore much smaller than the background field, which can practically complicate the unique separation of the background field from the measured total magnetic field  $\mathbf{B} = [0, 0, 2\pi f_B/\gamma]^\top$  [58]. Background field removal techniques aim at the removal of field map contributions from susceptibility sources outside the ROI. From first principles of magnetostatics [14], the magnetic fields in the absence of macroscopic current satisfy the following equations

$$\begin{aligned}\mathbf{B} &= \mu\mathbf{H} \\ \nabla \cdot \mathbf{B} &= 0 \\ \nabla \times \mathbf{H} &= 0,\end{aligned}$$

where the total magnetic field  $\mathbf{B}$  is related to the external magnetic field  $\mathbf{H}$  via the permeability  $\mu = 1 + \chi$ . Assuming a linear medium with scalar susceptibility  $\chi \ll 1$ , as it is valid for human tissue [3], from (2.50) it follows that

$$\nabla \times \frac{\mathbf{B}}{\mu} = \frac{1}{\mu} \nabla \times \mathbf{B} - \mathbf{B} \nabla \times \frac{1}{\mu} \quad (2.51a)$$

$$= \frac{1}{\mu} \nabla \times \mathbf{B} + \frac{1}{\mu^2} \mathbf{B} \times \mu = 0. \quad (2.51b)$$

Employing the vector identities

$$\nabla \times (f\mathbf{A}) = f(\nabla \times \mathbf{A}) - \mathbf{A} \times (\nabla f) \quad (2.52a)$$

$$\nabla \times (\mathbf{A} \times \mathbf{B}) = (\mathbf{B} \cdot \nabla)\mathbf{A} - (\mathbf{A} \cdot \nabla)\mathbf{B} + \mathbf{A}(\nabla \cdot \mathbf{B}) - \mathbf{B}(\nabla \cdot \mathbf{A}), \quad (2.52b)$$

and substituting  $1/\mu$  with  $\chi \ll 1$  leads to

$$\nabla^2 \mathbf{B} = \nabla \times (\mathbf{B} \times \nabla \chi) \quad (2.53a)$$

$$= \mathbf{B} \nabla^2 \chi - (\mathbf{B} \cdot \nabla) \nabla \chi. \quad (2.53b)$$

With the standard approximation of the dominating external main magnetic  $\mathbf{B} = B\hat{\mathbf{z}}$ , one can neglect the transverse components and the single  $z$ -component of the total field  $\mathbf{B}$  writes

$$\nabla^2 B = B \left( \nabla^2 \chi - \frac{\partial^2 \chi}{\partial z^2} \right).$$

## 2 Background Theory

In theory the total magnetic field  $B$  can be uniquely separated into the local ( $B_L$ ) and the background field ( $B_{bg}$ ) contributions

$$B = B_L + B_{bg} = d * (\chi_L + \chi_{bg}). \quad (2.54)$$

For a defined ROI  $\Omega$  in the imaging volume, by definition the local and the background field have a zero source distribution outside and inside of  $\Omega$ , respectively, and therefore, they obey the cases

$$\nabla^2 B_{bg} = \begin{cases} 0 & \forall \mathbf{r} \in \Omega \\ B \left( \nabla^2 \chi_{bg} - \frac{\partial^2 \chi_{bg}}{\partial z^2} \right) & \forall \mathbf{r} \notin \Omega \end{cases} \quad (2.55a)$$

$$\nabla^2 B_L = \begin{cases} B \left( \nabla^2 \chi_L - \frac{\partial^2 \chi_L}{\partial z^2} \right) & \forall \mathbf{r} \in \Omega \\ 0 & \forall \mathbf{r} \notin \Omega. \end{cases} \quad (2.55b)$$

For the BFR step the important observation is that the background field inside the ROI  $\Omega$  solves the Laplace equation

$$\nabla^2 B_{bg} = 0, \quad \mathbf{r} \in \Omega, \quad (2.56)$$

which governs the mathematical properties of the background field on which many BFR algorithms are based on [59]. By adhering to the Laplace equation (2.56), it follows that the background field is spherically harmonic and as such has the mean value property

$$B(\mathbf{r}) = (\rho * B)(\mathbf{r}),$$

for any spherical convolution kernel  $\rho(\mathbf{r})$ . A class of BFR algorithms [60] is based on the identity

$$B - \rho * B = (\delta - \rho) * B \quad (2.57a)$$

$$= B_L + B_{bg} - \rho * B_L - \rho * B_{bg} \quad (2.57b)$$

$$= B_L + B_{bg} - \rho * B_L - B_{bg} \quad (2.57c)$$

$$= (\delta - \rho) * B_L, \quad (2.57d)$$

where  $\delta$  is the convolution unit element, the Dirac distribution. Such deconvolution algorithms differ in the choice of suitable spherical kernels  $\rho$  and compute the deconvolution ( $*^{-1}$ )

$$B_L = (\delta - \rho) *^{-1} [(\delta - \rho) * B],$$

which involves the inherent assumption that there are no sources of the background field close to the boundary of the ROI  $\Omega$  as those would contribute to the convolution values at distances closer than half of the kernel width of  $\rho$  to the boundary  $\partial\Omega$ . Hence, the disadvantage of deconvolution algorithms can be the appearance of artifacts appearing close to the boundary  $\partial\Omega$ , where the assumption might not be valid. In extension to the original deconvolution method (Sophisticated Harmonic Artifact Reduction for Phase

## 2 Background Theory

data (SHARP) [59]), methods trying to mitigate those artifacts have been proposed which include varying radii of the deconvolution kernel (Variable-kernel Sophisticated Harmonic Artifact Reduction for Phase data (vSHARP) [61]) or additional regularization (Regularization-Enabled Sophisticated Harmonic Artifact Reduction for Phase data (RESHARP) [60]). The initial assumption of absent background field sources close to  $\partial\Omega$  still poses challenges to the application of BFR algorithms in body QSM with common reduced FOVs cropping the imaging object.

Besides the deconvolution algorithms, there is also the method of Projection onto Dipole Fields (PDF) [62], which is based on the different assumption of orthogonality of the local and background field, motivated by the Hilbert Projection Theorem [63]. Since  $B = d * \chi$  (see Equation (2.38)), any field  $B$  can be represented as an element in a Hilbert space spanned by the dipole moments  $\mathbf{d}(\mathbf{r})$ . According to (2.55), the local field  $B_L$  is spanned by dipoles inside the ROI,  $\{\mathbf{d}(\mathbf{r})|\mathbf{r} \in \Omega\}$ , whereas the background field is created by outside dipoles,  $\{\mathbf{d}(\mathbf{r})|\mathbf{r} \in \bar{\Omega}\}$ . The assumption is that  $\mathcal{D}_L \perp \mathcal{D}_{bg}$ , where  $\mathcal{D}_L = \text{span}\{\mathbf{d}(\mathbf{r})|\mathbf{r} \in \Omega\}$  and  $\mathcal{D}_{bg} = \text{span}\{\mathbf{d}(\mathbf{r})|\mathbf{r} \in \bar{\Omega}\}$ . The Projection Theorem then ensures that  $\arg \min_{B^* \in \mathcal{D}_{bg}} \|B - B^*\|_2$  has a unique value, which is the true background field  $B_{bg}$ . The local field, orthogonal to  $\mathcal{D}_{bg}$ , is determined by  $B - B_{bg}$ . With the separability (2.54) of the total field, the PDF method computes a susceptibility distribution outside the ROI  $\Omega$  by solving the minimization problem

$$\chi_{bg} = \arg \min_{\chi'_{bg}(\mathbf{r}), \mathbf{r} \in \bar{\Omega}} \|B - d * \chi'_{bg}\|_2, \quad (2.58)$$

and forward simulating the local field as

$$\mathbf{B}_L = B - d * \chi_{bg}.$$

The algorithmic formulation of PDF is already close to field-to-susceptibility DI methods, but restricted to the outside of a defined ROI by spatial masking. PDF has been shown to give accurate and robust results in brain QSM and was also extensively used in the studies for this thesis. However, the PDF method can also lead to significant artifacts close to the edges of the ROI, where the orthogonality assumption can be violated and the unregularized minimization (2.58) can result in over-fitting of field contributions from local sources. Hence PDF can be challenging, again especially in body QSM, when the imaging objects is cropped by the FOV and/or ROI.

A last method, which was primarily employed in this work, is the Laplacian Boundary Value (LBV) method [64]. LBV directly solves the Laplace equations (2.56) under the assumptive boundary condition that the measured total magnetic field at the boundary of the ROI is solely composed of the background field  $B_{bg}$ . The local field  $B_L$  at the border  $\partial\Omega$  is then assumed to vanish. The LBV problem for BFR is therefore

$$\nabla^2 B_{bg} = 0, \quad B_{bg}(\partial\Omega) \approx B,$$

which is typically solved by an iterative multi-grid method [65]. LBV shows a fast convergence towards a BFR result with significant less artifacts at ROI boundaries and could successfully be used in the body QSM study [57].

There are several more BFR techniques proposed in literature—often variations or extensions to the algorithms presented above. A comprehensive overview and comparisons can be found in [58].

### Field-to-Susceptibility Dipole Inversion

The next step after BFR and the last in a QSM processing pipeline is the field-to-susceptibility DI. Given the local tissue field  $B_L$  (2.54), presumably created only by susceptibility sources inside the ROI  $\Omega$ , dipole inversion aims to recover the underlying susceptibility distribution according to the convolution equation (2.38) describing a scalar tissue susceptibility model:

$$B_L(\mathbf{r}) = (d * \chi)(\mathbf{r}), \quad (2.59)$$

with  $d$  as the dipole kernel in the image domain (2.37). The forward dipole model (2.59) is typically transformed to the Fourier domain where the convolution becomes a point-wise multiplication

$$\tilde{B}_L(\mathbf{k}) = (\mathbf{D} \cdot X)(\mathbf{k}),$$

where  $\tilde{B}_L = \mathcal{F}\{B_L\}$ ,  $X = \mathcal{F}\{\chi\}$  and the transformed dipole kernel

$$\mathbf{D}(\mathbf{k}) = \mathcal{F}\{d(\mathbf{r})\} = \frac{1}{3} - \frac{k_z}{|\mathbf{k}|^2}.$$

After their magnetization many different susceptibility distributions can theoretically result in the same created magnetic field. Thus, it is clear that the relation of  $\chi$  to  $B_L$  is not a one-to-one, but a many-to-one mapping resulting in an ill-posed inverse problem to recover  $X(\mathbf{k})$  from the measured  $\tilde{B}_L$ . Furthermore, the field-to-susceptibility inversion is ill-conditioned, as the dipole kernel in Fourier space,  $\mathbf{D}(\mathbf{k})$ , goes to zero at the cone surface where  $k_z^2 = |\mathbf{k}|^2/3$ . The naive approach to discard this zero cone surface from a possible susceptibility reconstruction like

$$\chi(x) = \mathcal{F}^{-1}\{X(\mathbf{k})\}, \quad (2.60a)$$

$$X(\mathbf{k}) = \begin{cases} 0 & , \text{ where } k_z^2 = |\mathbf{k}|^2/3 \\ \mathbf{D}^{-1}(\mathbf{k}) \cdot \tilde{B}_L & , \text{ otherwise } \end{cases} \quad (2.60b)$$

is therefore not successful, because the noise present in all practical measurements of  $\tilde{B}_L$  will be amplified close to the zero cone surface, where the values of the dipole kernel  $\mathbf{D}$  are small. Such noise amplification features of the ill-conditioned field-to-susceptibility inversion in QSM lead to the infamous streaking artifacts—patterns in image-space with crossings at the magic angle of 54.7 deg of largely erroneous susceptibility values [2].

To prevent such streaking and select a possible susceptibility distribution according to additional a priori information, one needs to regularize the inverse field-to-susceptibility

## 2 Background Theory

problem. Such a regularization can be written in the form of the minimization problem to find  $X(\mathbf{k})$  via

$$X(\mathbf{k}) = \arg \min_{\chi'} \left\| \left( \tilde{B}_L - D \mathcal{F}\{\chi'\} \right) \right\|_2^2 + \lambda R[\chi'], \quad (2.61)$$

where the regularization term  $R[\chi]$  on the right added to the data fidelity term on the left incorporates prior information to the field-to-susceptibility inversion. In QSM literature the minimization (2.61) has been solved for many different regularizers  $R[\chi]$  and with different numerical algorithms. We briefly show two different methods, both examples of two possible classifications of QSM algorithms, a direct method and an iterative method, which were both used for the journal publication from Section 3.4.

A possibility to directly find a closed form solution to the inversion (2.61) is given for the regularizer

$$R_{\text{pc}}[\chi; \lambda] = \lambda \mathcal{F}\{\|\nabla \chi(\mathbf{k})\|_2^2\} = \lambda \|-i\mathbf{k}X(\mathbf{k})\|_2^2, \quad (2.62)$$

where  $\lambda$  is a hyperparameter balancing the data fidelity and the regularization term and that needs to be optimally fixed for each measured local field map  $\tilde{B}_L$ . As the gradient in image-space of the spatial susceptibility distribution adds to the cost function that is minimized in (2.61), the regularizer using the Euclidian norm promotes a susceptibility that is piecewise constant in space. The fact that for this regularizer, the regularization term and the data fidelity use the same Euclidian norm, simplifies the minimization problem, which can consequently be cast into the linear algebraic equation

$$(D^\dagger D + \lambda k^2)X = D^\dagger \tilde{B}_L,$$

solvable by simple inversion of the diagonal matrix  $(D^\dagger D + \lambda k^2)$  to obtain the susceptibility

$$\chi = \mathcal{F}^{-1}\{(D^\dagger D + \lambda k^2)^{-1} D^\dagger \tilde{B}_L\}. \quad (2.63)$$

Besides the obvious quick reconstruction time due to only the point-wise multiplication in-between a forward and an inverse Fourier transforms—on the order of a few second or even faster on modern personal computers—the closed-form solution has several drawbacks:

The regularizer (2.62) with the gradient operator does not take into account any prior information from the image-base domain, often leading to over-smoothed susceptibility distributions. Natural edges between different tissue types, where one would also expect different susceptibilities, are discarded in QSM inversion (2.63), which leads to a damping of the dynamic range of susceptibility values and blurred edges in the QSM reconstruction. Furthermore, the closed-form solution purely computed in k-space is not directly able to incorporate noise-weighting based on SNR information in image-space.

To overcome such limitations a number of different combinations of better suited data fidelity and regularization terms have been proposed. Here, we introduce one prominent example of an iterative field-to-susceptibility inversion, the Morphology-Enabled Dipole

## 2 Background Theory

Inversion (MEDI) technique [66, 67, 2]. The main idea of MEDI, is to incorporate prior information from the image domain into the QSM inversion by choosing a more complex regularizer, a different data fidelity term and additional, possibly dynamic, weights, all in the image domain in order to tightly control the noise amplification property of the inverse problem. As the name suggests, the prior in MEDI is based on the morphology of the imaging object that is determined from the complex raw input images from before the field mapping step. The MEDI regularizer is given by

$$R_{\text{MEDI}}[\chi; \lambda] = \lambda \|\mathbf{W}_g(\mathbf{r}) \nabla \chi(\mathbf{r})\|_1, \quad (2.64)$$

where the gradient-weighting  $\mathbf{W}_g$  is a morphological edge-mask given by

$$\mathbf{W}_g(\mathbf{r}) = \begin{cases} 0 & \text{for } L|I|(\mathbf{r}) < \tau \\ 1 & \text{otherwise} \end{cases},$$

where  $L$  is an edge-detecting operator from standard image processing such as the Canny or Sobel operator [68] acting on an input image  $|I|$  with its result heuristically thresholded by the parameter  $\tau$ . In the brain the threshold  $\tau$  is typically chosen such that the ratio of edges voxels to other voxels inside the GRE magnitude image of the masked brain is around 30 %. The  $\ell_1$  norm in the MEDI regularizer (2.64) ensures the promotion of sparse susceptibility distributions in the gradient domain, which reinforces the prior assumption of piecewise constant susceptibility distributions. The weighting  $\mathbf{W}_g$  practically switching off any regularization on morphological edges in the susceptibility map together with the  $\ell_1$  norm in (2.64) leads to a better streaking artifact reduction compared to the regularizer (2.62). In addition to the improved regularization term, MEDI type QSM algorithms also often use a different nonlinear formulation of the data fidelity term to more closely follow the noise distribution of the complex raw input images, where the susceptibility distribution enters the forward convolution model in the argument of a complex exponential [69, 70]. The corresponding full cost function to be optimized in MEDI then writes

$$X(\mathbf{k}) = \arg \min_{\chi'} \left\| \mathbf{W}_d (e^{iB_L} - e^{id*\chi'}) \right\|_2^2 + \lambda \|\mathbf{M} \nabla \chi(\mathbf{k})\|_1, \quad (2.65)$$

where the data fidelity term is also given in the image domain with the added data-weighting  $\mathbf{W}_d$ , which is practically determined by the SNR in the input images and possibly refined in iterative solvers. The nonlinear formulation of the data fidelity term ensures that the noise distribution in the measured field map  $B_L$  is Gaussian as this assumption is in line with the Bayesian interpretation of the QSM minimization [71]. The MEDI optimization (2.65) can be solved via several different algorithms. Popular methods in literature are the Split-Bregman or ADMM method [70] or Gauss-Seidel-like algorithms [2]. MEDI can be viewed as the starting point and basis of reference for most state-of-the-art iterative QSM algorithms and is often adapted to specific clinical research questions and applications by combination of linear or nonlinear data fidelity terms with different regularizers such as total variation or total generalized variation, zero-norm, Tikhonov, and more.

## 2 Background Theory

In our journal publication 3.4, we compared different MEDI type regularizer and a direct closed form QSM algorithm for the body QSM application of trabecular bone density mapping. For comparisons of several more different regularizers and single-step approaches in brain applications we refer to [72].

Besides the direct and iterative QSM inversion algorithms, there are other classes that we can only briefly mention here, namely single-step methods, Total Field Inversion (TFI), Deep-Learning-based QSM employing neural networks, and multi-orientation QSM methods. While single-step methods combine the BFR and the DI step into one formulation of a joint cost function [73], TFI does not perform any BFR, but inverts the total measured magnetic field after field mapping [74]. For Deep-Learning-based QSM, neural networks need to be trained using input training data and labeling QSM reconstructions from a different QSM method (supervised learning) in order to inherently represent a QSM forward model, which is then employed in the reconstruction (prediction) step for new input of unseen data [75]. Multi-orientation QSM methods use a more realistic tensor susceptibility model, whose parameter estimation needs scans of the same imaging object but with different orientations with respect to the main magnetic field  $\mathbf{H}_0$  [76, 77] and are therefore much more difficult to introduce into clinical practice. In a recent QSM reconstruction challenge, it became evident that under all state-of-the-art methods, iterative methods currently perform best for a controlled numerical brain phantom [78].

This concludes our treatment of background theory from basic concepts of MRI experiments to obtained parameter estimates in the form of quantitative anatomical maps of tissue properties. In the next chapters we summarize and discuss our applications of the above methods in the field of WFI and body QSM.

## 3 Comprising Journal Publications

This thesis comprises three original first-authored journal publications that cover a novel method for field map initialization in WFI (Section 3.2), a generalized framework for multi-parameter estimation from multi-echo signals (Section 3.3), and a proof-of-concept of body QSM measuring trabecular bone density (Section 3.4).

### 3.1 Compliance with Ethical Standards

All investigations performed in studies involving human participants were in accordance with the ethical standards of the institutional and/or national research committee and with the 1964 Helsinki declaration and its later amendments or comparable ethical standards. Informed consent was obtained from all individual participants included in the studies.

### 3.2 Journal Publication I: Improving Chemical Shift Encoding-Based Water–Fat Separation based on a Detailed Consideration of Magnetic Field Contributions

The publication entitled *Improving Chemical Shift Encoding-Based Water–Fat Separation based on a Detailed Consideration of Magnetic Field Contributions* was published in *Magnetic Resonance in Medicine* (ISSN: 1522-2594) on 9 February 2018 under the Creative Commons License (© ⓘ ⓘ). [79]. The article also appeared in *MRI of Obesity and Metabolic Disorders* [https://onlinelibrary.wiley.com/doi/toc/10.1002/\(ISSN\)1522-2594.MRI-obesity-metabolic-disorders](https://onlinelibrary.wiley.com/doi/toc/10.1002/(ISSN)1522-2594.MRI-obesity-metabolic-disorders). Results from this work were also presented in a previous conference submission [80], which was awarded the International Society for Magnetic Resonance in Medicine (ISMRM) Magna Cum Laude Merit Award and was invited for oral presentation at the ISMRM annual meeting 2016. Figure 5 of this journal publication was chosen for the cover of Volume 80 Issue 3 of *Magnetic Resonance in Medicine* (ISSN: 1522-2594) September 2018 [81].

#### 3.2.1 Abstract

##### Purpose

To improve the robustness of existing chemical shift encoding-based water–fat separation methods by incorporating a priori information of the magnetic field distortions in complex-based water–fat separation.

## **Methods**

Four major field contributions are considered: inhomogeneities of the scanner magnet, the shim field, an object-based field map estimate and a residual field. The former two are completely determined by spherical harmonic expansion coefficients directly available from the MR scanner. The object-based field map is forward simulated from air–tissue interfaces inside the FOV. The missing residual field originates from the object outside the FOV and is investigated by magnetic field simulations on a numerical whole body phantom. In vivo the spatially linear first order component of the residual field is estimated by measuring echo misalignments after demodulation of other field contributions resulting in a linear residual field. Gradient echo datasets of the cervical and the ankle region without and with shimming were acquired, where all four contributions were incorporated in the water–fat separation with two algorithms from the ISMRM water–fat toolbox and compared to water–fat separation with less incorporated field contributions.

## **Results**

Incorporating all four field contributions as demodulation steps resulted in reduced temporal and spatial phase wraps leading to almost swap-free water–fat separation results in all datasets.

## **Conclusion**

Demodulating estimates of major field contributions reduces the phase evolution to be driven by only small differences in local tissue susceptibility, which supports the field smoothness assumption of existing water–fat separation techniques.

### **3.2.2 Author Contribution**

The first author developed the methodology, performed the necessary adaptations to the online pulse sequence computations and the parameter export on the MR scanner (Philips Medical Systems, Best, The Netherlands), and implemented the offline software for post-processing and numerical simulations in Matlab (Mathworks, Natick, MA). After the study design for validation and reproducible testing in close collaboration with co-authors, the first author performed all experiments, analyzed and interpreted the data, and wrote the manuscript.

### **3.2.3 Original Article**

# Improving chemical shift encoding-based water–fat separation based on a detailed consideration of magnetic field contributions

Maximilian N. Diefenbach<sup>1</sup>  | Stefan Ruschke<sup>1</sup> | Holger Eggers<sup>2</sup> | Jakob Meineke<sup>2</sup> | Ernst J. Rummeny<sup>1</sup> | Dimitrios C. Karampinos<sup>1</sup>

<sup>1</sup>Department of Diagnostic and Interventional Radiology, Technical University of Munich, Munich, Germany

<sup>2</sup>Philips Research Laboratory, Hamburg, Germany

## Correspondence

Maximilian N. Diefenbach, Department of Diagnostic and Interventional Radiology, Klinikum rechts der Isar, Ismaninger Str 22, 81675 Munich, Germany.

Email: maximilian.diefenbach@tum.de  
Twitter: @diefenbach\_max

## Funding information

European Research Council, Grant/Award Number: 677661, ProFatMRI; Philips Healthcare

**Purpose:** To improve the robustness of existing chemical shift encoding-based water–fat separation methods by incorporating a priori information of the magnetic field distortions in complex-based water–fat separation.

**Methods:** Four major field contributions are considered: inhomogeneities of the scanner magnet, the shim field, an object-based field map estimate, and a residual field. The former two are completely determined by spherical harmonic expansion coefficients directly available from the magnetic resonance (MR) scanner. The object-based field map is forward simulated from air–tissue interfaces inside the field of view (FOV). The missing residual field originates from the object outside the FOV and is investigated by magnetic field simulations on a numerical whole body phantom. In vivo the spatially linear first-order component of the residual field is estimated by measuring echo misalignments after demodulation of other field contributions resulting in a linear residual field. Gradient echo datasets of the cervical and the ankle region without and with shimming were acquired, where all four contributions were incorporated in the water–fat separation with two algorithms from the ISMRM water–fat toolbox and compared to water–fat separation with less incorporated field contributions.

**Results:** Incorporating all four field contributions as demodulation steps resulted in reduced temporal and spatial phase wraps leading to almost swap-free water–fat separation results in all datasets.

**Conclusion:** Demodulating estimates of major field contributions reduces the phase evolution to be driven by only small differences in local tissue susceptibility, which supports the field smoothness assumption of existing water–fat separation techniques.

## KEYWORDS

B0 field estimation, chemical shift encoding-based water–fat separation, Dixon imaging, object-based field map estimation, water–fat imaging, water–fat separation

## 1 | INTRODUCTION

Chemical shift encoding-based water–fat imaging (WFI) has a wide range of clinical applications including fat suppression<sup>1,2</sup> and fat quantification.<sup>3,4</sup> In WFI, magnetic field

distortions are modeled as a nonlinear “field map” parameter in a complex water–fat signal model.<sup>5</sup> If the field map term is known, the linear water and fat parameters can be determined unambiguously. However, if the field map is unknown and there is no reasonable a priori estimate of the

This is an open access article under the terms of the Creative Commons Attribution-NonCommercial License, which permits use, distribution and reproduction in any medium, provided the original work is properly cited and is not used for commercial purposes.

© 2018 The Authors Magnetic Resonance in Medicine published by Wiley Periodicals, Inc. on behalf of International Society for Magnetic Resonance in Medicine

field map, solving the water–fat separation problem can result in ambiguous solutions often appearing as the infamous water–fat swaps—regions in the WFI output images, where the water and fat signal seem to be interchanged.<sup>1,6</sup>

To resolve water–fat swaps in WFI, there are many algorithms available that rely on the assumption that the field map term resembling the magnetic field in the MR scanner during a scan is a spatially smooth function.<sup>7–14</sup> Given good enough field map estimates in the neighborhood of a voxel (seeds), the assumption of an only mildly varying field map term over voxels allows to limit the range of possible field map values in that voxel, which can mitigate the ambiguity problem of the water–fat separation.<sup>1</sup> However, in cases where the assumption of field map smoothness over the voxel range is not met or reliable seed voxels are not available, water–fat separation remains challenging.

A recent work proposed the use of object-based information of the magnetic field to obtain a valuable field map initialization for standard WFI algorithms.<sup>15</sup> In this work, field distortions due to the object in the scanner are simulated starting from a rough estimate of the susceptibility map of the object in the scanner, which is a binary tissue–air mask of the FOV assigned corresponding susceptibilities. A demodulation of the so-called object-based fast field map estimate (OBFFME) from the complex source images served the role of the initialization of several standard water–fat separation algorithms from the ISMRM water–fat toolbox<sup>16</sup> and was shown to resolve many water–fat swaps in challenging anatomies in which air–tissue interfaces create field map terms fast varying in space. However, the air–tissue susceptibility map obtained in the OBFFME method by thresholding only holds information of the object inside the FOV, which results in a missing residual field after the demodulation of the OBFFME. Furthermore, results were shown primarily at 1.5 T and without considering the effect of other field map contributions.<sup>17,18</sup>

The purpose of the present work is to develop a field map demodulation method for WFI considering—in addition to the previously proposed OBFFME<sup>15</sup>—the magnetic field contribution from the missing residual field, inhomogeneities of the scanner magnet and the shimming gradients, all at 3 T.

## 2 | THEORY

Assuming the widely used single- $R_2^*$  multi-fat-peak water–fat voxel signal model

$$\begin{aligned} \hat{s}_n &= (W + c_n F) e^{(i2\pi f_B - R_2^*)t_n}, \\ c_n &= \sum_{p=1}^P a_p e^{i2\pi \Delta f_p t_n}, \quad \text{with} \quad \sum_{p=1}^P a_p = 1, \end{aligned} \quad (1)$$

the complex signal at the  $n$ -th echo  $\hat{s}_n \equiv \hat{s}(t_n)$ ,  $n=1, \dots, N$  is composed of the complex signal of water  $W$  and fat  $F$  that

share a common transverse relaxation rate  $R_2^*$ . The fat signal is modeled by an a priori known spectrum with  $P$  spectral peaks of corresponding relative amplitudes  $a_p$  and chemical shifts  $\Delta f_p$ .<sup>19</sup> The spatially dependent field map,  $f_B \equiv f_B(\mathbf{r})$ , accounts for the averaged magnetic field changes in a voxel affecting the effective precession frequency of each spectral peak and as such has a strong nonlinear effect on the phase of the signal  $\hat{s}_n$ . We model four different field map contributions:

$$f_B = \frac{\gamma}{2\pi} (\Delta B_0 + B_{\text{shim}} + B\hat{\chi} + B_r), \quad (2)$$

the scanner magnet inhomogeneities  $\Delta B_0$ , the shim field  $B_{\text{shim}}$ , the object-based field map estimate  $B\hat{\chi}$  and a residual field  $B_r$ .  $\gamma$  is the proton's gyromagnetic ratio.

### 2.1 | Contribution of scanner magnet inhomogeneities

The volume inside a MR scanner, where the main magnetic field itself is relatively constant, is limited to a region around the iso-center. In scans with large FOV or at large offcenter locations the main magnetic field is not constant in the whole imaging volume. Based on the magnet design of the scanner, the inhomogeneities of the main magnetic field can be described by a spherical harmonic expansion:

$$\Delta B_0(\mathbf{r}) = \sum_{\ell=1}^L \sum_{m=-L}^L C_{\ell m}^{\Delta B_0} Y_{\ell m}(r, \phi, \theta), \quad (3)$$

with the spherical harmonic functions  $Y_{\ell m}$  of order  $\ell$  and degree  $m$  with corresponding coefficients  $C_{\ell m}^{\Delta B_0}$  up to a maximum order  $L$ . These coefficients typically do not change from scan to scan and are determined by the hardware and its calibration.

### 2.2 | Contribution of shim field

When an object is placed in the main magnetic field, depending on its susceptibility the object gets magnetized and becomes itself a source of magnetic field.<sup>20</sup> To counter the magnetic field distortions due to the susceptibility-induced object-based field  $B_\chi$ , shimming is routinely used in clinical MR scans. After a 1D or 2D sequence module for measuring the object-based magnetic field  $B_\chi$  prior to the actual scan, electrical currents through special shim coils are computed to best possibly compensate for  $B_\chi$ . These coils are designed to create certain spherical harmonic magnetic fields and are therefore also typically described by a spherical harmonic expansion like Equation 3 with different coefficients  $C_{\ell m}^{\text{shim}}$ . While clinical systems up to 3 T often only have coils that can produce shim fields up to order  $L=2$ , high-field systems have shim coils producing fields up to order  $L=3$  or higher. Since the

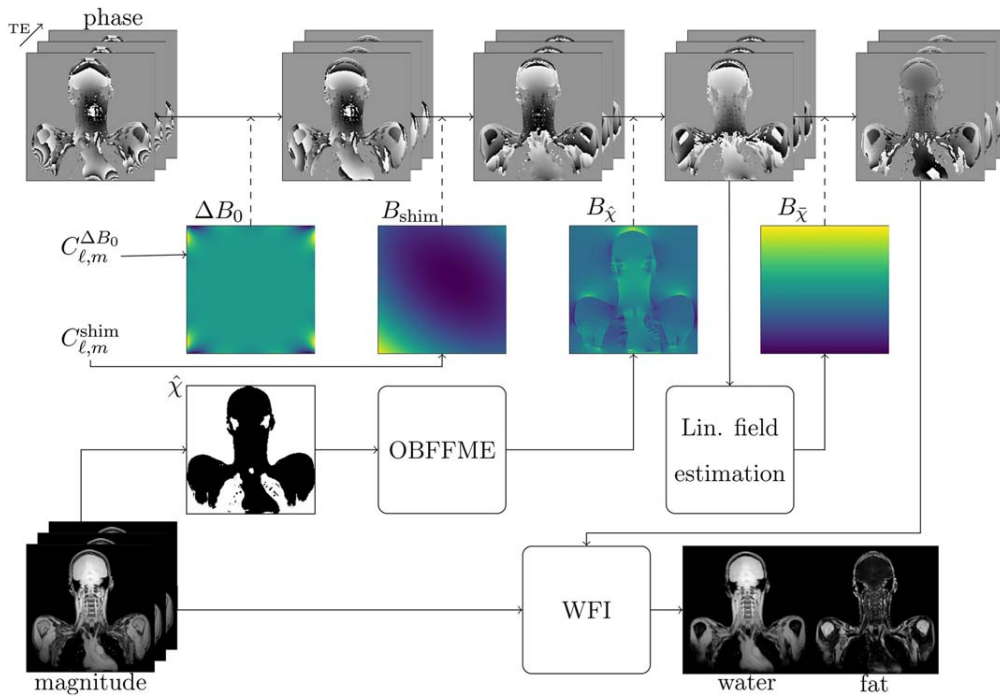


**FIGURE 1** Flowchart of the proposed method: four three-dimensional field map contributions (second row) are estimated from the coefficients  $C_{l,m}^{\dots}$  of spherical harmonic expansions and the complex source images (magnitude and phase): magnet inhomogeneities  $\Delta B_0$ , shim field  $B_{\text{shim}}$ , and object-based field map  $B_{\hat{\chi}}$  (computed through an object-based fast field map estimation<sup>15</sup>) and a residual linear field  $B_r$  (computed through a linear field estimation). Each field map contribution is demodulated (dashed arrows) from the phase before the input into a chemical shift encoding-based water–fat imaging (WFI) algorithm to separate water and fat images

magnetic field in the scanner changes from scan to scan, the coefficients  $C_{lm}^{\text{shim}}$  can be newly calculated and set before each scan. Spherical harmonics in Cartesian form are typically used for shimming (see Appendix).

### 2.3 | Contribution of object-based field map

The magnetic field distortions that the shim field tries to compensate for are mainly created by the object in the scanner. Given a susceptibility map  $\chi$  of the whole object and assuming  $\mathbf{B}_0 = B_0 \mathbf{e}_z$ , the resulting susceptibility-induced field map distortions  $B_\chi$  can be approximated in the forward model

$$B_\chi(\mathbf{r}) = B_0(d * \chi)(\mathbf{r}), \quad (4)$$

with the dipole kernel

$$d(\mathbf{r}) = \begin{cases} 0, & \text{for } \mathbf{r} = 0 \\ \frac{3\cos^2\theta - 1}{4\pi|\mathbf{r}|^3}, & \text{for } \mathbf{r} \neq 0, \end{cases}$$

which at the origin  $\mathbf{r} = 0$  is set to a “DC offset” of 0.<sup>21–23</sup> A susceptibility map of the whole object is typically not available and information about it can normally only be obtained from a scan with a FOV smaller than the object itself. According to Equation 4, the object’s total susceptibility-induced field is, therefore, separated in the so-called object-

based field map estimate  $B_{\hat{\chi}}$  and a residual field  $B_r$  created by the object’s susceptibility distribution outside the FOV<sup>24</sup>:

$$B_\chi = B_{\hat{\chi}} + B_r.$$

## 3 | METHODS

In four separate steps, the theoretical contributions to the field map (2) are estimated and demodulated from the complex source data prior to standard WFI algorithms. Figure 1 gives a flowchart overview of the proposed method, where each step is described in detail in the following sections.

### 3.1 | Scanner magnet inhomogeneities term

The information about the inhomogeneities of the scanner magnet was directly available in the scanner software as the coefficients  $C_{l,m}^{\Delta B_0}$  of the spherical harmonic expansion in Equation 3 in the scanner  $x$ – $y$ – $z$  system. To be able to demodulate  $\Delta B_0$ , it was then transformed to matrix size, voxel size, and orientation of the complex source images.

### 3.2 | Shim field term

The shim coefficients up to order  $L = 2$  were calculated by the scanner and available through the scanner software

similar to the coefficients  $C_{\ell,m}^{\Delta B_0}$ , but given in Cartesian scanner coordinates equal to the conventions in Ref. 25 given in the Appendix. The same transformation as for  $\Delta B_0$  needed to be applied before demodulation.

### 3.3 | Object-based field map term

An object-based field map estimate was obtained by the method described in Ref. 15. A maximum intensity projection across echoes was thresholded at 5% of its maximum value. The resulting binary tissue mask was assigned a susceptibility value of  $\chi(\text{tissue}) = -8.42$  ppm, the average of the reported susceptibilities of water,  $\chi(\text{water}) = -9.05$  ppm, and fat,  $\chi(\text{fat}) = -7.79$  ppm, inside the tissue region and  $\chi(\text{air}) = 0.34$  ppm for the outside air region.<sup>26,27</sup> From the obtained crude two-component susceptibility map, the OBFME was forward simulated with Equation 4 by zero-padding the susceptibility by a factor of 2 in all dimensions, solving the convolution in Fourier-space and removing the padding again. Lastly, the object-based field map was centered around its mean value inside the tissue region to not alter the center resonance frequency of the scan data once the object-based field map was demodulated.<sup>15</sup>

### 3.4 | Residual field term

The yielded OBFME is able to detect strong field changes near air–tissue interfaces inside the FOV. Background fields from tissue susceptibility sources  $\bar{\chi}$  outside the FOV cannot be incorporated in the OBFME and are therefore still encoded in the phase evolution of the demodulated signal  $s'_n$ . Through computer simulations it has recently been shown that forward simulations of the object-based field map with a FOV smaller than the object tend to result in a linear residual field.<sup>28</sup> We therefore model the resulting residual field as a spatially linear field contribution

$$B_r(\mathbf{r}) = B_0(d * \bar{\chi})(\mathbf{r}) = 2\pi\mathbf{a}\mathbf{r}, \quad (5)$$

with slope  $2\pi\mathbf{a}$  and location  $\mathbf{r}$ . Due to the Fourier shifting theorem, this linear field corresponds to a constant shift in the Fourier domain of the  $n$ -th echo source image,  $S_n(\mathbf{k}) = \text{FFT}\{s_n(\mathbf{r})\}$ . After the demodulation of the other field contributions the source images were bilaterally zero-padded in the direction where the FOV clips the object before applying a 3D fast Fourier transformation. Figure 4 gives an overviewing flowchart of the linear field estimation step. The distance of the maximum of the k-space magnitude with respect to the volumetric center of k-space corresponds to a shift  $\Delta\mathbf{k}_n$  for each echo  $n$ . With the assumption of a linear residual field as the origin of that linear k-space shift, the measured  $\Delta\mathbf{k}$  should then be linear across echo times  $t_n$

$$\Delta\mathbf{k}_n = -\mathbf{a}t_n. \quad (6)$$

Due to experimental inaccuracies in the estimation of  $\Delta\mathbf{k}_n$ , possibly due to phase errors in the signal  $s_n$ , it is important to stabilize the estimated linear phase contribution  $\gamma B_r t_n = 2\pi\mathbf{k}_n\mathbf{r}$  across echo times instead of directly demodulating the measured  $2\pi\mathbf{k}_n\mathbf{r}$ . Anything but a perfect linear time dependence of  $\Delta\mathbf{k}_n$  would interfere with the assumed signal model (1). Therefore, we linearly fitted the measured  $\Delta\mathbf{k}_n$  against the echo times  $t_n$  as  $\Delta\mathbf{k}_n = -\mathbf{a}t_n + \mathbf{b}$ , which directly holds the slope  $\mathbf{a}$  in Equation 5. According to Equation 6 the intercept  $\mathbf{b}$  should be zero. Generally, we observed that  $\Delta\mathbf{k}_n$  was well described by a linear time dependence, however possible phase errors especially in the first echo, which is more prone to those errors,<sup>29</sup> can lead to worse fittings with a considerably nonzero intercept  $\mathbf{b}$ . This was countered by replacing the first echo point by the origin in the  $\Delta\mathbf{k}$ - $t$  plane and fitting only  $\Delta\mathbf{k}_i = -\mathbf{a}t_i + \mathbf{b}$  with  $i=0, 2, 3, \dots, N$  and  $\Delta\mathbf{k}_0 = t_0 = 0$ , which yields fit parameters closer to the assumption (6). The possible content of the intercept  $\mathbf{b}$  is discussed below.

To investigate the validity of the residual field being linear in the case of the present in vivo scans, a numerical simulation based on the Duke phantom was performed similar to Ref. 30. The whole body mesh data were converted into a three-dimensional volume corresponding to a susceptibility map of 1.5 mm isotropic resolution. Three tissue regions together with the air region were assigned magnetic susceptibility values of  $-11.31$  ppm for bone,<sup>26</sup>  $-9.04$  ppm for soft tissue/water,<sup>31</sup>  $0.40$  ppm for air,<sup>31</sup> and  $4.32$  ppm for lung.<sup>32</sup> The above susceptibility values were referenced to air, so the outside region had 0 ppm susceptibility. The object's susceptibility map is shown in the first column of Figure 2. The corresponding field map in the cervical region was forward simulated as described above via Equation 4 with four different model sizes in the head–feet direction (HF0–HF3). Line profiles in head–feet direction through the middle of the center slice for each cropped model size (HF1–HF3) were compared to the same profile of the whole body field map (HF0) and their differences were linearly fitted in the head–feet region. The same simulation was repeated for the right leg of the Duke phantom (see Figure 3).

### 3.5 | In vivo measurements

To test the proposed method in an anatomy difficult for WFI due to concave geometries and many air–tissue interfaces, we scanned the cervical region of 10 healthy volunteers (6 female, 4 male, average age  $[27.7 \pm 2.8]$  years) in a 3 T scanner (Ingenia, Philips, Release 5.1.8, Best, The Netherlands); Informed written consent by all volunteers and approval by the institutional review board (Klinikum rechts der Isar, Technical University of Munich, Munich, Germany) was granted beforehand. All scans used a multi-echo gradient

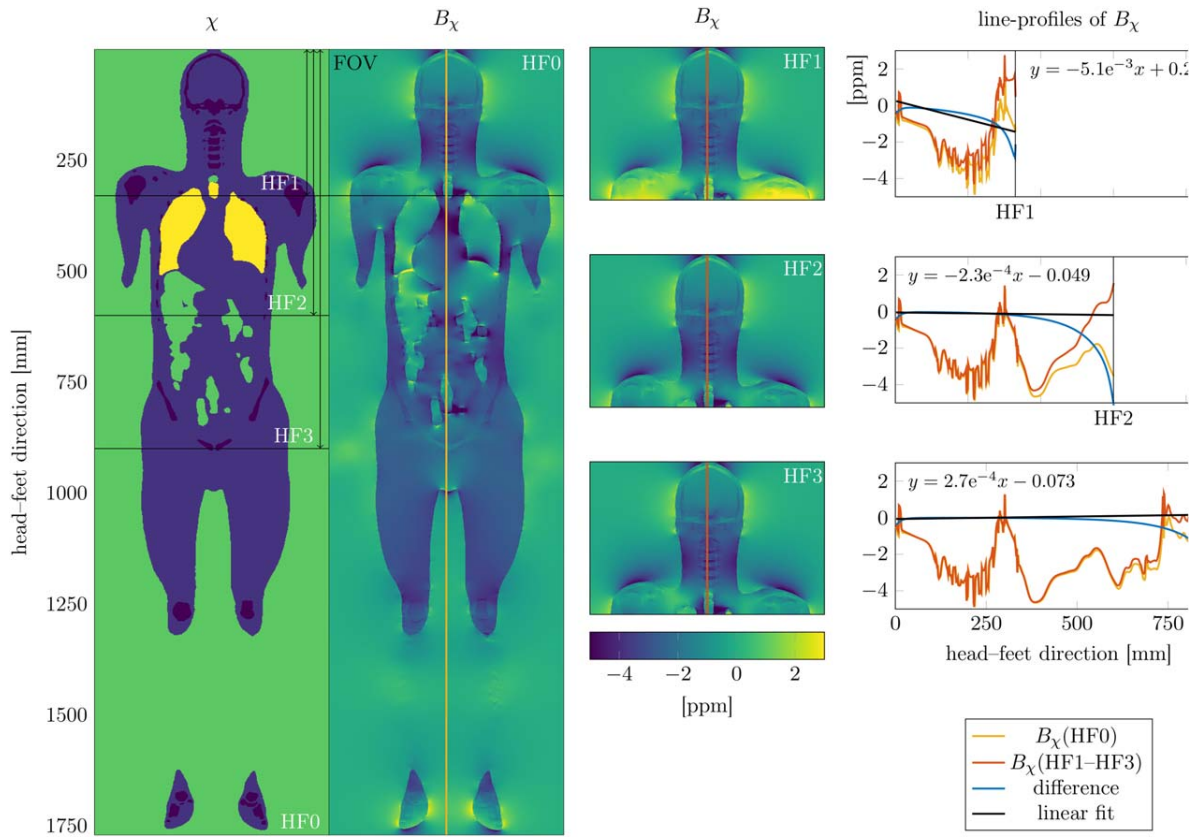


**FIGURE 2** Object-based fast field map estimates of a numerical whole body susceptibility phantom based on Duke<sup>30</sup>. Starting from a susceptibility map  $\chi$  (Column 1) with values stated at the end of Section 3, four object-based field maps  $B_\chi$  (Column 2, 3) are forward simulated via Equation 4, each with a different head–feet coverage (HF0–HF3). Visual comparisons inside a FOV equal in size to HF1 shows different results based on the head–feet coverage of the initial susceptibility map. Line plots show that the difference (blue) between the field map of the whole body simulation (yellow) and the cropped coverage (red) can be approximated by a linear function, indicated by a linear fit (black) in the FOV HF1

echo sequence with flyback gradients (monopolar) acquiring three echoes with one shot in a single TR, with  $TE_{\min} = 1.06$  ms,  $\Delta TE = 1.6$  ms, flip angle =  $3^\circ$ , orientation = coronal, readout direction = feet–head, FOV =  $450 \times 450 \times 224$  mm<sup>3</sup>, acquisition voxel size =  $2 \times 2 \times 4$  mm<sup>3</sup>, bandwidth/pixel = 1924.2 Hz, scan time = 1:08.7 minutes. Each cervical region per subject was scanned twice—once without any shim gradients and once with the default shim option switched on, where the shim volume was covering the whole FOV. This resulted in a total of 20 datasets to test the reproducibility of the proposed method across subjects.

Spherical harmonic expansion coefficients of the scanner magnet inhomogeneities and the shim field were automatically written to the raw data by modifications of the Gyrotools Recon Frame scanner patch<sup>33</sup> and later extracted from the raw data with the MRRecon software,<sup>33</sup> which was also used to reconstruct the raw data and transform the field contributions to the same coordinate system.

To estimate the effect of concomitant gradients and k-space misalignments due to gradient delays, we performed one coronal scan of the cervical region with the same sequence as described above, but with the implemented

scanner option to calculate the concomitant gradients online as well as an additional measurement of first order echo misalignments. The echo misalignments were measured by enabling the repetition of the monopolar gradient readout through the k-space center with opposite polarity and without any phase encoding gradients similar to the method described in Ref. 34. The same scan was repeated axially to cover the case where the readout dimension is anterior–posterior, different from the body axis along which the FOV clips the imaging object. For comparison the axial dataset and all estimated field map contributions were reformatted to the coronal perspective.

The proposed method was also tested in a different anatomy also typically challenging for WFI. The left ankle of one volunteer was scanned with the same sequence, also with two different frequency encoding directions, along the feet–head axis and the anterior–posterior axis.

### 3.6 | Demodulation of field map terms

Demodulation of all field map contributions is done by

$$s'_n = s_n e^{-i\gamma(\Delta B_0 + B_{\text{shim}} + B\hat{\chi} + B_r)} t_n,$$

which results in a complex signal modeled as

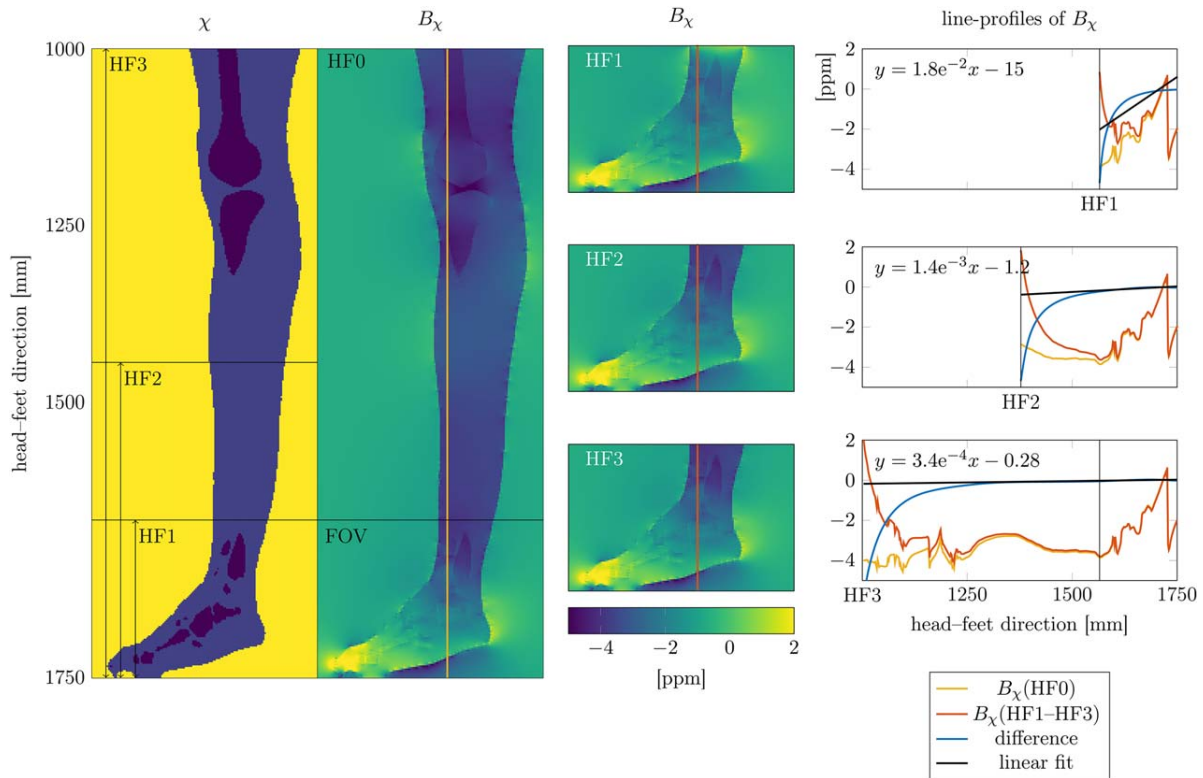


**FIGURE 3** Similar to Figure 2: Simulation of the object-based fast field map estimation in the ankle with the numerical whole body susceptibility phantom based on Duke.<sup>30</sup> The object-based fast field map estimate is computed for three different head–feet coverages (HF1–HF3) of only the right leg and related to the whole body simulation. Line plots show that the difference (blue) between the field map of the whole body simulation (yellow) and the cropped coverage (red). The residual linear field slope is indicated by a linear fit (black) in the FOV HF1. Note how the slope of the linear fit of the residual field decreases for larger head–feet coverages

$$s'_n = (W + c_n F) e^{(i2\pi\psi - R_n^2)t_n},$$

where the term  $\psi$  is now small compared to  $f_B$  in Equation 1, so that the smoothness assumption of the WFI algorithm is supported.

### 3.7 | Water–fat separation

Water–fat separation was performed with two previously published methods with MATLAB implementations available in the ISMRM water–fat toolbox<sup>16</sup>: a hierarchical IDEAL<sup>11</sup> and a graph cut algorithm.<sup>6</sup> The default settings of most algorithmic parameters as provided in the toolbox were kept. Only the range of field map values was adapted for the graph cut algorithm to allow values between [−1000 Hz, 1000 Hz] in steps of 4 Hz. For the assumed fat spectrum, a 10-peaks fat model was used as previously measured in bone–marrow.<sup>35</sup>

Three different post-processing schemes were performed: (1) standard water–fat separation with the raw source signal as direct input to the WFI algorithms without any demodulations, (2) the previously published method<sup>15</sup> with demodulation of the object-based field map estimate as the only

preprocessing step, and (3) the proposed method with all four demodulation steps.

Based on the water and fat images of the WFI results of all volunteer scans in the cervical region, datasets were visually rated and categorized in datasets with and without water–fat swaps, where regions in the heart and only a few voxels close to the object boundaries were not regarded. The overall counts of datasets with and without residual water–fat swaps served as a more global metric on how the proposed method performed in a challenging anatomy across all 20 datasets.

## 4 | RESULTS

### 4.1 | Numerical simulation results

Columns 2 and 3 of Figure 2 show the results of the Duke phantom simulation. The line profiles in Column 4 show that the difference in the field maps (red) of a whole body simulation (HF0, yellow) to a smaller size simulation (HF1–HF3, light blue) are for the most part linear in the head–feet direction, which is also confirmed by the linear fit of the difference (black) inside the FOV (HF1 in Column 4). As more

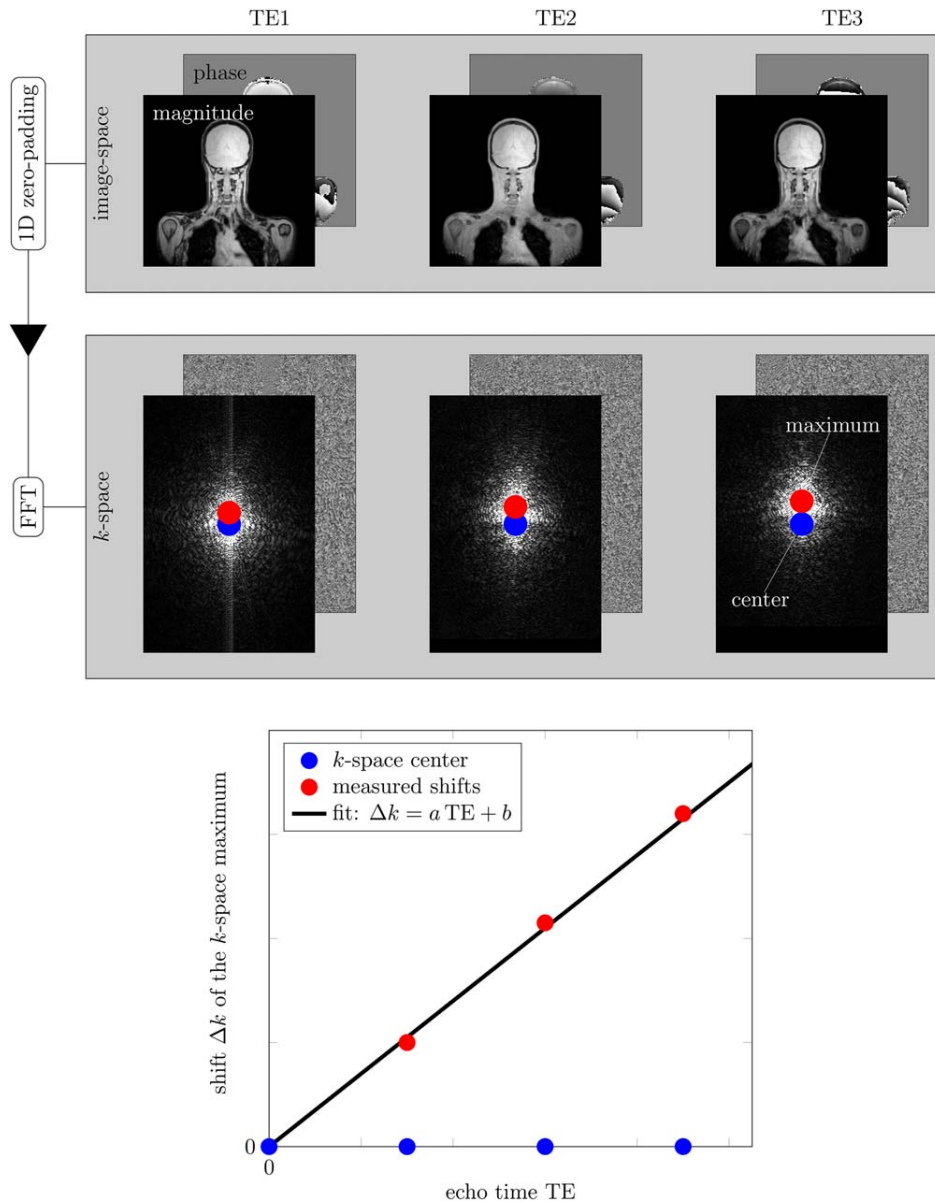


**FIGURE 4** Flow chart illustrating proposed residual linear field estimation. After the demodulation of all other field map contributions, the complex multi-echo source data is first zero-padded in the dimension where the FOV crops the imaging object. Second, each echo is Fourier-transformed and the offset of the voxel of maximum k-space energy and the k-space center is measured. The fitted slope of measured offsets versus echo time yields the  $a$  in Equation 6

coverage in head–feet direction is used for the simulation, the slope of the linear fit vanishes, which indicates that the residual field is created by the cropped objects regions outside the FOV. The same effect can be seen from the results of the numerical simulation of Duke’s leg shown in Figure 3.

## 4.2 | In vivo WFI results

The phase of all echoes after stepwise demodulation of each estimated field map contribution gradually becomes more

homogeneous with less phase wraps, which improves the intermediate WFI results until swap-free water–fat separation is achieved, as shown in Figure 5. The demodulation of the scanner magnet inhomogeneities removes the characteristic “ripple” phase wraps near the edge of the FOV (red arrows). More phase wraps are clearly removed by demodulating the shim field (blue arrow). In the concave neck regions it is easily observable how the demodulation of the object-based field map spatially flattens the phase (orange arrows). After the OBFFME demodulation step, the number of phase wraps almost perpendicular to the head–feet direction increases

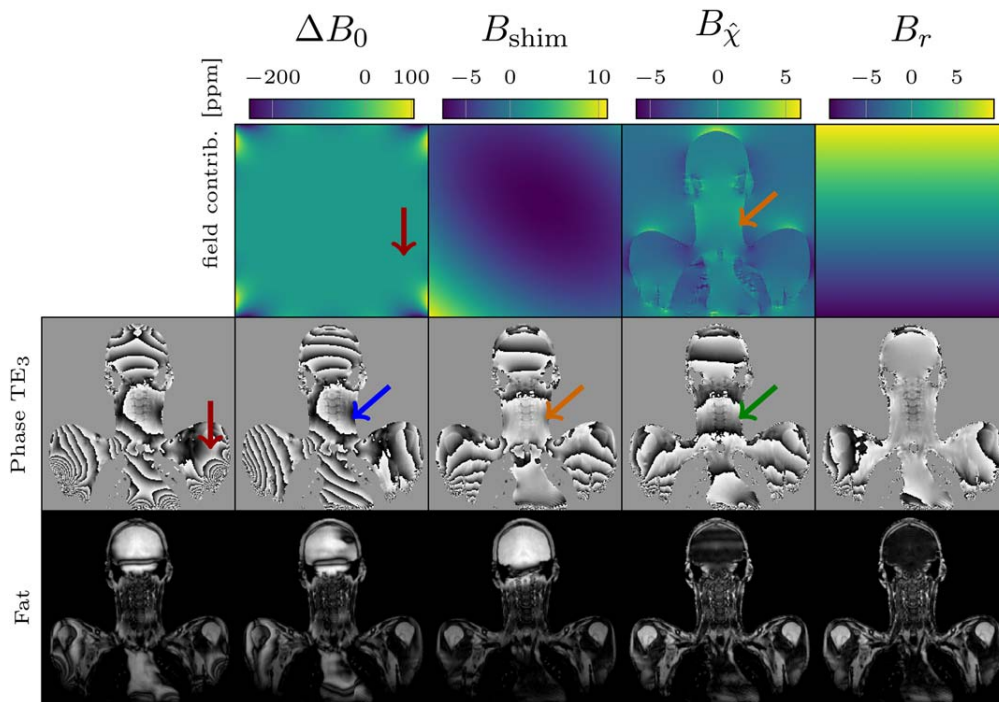


**FIGURE 5** Example of stepwise demodulation of field map contributions. First row shows scanner magnet inhomogeneities  $\Delta B_0$ , shim field  $B_{\text{shim}}$ , object-based field map  $B_{\hat{\chi}}$ , residual linear field  $B_r$ . Row 2 shows phase images of the third echo at  $\text{TE}_3$ . Row 3 shows fat images of intermediate hIDEAL<sup>11</sup> results. Each column shows the phase and fat images after the additional demodulation of the field map contribution in row 1. Arrows indicate specific features of field map contributions that are removed from the phase images by the demodulation step. Extended version, Supporting Information Figure S1

with echo time (green arrow). This indicates the residual linear background field contribution, which is removed from the phase evolution by the linear field demodulation step, resulting in homogeneous phase images in space and time, which furthermore allows for swap-free water–fat separation.

To determine the performance of the proposed method over a larger number of acquired volunteer scans, Table 1 sums up the cervical datasets that show water–fat swaps somewhere in the imaging volume disregarding the heart and the very edge voxels of the object. Numbers in parenthesis do not count the characteristic ripples at the edge of the FOV due to the scanner magnet inhomogeneities. None of the WFI algorithms were able to reconstruct swap-free results on their own. While the previous method<sup>15</sup> is able to reduce only few swaps if no shimming is used, the proposed method leads to a 100% reduction of water–fat swaps for the hIDEAL algorithm and a significant reduction from 20 to 5 datasets suffering swaps for the graph cut algorithm. In these nonresolved graph cut datasets, fat suppression was still good; remaining swaps would not reduce clinical evaluation as only a few slices showed a few swapped voxels on a thin fringe line, which might be resolvable by further optimizing the parameters of the water–fat separation algorithm.

Figure 6 shows the water images of two example datasets with shim off (left) and shim on (right), where only the proposed method was able to successfully resolve all water–fat swaps. Arrows point to regions, where the additional field

map contributions could remove characteristic swaps. Although some datasets reconstructed by both algorithms without (“std. WFI”) and with (“previous”) the OBFFME demodulation showed good water–fat separation, all datasets suffered from high frequency water–fat swaps at the same location where the scanner magnet inhomogeneities cause ripple phase wraps. These ripple like water–fat swaps were resolved in all cases by the demodulation of the scanner magnet inhomogeneities.

Figures 7 and 8 show the effect of two remaining field map contributions—concomitant gradients and gradient delay echo misalignments. In the same scheme as Figure 5, the evolving phase images and the intermediate hIDEAL WFI results are shown columnwise after demodulation of each field map contribution. To compare the order of magnitude of the effect of each field contribution on the phase, the two terms  $\Phi_{\text{graddelay}}(t) = \mathbf{a}_{\text{graddelay}} \mathbf{r}t / \omega_0$  and  $\Phi_{\text{concom}}(t) = \gamma B_{\text{concom}} t / \omega_0$  are displayed, where  $\mathbf{a}_{\text{graddelay}}$  is the measured k-space shift due to gradient delays,  $B_{\text{concom}}$  is the concomitant gradient field, and  $\omega_0$  is the center frequency. Column 1 starts with the phase images after demodulation of the scanner magnet inhomogeneities, the shim field and the OBFFME. While Figure 7 shows the coronal scan with the frequency–phase–slice encoding coordinates indicated in the upper left, Figure 8 shows the coronal reformatting of the dataset from the same volunteer which was scanned axially and therefore has a different frequency–phase–slice encoding

**TABLE 1** Number of cervical datasets showing water–fat swaps (numbers in parenthesis do not count the characteristic ripples at the edge of the FOV due to the scanner magnet inhomogeneities)

	hIDEAL			Graph cut		
	Total	Shim off	Shim on	Total	Shim off	Shim on
std. WFI	20 (16)	10 (6)	10 (10)	20 (10)	10 (7)	10 (3)
previous	20 (14)	10 (4)	10 (10)	20 (11)	10 (5)	10 (6)
<b>proposed</b>	<b>0</b>	<b>0</b>	<b>0</b>	<b>5</b>	<b>2</b>	<b>3</b>

Compared are the results of two algorithms—hIDEAL<sup>11</sup> and graph cut<sup>6</sup>—in two scans with and without shimming, where three different processing schemes were performed: Standard water–fat imaging (std. WFI) without any demodulation steps, the previously investigated method<sup>15</sup> with one demodulation steps (previous), and the proposed method with four incorporated demodulation steps (proposed).

coordinate system. While in the former case (Figure 7) the frequency-encoding direction is parallel to the body axis on which the object is clipped by the FOV, in the latter case (Figure 8) the two directions are perpendicular. By comparing Figures 7 and 8, one can see that the residual field that was assumed to be linear along the axis of the object region outside the FOV is not only much larger than the concomitant gradients and gradient delay contributions but also separable when the clip axis and the frequency-encoding axis is not the same.

Figure 9 similarly shows the stepwise results of the proposed method for the shim-off ankle scan with alternating frequency- and phase-encoding directions. Due to the smaller FOV and the geometry of the anatomy, the magnet inhomogeneities are smaller and ripple-creating field variation are only present in air regions inside the FOV, which is why the magnet inhomogeneity column is not displayed. In this scenario without shimming, the WFI algorithms cannot resolve the swap in the leg as illustrated by the graph cut results in rows 4 and 5. The presence of phase wraps along the body axis indicates a linear residual field contribution after the demodulation of the object-based field map estimate. After the proposed demodulation of the estimated residual linear field, the graph cut algorithm yields swap-free water–fat images. This is true in both subplots of Figure 9, where the frequency and phase encoding directions are switched, which shows that the residual linear field remains varying along the head–feet axis and is independent of encoding directions.

## 5 | DISCUSSION

The focus of the present study was to develop a method to improve WFI in challenging anatomical regions by reducing water–fat swaps via a better field map initialization of existing algorithms. Compared to the previous work,<sup>15</sup> three

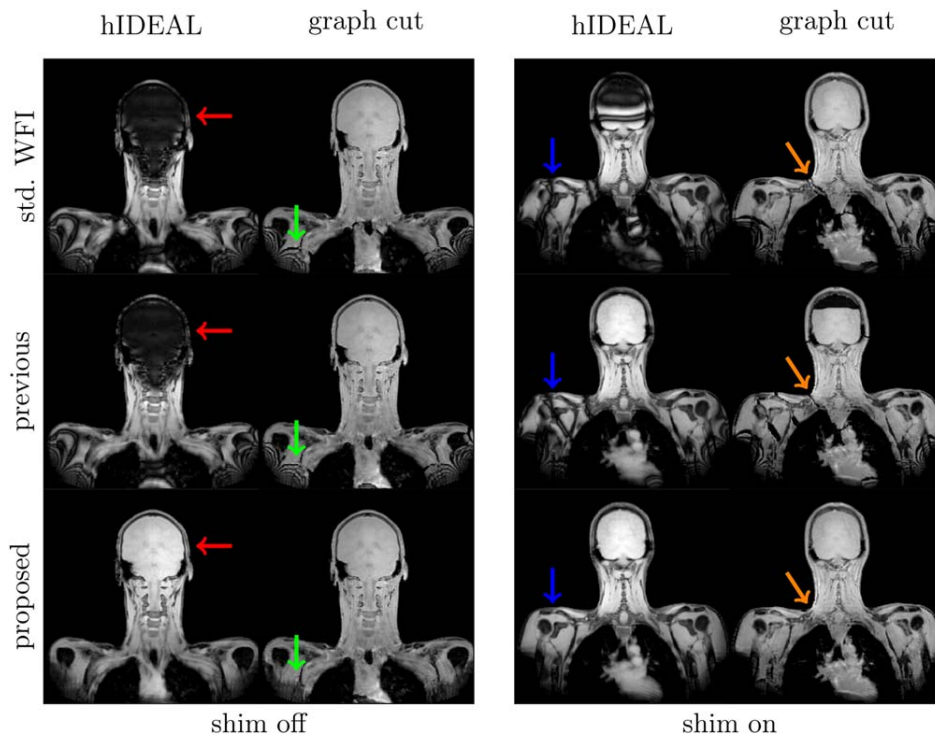


**FIGURE 6** Comparison of the proposed method to previous methods without (“std. WFI”) and with (“previous”) a single demodulation step of the object-based field map estimate before two WFI methods.<sup>6,11</sup> Water images of the WFI results, shown for one case with shim off (left two columns) and one case with shim on (right two columns). Only the proposed method solved the water–fat separation correctly resulting in swap-free water–fat separation in the shown datasets. WFI results for the two algorithms can be subject to different scaling as the images are direct output of the implementations

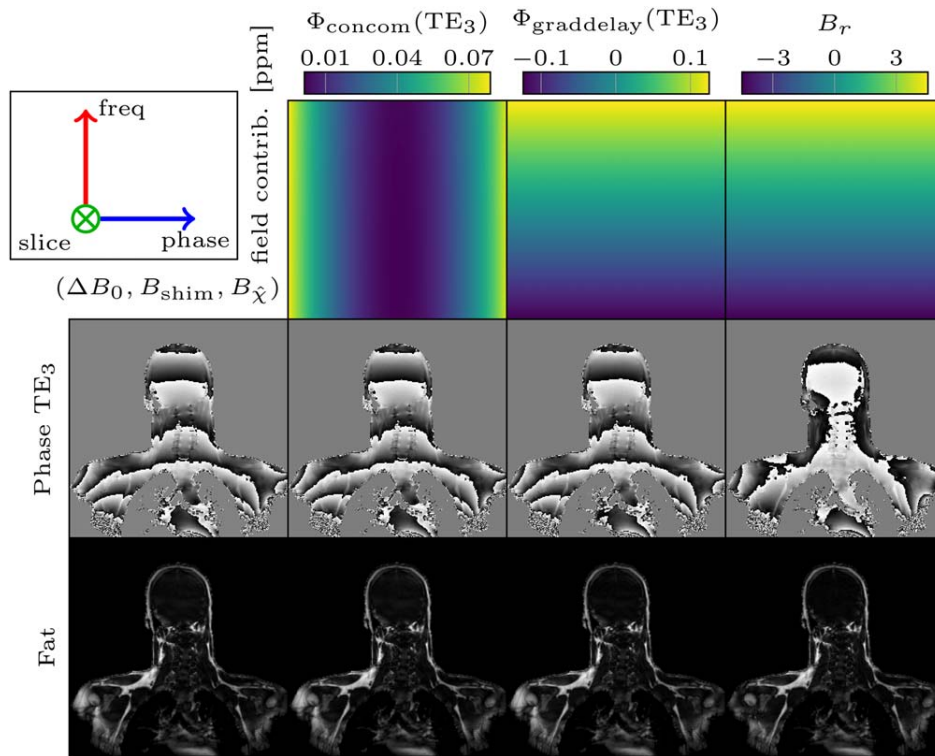


**FIGURE 7** Example of stepwise demodulation of two additional field map contributions—concomitant gradients and gradient delays—in coronal scans of the cervical region. Row 1 displays the field map contributions. Columns display phase at the latest echo  $TE_3$  and fat images from intermediate hIDEAL<sup>11</sup> results after demodulating scanner magnet inhomogeneities  $\Delta B_0$ , shim field  $B_{\text{shim}}$ , object-based field map  $B_{\hat{\chi}}$  (Column 1) and after additionally demodulating concomitant gradients (Column 2), gradient delays (Column 3), and residual linear field  $B_r$  (Column 4). Note that the residual linear field  $B_r$  is an order of magnitude greater than the phase term  $\Phi_{\text{graddelay}}(TE_3) = \mathbf{a}_{\text{graddelay}} \mathbf{r}TE_3 / \omega_0$  resulting from the measured k-space shift  $\mathbf{a}_{\text{graddelay}}$  due to gradient delays.  $\omega_0$  is the center frequency. Here, the dimension in which the FOV crops the object coincides with the frequency dimension. The phase term  $\Phi_{\text{graddelay}}(TE_3) = \gamma B_{\text{concom}} TE_3 / \omega_0$  is two orders of magnitude smaller than the estimated residual linear field. Extended version, Supporting Information Figure S2

additional contributions to the field map were taken into account: inhomogeneities of the scanner magnet, the shim field, and a susceptibility-induced field from object field sources outside the FOV.

As clinical scanners only have shim coils that can produce spherical harmonic fields up to a certain order, the shim field will never totally compensate for the object-based field. In Ref. 15, it was therefore recommended to not perform shimming and only rely on the demodulation of the object-based field map estimate. In the presented in vivo measurements without shimming, WFI with solely demodulating the OBFFME could only resolve swaps in 2 out of 10 datasets compared to WFI without any demodulation.

The characteristic ripples at the edge of the large-FOV phase images come from high orders in the spherical harmonic expansion of the scanner magnet inhomogeneities, which have very high field map values compared to the other contributions (Figure 5, top row). Such strong scanner magnet inhomogeneities can lead to increased intra-voxel dephasing and consequently signal loss, which was observed in some datasets at the top of the skull. Having the shim options on and later

demodulating it, proved successful in avoiding some of such intravoxel dephasing-induced signal losses (not shown).

The coarse two-component object-based field map estimate is targeted to simulate the large field map variations originating from the air–tissue interfaces inside the FOV and faces three main challenges. First, the OBFFME is only applicable in 3D-tomography and not in 2D imaging techniques where there are a limited number of slices. Second, the thresholding process in the OBFFME to obtain the initial crude two-component susceptibility map falsely assigns signal voids due to short  $T_2/T_2^*$  bone regions to also have the susceptibility of air. This leads to only very few incorrectly estimated voxels in the brain and did not significantly diminish the quality of the water–fat separation. In anatomies where no air is located inside the tissue, for example, in the extremities, it is easy to assign the susceptibility of bone to any signal voids inside the object and simulate the OBFFME starting with a three-component susceptibility map (air, tissue, bone). Third, neglecting susceptibility sources outside the FOV proved to be of much higher importance than the mis-assignment of susceptibility in air/bone regions.

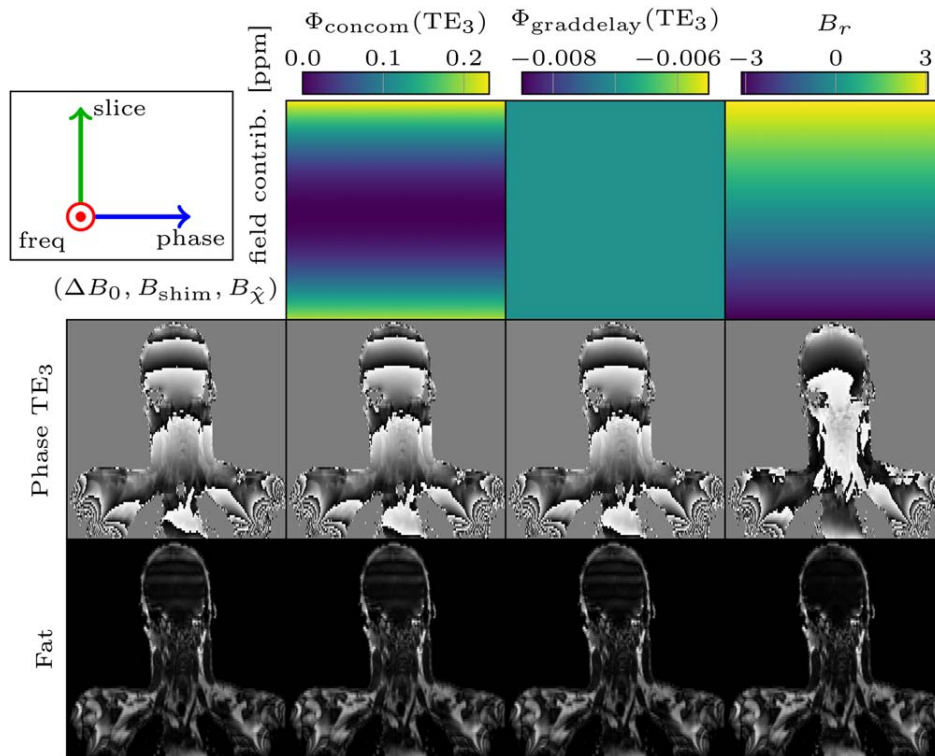


**FIGURE 8** Similar to Figure 7: Stepwise demodulation of field contributions in the dataset from the same volunteer scan with different frequency–phase–slice encoding coordinate system. The two additional field map contributions—concomitant gradients and gradient delays—remain much smaller than the estimated residual linear field  $B_r$ . Here the frequency encoding dimension is perpendicular to the dimension of the cropped object indicating that the residual field  $B_r$  cannot be explained by timing errors in the readout. Extended version, Supporting Information Figure S3

The phase images after the third demodulation step showed a missing linear field map contribution and k-space shifts increasing with the echo time. The forward simulation based on the Duke four-component susceptibility map showed the presence of a residual field term originating from object regions that lie outside of the FOV. The relation of the extent of the clipped object regions to the object region inside the FOV influences the nonlinearity (and monotony) of the residual field term along the axis where the FOV clips the objects, most often the body axis. This heuristic result was also obtained in a previous work.<sup>28</sup> Here, we approximated the residual field by only its first order, which allowed to estimate its presence by a shift in k-space, which linearly depends on echo time.

Instead of demodulating the OBFFME and then measuring a residual linear field, one could also try to interpolate the susceptibility map from the thresholding step in the OBFFME method beyond the FOV, for example, by using a replicative padding of the edge voxels instead of zero-padding in the forward simulation step. While this can work in scenarios where the object regions outside the FOV are fairly cylindrically shaped, in general mismatch between true and interpolated geometry lead to the introduction of more artificial field contributions.

Once the k-space shifts are measured, a robust fit (6) of the  $\Delta \mathbf{k}_n - t_n$  slope  $\mathbf{a}$  needs to be performed. We found that neglecting the shift of the first echo and instead using the point  $t_0 = 0$  where the shift should be zero resulted in the best performance of the currently tested WFI algorithms. Neglecting the first echo shift improves the fit as the phase image of the first echo is known to be more prone to phase errors.<sup>29</sup> With the assumption of a linear background field one can also subsequently deduce that at the interpolated zero echo time, no shift in k-space should be present. In our gradient echo sequence with flyback gradients, there are also other possible origins of linear phase shifts, such as gradient delays in the hardware or eddy currents, which can lead to the non-zero intercept  $\mathbf{b}$  of the linear  $\Delta \mathbf{k}_n - t_n$  fit.<sup>34,36</sup> Therefore, if the frequency-encoding direction is parallel to the axis on which the FOV clips the object, demodulation of linear field  $2\pi(\mathbf{a}t_n + \mathbf{b})\mathbf{r}$  might also remove contributions from other possible origins of linear phase shifts. The cervical and ankle scans with switched frequency–phase–slice encoding axis (Figures 7–9) show that the linear phase rolls due to concomitant gradients and gradient delays are present and separable from the estimated residual linear field from object regions outside the FOV. The residual linear field varies along the axis on which the FOV clips the objects and the orientations of concomitant gradients and linear field ramps due to

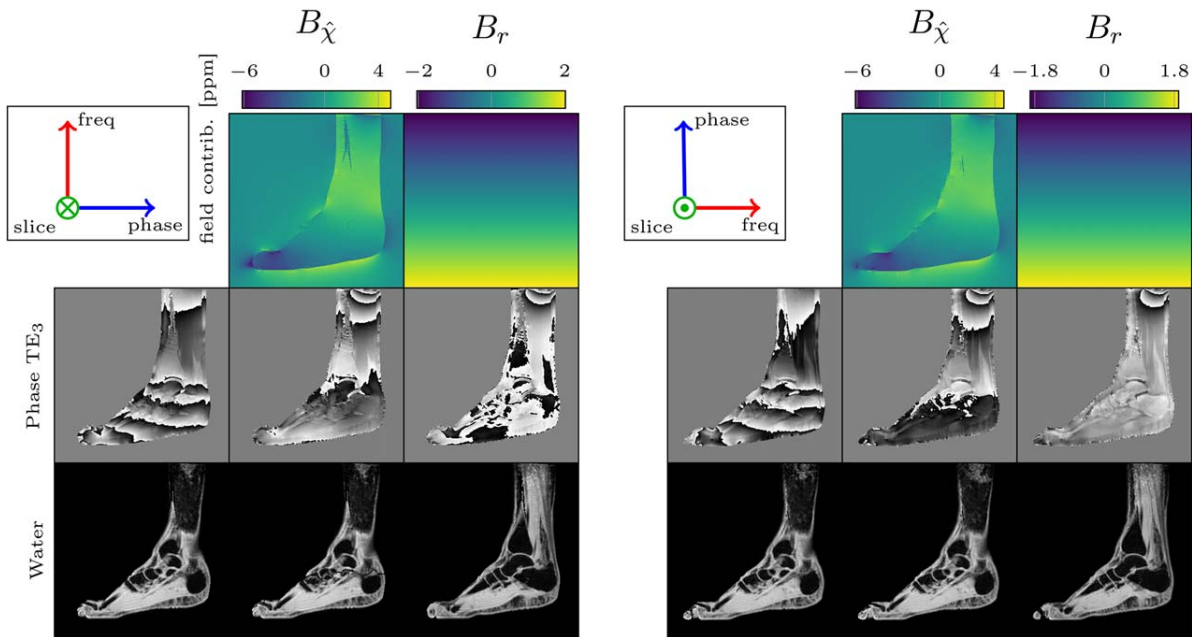


**FIGURE 9** Stepwise demodulation in the ankle dataset with shim off for alternated frequency and phase encoding direction. Left: frequency encoding direction along feet–head. Right: frequency encoding direction along anterior–posterior. Due to the smaller FOV the magnet inhomogeneities are negligible in the tissue regions (not shown). Demodulation of the object-based fast field map estimate leaves a linear residual field component. After demodulation of the estimated linear field, the graph cut algorithm is able to resolve all swaps as shown in row 3. Extended version, Supporting Information Figure S4

gradient delays depend on the frequency-encoding direction. However, in scans in which both axes coincide (Figures 7 and 9) the concomitant gradient and the gradient delay contributions were at least an order of magnitude smaller than the others. This was also confirmed by one dominant component in the measured  $\mathbf{a}$  in Equation 6, precisely the one corresponding to the axis where the object is clipped.

The additional demodulation of the concomitant gradients and artificial field map variations due to echo misalignments caused by gradient delays showed how the proposed method is easily extensible to also include more field map contributions. In scans that aim at measuring quantitative parameters in the water–fat signal model with more echoes often in several interleaves, echo-wise concomitant gradients as well as echo misalignments are more important than in the here demonstrated qualitative WFI application.<sup>34,37</sup>

While the present study shows the benefit of incorporating the described field map contributions as a priori knowledge to the water–fat separation problem, it has several limitations. First, the results shown here focused on the WFI performance with respect to fat suppression and used a three echo sequence to scan the cervical anatomy in a limited number of volunteers. However, the cervical region is one of the most challenging areas and the double scanning of each volunteer with two shim options gave 20 datasets that can be regarded as worst case scenarios of a priori unknown field distortions, in which, due to the large FOV, WFI was tested in a high number of slices. The successful applicability of the proposed method could also be shown in a total of four

ankle scans—in combinations of coronal and axial scans with and without shim.

Second, only two algorithms from the ISMRM water–fat toolbox were used to compare the different demodulation/initialization schemes. Both represent different classes of algorithms. The hIDEAL algorithm solves the water–fat problem voxel-wise at multiple scales, whereas the graph cut algorithm searches an optimal cut through a graph consisting of all voxels as the graph’s nodes. The available implementations gave reasonable computation times to perform the different schemes for all acquired datasets. The graph cut needed approximately up to 30 minutes per data set, the hIDEAL algorithm only around 30 seconds per data set without significant time dependence on the demodulated field contributions. Other available implementations of different algorithms in the toolbox were not studied in the context of this work, either because they do not assume strictly the same signal model (1), they try to separate water and fat in the Fourier domain or they were much slower to be practical in comparisons of many datasets.

In experimental scenarios where phase information is of interest, for example, in susceptibility-weighted imaging or quantitative susceptibility mapping, one is interested in small phase changes originating from differences in tissue susceptibilities much smaller than between air and tissue. Our proposed method of demodulating most of the largest field contributions might be viewed as a way of separating those large phase contributions from the fine “local” phase differences, resulting in a local tissue field map after a WFI

algorithm with a nonsmoothed quantitative field map output. Total field inversion<sup>38</sup> on such a field map might also prove interesting as the presently proposed demodulation step also resembles a possible preconditioning.

As the proposed method starts from complex source data and scanner output information independent of the MR pulse sequence, the technique can therefore also easily be translated to different sequences such as, for example, bipolar multi-gradient echo or single- or multi-shot pulse sequences, whose treatment is outside of the scope of this work. Furthermore, the information about the field map contribution estimated here is potentially valuable in MR application that use field map estimates for correction purposes such as, for example, k-space WFI methods, echo planar imaging or deblurring in nonCartesian imaging.

Example MATLAB code to estimate and demodulate the considered magnetic field contributions is freely available for download at [https://github.com/maxdiefenbach/MRI\\_field\\_contributions.git](https://github.com/maxdiefenbach/MRI_field_contributions.git) (SHA-1 = 11d95a993fc5c70bc20ebf2b2107d3e3a3886534). Extended versions of Figures 5–8, and 9 are available online as supplementary material (Supporting Information Figures S1–S4).

## 6 | CONCLUSION

We proposed a methodological framework for good field map initialization for WFI through modeling and demodulating four major field map contributions, inhomogeneities of the scanner magnet, the shim field, an object-based field estimate and a residual field, from the complex multi-echo signal prior to standard algorithms. The proposed method resulted in almost swap-free WFI results and performed significantly better than the stand-alone algorithms with and without demodulation of only the object-based field map estimate. The complex signal after all four demodulations contains interesting phase information possibly valuable for quantitative parameter estimation methods.

## ACKNOWLEDGMENTS

The authors thank the contributors of the ISMRM Fat–Water Toolbox for the publication of their algorithm implementations and Michael Schär for help with the transformation of the field contributions to the imaging volume. The present work was supported by the European Research Council (grant agreement no 677661, ProFatMRI) and Philips Healthcare.

## CONFLICT OF INTEREST

Dr. Holger Eggers and Dr. Jakob Meineke are employees of Philips Healthcare.

## ORCID

Maximilian Diefenbach  <http://orcid.org/0000-0002-5581-885X>

## REFERENCES

- [1] Ma J. Dixon techniques for water and fat imaging. *J Magn Reson Imaging*. 2008;28:543–558.
- [2] Bley TA, Wieben O, François CJ, Brittain JH, Reeder SB. Fat and water magnetic resonance imaging. *J Magn Reson Imaging*. 2009;31:4–18.
- [3] Reeder SB, Cruite I, Hamilton G, Sirlin CB. Quantitative assessment of liver fat with magnetic resonance imaging and spectroscopy. *J Magn Reson Imaging*. 2011;34:729–749.
- [4] Hu HH, Kan HE. Quantitative proton MR techniques for measuring fat. *NMR Biomed*. 2013;26:1609–1629.
- [5] Reeder SB, Wen Z, Yu H, et al. Multicoil dixon chemical species separation with an iterative least-squares estimation method. *Magn Reson Med*. 2003;51:35–45.
- [6] Hernando D, Kellman P, Haldar JP, Liang ZP. Robust water/fat separation in the presence of large field inhomogeneities using a graph cut algorithm. *Magn Reson Med*. 2009;63:79–90.
- [7] Yu H, Reeder SB, Shimakawa A, Brittain JH, Pelc NJ. Field map estimation with a region growing scheme for iterative 3-point water-fat decomposition. *Magn Reson Med*. 2005;54:1032–1039.
- [8] Hernando D, Haldar JP, Sutton BP, Ma J, Kellman P, Liang ZP. Joint estimation of water/fat images and field inhomogeneity map. *Magn Reson Med*. 2008; 59:571–580.
- [9] Lu W, Hargreaves BA. Multiresolution field map estimation using golden section search for water-fat separation. *Magn Reson Med*. 2008;60:236–244.
- [10] Berglund J, Johansson L, Ahlström H, Kullberg J. Three-point Dixon method enables whole-body water and fat imaging of obese subjects. *Magn Reson Med*. 2010;63:1659–1668.
- [11] Tsao J, Jiang Y. Hierarchical ideal: fast, robust, and multiresolution separation of multiple chemical species from multiple echo times. *Magn Reson Med*. 2012;70:155–159.
- [12] Sharma SD, Hu HH, Nayak KS. Accelerated water-fat imaging using restricted subspace field map estimation and compressed sensing. *Magn Reson Med*. 2011;67:650–659.
- [13] Cui C, Wu X, Newell JD, Jacob M. Fat water decomposition using globally optimal surface estimation (goose) algorithm. *Magn Reson Med*. 2014;73:1289–1299.
- [14] Liu J, Drangova M. Method for b0 off-resonance mapping by non-iterative correction of phase-errors (b0-nice). *Magn Reson Med*. 2014;74:1177–1188.
- [15] Sharma SD, Artz NS, Hernando D, Horng DE, Reeder SB. Improving chemical shift encoded water-fat separation using object-based information of the magnetic field inhomogeneity. *Magn Reson Med*. 2014;73:597–604.
- [16] Hu HH, Börner P, Hernando D, et al. Ismrm workshop on fat-water separation: insights, applications and progress in MRI. *Magn Reson Med*. 2012;68:378–388.
- [17] Diefenbach MN, Ruschke S, Kooijman H, et al. Improving chemical shift-encoded water-fat separation based on a detailed

- consideration of magnetic field contributions. In Proceedings of 24th Annual Meeting of ISMRM, Singapore, 2016. p. 0576.
- [18] Eggers H, GeertsOssevoort L, Mulder G, Bos C. Incorporation of prior knowledge of main field inhomogeneity in Dixon methods. In Proceedings of 24th Annual Meeting of ISMRM, Singapore, 2016. p. 3266.
- [19] Yu H, Shimakawa A, McKenzie CA, Brodsky E, Brittain JH, Reeder SB. Multiecho water-fat separation and simultaneous  $r_2^*$  estimation with multifrequency fat spectrum modeling. *Magn Reson Med*. 2008;60:1122–1134.
- [20] Jackson JD. Classical Electrodynamics. New York, NY: Wiley; 2007.
- [21] Salomir R, de Senneville BD, Moonen CT. A fast calculation method for magnetic field inhomogeneity due to an arbitrary distribution of bulk susceptibility. *Concepts Magn Reson*. 2003;19B:26–34.
- [22] Marques JP, Bowtell R. Application of a Fourier-based method for rapid calculation of field inhomogeneity due to spatial variation of magnetic susceptibility. *Concepts Magn Reson B*. 2005;25:65–78.
- [23] Koch KM, Papademetris X, Rothman DL, de Graaf RA. Rapid calculations of susceptibility-induced magnetostatic field perturbations for in vivo magnetic resonance. *Phys Med Biol*. 2006;51:6381–6402.
- [24] Schweser F, Robinson SD, de Rochefort L, Li W, Bredies K. An illustrated comparison of processing methods for phase MRI and QSM: removal of background field contributions from sources outside the region of interest. *NMR Biomed*. 2016;30:e3604.
- [25] Schär M, Kozerke S, Fischer SE, Boesiger P. Cardiac SSFP imaging at 3 tesla. *Magn Reson Med*. 2004;51:799–806.
- [26] Hopkins JA, Wehrli FW. Magnetic susceptibility measurement of insoluble solids by NMR: magnetic susceptibility of bone. *Magn Reson Med*. 1997;37:494–500.
- [27] Schenck JF. The role of magnetic susceptibility in magnetic resonance imaging: MRI magnetic compatibility of the first and second kinds. *Med Phys*. 1996;23:815–850.
- [28] Dewal RP, Yang QX. Volume of interest-based Fourier transform method for calculation of static magnetic field maps from susceptibility distributions. *Magn Reson Med*. 2015;75:2473–2480.
- [29] Hernando D, Hines CDG, Yu H, Reeder S. Addressing phase errors in fat-water imaging using a mixed magnitude/complex fitting method. *Magn Reson Med*. 2011;67:638–644.
- [30] Gosselin MC, Neufeld E, Moser H, et al. Development of a new generation of high-resolution anatomical models for medical device evaluation: the virtual population 3.0. *Phys Med Biol*. 2014;59:5287–5303.
- [31] Collins CM, Yang B, Yang QX, Smith MB. Numerical calculations of the static magnetic field in three-dimensional multi-tissue models of the human head. *Magn Reson Imaging*. 2002;20:413–424.
- [32] Maril N, Collins CM, Greenman RL, Lenkinski RE. Strategies for shimming the breast. *Magn Reson Med*. 2005;54:1139–1145.
- [33] Gyrotools LLC. Recon frame: Mrecon, scanner software patch, pack'n go tool. <http://www.gyrotools.com/products/gt-recon.html/>.
- [34] Ruschke S, Eggers H, Kooijman H, et al. Correction of phase errors in quantitative water-fat imaging using a monopolar time-interleaved multi-echo gradient echo sequence. *Magn Reson Med*. 2016;78:984–996.
- [35] Ren J, Dimitrov I, Sherry AD, Malloy CR. Composition of adipose tissue and marrow fat in humans by  $^1\text{H}$  NMR at 7 Tesla. *J Lipid Res*. 2008;49:2055–2062.
- [36] Yu H, Shimakawa A, McKenzie CA, et al. Phase and amplitude correction for multi-echo water-fat separation with bipolar acquisitions. *J Magn Reson Imaging*. 2010;31:1264–1271.
- [37] Colgan TJ, Hernando D, Sharma SD, Reeder SB. The effects of concomitant gradients on chemical shift encoded MRI. *Magn Reson Med*. 2016;78:730–738.
- [38] Liu Z, Kee Y, Zhou D, Wang Y, Spincemaille P. Preconditioned total field inversion (TFI) method for quantitative susceptibility mapping. *Magn Reson Med*. 2016;78:303–315.

## SUPPORTING INFORMATION

Additional Supporting Information may be found online in the supporting information tab for this article.

**Figure S1** Example of stepwise demodulation of field map contributions. First row shows scanner magnet inhomogeneities  $\Delta B_0$ , shim field  $B_{\text{shim}}$ , object-based field map  $B\hat{\chi}$ , residual linear field  $B_r$ . Rows 2–4 show phase images of  $\text{TE}_1$ – $\text{TE}_3$ . Rows 5 and 6 show intermediate hIDEAL result water and fat images, respectively. Each column shows the phase and water–fat images after the additional demodulation of the field map contribution in row 1.

**Figure S2** Example of stepwise demodulation of two additional field map contributions—concomitant gradients and gradient delays—in coronal scans of the cervical region. Each column shows the phase and water–fat images after the additional demodulation of the field map contribution in row 1. Rows 2–4 show phase images of  $\text{TE}_1$ – $\text{TE}_3$  after demodulating scanner magnet inhomogeneities  $\Delta B_0$ , shim field  $B_{\text{shim}}$ , object-based field map  $B\hat{\chi}$  (Column 1) and demodulating concomitant gradients (Column 2), gradient delays (Column 3), and residual linear field  $B_r$  (Column 4). Rows 5 and 6 show intermediate hIDEAL result water and fat images, respectively.

**Figure S3** Stepwise demodulation of field contributions in the dataset from the same volunteer scan as in Figure 11 but with different frequency–phase–slice encoding coordinate system. The two additional field map contributions—concomitant gradients and gradient delays—remain much smaller than the estimated residual linear field  $B_r$ . Here the frequency encoding dimension is perpendicular to the dimension of the cropped object indicating that the residual field  $B_r$  cannot be explained by timing errors in the readout.

**Figure S4** Stepwise demodulation in the ankle dataset with shim off for alternated frequency and phase encoding direction. Left: frequency encoding direction along feet–head. Right: frequency encoding direction along anterior–posterior. Due to the smaller FOV the magnet inhomogeneities are negligible in the tissue regions (not shown). Demodulation of the object-based fast field map estimate leaves a linear residual field component. After demodulation of the estimated linear

field, the graph cut algorithm is able to resolve all swaps as shown in row 5 and 6.

**How to cite this article:** Diefenbach MN, Ruschke S, Eggers H, Meineke J, Rummeny EJ, Karampinos DC. Improving chemical shift encoding-based water-fat separation based on a detailed consideration of magnetic field contributions. *Magn. Reson. Med.* 2018;00:1–15. <https://doi.org/10.1002/mrm.27097>

## APPENDIX

### Main field inhomogeneities

Scanner parameters  $C_{\ell,0}^{\Delta B_0}$  in units of mT up to  $\ell_{\max}=30$  describe the inhomogeneities of the main magnetic field as

$$\Delta B_0 = \sum_{\ell} C_{\ell,0}^{\Delta B_0} Y_{\ell,0},$$

where only the solid harmonics  $Y_{\ell,0} = (r/r_0)^{\ell} P_{\ell,0}(\cos(\theta))$  were needed due to symmetry considerations.  $P_{\ell,m}$  are the

Legendre polynomials of degree  $\ell$  and order  $m$  and  $r_0$  is a reference radius.

### Shim field

The shim field was characterized by the eight coefficients of the expansion in Cartesian spherical harmonics Z, X, Y, Z2, ZX, ZY, X2–Y2, 2XY that ranged as  $C_{\ell,m}^{\text{shim}} \in [-1, 1]$  mT/m $^{\ell}$ , with the following Cartesian function definitions<sup>25</sup>:

$$Z = z$$

$$X = x$$

$$Y = y$$

$$Z2 = z^2 - \frac{1}{2}(x^2 + y^2)$$

$$ZX = zx$$

$$ZY = zy$$

$$X2 - Y2 = x^2 - y^2$$

$$2XY = 2xy$$

### 3.3 Journal Publication II: Generalized Parameter Estimation in Multi-Echo Gradient-Echo-Based Chemical Species Separation

The publication entitled *Generalized Parameter Estimation in Multi-Echo Gradient-Echo-Based Chemical Species Separation* was submitted to Quantitative Imaging in Medicine and Surgery (QIMS, ISSN 2223-4292) on 22 July 2019 and accepted for publication on 13 December 2019. The article [38] will be published for open access in the QIMS February issue of 2020. The work also resulted in two previous conference submissions [82] and [83].

#### 3.3.1 Abstract

##### Purpose

To develop a generalized formulation for multi-echo gradient-echo-based chemical species separation for all MR signal models described by a weighted sum of complex exponentials with phases linear in the echo time.

##### Methods

Constraints between estimation parameters in the signal model were abstracted into a matrix formulation of a generic parameter gradient. The signal model gradient was used in a parameter estimation algorithm and the Fisher information matrix. The general formulation was tested in numerical simulations and against literature and in vivo results.

##### Results

The proposed gradient-based parameter estimation and experimental design framework is universally applicable over the whole class of signal models using the matrix abstraction of the signal model-specific parameter constraints as input. Several previous results in magnetic-field mapping and water-fat imaging with different models could successfully be replicated with the same framework and only different input matrices.

##### Conclusion

A framework for generalized parameter estimation in multi-echo gradient-echo MR signal models of multiple chemical species was developed and validated and its software version is freely available online.

#### 3.3.2 Author Contribution

The first author developed the mathematical formalism and its software implementation in the Python programming language (Anaconda distribution of Python 3.6, <https://www.anaconda.com>). He performed the data acquisition, reconstruction and post-processing of the test datasets, created all numerical simulations and wrote the manuscript.

**3.3.3 Original Article**

# Generalized Parameter Estimation in Multi-Echo Gradient-Echo-Based Chemical Species Separation

Maximilian N. Diefenbach<sup>1\*</sup>, Chunlei Liu<sup>2</sup>, Dimitrios C. Karampinos<sup>1</sup>

<sup>1</sup> Department of Diagnostic and Interventional Radiology, School of Medicine, Technical University of Munich, Munich, Germany

<sup>2</sup> Department of Electrical Engineering and Computer Sciences, & Helen Wills Neuroscience Institute, University of California, Berkeley

\* Corresponding author:

**Name:** Maximilian N. Diefenbach  
**Department:** Department of Diagnostic and Interventional Radiology  
Klinikum rechts der Isar  
**Institute Address:** Ismaninger Str 22  
81675 Munich  
Germany  
**E-mail:** maximilian.diefenbach@tum.de

**Running Title:** Generalized Chemical Species Separation

## Abstract

- **Purpose:** To develop a generalized formulation for multi-echo gradient-echo-based chemical species separation for all MR signal models described by a weighted sum of complex exponentials with phases linear in the echo time.
- **Methods:** Constraints between estimation parameters in the signal model were abstracted into a matrix formulation of a generic parameter gradient. The signal model gradient was used in a parameter estimation algorithm and the Fisher information matrix. The general formulation was tested in numerical simulations and against literature and in vivo results.
- **Results:** The proposed gradient-based parameter estimation and experimental design framework is universally applicable over the whole class of signal models using the matrix abstraction of the signal model-specific parameter constraints as input. Several previous results in magnetic-field mapping and water-fat imaging with different models could successfully be replicated with the same framework and only different input matrices.
- **Conclusion:** A framework for generalized parameter estimation in multi-echo gradient-echo MR signal models of multiple chemical species was developed and validated and its software version is freely available online.

## Keywords

parameter estimation, VARPRO, noise analysis, Cramér-Rao lower bound, water-fat imaging, fatty acid composition

## Introduction

Multi-echo gradient echo imaging is a powerful imaging method in the range of quantitative MRI paradigms. Techniques like chemical shift encoding-based water-fat separation (1), fatty acid composition mapping (2), myelin water imaging (3), chemical shift encoding-based separation of metabolites (4), and quantitative susceptibility mapping (QSM) (5) have been based on multi-echo gradient-echo imaging to quantify spatially-resolved maps of the proton density fat fraction, the fat unsaturation, the myelin water fraction, the metabolite concentrations and the mean tissue magnetic susceptibility, respectively.

The analysis of multi-echo gradient-echo imaging measurements is typically based on the complex MR data. Specifically, the excitation pulse of most multi-echo gradient-echo sequences has a finite bandwidth and thus not only protons at the center frequency are excited but also other chemical species, molecules with different chemical shifts, contribute to the MR signal formation. By sampling the MR signal at multiple echo times after the excitation pulse in a multi-echo gradient-echo imaging experiment, the presence of the different chemical species is encoded in the total MR signal. After the reconstruction of the single echo images, an assumed signal model is typically fit to the complex signal evolution measured at each image voxel. There is a plethora of different signal models that has been used in the literature (2,6–10). It is typically necessary to select the sampled echo times based on the noise properties of the assumed signal model (11) and to derive a parameter estimation scheme, often involving analytical computation of the derivatives with respect to the parameters of interest (1). Most existing works provide experimental design and parameter estimation strategies tailored to the details of the assumed signal model. Therefore, comparison of signal models requires reproduction of the methods from different sources, like previously attempted for the chemical shift encoding-based water-fat separation within the ISMRM fat-water toolbox (12).

The purpose of the present work is to develop a generalized formulation of multi-echo gradient-echo-based chemical species separation for all MR signal models described by a weighted sum of complex exponentials with phases linear in echo time and to provide parameter estimation for such signal models using an open source software framework based on the conventions of the ISMRM fat-water toolbox.

## Methods

Generally, the complex MR signal in one voxel  $s_n \equiv s(t_n)$ , sampled at echo times  $t_n$ ,  $n = 1, \dots, N$ , behaves according to

$$s_n = \sum_{m=1}^M \rho_m e^{i\phi_m} e^{(i\omega_m - R_m) t_n}, \quad [1]$$

where the contribution to the signal from every chemical species  $m = 1, \dots, M$  is characterized by its magnitude  $\rho_m$ , phase after the RF-excitation (at  $t = 0$ )  $\phi_m$ , resonance frequency  $\omega_m$  and transverse relaxation rate  $R_m$ .

Since estimating the whole set of model parameters  $\{\varrho_m, \phi_m, \omega_m, R_m\}$ ,  $m = 1, \dots, M$  would require an impractical amount of observations  $s_n$ , it is necessary to reduce the number of parameters on the right hand side of [1]. Model parameters can be fixed by a priori values or constraints based on physically meaningful assumptions. Relations between different parameters can be incorporated by inserting indicator functions in the partial derivatives of [1]:

$$\frac{\partial s_n}{\partial \hat{\varrho}_l} = \sum_{m=1}^M \mathbb{1}_{\hat{\varrho}_l}(\varrho_m) e^{i\phi_m} e^{(i\omega_m - R_m) t_n} \quad [2a]$$

$$\frac{\partial s_n}{\partial \hat{\phi}_l} = i \sum_{m=1}^M \mathbb{1}_{\hat{\phi}_l}(\phi_m) \varrho_m e^{i\phi_m} e^{(i\omega_m - R_m) t_n} \quad [2b]$$

$$\frac{\partial s_n}{\partial \hat{\omega}_l} = i t_n \sum_{m=1}^M \mathbb{1}_{\hat{\omega}_l}(\omega_m) \varrho_m e^{i\phi_m} e^{(i\omega_m - R_m) t_n} \quad [2c]$$

$$\frac{\partial s_n}{\partial \hat{R}_l} = -t_n \sum_{m=1}^M \mathbb{1}_{\hat{R}_l}(R_m) \varrho_m e^{i\phi_m} e^{(i\omega_m - R_m) t_n}, \quad [2d]$$

where the indicator functions

$$\mathbb{1}_a(b) = \begin{cases} c & \text{if } a = b \\ 0 & \text{otherwise} \end{cases} \quad [3]$$

can be scaled with constant factors  $c$  to fix certain relational parameter assumptions. Notationally we distinguish free model parameters to be estimated with a hat and refer to their whole set as  $\boldsymbol{\beta} = \{\hat{\varrho}, \hat{\phi}, \hat{\omega}, \hat{R}\}$ . An example for a possible model-specific parameter relation is given by the indicator function

$$\text{Example: } \mathbb{1}_{\hat{R}_1}(R_m) = \begin{cases} 1 & \text{if } \hat{R}_1 = R_m, \forall m > 1 \\ 0 & \text{otherwise,} \end{cases} \quad [4]$$

where compared to [3] the following substitutions were made:  $a = \hat{R}_1$ ,  $b = R_m$ ,  $c = 1$ . The indicator function [4] states that in such a signal model, there is only one free relaxation variable  $\hat{R}_1$  to be estimated and all relaxation rates of the other chemical species  $R_m$ ,  $m = 2, \dots, M$  behave according to the same partial derivative [2d]. As shown in the next section, the indicator functions can be combined to so-called constraint matrices that capture all parameter relations of one parameter type ( $\rho$ ,  $\phi$ ,  $\omega$ ,  $R$ ) across all chemical species  $m = 1, \dots, M$ .

## Matrix formulation

Starting from the general signal Equation [1], we can write the voxel signal model in a multi-observation matrix formulation as

$$\mathbf{s}(\beta) = \mathbf{A}(\hat{\omega}, \hat{\mathbf{R}})\mathbf{P}(\hat{\phi})\varrho(\hat{\varrho}) \quad [5]$$

where we defined

$$\begin{aligned} \mathbf{s} &= [s_1, \dots, s_N]^T, \\ (\varrho)_m &= \varrho_m, \quad (\phi)_m = \phi_m, \quad (\omega)_m = \omega_m, \quad (\mathbf{R})_m = R_m, \quad m = 1, \dots, M \\ \mathbf{A} &= \begin{pmatrix} e^{(i\omega_1 - R_1)t_1} & \dots & e^{(i\omega_M - R_M)t_1} \\ \vdots & & \vdots \\ e^{(i\omega_1 - R_1)t_N} & \dots & e^{(i\omega_M - R_M)t_N} \end{pmatrix}, \quad \mathbf{P} = \begin{pmatrix} e^{i\phi_1} & & \\ & \ddots & \\ & & e^{i\phi_M} \end{pmatrix} \end{aligned} \quad [6]$$

with omitted matrix entries being zero. In the matrix notation [5], the parameter relations described by the indicator functions [3] can be defined as constraint matrices  $\mathbf{C}_x, x \in \{\varrho, \phi, \omega, r\}$ , in the same way as the Kronecka symbol  $\delta_{ij}$  corresponds to the entries of an identity matrix. For the example of indicator functions [4] —for signal models in which all relaxation rates are constrained by  $R_{m>1} = \hat{R}_1$ —the corresponding constraint matrix is given by

$$\text{Example: } \mathbf{C}_R = \begin{pmatrix} 1 & 0 & \dots & 0 \\ 1 & 0 & \dots & 0 \\ \vdots & \vdots & \ddots & \vdots \\ 1 & 0 & \dots & 0 \end{pmatrix}. \quad [7]$$

In general, the constraint matrices corresponding to the indicator functions [3] are square with the same row number as the number  $M$  of present chemical species. The upper triangular part in each constraint matrix holds only zeros. Non-zero elements on the diagonal represent the parameters of interest that are solved for in the parameter estimation (the first entry of the example  $\mathbf{C}_R$  [7] corresponding to the free variable  $\hat{R}_1$ ). Non-zero elements on the lower triangular part of the matrices describe constrained parameters based on the specific relations of the chosen model (corresponding to  $R_{m>2}$  in [4]). As columns of all zeros in the constraint matrices do not hold any information about parameter relations, they are removed, which reduces the matrix sizes and avoids rank-deficiencies. Consequently, nonzero elements of corresponding parameter of interest might not be on the diagonal of the resulting rectangular matrices any more, but the number of model unknowns is represented by the column number of all constraint matrices after the removal of the zero-columns. In the above Example [7], the constraint matrix is consequently reduced to rectangular size  $M \times 1$ ,

$$\text{Example: } \mathbf{C}_R = \begin{pmatrix} 1 \\ 1 \\ \vdots \\ 1 \end{pmatrix}. \quad [8]$$

Further examples for sets of constraint matrices for common signal models in literature are given in the Results section. Thereby, we show the full square constraint matrices visualizing the full indicator functions of each parameter constraint before the removal of zero-columns. The constraint matrices with zero-columns removed are summarized in Table 1.

With all indicator functions in [3] combined to constraint matrices, the Jacobian for signal models of the form [1] can be written as

$$\begin{aligned} \mathbf{J} &= \begin{bmatrix} \frac{\partial \mathbf{s}}{\partial \hat{\varrho}}, \frac{\partial \mathbf{s}}{\partial \hat{\phi}}, \frac{\partial \mathbf{s}}{\partial \hat{\omega}}, \frac{\partial \mathbf{s}}{\partial \hat{\mathbf{R}}} \end{bmatrix} \\ &= [\mathbf{A}P\mathbf{C}_{\varrho}, i\mathbf{A}D\mathbf{C}_{\phi}, iT\mathbf{A}D\mathbf{C}_{\omega}, -T\mathbf{A}D\mathbf{C}_R], \end{aligned} \quad [9]$$

where  $\mathbf{T} = \text{diag}(t_1, \dots, t_N)$  and  $\mathbf{D} = \text{diag}(\mathbf{P}\hat{\varrho})$ . With the generalized Jacobian [9] one can formulate parameter estimation as well as an optimal echo time selection algorithms for all models of the class [1]. As shown in the next sections, the model-specific constraint matrices then become input parameters for the algorithms.

## Parameter estimation

The generalized formulation of the Jacobian in Equation [9] allows to develop a parameter estimation algorithm that is independent of an a priori choice of the signal model: The concrete specification of the constraint matrices can be treated as final input to the algorithm, which is written down in terms of unspecified constraint matrices. With the multi-observation formulation [6], the parameter estimation problem can be cast as the following minimizing of the norm of the residual vector  $\mathbf{e}$ ,

EQ [10]

$$\min \|\mathbf{e}\|_2, \quad \mathbf{e} = \mathbf{s} - \mathbf{A}P\hat{\varrho}. \quad [10]$$

The above optimization problem can be iteratively solved via alternating Gauss-Newton updates of the linear ( $\boldsymbol{\beta}_{\text{lin}} = \hat{\varrho}$ ) and nonlinear parameters ( $\boldsymbol{\beta}_{\text{nonlin}} = \{\hat{\phi}, \hat{\omega}, \hat{\mathbf{R}}\}$ ) in [1] in a variable projection method (VARPRO) [13].

---

**Algorithm 1** Generalized VARPRO algorithm for parameter estimation from complex multi-species MR signals.

---

**Require:**  $\beta_{\text{nonlin}}^{(0)}$

**while**  $\|e\|_2 > \epsilon \quad \wedge \quad n < N_{\text{max}}$

**do**

**update linear parameters**

$$\beta_{\text{lin}}^{(n+1)} = \mathbf{B}^+(\beta_{\text{nonlin}}^{(n)}) \mathbf{s}$$

**update nonlinear parameters**

$$\Delta\beta_{\text{nonlin}}^{(n+1)} = \mathbf{J}^+ \left( \mathbf{s} - \mathbf{B}(\beta_{\text{nonlin}}^{(n)})\beta_{\text{lin}}^{(n+1)} \right)$$

$$\beta_{\text{nonlin}}^{(n+1)} = \beta_{\text{nonlin}}^{(n)} + \Delta\beta_{\text{nonlin}}^{(n+1)}$$

**compute residual**

$$\|e\|_2 = \|\mathbf{s} - \mathbf{B}(\beta_{\text{nonlin}}^{(n+1)})\beta_{\text{lin}}^{(n+1)}\|_2,$$

**end while**

---

where  $\mathbf{B}^+$  refers to the Moore–Penrose pseudo inverse,  $\mathbf{B}^+ = (\mathbf{A}^\dagger \mathbf{A})^{-1} \mathbf{P}^\dagger \mathbf{A}^\dagger$ ,  $\mathbf{A}^\dagger$  is the Hermitian conjugate of  $\mathbf{A}$ , and similarly for  $\mathbf{J}^+$ . Note that the pseudo-code, hereafter Algorithm [1], largely resembles previously developed algorithms in water–fat imaging like the “Iterative Decomposition of water and fat with Echo Asymmetry and Least-squares estimation” (IDEAL) (14) or the VARPRO variant (15), but is not specific to the voxel signal model thanks to the use of the generalized Jacobian  $\mathbf{J}$ .

The initialization  $\beta_{\text{nonlin}}^{(0)}$  needs to be close enough to the global minimum of the residual norm to ensure convergence to the true parameter values, which is typically achieved by an initialization of the nonlinear parameters  $\hat{\omega}$  by global methods incorporating voxel neighborhood information (16–19). The iteration is stopped after  $N_{\text{max}}$  steps.

## Noise performance analysis

Based on the noise properties of the assumed signal model—fixed by the choice of constraint matrices—the MR experiments can be optimally designed e.g. in terms of the selection of echo times. The typically employed Cramér–Rao lower bound (CRLB) on the minimal noise variance is based on the Fisher Information Matrix (FIM) defined as the expectation value ( $\mathbb{E}[\dots]$ ) of the second derivative of the log-likelihood  $\ln \mathcal{L}$ ,

$$\mathbf{I}_{kl} = \mathbb{E} \left[ \frac{\partial}{\partial \beta_l} \frac{\partial}{\partial \beta_k} \ln \mathcal{L} \right], \quad [11]$$

where the likelihood

$$\mathcal{L} \sim \exp\left(-\frac{1}{2\sigma^2}\|\mathbf{s} - \mathbf{A}\mathbf{P}\varrho\|_2^2\right) \quad [12]$$

and the definitions from [6] apply. In the case of additive white Gaussian noise with variance  $\sigma^2$ , it can be shown (20) that the FIM is given by

$$\mathbf{I} = \frac{1}{\sigma^2} \text{Re}\{\mathbf{J}^\dagger \mathbf{J}\}, \quad [13]$$

with the Jacobian  $\mathbf{J}$  from Equation [9]. Therefore, the Fisher Information Matrix can be generally written as

$$\mathbf{I} = \frac{1}{\sigma^2} \text{Re} \begin{pmatrix} \mathbf{C}_\varrho^\top \mathbf{P}^\dagger \mathbf{A}^\dagger \mathbf{A} \mathbf{P} \mathbf{C}_\varrho & i\mathbf{C}_\varrho^\top \mathbf{P}^\dagger \mathbf{A}^\dagger \mathbf{A} \mathbf{D} \mathbf{C}_\phi & i\mathbf{C}_\varrho^\top \mathbf{P}^\dagger \mathbf{A}^\dagger \mathbf{A} \mathbf{D} \mathbf{C}_\omega & -\mathbf{C}_\varrho^\top \mathbf{P}^\dagger \mathbf{A}^\dagger \mathbf{A} \mathbf{D} \mathbf{C}_R \\ -i\mathbf{C}_\phi^\top \mathbf{D}^\dagger \mathbf{A}^\dagger \mathbf{A} \mathbf{P} \mathbf{C}_\varrho & \mathbf{C}_\phi^\top \mathbf{D}^\dagger \mathbf{A}^\dagger \mathbf{A} \mathbf{D} \mathbf{C}_\phi & \mathbf{C}_\phi^\top \mathbf{D}^\dagger \mathbf{A}^\dagger \mathbf{A} \mathbf{T} \mathbf{A} \mathbf{D} \mathbf{C}_\omega & i\mathbf{C}_\phi^\top \mathbf{D}^\dagger \mathbf{A}^\dagger \mathbf{A} \mathbf{T} \mathbf{A} \mathbf{D} \mathbf{C}_R \\ -i\mathbf{C}_\omega^\top \mathbf{D}^\dagger \mathbf{A}^\dagger \mathbf{A} \mathbf{P} \mathbf{C}_\varrho & \mathbf{C}_\omega^\top \mathbf{D}^\dagger \mathbf{A}^\dagger \mathbf{A} \mathbf{T} \mathbf{A} \mathbf{D} \mathbf{C}_\phi & \mathbf{C}_\omega^\top \mathbf{D}^\dagger \mathbf{A}^\dagger \mathbf{A} \mathbf{T}^2 \mathbf{A} \mathbf{D} \mathbf{C}_\omega & i\mathbf{C}_\omega^\top \mathbf{D}^\dagger \mathbf{A}^\dagger \mathbf{A} \mathbf{T}^2 \mathbf{A} \mathbf{D} \mathbf{C}_R \\ -\mathbf{C}_R^\top \mathbf{D}^\dagger \mathbf{A}^\dagger \mathbf{A} \mathbf{P} \mathbf{C}_\varrho & -i\mathbf{C}_R^\top \mathbf{D}^\dagger \mathbf{A}^\dagger \mathbf{A} \mathbf{T} \mathbf{A} \mathbf{D} \mathbf{C}_\phi & -i\mathbf{C}_R^\top \mathbf{D}^\dagger \mathbf{A}^\dagger \mathbf{A} \mathbf{T}^2 \mathbf{A} \mathbf{D} \mathbf{C}_\omega & -\mathbf{C}_R^\top \mathbf{D}^\dagger \mathbf{A}^\dagger \mathbf{A} \mathbf{T}^2 \mathbf{A} \mathbf{D} \mathbf{C}_R \end{pmatrix} \quad [14]$$

The Cramér-Rao lower bounds on the parameter variances are given by  $\text{CRLB} = \mathbf{I}^{-1} \leq \text{var}\boldsymbol{\beta}$ , yielding the theoretically minimal variances (and covariances) of the parameter estimates (20). Minimizing the CRLB over model parameters of interest and/or different echo samplings can be used for optimal experimental design (11).

## Experimental validation

To demonstrate the validity and generality of the proposed generalized formulation, we selected well-established parameter estimation results from literature on chemical shift encoding-based water-fat separation assuming signal models of increasing complexity.

### No/Single/Double- $R_2^*$ water-fat signal models

The treatment of different water-fat signal models is analogous and in the following we show the usage of generalized formulation and the setup of specific constraint matrices for the widely used single- $R_2^*$  water-fat signal model: The signal evolution across echo times  $t_n$  is given by

$$s_n = (W + d_n F) e^{i(\omega - R_2^*) t_n} \quad [15a]$$

$$\text{with } d_n \equiv d(t_n) = \sum_{p=1}^P \alpha_p e^{i\Delta\omega_p t_n} \quad \text{and} \quad \sum_{p=1}^P \alpha_p = 1, \quad [15b]$$

where  $W, F \in \mathbb{C}$  are the complex signals of the water and fat components. According to [15b] fat itself consists of several chemical species, but with a priori known relative

amplitudes and chemical shifts. The specified single- $R_2^*$  water-fat signal model [15] is of the general form [1], which is made evident by the following correspondences (and constraints): We can assign  $W = \hat{\rho}_1 \exp(i\hat{\phi}_1)$ ,  $F\alpha_1 = \hat{\rho}_2 \exp(i\hat{\phi}_2)$ ,  $\omega = \hat{\omega}_1$ , and  $R_2^* = \hat{R}_1$ , where the consequent constraints on the a priori known fat parameters are then given by  $\rho_m \exp(i\phi_m) = F\alpha_{p=m-1}$ ,  $\omega_m = \omega - \Delta\omega_{p=m-1}$ , and  $R_m = R_2^*$  for all  $m \in \{2, \dots, M\}$ . Note that the parameter  $\omega$  in [15a], often called the field map, can be regarded as the resonance frequency of the water species, here  $m = 1$ , and the resonance frequencies of all other fat species are just the field map shifted by the known chemical shifts  $\Delta\omega_{p=m-1}$ . Similarly, the relaxation rates of each chemical species in the fat molecule is constrained to be the same as  $R_2^*$  as for the water species. The number of parameters in [15] is therefore reduced to six real unknowns, namely the magnitude and phase of  $W$ ,  $F$ , respectively,  $\omega$ , and  $R_2^*$ . As the measurements are complex, at least three observations (complex MR signal at three echo times) are needed to solve system of equations [10].

The relational assumptions for the parameter constraints that reduce the parameter space from [1] to only the six variables in [15] can be formulated in the following constraint matrices:

$$\begin{aligned} \mathbf{C}_\rho &= \begin{pmatrix} 1 & 0 & 0 & \dots & 0 \\ 0 & \alpha_1 & 0 & \dots & 0 \\ \vdots & \vdots & \vdots & \ddots & \vdots \\ 0 & \alpha_P & 0 & \dots & 0 \end{pmatrix}, & \mathbf{C}_\phi &= \begin{pmatrix} 1 & 0 & 0 & \dots & 0 \\ 0 & 1 & 0 & \dots & 0 \\ \vdots & \vdots & \vdots & \ddots & \vdots \\ 0 & 1 & 0 & \dots & 0 \end{pmatrix}, \\ \mathbf{C}_\omega &= \begin{pmatrix} 1 & 0 & \dots & 0 \\ 1 & 0 & \dots & 0 \\ \vdots & \vdots & \ddots & \vdots \\ 1 & 0 & \dots & 0 \end{pmatrix}, & \mathbf{C}_R &= \begin{pmatrix} 1 & 0 & \dots & 0 \\ 1 & 0 & \dots & 0 \\ \vdots & \vdots & \ddots & \vdots \\ 1 & 0 & \dots & 0 \end{pmatrix} \end{aligned} \quad [16]$$

For the parameter estimation algorithm, the initialization of resonance frequencies is set to  $\vec{\omega}^{(0)} = [\hat{\omega}^{(0)} + \Delta\omega_1, \dots, \hat{\omega}^{(0)} + \Delta\omega_P]^T$ . The two very similar water-fat signal models, the signal model without any  $R_2^*$  decay,

EQ [17]

$$s_n = (W + d_n F) e^{i\omega t_n}, \quad [17]$$

and the double- $R_2^*$  model with separate relaxation constants for water  $R_{W,2}^*$  and fat  $R_{F,2}^*$ ,

EQ [18]

$$s_n = \left( W e^{-R_{W,2}^* t} + d_n F e^{-R_{F,2}^* t} \right) e^{i\omega t_n}, \quad [18]$$

are translated into the same set of constraint matrices as for the single- $R_2^*$  model [16], whereas only  $\mathbf{C}_R$  is set to the zero-matrix in case of no  $R_2^*$  or the first subcolumn below the diagonal in  $\mathbf{C}_R$  is shifted by one column for the double- $R_2^*$  model, respectively:

$$\text{single-}R_2^*: \mathbf{C}_R = \begin{pmatrix} 1 & 0 & \cdots & 0 \\ 1 & 0 & \cdots & 0 \\ \vdots & \vdots & \ddots & \vdots \\ 1 & 0 & \cdots & 0 \end{pmatrix} \longrightarrow \text{no-}R_2^*: \mathbf{C}_R = \begin{pmatrix} 0 & 0 & 0 & \cdots & 0 \\ 0 & 0 & 0 & \cdots & 0 \\ \vdots & \vdots & \vdots & \ddots & \vdots \\ 0 & 0 & 0 & \cdots & 0 \end{pmatrix} \quad [19a]$$

$$\longrightarrow \text{double-}R_2^*: \mathbf{C}_R = \begin{pmatrix} 1 & 0 & 0 & \cdots & 0 \\ 0 & 1 & 0 & \cdots & 0 \\ \vdots & \vdots & \vdots & \ddots & \vdots \\ 0 & 1 & 0 & \cdots & 0 \end{pmatrix}. \quad [19b]$$

For the three water-fat signal models above we performed exemplary in vivo parameter mapping and a Cramér-Rao noise performance analysis.

- Parameter mapping: For all three models, without  $R_2^*$  [19a], with single- [16] and double- $R_2^*$  [19b] signal model, we computed quantitative parameter maps using the Algorithm [1] in vivo at in a spine dataset from a 62 year old female osteoporosis patient, where the details of the time-interleaved multi-gradient-echo (TIMGRE, (21)) MR scan with monopolar (flyback gradient) readout included: six echoes in two interleaves, TR/TE<sub>min</sub>/TE = (9.9/1.33/1.1) ms, bandwidth = 1504.4 Hz/pix, FOV = (220 x 220 x 80) mm<sup>3</sup>, voxel size = (1.8 mm)<sup>3</sup>, flip angle = 3°, scan time = 4:30 min.
- Cramér-Rao analysis: Assuming the single- $R_2^*$  signal model, we computed the FIM and the CRLBs for varying proton-density fat fraction, PDFF  $\in [0, 100]$  in a simulated six-echo multi-fat-peak signals in human liver tissue (22) at with fixed parameters including first echo time TE<sub>1</sub> = 1 ms, echo spacing  $\Delta$ TE = 1 ms,  $R_2^* = 5 \text{ s}^{-1}$ , field map  $\omega/2\pi = 10 \text{ Hz}$ . To compare the result to the previous study (11), we employed a noise measure of comparable number of signal averages (NSA), which is computed by dividing the inverse single diagonal elements of the FIM to the CRLBs times the number of echoes  $N_{\text{TE}}$  as

$$\text{NSA}_k = \frac{N_{\text{TE}}}{\mathbf{I}_{kk} \mathbf{I}_{kk}^{-1}}. \quad [20]$$

To compare this theoretical noise measure to the parameter estimation by the Algorithm [1], we performed a Monte-Carlo analysis for each experimental point by simulation of 10<sup>5</sup> independent noise realizations with a signal-to-noise-ratio of SNR = 100. In the same spine dataset as above, we computed anatomical maps of the NSA for all tissue parameters resulting from the in vivo parameter mapping.



The tissue parameters describing fatty acid composition, the saturation fraction SF, unsaturation fraction UF, poly-unsaturation PUF, and mono-unsaturation MUF fraction are determined as:

$$SF = 1 - \left| \frac{F_3}{3F_1} \right|, \quad UF = 1 - SF, \quad PUF = \left| \frac{F_4}{3F_1} \right|, \quad MUF = UF - PUF \quad [24]$$

We applied the proposed formulation for fatty acid composition parameter mapping in vivo in the gluteal region of a healthy volunteer, who was scanned at with a time-interleaved multi-gradient echo sequence (two interleaves à ten echoes) with monopolar gradients (21), TR = 24 ms, number of echoes  $N_{TE}=20$ , TE1= 1.5 m,  $\Delta TE = 1.0$  ms, flip angle = 5°, bandwidth = 961.5 Hz/pixel, FOV = 400 x 300 x 140 mm<sup>3</sup>, 2.0 mm isotropic resolution, SENSE factor = 2.5 and scan time = 3 min 8 sec (24).

## Results

In this section, we demonstrate how the developed generalized formulation for parameter estimation and optimal experimental design in terms of noise performance for model parameters can be applied in the chosen subset of common quantitative MRI scenarios.

**Table 1**, as the main result of this work, gives a non-exhaustive overview of several complex gradient-echo-based multi-species signal models from literature and their representation as constraint matrices in the proposed generalized formulation.

**Figure 1** compares the parameter mappings in the spine dataset for the water-fat signal models with no, single- and double- $R_2^*$ , all generated with the same Algorithm [1] but with different corresponding constraint matrices. The PDFFF was computed using the magnitude discrimination approach (25). It is apparent how the estimation of an increasing number of parameters at constant number of echoes results in a lower noise performance.

**Figure 2** gives the result of the performed Cramér-Rao analysis and extends the result from (11) from a three-echo signal of a single-peak fat model without  $R_2^*$ -relaxation to the common case of a six-echo sampling of a multi-peak fat model with common  $R_2^*$ . The Monte-Carlo noise estimates for the NSA of all estimated parameters closely follow the theoretical CRLBs demonstrating consistency between the parameter estimation scheme and the FIM optimal design formalism, demonstrating consistency between estimation algorithm, Cramér-Rao simulation and literature.

**Figure 3** displays anatomical maps for uncertainty quantification of the parameter maps in the spine dataset from Figure 1. Assuming the estimated parameter maps as the true tissue parameters, the noise estimates are computed in each voxel for all models via Equation [20]. The same noise behavior than in the theoretical assessment in Figure 2 can be observed: parameters containing fat magnitude and phase information are best estimated in lower fat fraction regions (compare to Figure 1), while in regions with high fat fraction, water parameters show higher NSA. The field map and relaxation rate estimates are not largely affected by different underlying fat fraction.

**Figure 4** shows the capability of the generalized formulation to generate parameter maps for more complex models, like the fatty acid composition model, by only changing the constraint matrices as input for the implemented parameter estimation functions. While in the top row of subplots in Figure 4 the quantitative parameters common for the standard single- $R_2^*$  and the fatty acid composition model are compared, the lower row shows the derived additional quantitative parameter maps [24], with complementary information about fatty acid composition.

In the Supplementary Materials we also gave an example for optimal echo time selection in terms of signal-to-noise ratios in the estimates shown in **Figure S1**.

## Discussion

In this work, we developed a generalized formulation for the processing of multi-echo gradient-echo MR signals of multiple chemical species. We demonstrated how the developed signal analysis framework allows parameter estimation and noise performance analysis over a broad range of signal models that have the form of a weighted sum over complex exponentials, whose phase terms depend linearly on the echo time. The main result of the present study is the demonstration of the abundance of parameter estimation techniques that can be derived from the developed framework by changing simple input matrices. Therefore, the value and novelty of the presented work lie within the generality of the method across multiple different signal models rather than re-implementation of each specific signal model.

## Generalized Formulation

The main advantage of the proposed framework is the abstraction of model-specific relations between estimation parameters into a matrix formulation. The constraint matrices select the derivatives of the general signal model and describe how the model varies with each property of the present chemical species. The model Jacobian, the combined model derivatives, allows to not only derive general mathematical results like the generalized FIM [11], but also to develop programming code reusable for parameter estimation in the whole signal model class of summed complex exponentials. These two, computational and mathematical, abstraction benefits to handle a large class of signal models for parameter estimation or optimal experimental design are demonstrated in Figure 1 and the noise performance analysis in Figure 2.

Given a signal model of interest, one can follow three steps to apply the presented parameter estimation and noise performance analysis analogously to the example for the single- $R_2^*$  model [15]: 1) Reformulate the signal model to the general form of a weighted sum of complex exponentials with time-linear arguments, Equation [1]. 2) Identify the variable mappings between original formulation and the general one together with the parameter constraints in the form of indicator functions for each parameter type. 3) Translate the indicator functions to  $M \times M$  matrices and remove any zero-columns.

As a consistency check one can compare the number of columns of all resulting rectilinear constraint matrices being equal the number of unknowns in the model. The constraint matrices are then input to the presented generalized methods.

## Formulation validation and testing

To show the validity and generality of the proposed methods, we followed two motives.

First, the intrinsic consistency between the FIM-based noise analysis and the parameter estimation was tested in numerical simulations and Monte-Carlo and in vivo parameter estimations. Figure 2 demonstrates how the proposed formulation can reproduce established results from water-fat imaging literature. When no parameter relations are incorporated, the noise analysis is identical to previous results in MR spectroscopy literature (26,27). Similar to previous studies in water-fat separation, like for example by Pineda et al. (11), the comparison between the theoretical NSAs, here computed with the generalized FIM, and the implemented estimation algorithm in independently generated noisy signals shows the consistency between the noise analysis and the parameter estimation in the generalized formulation, exemplary for a six-echo sampling and a multi-fat-peak single- $R_2^*$  model.

Second, we showed reproducibility of established results with the generalized formulation in a subset of signal models previously studied in literature, primarily in water-fat imaging. Besides signal models with lower number of parameters, the more complex water-fat signal model to compute fatty acid composition parameters can similarly be represented as a set of constraint matrices. Figure 4 demonstrates how the proposed generalized formulation allows flexible formulation of the parameter estimation algorithm by choosing the corresponding constraint matrix inputs. The resulting fatty acid composition parameters are in close agreement with previous studies (2,10,23).

## Limitations

The validity and versatility of the proposed generalized formulation could be demonstrated in this work, however, the formulation and the present study has some limitations.

First, the utilized constraint matrices are only able to encode linear parameter relations. While scalings between parameters, as e.g. the fat peak amplitudes in the magnitude constraint matrix, are direct elements in the constraint matrices, constant offsets between different parameters, as e.g. for a priori chemical shifts between fat peak resonance frequencies, are described by initial values in the parameter estimation algorithm. Higher order relations between different model parameters are not part of the generalized formulation.

Second, the generalized formulation is only suitable for the complex signal models in the class of summed exponentials up to now. The exponential arguments are only linear in the echo times and higher orders were not considered.

Third, it is often desirable to be able to constrain the phases  $\phi$  of multiple chemical species to be equal. While the formulation naturally allows for these phase constraints, the Algorithm 1 in its current form does not lead to fully phase constraint results as the update

of the linear magnitude parameters  $\mathbf{g}$  does not enforce their realness, only the phase updates are constrained. While this feature was not used in this study, the realness-enforcing algorithmic update of the linear parameters can be implemented according to the update step in (28).

Fourth, in practice the phase of the measured signal may sometimes be discarded due to possible phase errors of various sources. The resulting magnitude-based signal models are not described by the developed generalized formulations in this work, however the same concept of capturing parameter relations in matrix form are applicable considering the different noise distribution in the signal magnitude.

## Free software / reproducibility research

The computer programs to implement the algorithms described above were developed in the Python programming language (Anacoda distribution of Python 3.6, <https://www.anaconda.com>). We made extensive use of the numpy, scipy, and numba module, which allowed for machine compiled and parallelized code execution ready for practical MRI applications with large (3D) multi-echo datasets. The developed computer programs used the data-structure of the ISMRM fat-water toolbox and are fully compatible with other routines within the ISMRM fat-water toolbox. Therefore, the presently developed software routines can be considered as an extension of the ISMRM toolbox allowing the adoption of signal models not included in the original ISMRM fat-water toolbox (12). To adhere to the idea of reproducible research, all code is freely available at the URL [https://github.com/maxdiefenbach/MR\\_CSS/](https://github.com/maxdiefenbach/MR_CSS/) together with the scripts to generate all Figures from this publication.

## Conclusion

We developed a formulation for multi-echo gradient-echo-based chemical species separation which allows to generalize gradient-based optimization algorithm development for the class of signal models described by a weighted sum of complex exponentials with phase terms linear in the echo time.

## Acknowledgment

The present work was supported by the European Research Council (grant agreement No 677661, ProFatMRI). This work reflects only the authors view and the EU is not responsible for any use that may be made of the information it contains. The authors also acknowledge research support from Philips Healthcare.

## References

1. Reeder SB, Wen Z, Yu H, Pineda AR, Gold GE, Markl M, et al. Multi-Coil Dixon Chemical Species Separation with an Iterative Least-Squares Estimation Method. *Magnetic Resonance in Medicine*. 2003;51(1):35-45. DOI: [10.1002/mrm.10675](https://doi.org/10.1002/mrm.10675)
2. Berglund J, Ahlström H, Kullberg J. Model-Based Mapping of Fat Unsaturation and Chain Length by Chemical Shift Imaging-Phantom Validation and in Vivo Feasibility. *Magnetic Resonance in Medicine*. 2012;68(6):1815-27. DOI: [10.1002/mrm.24196](https://doi.org/10.1002/mrm.24196)
3. Alonso-Ortiz E, Levesque IR, Pike GB. MRI-Based Myelin Water Imaging: A Technical Review. *Magnetic Resonance in Medicine*. 2014;73(1):70-81. DOI: [10.1002/mrm.25198](https://doi.org/10.1002/mrm.25198)
4. Wiesinger F, Weidl E, Menzel MI, Janich MA, Khagai O, Glaser SJ, et al. Ideal Spiral CSI for Dynamic Metabolic MR Imaging of Hyperpolarized [1-13c]pyruvate. *Magnetic Resonance in Medicine*. 2011;68(1):8-16. DOI: [10.1002/mrm.23212](https://doi.org/10.1002/mrm.23212)
5. Wang Y, Liu T. Quantitative Susceptibility Mapping (QSM): Decoding MRI Data for a Tissue Magnetic Biomarker. *Magnetic Resonance in Medicine*. 2014;73(1):82-101. DOI: [10.1002/mrm.25358](https://doi.org/10.1002/mrm.25358)
6. Hernando D, Liang Z-P, Kellman P. Chemical Shift-Based Water/fat Separation: A Comparison of Signal Models. *Magnetic Resonance in Medicine*. 2010;64(3):811-22. DOI: [10.1002/mrm.22455](https://doi.org/10.1002/mrm.22455)
7. Bydder M, Yokoo T, Hamilton G, Middleton MS, Chavez AD, Schwimmer JB, et al. Relaxation Effects in the Quantification of Fat Using Gradient Echo Imaging. *Magnetic Resonance Imaging*. 2008;26(3):347-59. DOI: [10.1016/j.mri.2007.08.012](https://doi.org/10.1016/j.mri.2007.08.012)
8. Yu H, Shimakawa A, McKenzie CA, Brodsky E, Brittain JH, Reeder SB. Multi-Echo Water-Fat Separation and Simultaneous R2\* Estimation with Multi-Frequency Fat Spectrum Modeling. *Magnetic Resonance in Medicine*. 2008;60(5):1122-34. DOI: [10.1002/mrm.21737](https://doi.org/10.1002/mrm.21737)
9. Peterson P, Månsson S. Fat Quantification Using Multi-Echo Sequences with Bipolar Gradients: Investigation of Accuracy and Noise Performance. *Magnetic Resonance in Medicine*. 2013;71(1):219-29. DOI: [10.1002/mrm.24657](https://doi.org/10.1002/mrm.24657)
10. Schneider M, Janas G, Lugauer F, Hoppe E, Nickel D, Dale BM, et al. Accurate Fatty Acid Composition Estimation of Adipose Tissue in the Abdomen Based on Bipolar Multi-Echo Mri. *Magnetic Resonance in Medicine*. 2018;81(4):2330-46. DOI: [10.1002/mrm.27557](https://doi.org/10.1002/mrm.27557)
11. Pineda AR, Reeder SB, Wen Z, Pelc NJ. Cramér-Rao Bounds for Three-Point Decomposition of Water and Fat. *Magnetic Resonance in Medicine*. 2005;54(3):625-35. DOI: [10.1002/mrm.20623](https://doi.org/10.1002/mrm.20623)
12. Hu HH, Börnert P, Hernando D, Kellman P, Ma J, Reeder S, et al. ISMRM Workshop on Fat-Water Separation: Insights, Applications and Progress in MRI. *Magnetic Resonance in Medicine*. 2012;68(2):378-88. DOI: [10.1002/mrm.24369](https://doi.org/10.1002/mrm.24369)

13. Golub G, Pereyra V. Separable Nonlinear Least Squares: The Variable Projection Method and Its Applications. *Inverse Problems*. 2003;19(2):R1-R26. DOI: [10.1088/0266-5611/19/2/201](https://doi.org/10.1088/0266-5611/19/2/201)
14. Reeder SB, Pineda AR, Wen Z, Shimakawa A, Yu H, Brittain JH, et al. Iterative Decomposition of Water and Fat with Echo Asymmetry and Least-Squares Estimation (ideal): Application With Fast Spin-Echo Imaging. *Magnetic Resonance in Medicine*. 2005;54(3):636-44. DOI: [10.1002/mrm.20624](https://doi.org/10.1002/mrm.20624)
15. Hernando D, Haldar JP, Sutton BP, Ma J, Kellman P, Liang Z-P. Joint Estimation of Water/fat Images and Field Inhomogeneity Map. *Magnetic Resonance in Medicine*. 2008;59(3):571-80. DOI: [10.1002/mrm.21522](https://doi.org/10.1002/mrm.21522)
16. Hernando D, Kellman P, Haldar JP, Liang Z-P. Robust Water/fat Separation in the Presence of Large Field Inhomogeneities Using a Graph Cut Algorithm. *Magnetic Resonance in Medicine*. 2009;63(1):NA-A. DOI: [10.1002/mrm.22177](https://doi.org/10.1002/mrm.22177)
17. Berglund J, Johansson L, Ahlström H, Kullberg J. Three-Point Dixon Method Enables Whole-Body Water and Fat Imaging of Obese Subjects. *Magnetic Resonance in Medicine*. 2010;63(6):1659-68. DOI: [10.1002/mrm.22385](https://doi.org/10.1002/mrm.22385)
18. Berglund J, Skorpil M. Multi-Scale Graph-Cut Algorithm for Efficient Water-Fat Separation. *Magnetic Resonance in Medicine*. 2016;78(3):941-9. DOI: [10.1002/mrm.26479](https://doi.org/10.1002/mrm.26479)
19. Cui C, Shah A, Wu X, Jacob M. A Rapid 3d Fat-Water Decomposition Method Using Globally Optimal Surface Estimation (R-GOOSE). 2017;79(4):2401-7. DOI: [10.1002/mrm.26843](https://doi.org/10.1002/mrm.26843)
20. Scharf L, McWhorter L. Geometry of the Cramér-Rao Bound. [1992] IEEE Sixth SP Workshop on Statistical Signal and Array Processing. nil;5-8. DOI: [10.1109/ssap.1992.246835](https://doi.org/10.1109/ssap.1992.246835)
21. Ruschke S, Eggers H, Kooijman H, Diefenbach MN, Baum T, Haase A, et al. Correction of Phase Errors in Quantitative Water-Fat Imaging Using a Monopolar Time-Interleaved Multi-Echo Gradient Echo Sequence. *Magnetic Resonance in Medicine*. 2016;78(3):984-96. DOI: [10.1002/mrm.26485](https://doi.org/10.1002/mrm.26485)
22. Hamilton G, Yokoo T, Bydder M, Cruite I, Schroeder ME, Sirlin CB, et al. In Vivo Characterization of the Liver Fat <sup>1</sup>H MR Spectrum. *NMR in Biomedicine*. 2010;24(7):784-90. DOI: [10.1002/nbm.1622](https://doi.org/10.1002/nbm.1622)
23. Peterson P, Månsson S. Simultaneous Quantification of Fat Content and Fatty Acid Composition Using MR Imaging. *Magnetic Resonance in Medicine*. 2012;69(3):688-97. DOI: [10.1002/mrm.24297](https://doi.org/10.1002/mrm.24297)
24. Franz D, Diefenbach MN, Treibel F, Weidlich D, Syväri J, Ruschke S, et al. Differentiating Supraclavicular From Gluteal Adipose Tissue Based on Simultaneous PDFF and T2\* Mapping Using a 20-echo Gradient-Echo Acquisition. *Journal of Magnetic Resonance Imaging*. 2019;nil(nil):nil. DOI: [10.1002/jmri.26661](https://doi.org/10.1002/jmri.26661)

25. Liu C-Y, McKenzie CA, Yu H, Brittain JH, Reeder SB. Fat Quantification with Ideal Gradient Echo Imaging: Correction of Bias from T1 and Noise. *Magnetic Resonance in Medicine*. 2007;58(2):354-64. DOI: [10.1002/mrm.21301](https://doi.org/10.1002/mrm.21301)
26. Nguyen H, Gahvari Z, Haldar J, Do M, Liang Z-P. Cramér-Rao bound analysis of echo time selection for <sup>1</sup>H-MR spectroscopy. Dans: 2009 Annual International Conference of the IEEE Engineering in Medicine and Biology Society. 2009. p. nil.
27. Cavassila S, Deval S, Huegen C, Ormondt D van, Graveron-Demilly D. Cramér-Rao Bounds: An Evaluation Tool for Quantitation. *NMR in Biomedicine*. 2001;14(4):278-83. DOI: [10.1002/nbm.701](https://doi.org/10.1002/nbm.701)
28. Bydder M, Yokoo T, Yu H, Carl M, Reeder SB, Sirlin CB. Constraining the Initial Phase in Water-Fat Separation. *Magnetic Resonance Imaging*. Elsevier Inc. 2011;29(2):216-21. DOI: [10.1016/j.mri.2010.08.011](https://doi.org/10.1016/j.mri.2010.08.011)
29. Liu T, Wisnieff C, Lou M, Chen W, Spincemaille P, Wang Y. Nonlinear formulation of the magnetic field to source relationship for robust quantitative susceptibility mapping. *Magnetic Resonance in Medicine* 2012; 69:467–476. DOI: [10.1002/mrm.24272](https://doi.org/10.1002/mrm.24272)
30. Yu H, McKenzie CA, Shimakawa A, Vu AT, Brau AC, Beatty PJ, Pineda AR, Brittain JH, Reeder SB. Multi-echo reconstruction for simultaneous water-fat decomposition and T2\* estimation. *Journal of Magnetic Resonance Imaging* 2007; 26:1153–1161. DOI: [10.1002/jmri.21090](https://doi.org/10.1002/jmri.21090)
31. Karampinos DC, Yu H, Shimakawa A, Link TM, Majumdar S. Chemical shift-based water/fat separation in the presence of susceptibility-induced fat resonance shift. *Magnetic Resonance in Medicine* 2012; 68:1495–1505. DOI: [10.1002/mrm.24157](https://doi.org/10.1002/mrm.24157)
32. Reeder SB, Bice EK, Yu H, Hernando D, Pineda AR. On the performance of T2\* correction methods for quantification of hepatic fat content. *Magnetic Resonance in Medicine* 2011; 67:389– 404. DOI: [10.1002/mrm.23016](https://doi.org/10.1002/mrm.23016)

## List of Figures

- **Table 1:** Common complex-based MR signal models and their representations as sets of constraint matrices in the proposed generalized formulation for chemical species separation
- **Figure 1:** Quantitative parameter maps estimated with the same VARPRO Algorithm 1 employing three different sets of constraint matrices for the no- $R_2^*$ - (left column), the single- $R_2^*$  (middle column), and the double- $R_2^*$  (right column) water-fat model as algorithmic input. For reference the maximum intensity projection across echo times ( $MIP_{TE}$ ) is shown in the lower left corner.
- **Figure 2:** Cramér-Rao lower bounds with Monte-Carlo estimates of parameter noise in a single- $R_2^*$  water-fat model. Experimental setting is defined by: number of echoes  $N_{TE} = 6$ , first echo time  $TE_1 = 1$  ms, echo spacing  $\Delta TE = 1$  ms,  $B_0 = 3$  T,  $R_2^* = 5$  s $^{-1}$ , field map  $\omega/2\pi = 10$  Hz. The Monte-Carlo simulation was performed with  $10^5$  independent noise realizations with signal-to-noise-ratio,  $SNR = 100$ . The result is an extension of (11) from a single-fat-peak model without  $R_2^*$ -decay to a multi-peak fat model (22) with a single  $R_2^*$ . The agreement of the Monte-Carlo simulation with the theoretical number of signal averages (NSA) validates the consistency of the parameter estimation Algorithm 1 and the general Fisher information from Equation [11].
- **Figure 3:** Anatomical maps showing estimated parameter uncertainty calculated as the Cramér-Rao lower bounds on the NSA noise measure for the estimated parameters from Figure 1, which are assumed to be the true underlying tissue parameters. Comparison of tissues with different proton density fat fraction (PDFF) is in agreement with theoretical results from Figure 2. For reference the maximum intensity projection across echo times ( $MIP_{TE}$ ) is shown in the lower left corner.
- **Figure 4:** Quantitative parameter maps estimated with a more complex water-fat model describing additional fatty acid composition parameters. Experimental setting is defined by a monopolar time-interleaved multi-gradient-echo sequence with parameters:  $TR = 24$  ms, number of echoes  $N_{TE}=20$  in two interleaves,  $TE_1= 1.5$  m,  $\Delta TE = 1.0$  ms, flip angle =  $5^\circ$ , bandwidth = 961.5 Hz/pixel,  $FOV = 400 \times 300 \times 140$  mm $^3$ , 2.0 mm isotropic resolution, SENSE factor = 2.5 and scan time = 3 min 8 sec . The dataset of 20 acquired echoes in the gluteal fat region allows to solve for a set of constraints matrices that include 12 independent parameters. **Top row:** maximum intensity projection over echo times, proton-density fat fraction, field map and common  $R_2^*$ . **Bottom row:** parameter maps for additional tissue fat properties in the gluteal region. Values are in close agreement with previous studies (2,10,23).



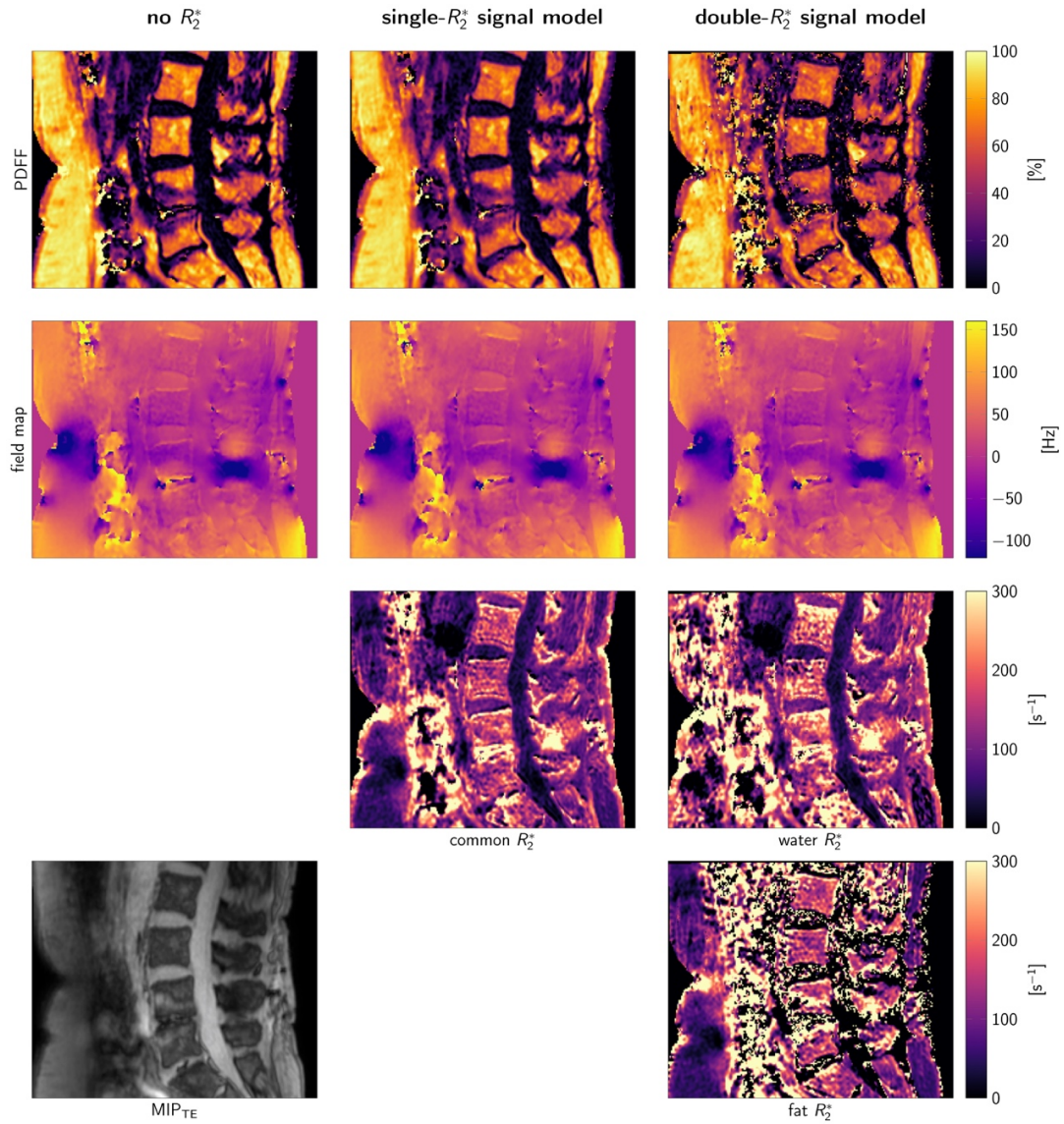


Figure 1: Quantitative parameter maps estimated with the same VARPRO Algorithm 1 employing three different sets of constraint matrices for the no- $R_2^*$ - (left column), the single- $R_2^*$  (middle column), and the double- $R_2^*$  (right column) water-fat model as algorithmic input. For reference the maximum intensity projection across echo times ( $MIP_{TE}$ ) is shown in the lower left corner.

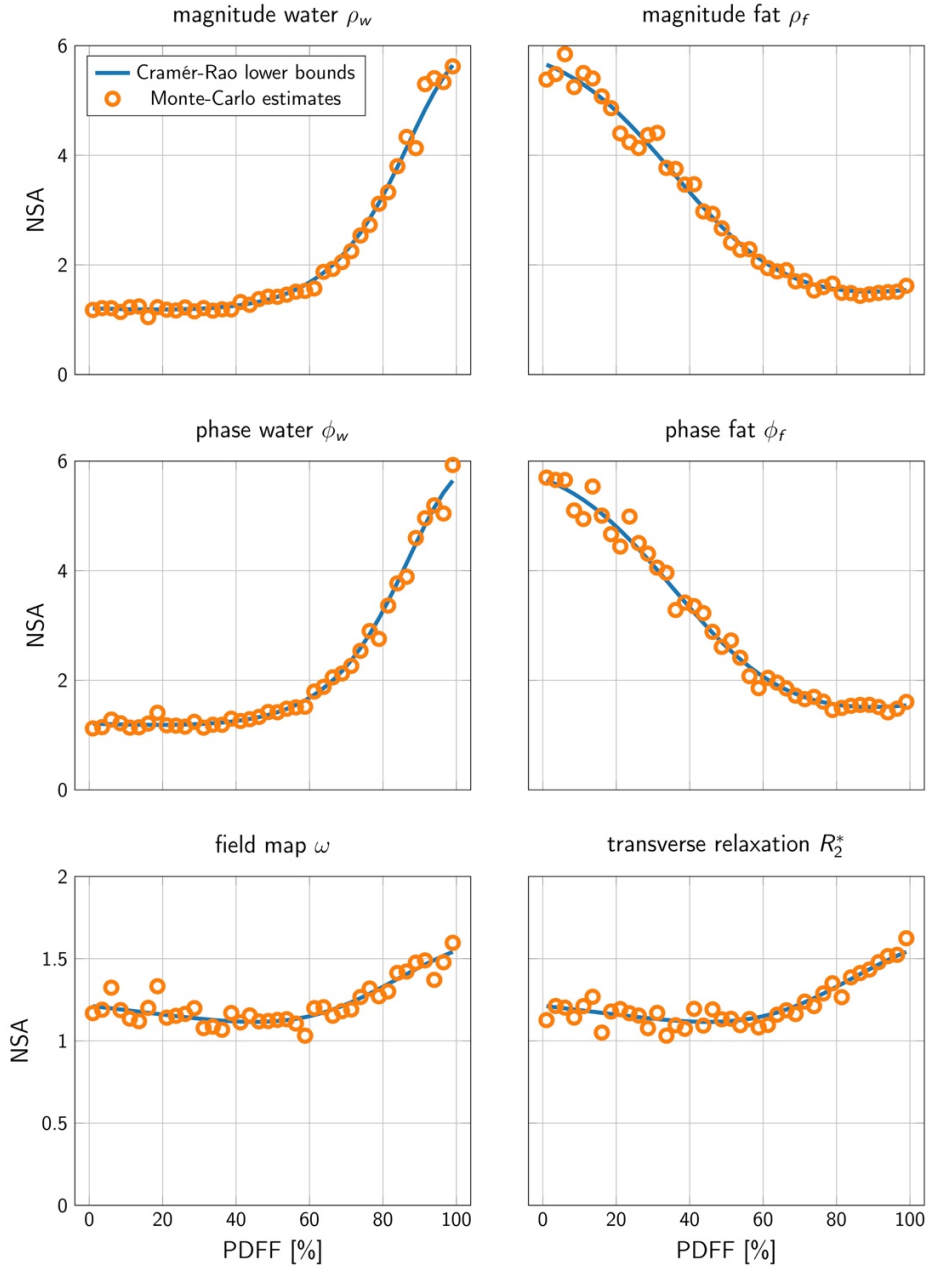


Figure 2: Cramér-Rao lower bounds with Monte-Carlo estimates of parameter noise in a single- $R_2^*$  water-fat model. Experimental setting is defined by: number of echoes  $N_{TE} = 6$ , first echo time  $TE_1 = 1$  ms, echo spacing  $\Delta TE = 1$  ms,  $B_0 = 3$  T,  $R_2^* = 5$  s $^{-1}$ , field map  $\omega/2\pi = 10$  Hz. The Monte-Carlo simulation was performed with  $10^5$  independent noise realizations with signal-to-noise-ratio,  $SNR = 100$ . The result is an extension of (11) from a single-fat-peak model without  $R_2^*$ -decay to a multi-peak fat model (22) with a single  $R_2^*$ . The agreement of the Monte-Carlo simulation with the theoretical number of signal averages (NSA) validates the consistency of the parameter estimation Algorithm 1 and the general Fisher information from Equation [11].

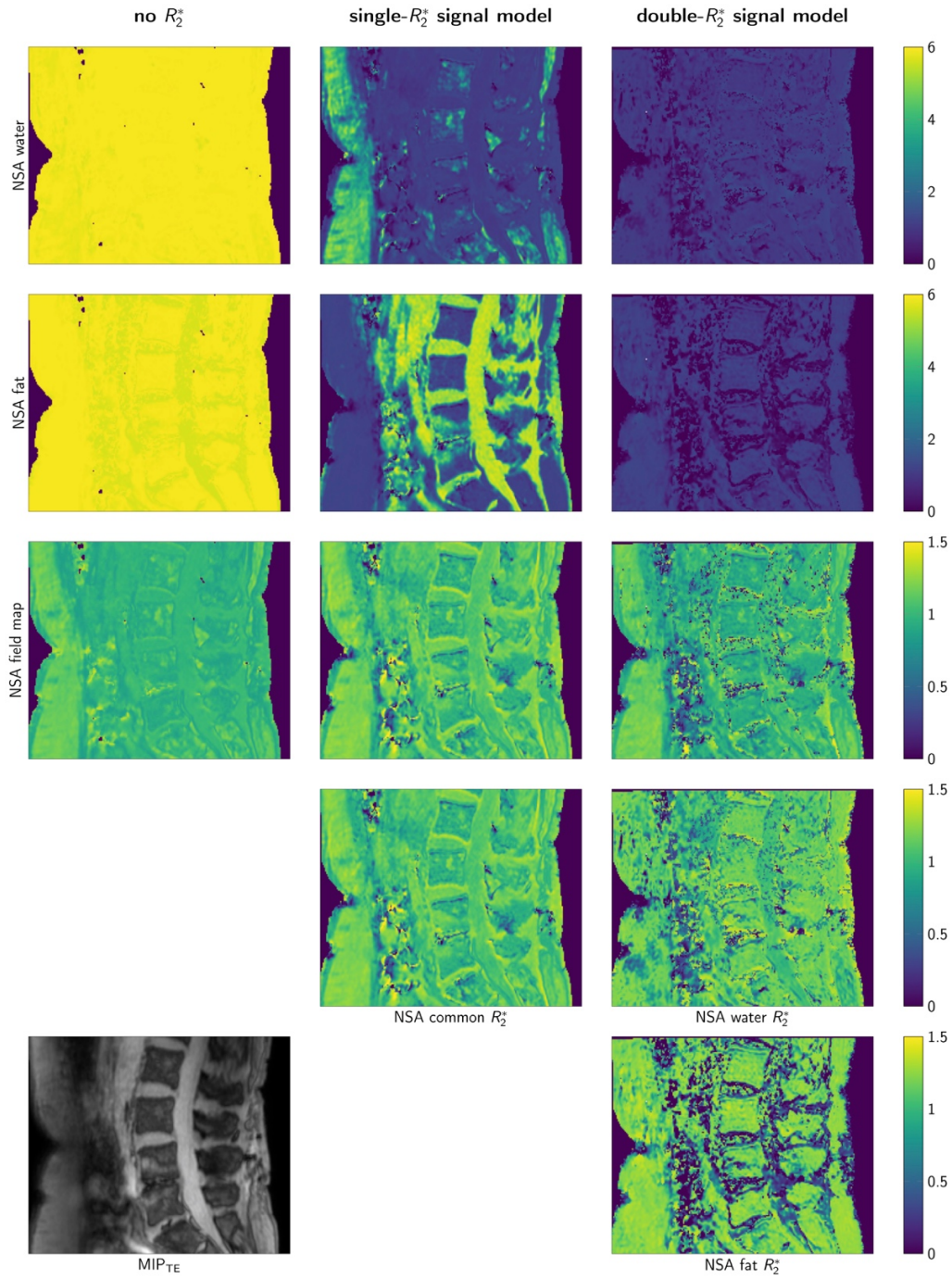
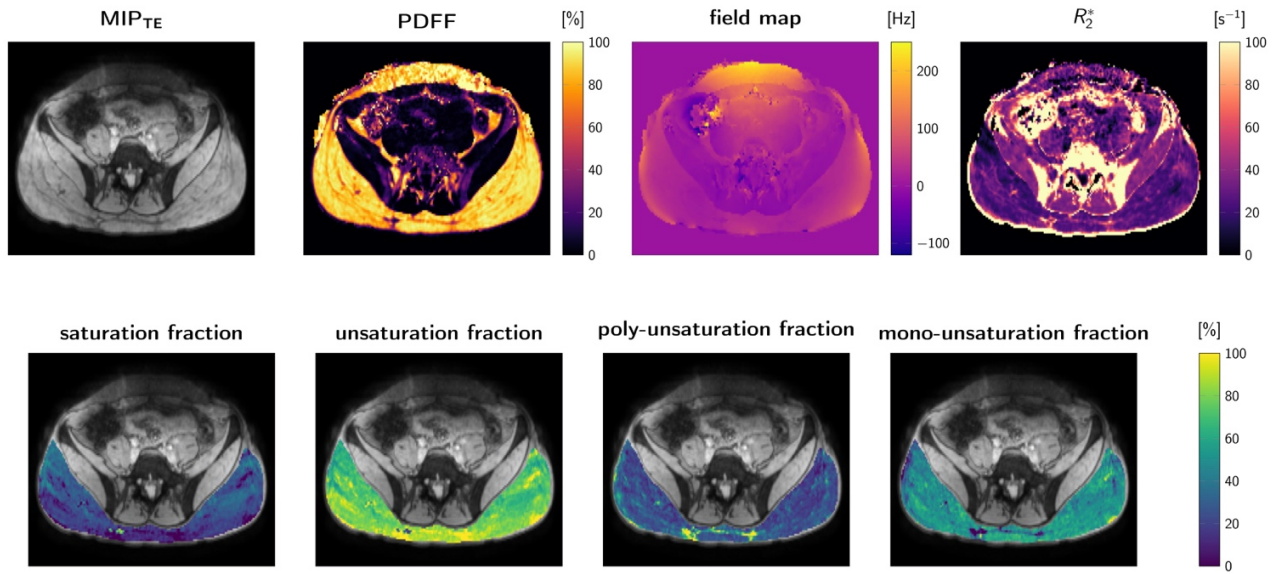


Figure 3: Anatomical maps showing estimated parameter uncertainty calculated as the Cramér-Rao lower bounds on the NSA noise measure for the estimated parameters from Figure 1, which are assumed to be the true underlying tissue parameters. Comparison of tissues with different proton density fat fraction (PDFF) is in agreement with theoretical results from Figure 2. For reference the maximum intensity projection across echo times ( $MIP_{TE}$ ) is shown in the lower left corner.



*Figure 4:* Quantitative parameter maps estimated with a more complex water-fat model describing additional fatty acid composition parameters. Experimental setting is defined by a monopolar time-interleaved multi-gradient-echo sequence with parameters: TR = 24 ms, number of echoes  $N_{TE}=20$  in two interleaves, TE1= 1.5 m,  $\Delta TE = 1.0$  ms, flip angle =  $5^\circ$ , bandwidth = 961.5 Hz/pixel, FOV = 400 x 300 x 140 mm<sup>3</sup>, 2.0 mm isotropic resolution, SENSE factor = 2.5 and scan time = 3 min 8 sec . The dataset of 20 acquired echoes in the gluteal fat region allows to solve for a set of constraints matrices that include 12 independent parameters. **Top row:** maximum intensity projection over echo times, proton-density fat fraction, field map and common  $R_2^*$ . **Bottom row:** parameter maps for additional tissue fat properties in the gluteal region. Values are in close agreement with previous studies (2,10,23).

### 3.4 Journal Publication III: On the Sensitivity of Quantitative Susceptibility Mapping for Measuring Trabecular Bone Density

The publication entitled *On the sensitivity of QSM for measuring trabecular bone density* was published in Magnetic Resonance in Medicine (ISSN: 1522-2594) on 28 September 2018 under the Creative Commons License (CC BY-NC-ND) [57]. The work also resulted in two previous conference submissions [84] and [85], which were both awarded the ISMRM Magna Cum Laude Merit Award and invited for oral presentation at the ISMRM annual meetings 2016 and 2018, respectively.

#### 3.4.1 Abstract

##### Purpose

To develop a methodological framework to simultaneously measure  $R_2^*$  and magnetic susceptibility in trabecularized yellow bone marrow and to investigate the sensitivity of QSM for measuring trabecular bone density using a non-UTE multi-gradient echo sequence.

##### Methods

The ankle of 16 healthy volunteers and two patients was scanned using a Time-Interleaved Multi-Gradient-Echo (TIMGRE) sequence. After field mapping based on water-fat separation methods and background field removal based on the Laplacian boundary value method, three different QSM dipole inversion schemes were implemented. Mean susceptibility values in regions of different trabecular bone density in the calcaneus were compared to the corresponding values in the  $R_2^*$  maps, BV/TV estimated from high resolution imaging (in 14 subjects), and CT attenuation (in two subjects). In addition, numerical simulations were performed in a simplified trabecular bone model of randomly positioned spherical bone inclusions to verify and compare the scaling of  $R_2^*$  and susceptibility with BV/TV.

##### Results

Differences in calcaneus trabecularization were well depicted in susceptibility maps, in good agreement with high-resolution MR and CT images. Simulations and in vivo scans showed a linear relationship of measured susceptibility with BV/TV and  $R_2^*$ . The ankle in vivo results showed a strong linear correlation between susceptibility and  $R_2^*$  ( $R^2 = 0.88, p < 0.001$ ) with a slope and intercept of  $-0.004 \text{ s} \cdot \text{ppm}$  and  $0.2 \text{ ppm}$ , respectively.

##### Conclusion

A method for multi-parametric mapping including  $R_2^*$ -mapping and QSM was developed for measuring trabecularized yellow bone marrow, showing good sensitivity of QSM for

measuring trabecular bone density.

### **3.4.2 Author Contribution**

Together with the co-authors the first author designed the study and set up the MR pulse sequence protocol (Philips Medical Systems, Best, The Netherlands). He developed the complete post-processing pipeline using Matlab (Mathworks, Natick, MA) and the proprietary ReconFrame software (GyroTools, Zurich, Switzerland) and the validating numerical simulations using Python (Anacoda distribution of Python 3.6, <https://www.anaconda.com>). He performed all in vivo and in silicio experiments, analyzed and interpreted the data, and wrote the paper.

### **3.4.3 Original Article**

# On the sensitivity of quantitative susceptibility mapping for measuring trabecular bone density

Maximilian N. Diefenbach<sup>1</sup> | Jakob Meineke<sup>2</sup> | Stefan Ruschke<sup>1</sup> |  
Thomas Baum<sup>3</sup> | Alexandra Gersing<sup>1</sup> | Dimitrios C. Karampinos<sup>1</sup>

<sup>1</sup>Department of Diagnostic and Interventional Radiology, Technical University of Munich, Munich, Germany

<sup>2</sup>Philips Research Laboratory, Hamburg, Germany

<sup>3</sup>Department of Diagnostic and Interventional Neuroradiology, Technical University of Munich, Munich, Germany

Correspondence Maximilian N. Diefenbach, Department of Diagnostic and Interventional Radiology, Klinikum rechts der Isar, Ismaninger Str 22, 81675 Munich, Germany. maximilian.diefenbach@tum.de

**Purpose:** To develop a methodological framework to simultaneously measure  $R_2^*$  and magnetic susceptibility in trabecularized yellow bone marrow and to investigate the sensitivity of Quantitative Susceptibility Mapping (QSM) for measuring trabecular bone density using a non-UTE multi-gradient echo sequence.

**Methods:** The ankle of 16 healthy volunteers and two patients was scanned using a time-interleaved multi-gradient-echo (TIMGRE) sequence. After field mapping based on water-fat separation methods and background field removal based on the Laplacian boundary value method, three different QSM dipole inversion schemes were implemented. Mean susceptibility values in regions of different trabecular bone density in the calcaneus were compared to the corresponding values in the  $R_2^*$  maps, bone volume to total volume ratios (BV/TV) estimated from high resolution imaging (in 14 subjects), and CT attenuation (in two subjects). In addition, numerical simulations were performed in a simplified trabecular bone model of randomly positioned spherical bone inclusions to verify and compare the scaling of  $R_2^*$  and susceptibility with BV/TV.

**Results:** Differences in calcaneus trabecularization were well depicted in susceptibility maps, in good agreement with high-resolution MR and CT images. Simulations and in vivo scans showed a linear relationship of measured susceptibility with BV/TV and  $R_2^*$ . The ankle in vivo results showed a strong linear correlation between susceptibility and  $R_2^*$  ( $R^2 = 0.88$ ,  $p < 0.001$ ) with a slope and intercept of  $-0.004$  and  $0.2$  ppm, respectively.

**Conclusions:** A method for multi-parametric mapping, including  $R_2^*$ -mapping and QSM was developed for measuring trabecularized yellow bone marrow, showing good sensitivity of QSM for measuring trabecular bone density.

## KEYWORDS

susceptibility mapping, trabecular bone density

## 1 | INTRODUCTION

Osteoporosis remains the main clinical driver for trabecular bone MRI. It is defined as the medical condition of low

bone mineral mass and density. Fractures due to osteoporotic bone loss greatly reduce individual quality-of-life and have an increasing prevalence in all demographic groups. In the United States and also in Europe, up to one in three

© 2018 The Authors Magnetic Resonance in Medicine published by Wiley Periodicals, Inc. on behalf of International Society for Magnetic Resonance in Medicine.

This is an open access article under the terms of the Creative Commons Attribution NonCommercial License, which permits use, distribution and reproduction in any medium, provided the original work is properly cited and is not used for commercial purposes.

post-menopausal women is estimated to experience bone fractures due to decreased bone densities.<sup>1,2</sup> Osteoporosis can be treated successfully if diagnosed at an early stage: bone mineral density (BMD) measurements based on dual energy X ray absorptiometry (DEXA) are currently the gold standard for osteoporosis screening.<sup>3</sup> However, BMD of healthy and osteoporotic patients overlap and have low accuracy in predicting fracture risk. Quantitative Computed Tomography (QCT) measurements allow the simultaneous assessment of BMD and bone microstructure, improving the ability to predict biomechanical bone strength and eventually fracture risk. However, QCT is associated with increased radiation dose<sup>4</sup> compared to DEXA. MRI has been previously proposed and is highly desirable for osteoporosis screening, thanks to its non-invasiveness. However, high-resolution MR trabecular bone imaging remains limited to distal skeletal sites and is not feasible due to its low sensitivity in major osteoporosis sites like the spine.<sup>5</sup>

The acquisition of multiple echoes in lower resolution gradient echo MRI enables the measurements of bone marrow effective properties as an alternative way to indirectly assess trabecular bone network health. Previously, gradient echo-based  $R_2^*$ -mapping has been proposed as an indirect measure of trabecular density.<sup>6-8</sup> The susceptibility difference between the bony trabeculae—showing no MR signal in normal gradient echo MRI sequences—and the MR signal generating bone marrow in the intra-trabecular space, causes large inhomogeneities of the induced magnetic field.<sup>6</sup> Such field inhomogeneities on the scale of the trabecular network lead to the dephasing of proton spins in bone marrow and consequently result in an accelerated relaxation due to intra-voxel dephasing on a voxel scale not resolving trabeculae directly. However, the mechanism of trabecular bone growing predominantly in the direction of the greatest force load<sup>9</sup> and the formation of connected rod-like and plate-like structures<sup>10,11</sup> give trabecular networks an inherently complex topology. Both,<sup>6</sup> numerical simulations as well as the theoretical analyses predict that in the static dephasing regime<sup>6</sup> at time scales on which diffusion effects become negligible as the dephasing field inhomogeneities are much stronger than the signal decay due to diffusive motion—the intra-voxel dephasing can be effectively described by a mono-exponential decay with decay rate  $R_2'$ . In addition, theoretical analysis also indicates a strong dependence of the intra-voxel dephasing on the orientation of trabecular bone with respect to the magnetic field, the main field strength, the voxel size and the intra-voxel distribution of bone inclusions; all effects which were also experimentally observed in previous phantom studies.<sup>7,12,13</sup> The dependence of  $R_2^*$  on all above parameters has reduced the robustness of  $R_2^*$ -mapping measuring trabecular bone density in clinical applications.

Quantitative susceptibility mapping (QSM) has been emerging as a technique to measure, a fundamental tissue

property, the average magnetic susceptibility per voxel, independent of field-strength.<sup>14</sup> In the past QSM has been extensively studied in the brain, resulting in numerous neurological applications, such as for example, identification of multiple sclerosis lesions,<sup>15,16</sup> the discrimination of cerebral micro-bleeds and intracranial calcifications<sup>17</sup> or monitoring of iron deposition.<sup>18</sup> This success motivated applications of QSM outside the brain and already encouraged QSM for breast imaging,<sup>19</sup> measuring liver iron content,<sup>20</sup> and imaging of cortical bone.<sup>21</sup> Similar to cortical bone, trabecular bone is diamagnetic and has a lower susceptibility than water, and therefore, most soft-tissues. As the apparent transverse relaxation rate in cortical bone is very large,  $R_2^* \sim 2500 \text{ s}^{-1}$ ,<sup>22</sup> ultra-short echo time MRI needs to be performed to obtain phase information inside voxels of cortical bone for reliable QSM.<sup>21</sup> Voxels containing trabecular bone show MR signal due to the surrounding bone marrow and in theory, their averaged scalar magnetic susceptibility scales linearly with the ratio of bone volume to total volume (BV/TV). Following Wiedeman's additivity law, a mixture of different components constitutes a bulk magnetic susceptibility, which is the sum of the proportionate susceptibilities of each component in the mixture.<sup>23</sup> Therefore, QSM is a natural candidate to indirectly measure trabecular bone density non-invasively.

QSM reconstructs tissue magnetic susceptibility from the phase information of MRI gradient-echo data,<sup>24</sup> which involves three main conceptual steps<sup>14</sup>: (i) estimation of the magnetic field inside the scanner, (ii) removal of field contributions not originating from susceptibility sources inside a defined region of interest (ROI), and (iii) solving the field-to-susceptibility inverse problem. All three steps face technical challenges when applying QSM in the body. First, the total magnetic field needs to be estimated. In brain QSM, where typically a tight brain mask is defined as ROI, scaling of unwrapped single echo phase images,<sup>25</sup> dual echo phase subtraction<sup>26</sup> or voxel-wise nonlinear fitting of a single frequency component to the phase evolution over multiple echoes<sup>27</sup> is used to obtain a field map. In body QSM, however, the presence of fat needs to be accounted for as the chemical shifts of its spectral resonances cause a complex multi-exponential phase evolution in voxels with non-zero fat fraction.<sup>28</sup> The parameter estimation problem for the field mapping step in body QSM is therefore the same as for complex-based water-fat separation methods.<sup>29</sup> However, as the field map is the primary parameter of interest it cannot be treated as a mere nuisance parameter, which is often subject to (multi-scale) smoothing in some current water-fat separation algorithms.<sup>30,31</sup> For the second background field removal step there are several techniques available that can be loosely categorized into two approaches: kernel-convolution-based methods such as the Laplacian Boundary Value method (LBV)<sup>32</sup> or Sophisticated Harmonic Artifact Reduction for Phase data (SHARP)<sup>33</sup> and minimum-norm methods, such as Projection onto Dipole Fields (PDF).<sup>34</sup> However, all these techniques have

not been thoroughly studied in body applications. The third field-to-susceptibility step poses an ill-posed, ill-conditioned inverse problem and can be solved by means of regularization.<sup>35</sup> In its Bayesian interpretation, the employment of different regularizations corresponds to the introduction of different prior knowledge about the underlying susceptibility distribution.<sup>36</sup> The most common regularizer used in QSM is total variation (TV),<sup>37,38</sup> in combinations with or without morphological edges weightings<sup>39</sup> and evaluated with the  $\ell_1$  or  $\ell_2$  norm.<sup>40,41</sup> TV promotes piece-wise constant susceptibility distributions in the QSM reconstructions, whereas the recently proposed total generalized variation (TGV) allows also for more linear susceptibility variations.<sup>42,43</sup> The question of which regularization scheme is best for the MRI application and clinical question at hand is still subject of ongoing research<sup>44</sup> across body regions and applications. The purpose of the present study is to develop a methodology for simultaneous  $R_2^*$ -mapping and QSM of trabecularized bone marrow and to assess the sensitivity of QSM for measuring trabecular bone density using both numerical simulations and in vivo measurements. Some results of this work have been preliminarily reported in.<sup>45-47</sup>

## 2 | METHODS

The feasibility of QSM for trabecular bone density mapping and its performance compared to relaxometry was evaluated in in vivo scans of the ankle region and in numerical simulations of a simplified trabecular bone model.

### 2.1 | In vivo measurements

Fourteen volunteers ((35 ± 16)years) were scanned in a 3 T scanner (Ingenia, Philips, Release 5.1.8, Best, The Netherlands) after informed written consent by each volunteer and approval by the institutional review board (Klinikum rechts der Isar, Technical University of Munich, Munich, Germany).

#### 2.1.1 | MR sequence parameters

A time-interleaved multi-gradient-echo sequence (TIMGRE) was used to acquire complex source images of the ankle with a total of nine echoes in three acquisitions employing flyback gradients (monopolar read-out).<sup>48</sup> Using an eight-channel foot coil, scan parameters included TR = 13 ms, TE<sub>min</sub> = 1.25 ms, ΔTE = 0.7 ms, no partial Fourier encoding, flip angle = 5°, orientation = sagittal, readout direction = feet-head, field of view (FOV) = 220 × 220 × 102 mm<sup>3</sup>, acquisition voxel size = (1.5 mm)<sup>3</sup>, bandwidth/pixel = 1431.4 Hz, scan time = 7 minutes 30.1 s, SENSE reduction factor = 1.

Additionally, all volunteer scans included a balanced steady-state free precession sequence (bSSFP) with two phase cycles, TR = 8.5 ms, TE = 3.4 ms, no partial Fourier

encoding, scan time = 7 minutes 29.1 s and a voxel size of 0.3 × 0.3 × 0.9 mm<sup>3</sup> at a slice coverage of only the calcaneus (FOV = 220 × 220 × 60 mm<sup>3</sup>) that was used to obtain an apparent measure of trabecular bone density.

### 2.1.2 | Post-processing

The TIMGRE images were subject to the QSM postprocessing pipeline outlined in Figure 1.

First, raw k-space data was reconstructed with MRecon.<sup>49</sup> Sensitivity maps acquired in pre-scans were used in the SENSE algorithm to combine separate coil images<sup>50</sup> without any parallel imaging reduction.

To estimate the total magnetic field, a complex-based water-fat separation algorithm assuming a known seven-peak fat-spectrum<sup>28</sup> with a single- $R_2^*$ -correction was initialized with a multi-seed region growing scheme from.<sup>51</sup> Further details connected to the voxel signal model equation are given in the Supporting Information S1. The water-fat separation employed for magnetic field mapping yielded, besides the total magnetic field, a quantitative proton-density fat fraction map available from the complex water  $W$  and fat  $F$  results as  $|F|/|W + F|$  and a  $R_2^*$  map.

To estimate and extract the local field from the total field map, the Laplacian boundary value method (LBV)<sup>32</sup> from the MEDI toolbox<sup>52</sup> was used.

To estimate a susceptibility map by performing dipole-inversion, the following MEDI cost function<sup>39</sup> regularized by Total Variation (TV) was optimized:

$$\chi = \underset{\chi'}{\operatorname{argmin}} \| |W_d(\gamma B_0 F^\dagger D F \chi' - f_L)| \|_2 + \lambda \| W_g \nabla \chi' \|_{\ell_p}, \quad (1)$$

where  $W_d$  was the data weighting,  $F$  Fourier transformation,  $D$  the dipole kernel in k-space defined by  $D(|\mathbf{k}| \neq 0) = 1/3 - k_z^2/|\mathbf{k}|^2$  and  $D(|\mathbf{k}| = 0) = 0$ ,  $f_L$  the local field,<sup>14</sup> and  $W_g$  the gradient weighting. Note that we assumed the main magnetic field as pointing along the  $z$ -axis,  $\mathbf{B}_0 = B_0 \hat{\mathbf{z}}$ ,  $\gamma$  is the proton's gyromagnetic ratio.

Three different dipole-inversion schemes were implemented: (i) a closed form  $\ell_2$ -regularized solution of (1) with  $W_d = W_g = 1$ ,<sup>40</sup> (ii) an optimization of the  $\ell_2$ -regularized MEDI costfunc<sup>38</sup> solved by the conjugate gradients method, and (iii) an optimization of the TV-MEDI cost function<sup>39</sup> solved by Nesterov's algorithm.<sup>53</sup> For the two MEDI optimizations, the gradient weighting  $W_g$  was obtained by thresholding the absolute value of the forward gradient on the water-fat opposed phase image  $|W - F|$  such that 40% of the voxels in the tissue region belong to edges and are weighted by a value of 0.01, whereas all other voxels in  $W_g$  were set to 1. For the data weighting mask  $W_d$  the maximum intensity projection across echo times (MIP<sub>TE</sub>) was scaled to the dynamic range [0, 1]. The regularization parameter  $\lambda$  was chosen by visually comparing the quality of susceptibility maps

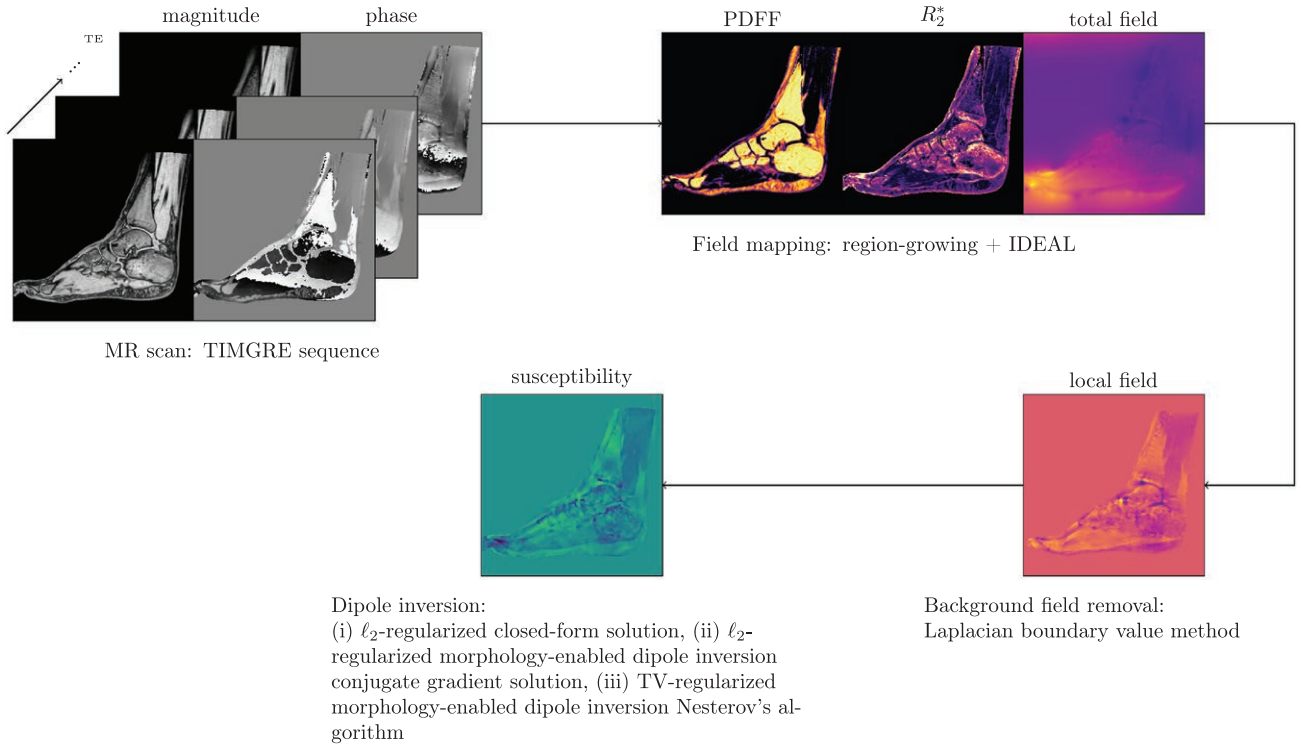


**FIGURE 1** Flowchart overview of the post-processing pipeline for quantitative susceptibility mapping for trabecular bone density mapping

from the first volunteer dataset reconstructed with a range of  $\lambda$ 's from 0.0001 to 1 varied on a log-scale. This selection of  $\lambda$  was also guided by plotting an L-curve heuristic as the discrepancy  $\|(F^\dagger DF\chi - f_L)\|_2^2$  after the reconstruction versus  $\lambda$ , which is shown in Supporting Information Figure S2.

The susceptibility maps were not subject to any referencing, the absolute range of values was unchanged for all subject datasets and the DC offset of the dipole kernel was zero.

To access the measurement of trabecular bone density in the quantitative susceptibility maps across all subjects, two ROIs inside the calcaneus were drawn in the lower-resolution TIMGRE magnitude images of each subject where the calcaneus is known to have different BV/TV ratios, the subtalar and the tuber calcanei, both depicted in the top right of Figure 4.<sup>7</sup> The third distinct region in the calcaneus with much less BV/TV, the cavuum calcanei, was not included in the ROI analysis as increased vascularization in this region complicates QSM measurements. The ROI label masks created in 3D Slicer (Version 4.7,<sup>54</sup>) were used to extract label statistics in the quantitative maps derived from the TIMGRE source images.

After linear registration of the bSSFP to the TIMGRE images using SimpleITK<sup>55</sup> and resampling the label masks to the bSSFP orientation, a measure of apparent BV/TV was determined in each ROI by the histogram-based double-thresholding method described in.<sup>56</sup>

Measures of central tendency inside the defined ROIs were extracted for all quantitative parameters. Correlations between the mean values were investigated by linear regression.

### 2.1.3 | Computer tomography patient scans

The post-processing of the TIMGRE scan described above was also applied for two patients (one male age 70, one female age 76) that were equally informed and asked to participate in the study as the healthy volunteers. As part of their clinical care, low-dose whole body CT images were taken and approved to be evaluated for this work.

The calcaneus in the TIMGRE and the CT images were manually registered until complete line-up. Besides visual comparison of CT images in Hounsfield units and the estimated parameter maps, ten ROIs were drawn in the subtalar and the tuber calcanei, respectively, for each patient dataset. Again linear regression was performed to correlate  $R_2^*$  and susceptibility with CT attenuation.

## 2.2 | Numerical simulations

Similar to previous work simulating magnetic fields in trabecular bone,<sup>57,58</sup> we forward simulated magnetic field distortions created by a simple trabecular bone model. In a cubic box of  $128 \times 128 \times 128$  voxels, spherical inclusions resembling the trabecular bone volume inside a ROI were randomly positioned in space with the possibility to overlap. The cubic ROI was centered in an empty three dimensional cube with an edge length three times as large. According to the same forward model as in Equation (1),  $f_B = \gamma B_0 F^\dagger DF\chi$ , the field map  $f_B$  was simulated with one fixed  $B_0$ -direction with varying

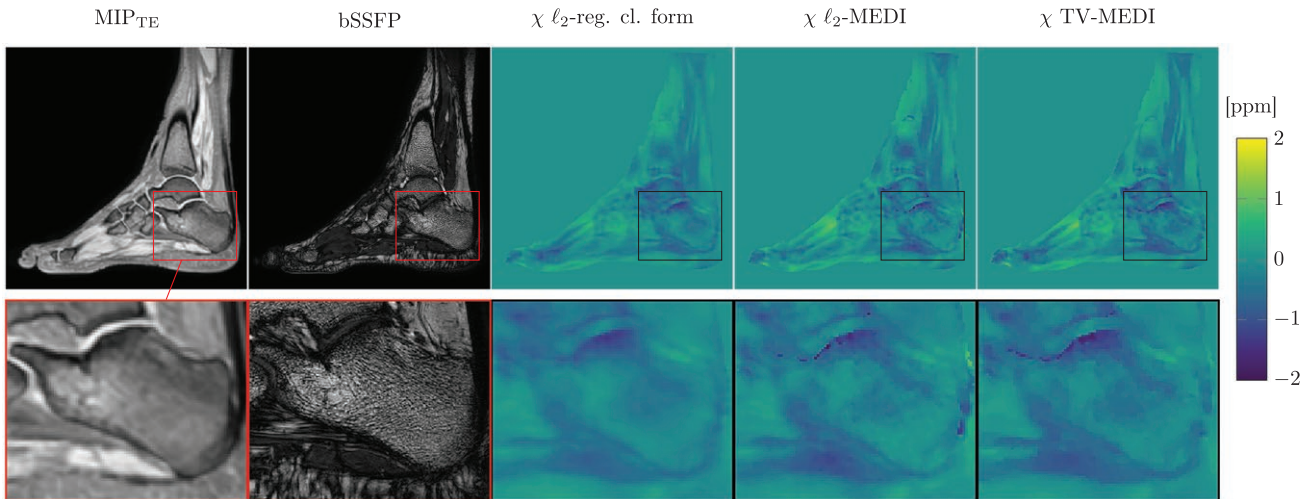


**FIGURE 2** Visual comparison of different dipole inversion methods for quantitative susceptibility mapping (QSM) in the calcaneus. Column 1: maximum intensity projection over echo times in MR scan used for QSM. Column 2: high-resolution image from a balanced steady state free-precession (bSSFP) sequence. Column 3–5: QSM result from a  $\ell_2$ -total variation regularized closed form susceptibility solution,<sup>40</sup> an  $\ell_2$ -total variation (TV) regularized morphology-enabled dipole inversion (MEDI),<sup>38</sup> and a TV-MEDI, respectively<sup>66</sup>

susceptibility difference of the trabecular bone inclusions to the surrounding,  $\Delta\chi = (-0.5, -1.0, -1.5, -2.0)$  ppm, varying number of spherical inclusions,  $N=100,150,\dots,300$ , and varying radii,  $r = (5, 10, 15, 20)$  voxel units. All inclusions were simulated to have the same radius and susceptibility. Each combination of the parameters  $\Delta\chi$ ,  $N$  and  $r$  was explored by a Monte-Carlo program in 100 different spatial configurations of the inclusions. The program was implemented in the Python programming language (Python version 3.5.4) making use of the default random number generator from the numpy module (numpy version 1.14.2).

The spectral density function, an auto-binned histogram of all field values outside the spherical bone inclusions, was subject to a Lorentzian fit. The full-width at half maximum (FWHM) of the fitted Lorentzian curve was employed as a measure of the reversible relaxation rate  $R'_2$ . To re-invert the noise-free field maps to susceptibility, the simple closed-form Tikhonov-TV regularized solution<sup>40</sup> was used and the mean susceptibility value inside the cubic trabecular bone ROI was taken for comparison. The simulation resulted in two effective parameters resembling  $R_2^*$  and susceptibility  $\chi$  for the whole ROI for all configurations of spherical inclusions (of varying BV/TV) inside the box.

### 3 | RESULTS

#### 3.1 | In vivo measurements

Figure 2 shows a comparison of the three different dipole inversions next to the maximum intensity projection over echo times (MIP<sub>TE</sub>) and the co-registered bSSFP scan in

one exemplary subject. Due to its short  $R_2^*$ , trabecular bone shows no MR signal in non-UTE sequences and is only visible indirectly as the bone marrow in the intra-trabecular space exhibits strong MR signal. As visible in the bSSFP scan in Figure 2, bottom row, second column, high trabecular density is indicated by denser black signal drop out regions like in the subtalar. In regions with less trabeculae, bone marrow fills more volume and consequently MR signal is brighter as observed in the tuber calcanei. For all dipole inversions, the susceptibility map closely follows the trabecular bone density in the calcaneus and depicts regions of varying BV/TV in the same dynamic range but with different textures. Edges in the  $\ell_2$ -regularized closed form solution (third column) show up smooth and transitions between regions of higher and lower BV/TV appear continuous. In contrast the  $\ell_2$ -MEDI result (fourth column) shows a lot more finer variations and subtalar and tuber calcanei areas seem to show more susceptibility variance compared to the closed form solution. The fifth column shows the TV-regularized MEDI result in which the edges of the calcaneus are depicted more clearly compared to the closed form solution, while the variance of susceptibility in subtalar and tuber calcanei regions appears lower compared to  $\ell_2$ -MEDI. The same difference were observed in visual comparison of the three implemented dipole inversions in all acquired datasets; In all cases the TV-regularized MEDI showed visually the best results in terms of homogeneous susceptibility in regions with different BV/TV, defined edges in susceptibility following the magnitude images and suppressed streaking in all orientations. TV-MEDI also showed the highest correlations with apparent BV/TV and  $R_2^*$  than the other dipole inversions in regression analysis of ROI statistics below.

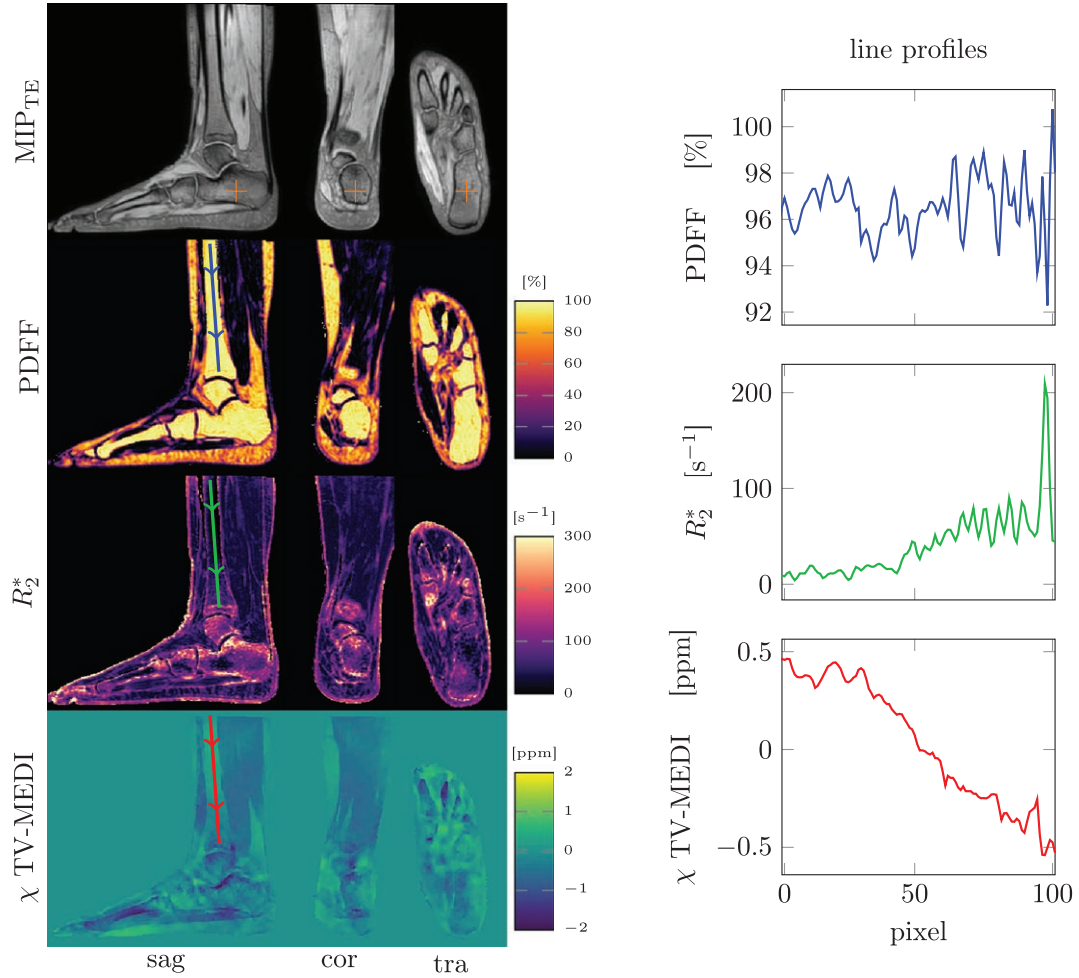


**FIGURE 3** Quantitative parameter maps in an exemplary ankle dataset (left) and corresponding line profiles in the distal tibia. With constant proton density fat fraction (PDFF), the transverse relaxation rate  $R_2^*$  increases and the susceptibility  $\chi$ —estimated with an  $\ell_1$ -total variation (TV) regularized morphology-enabled dipole inversion—decreases toward the end of the tibia, where trabecularization increases

The degree of smoothing and the streaking reduction is not only dependent on the chosen regularizer in Equation (1), but also on the regularization parameter  $\lambda$ . For each of the three different regularizers, the optimal regularization parameter was determined by comparing the visual appearance of resulting susceptibility maps while changing  $\lambda$  on a log-scale. The computed L-curves, showing the discrepancy  $\|(F^\dagger DF \chi_{\text{est}}(\lambda) - f_L)\|_2^2$  versus  $\lambda$ , were computed for one subject and are shown in Supporting Information Figure S2. While these curves showed a local minimum in the range of  $\lambda$ 's for all implemented dipole inversions, based on visual considerations about the greater reduction of streaking artifacts, the chosen  $\lambda$ 's were in the vicinity of the L-curve minimum but about one order of magnitude larger. The  $\lambda$ 's obtained in the above way in one subjects were set in the reconstructions for all other datasets and had the following values:  $\lambda(\ell_2 \text{ cl. form}) = 0.2$ ,  $\lambda(\ell_2\text{-MEDI}) = 0.1$ ,  $\lambda(\text{TV-MEDI}) = 0.03$ . The voxel size and FOV, which would also effect the choice of an optimal regularization parameter, were kept the

same in all acquired datasets and consequently did not alter the optimality of the chosen  $\lambda$ 's.

In Figure 3 one can observe the high proton-density fat fraction close to 100% in the ankle bone marrow of another exemplary healthy volunteer dataset. Line plots in the annotated regions of linearly increasing trabecularization in the distal tibia from superior to inferior is traceable in both quantitative MR parameter maps, showing the sensitivity of QSM on trabecular bone density.

To be able to assess the ability of QSM to map trabecularized bone marrow regions of different BV/TV quantitatively, the mean values of apparent BV/TV from the bSSFP scan and the reconstructed  $R_2^*$  and susceptibility from the TIMGRE inside two defined ROIs—subtalar and the tuber calcanei—scan were correlated. Figure 4 shows pair plots with all regression results. Mean ROI values of all parameters are clearly separated for both subtalar (blue) and tuber calcanei (red). For the two ROIs, averaged quantitative estimates for all subject datasets cluster also distinctively on all

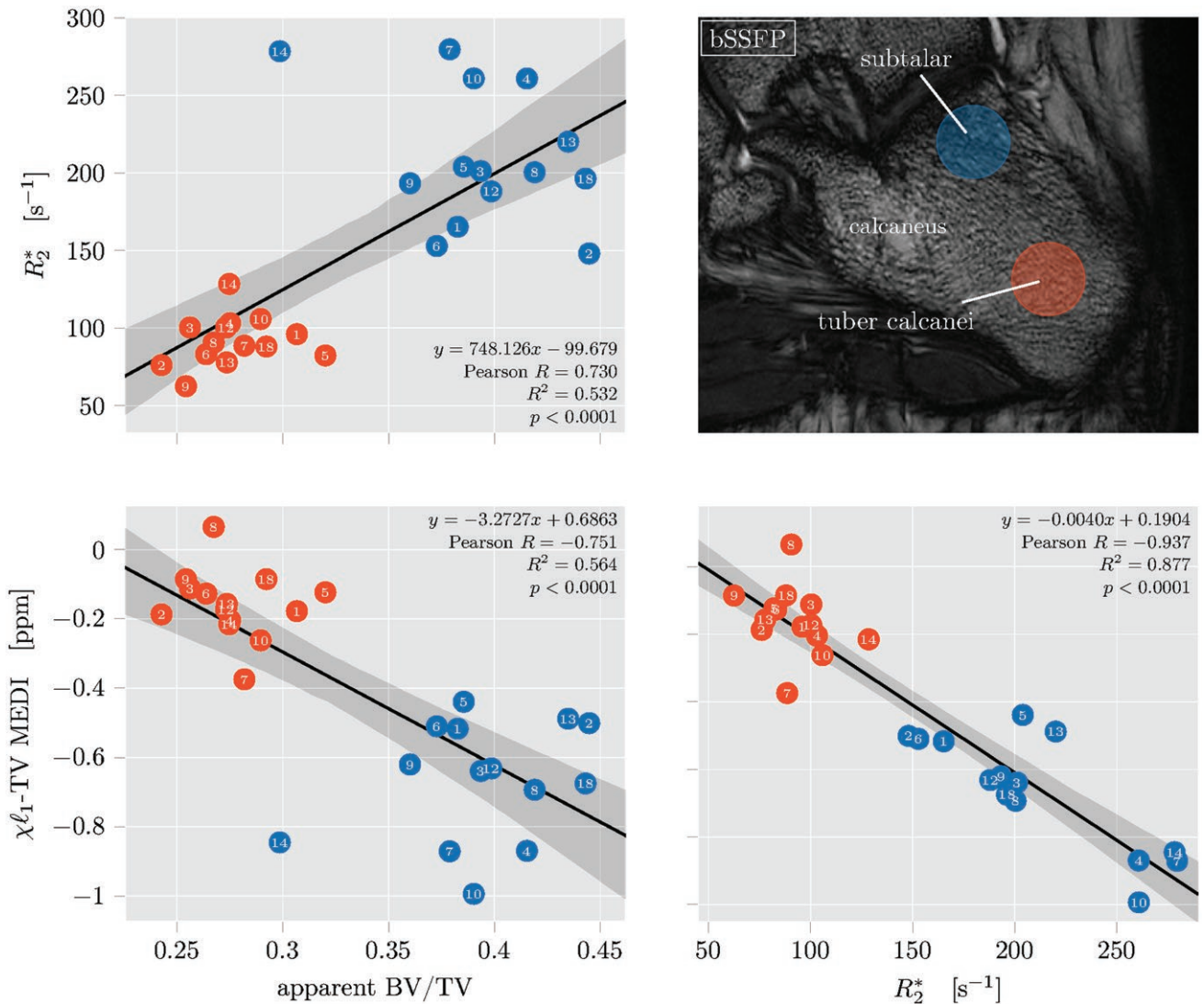


**FIGURE 4** Results of regression analysis of ROI label statics for 15 ankle datasets. In each datasets two ROI's of different trabecular bone density in the calcaneus were defined—the subtalar densely trabecularized and the tuber calcanei showing less trabecularization in the high-resolution balanced steady state free-precession (bSSFP) scan (top right)

parameter axes, even though, no referencing was used before extraction of ROI statistics. The regression results confirm the expected trends of the subtalar ROI with higher BV/TV showing larger apparent BV/TV, larger  $R_2^*$  and more diamagnetic (lower) susceptibility and the tuber calcanei with lower BV/TV showing lower apparent BV/TV, lower  $R_2^*$  and less diamagnetic (larger) susceptibility. All correlations appear to be highly significant ( $p < 0.001$ ) but with differences in the explainable variance. While the regression of parameters estimated with different sequences,  $R_2^*$  or TV-MEDI susceptibility versus apparent BV/TV, show mild correlations of  $R^2(R_2^* \text{ vs. app. BV/TV}) = 0.53$  and  $R^2(\chi \text{ vs. app. BV/TV}) = 0.56$ , correlation is strong between parameters from the TIMGRE sequence as  $R^2(\chi \text{ vs. } R_2^*) = 0.88$ .

In the apparent BV/TV a clear outlier value from subject dataset 14 can be detected, while the overall spread of BV/TV values in all subjects is larger than for  $R_2^*$  and susceptibility.

The same regression plots with susceptibility values from different dipole inversions systematically show less strong correlations between  $\chi$  and all other parameters and are shown in the Supporting Information Figure S3.

Figure 5 clearly shows how the subtalar region with higher bone mineral mass and density exhibits the largest CT attenuation inside the calcaneus. The increased BV/TV in subtalar region also results in greater intra-voxel dephasing indicated by larger  $R_2^*$  and more diamagnetic averaged susceptibility. Due to the lower number of patient datasets compared to the number of healthy volunteer datasets, ten smaller ROIs were drawn in the patients' subtalar and tuber calcanei regions, respectively, to be able to perform a similar regression analysis as compared to TIMGRE–bSSFP regression in the healthy volunteers above. Figure 6 shows pair plots of the TIMGRE–QCT regression results in the two patient datasets. Again, large ROI values of CT attenuation in more trabecularized regions

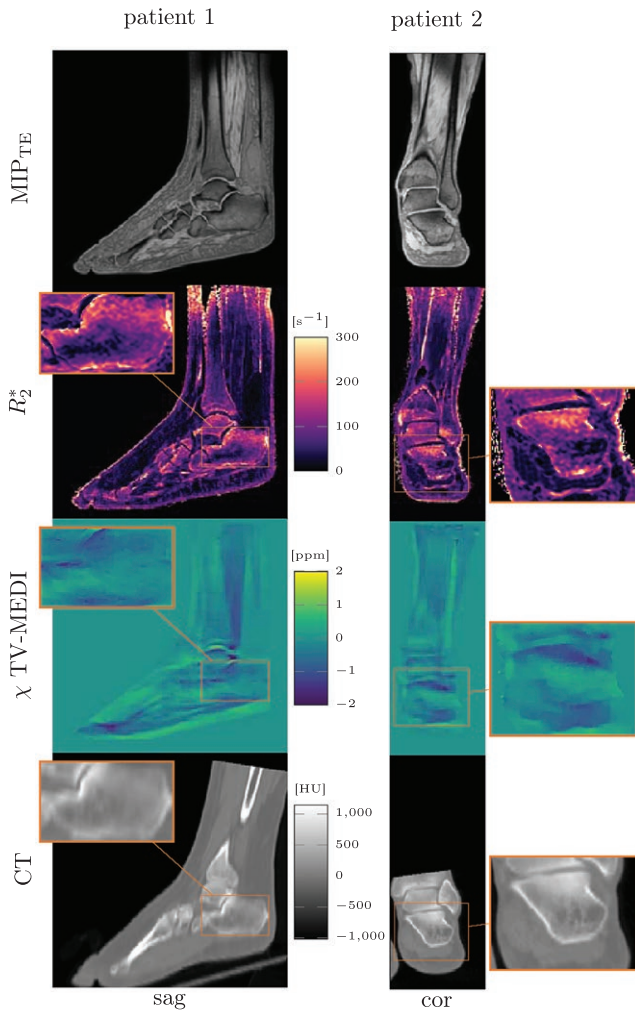


**FIGURE 5** Quantitative parameter maps estimated from the MR time-interleaved multi-gradient echo scan compared to computed tomography (CT) available in two patient datasets. The susceptibility  $\chi$ —estimated with an  $\ell_1$ -total variation (TV) regularized morphology-enabled dipole inversion—depicts regions of greater trabecular density (high CT attenuation) with more diamagnetic values. An extended version of this Figure including all orientations is available as Supporting Information Figure S4

correlate significantly with larger  $R_2^*$  and lower susceptibility ( $p < 0.0001$  for regressions between all parameters). While here,  $R_2^*$  correlates much stronger with CT attenuation ( $R^2(R_2^* \text{ vs. CT}) = 0.81$ ) than  $R_2^*$  with apparent BV/TV before, the correlations of susceptibility versus CT attenuation and  $R_2^*$  are weaker ( $R^2(\chi \text{ vs. CT}) = 0.64$  and  $R^2(\chi \text{ vs. } R_2^*) = 0.50$ ).

Again, Figures showing the incorporated QSM results of the other dipole inversion are available in Supporting Information Figures S5. Similar to the TIMGRE–bSSFP comparison, TV-MEDI performed better in visual rating and correlation to QCT than the other dipole inversions.

Close observation of the susceptibility maps in the calcaneus of patient 1 (male) and patient 2 (female) in Figure 5

shows a difference in the dynamic range. The difference of susceptibility in the subtalar and the tuber calcanei appears larger in patient 1 as in patient 2. In Figure 6 one can also observe this inter-patient variation as the difference of  $\chi$  values of subtalar (red) and cavuum calcanei (blue) in the regression plots of the bottom row is greater for the patient 1 than for patient 2 (see labeled points separately).

### 3.2 | Numerical simulations

In Figure 7, the results summarizing the numerical simulations are shown. In each row two parameters of the simplified trabecular bone model of spherical inclusions are kept fixed, while the third parameter is varying—either  $\Delta\chi$  (top row, red curves),  $N_{\text{inclusions}}$  (middle row, green curves), or radius  $r$  (bottom row, blue curves). Column-wise, from left to right, BV/TV (disc markers),  $R_2^*$  (square markers), or mean susceptibility (triangle markers) are plotted.

When the susceptibility difference  $\Delta\chi$  is linearly increased while  $N_{\text{inclusions}} = 200$  and  $r = 10$ , BV/TV stays constant,  $R_2^*$  and susceptibility increase linearly as expected.

When the number of inclusions  $N_{\text{inclusions}}$  is increased for fixed  $\Delta\chi = -1$  ppm and  $r = 10$ , both BV/TV and  $\chi_{\text{est.}}$  increase linearly with slight deviations as the spherical inclusions are allowed to overlap.

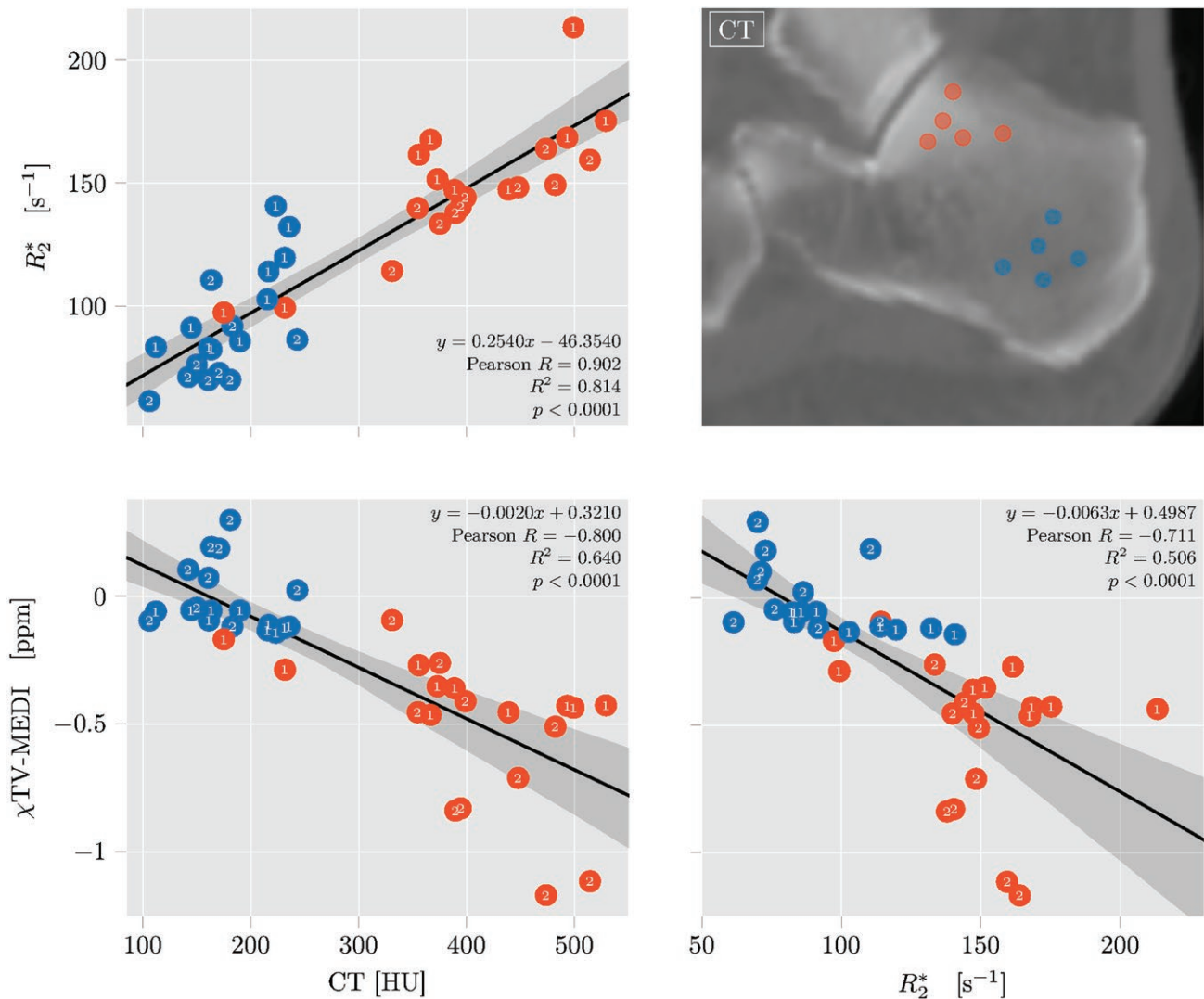
For fixed  $\Delta\chi = -1$  ppm,  $N_{\text{inclusions}} = 200$  and increasing radii of the spherical inclusions, both BV/TV and  $\chi_{\text{est.}}$  follow an expected  $r^3$  volumetric increase, while the apparent measure on  $R_2^*$  deviates from this trend. Again, deviations from the  $r^3$  curve are observable due to the overlapping of bony spheres in the model.

Figure 8 plots  $R_2^*$  (top) and the estimated mean susceptibility  $\chi_{\text{est.}}$  (bottom) against the BV/TV over all simulated configurations of bony spheres.  $\chi_{\text{est.}}$  clearly obeys a linear relationship with the exact slope depending on the susceptibility value of the spherical inclusions with respect to the surrounding, while the  $R_2^*$  versus BV/TV does not show a similar linear increase.

Error bars for all numerical results determined by taking the variance over all Monte-Carlo events are negligible (smaller than the marker size in both Figures 7 and 8), which can be easily explained by the translational invariance of the spherical inclusions inside the ROI, while the occurring cropping of spheres at the ROI edges is only of minor importance as their radius is small compared to the edge length.

## 4 | DISCUSSION

In this work, we addressed the feasibility of QSM for trabecular bone imaging. The presented results show a clear sensitivity of QSM on trabecular bone volume density. Visually the in vivo susceptibility maps were able to differentiate regions of different BV/TV as shown in the distal tibia (Figure 3) and



**FIGURE 6** Results of regression analysis of ROI label statistics in two ankle datasets in two regions of different trabecular bone density in the calcaneus—the subtalar densely trabecularized and the tuber calcanei showing less trabecularization in the high-resolution balanced steady state free-precession (bSSFP) scan (top right); (10 more ROI's not visible in the displayed slice)

the calcaneus regions, subtalar and tuber calcanei (Figure 5). Quantitative regression results of extracted ROI statistics in the calcaneus regions also confirm a good sensitivity of QSM for trabecular bone density quantification. (Figures 4 and 6). Numerical simulation of the simplified trabecular bone model of overlapping randomly distributed spherical bone inclusions inside a cubic ROI were able to show the same sensitivity of QSM on BV/TV.

In the ankle region, bone marrow almost exclusively consists of fatty yellow bone even in young healthy volunteers, visible as the almost 100% proton density fat fraction inside the bones in Figure 3. Thus, it is valid to assume there are only two components of constant susceptibility in the trabecularized bone marrow of the calcaneus, bone and fat. While bone has no MR signal at the echo times used in this study ( $\geq 1$  ms) due to its fast relaxation, the protons in the fat molecules generate signal, which exhibits a complex phase evolution due

the multiple resonances present in the fat spectrum. Effects of signal interference between fat resonances on the multi-gradient-echo data and therefore on the measured total field map and  $R_2^*$ -map are considered in the present work as the water-fat separation algorithm takes the spectral complexity of fat into account. Hence, the contrast in the measured field map and  $R_2^*$  is mainly driven by magnetic field inhomogeneities induced by magnetic surface currents at the trabeculae-bone marrow interfaces. On a voxel scale the inhomogeneities created by the susceptibility difference of the trabecular bone network to inter-trabecular space leads to an intra-voxel dephasing. The consequent increase of the dominant  $R_2'$  contribution to the apparent relaxation  $R_2^*$  inside the voxel is primarily observable in the magnitude decay of the bone marrow signal.

The phase changes inside the bone marrow translate to the measured total field map. As the trabecular size is only in the range of 100–150  $\mu\text{m}$  and inter-trabecular spacing is in

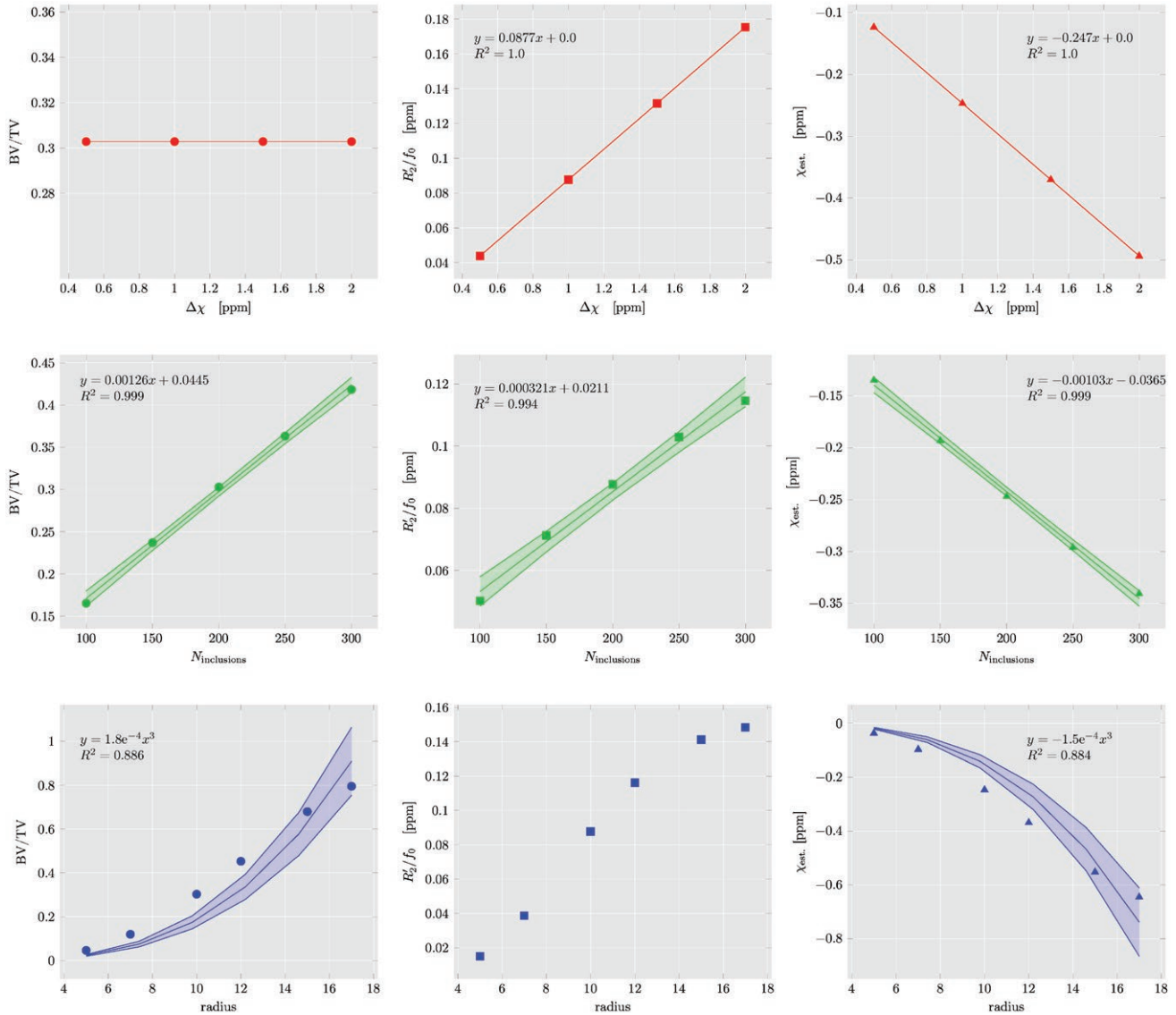


**FIGURE 7** Numerical simulation results in a simplified trabecular bone model consisting of randomly located spherical bone inclusions inside a cubic ROI, with varying relative susceptibility difference to their surrounding ( $\Delta\chi_{\text{ext}}$ , top row, red curves), number ( $N_{\text{inclusions}}$ , middle row, green curves), and radius ( $r$ , bottom row, blue curves). Plotted are the ratio of bone volume to total volume (BV/TV, first column), the  $R_2^*$  decay rate (FWHM of a Lorentzian fitted to the spectral density function), the dominant and reversible part of transverse relaxation rate  $R_2^*$  (second column), and the mean susceptibility inside the ROI after a  $\ell_2$ -total variation regularized closed form susceptibility solution

the range of 300–600  $\mu\text{m}$ ,<sup>5</sup> the created field inhomogeneities are averaged over typical MR voxel sizes around 1  $\text{mm}^3$  or bigger, leaving no or only a little local frequency offset due to the presence of trabeculae inside a voxel. In cylindrical trabecular bone models this total absence of a local frequency offset is theoretically derived in<sup>6</sup> and in the presently studied trabecular bone model of spherical inclusions is only very small. However, as the susceptibility of bony trabeculae and bone marrow fat proportionally add up inside a voxel (due to Wiedemann’s additivity law), a bulk susceptibility effect of the bone–fat mixture in the voxel is exerted on the surrounding, which scales linearly with the BV/TV inside the voxel.

The averaging out of local frequency shifts from the induced field inhomogeneities created by the trabeculae–bone marrow interfaces takes place in an arbitrarily big ROI’s containing trabecular structures and the ROI’s bulk susceptibility effect on the outside depends not only on the mean susceptibility but also on the shape of the ROI.<sup>6</sup> In gradient-echo MRI data the susceptibility effect inside the ROI is therefore encoded in the phase evolution of the ROI’s outside. The global field-to-susceptibility inversion step of QSM, conceptually a deconvolution with a kernel (the dipole kernel) of equal dimension as the field map, is therefore able to estimate susceptibility differences from trabecular bone regions of different BV/TV,

because the information about the bulk susceptibility effect on the rest of the FOV is present and exploitable even though theoretically the effect is absent inside of the trabecular bone.

Sensitivity of QSM on trabecular bone density in vivo was demonstrated in the gradient echo sequence with standard echo times, where bone does not exhibit MR signal. The present work could showcase the possibility of QSM on visualizing bulk susceptibility effects of trabecularized yellow bone marrow not only in the calcaneus, but also in the distal tibia. Along the dia-, meta-, and epiphysis, where trabecularization increases the susceptibility profiles show increasingly diamagnetic values. While differences in trabecular bone density could be detected, cortical bone could not be imaged reliably by the complete QSM post-processing. In the imaging volume there is no susceptibility information about thicker cortical bone structures, if their geometries do not lead to field distortions in the outside regions of the cortical bone. The fundamental limitation of QSM to detect MR invisible susceptibility inclusions that do not create local field contributions outside the inclusion can be seen in Figure 9. In the dataset shown in Figure 9, exemplary for all ankle datasets, the os meta tarsi, one of the longer bones in the foot leading to the toes clearly shows a strong diamagnetic value (dark) in the

susceptibility map, while the cortical bone of the distal tibia which typically points along the main magnetic field  $B_0$  is not visible in the susceptibility map due to the lack of MR signal within the cortical bone tissue and the absence of field distortions on its outside. Consequently, for the focus on cortical bone, MR phase information in the inside of the bone is necessary to reliably estimate its susceptibility, which manifests the need for ultra-short echo time (UTE) imaging to provide MR signal inside bone as in.<sup>21</sup> In the context of traditional osteoporosis screening however, the characterization of bone loss in the trabecular bone network is of primary interest. QSM for trabecular bone imaging showed sufficient sensitivity on BV/TV based on the non-UTE acquisition employed in this work.

We found that the exact appearance of trabecularized regions in the reconstructed susceptibility maps depends on the regularization techniques being used in the dipole inversion step of the QSM pipeline. Many different regularization techniques were proposed.<sup>44</sup> In this work, we implemented and compared three different regularization schemes: a closed form solution with an  $\ell_2$  total variation (TV) regularization, an  $\ell_2$ -MEDI and a TV-MEDI. By visual comparison of the TV-MEDI approach appeared to have the best compromise between piece-wise constant regions of averaged

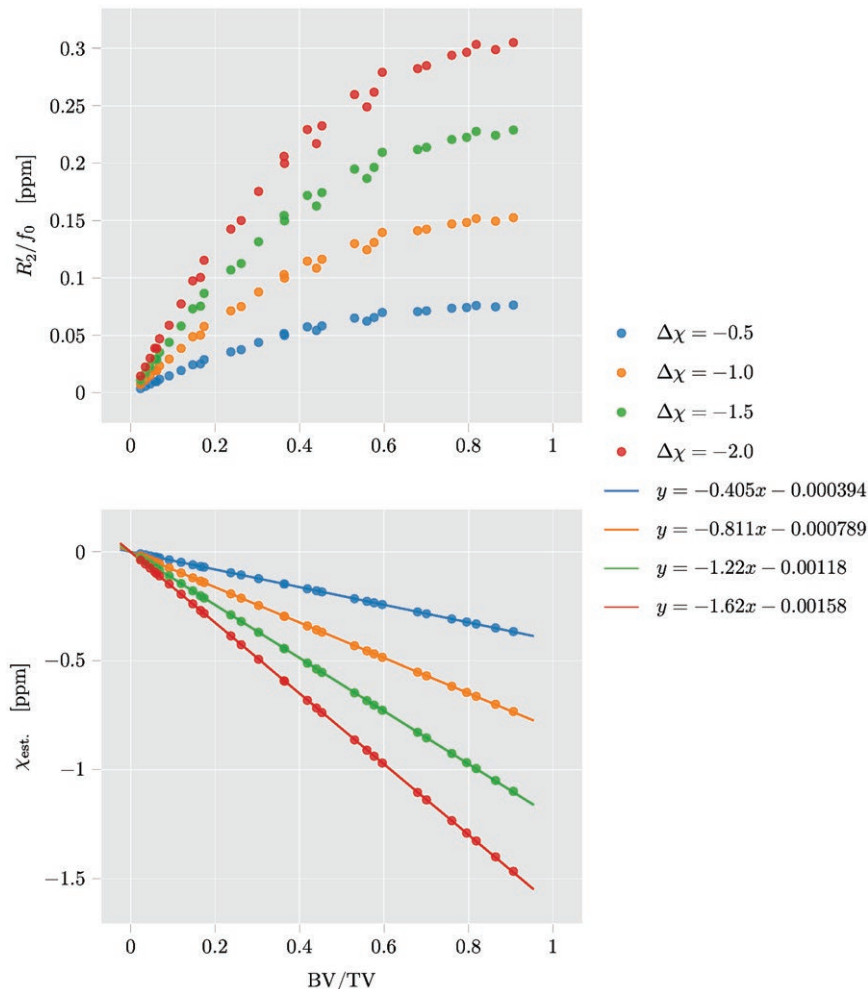


**FIGURE 8** Effective parameters simulated in a simplified trabecular bone model consisting of randomly located spherical bone inclusions inside a cubic ROI plotted against the bone volume to total volume (BV/TV). Top: the  $R_2'$  decay rate (FWHM of a Lorentzian fitted to the spectral density function). Bottom: mean susceptibility inside the cubic ROI after a  $\ell_2$ -total variation regularized closed form susceptibility solution

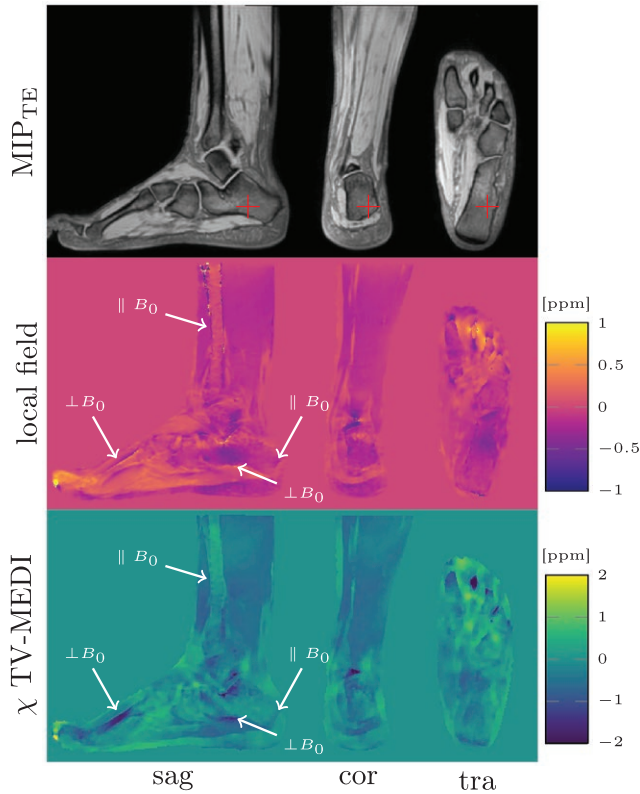


**FIGURE 9** Illustration of the inability of the proposed quantitative susceptibility mapping (QSM) pipeline to measure cortical bone structures whose edges are aligned with the main magnetic field  $B_0$ , here pointing in feet-head direction. The cortical bone of the os metatarsi II in the foot is correctly assigned a diamagnetic susceptibility, because its perpendicular orientation to  $B_0$  leads to magnetic field distortions in the surrounding. In contrast the cortical bone of the distal tibia in the leg does not show the same susceptibility as its parallel orientation with respect to  $B_0$  does not lead to field distortion on its outside, which renders it invisible to QSM. In the employed MR sequence without acquiring ultra short echo times (non-UTE) no phase information is available inside of the cortical bone regions

voxel susceptibility and sharp features appearing at edges of tissues with different susceptibility. While the closed form solution appeared always over-smoothed compared to TV-MEDI, the  $\ell_2$ -MEDI showed a high variance of susceptibility values inside trabecular bone regions, independent of the regularization parameter (see Supporting Information Figure S2). Besides this visual comparison, the regression of the quantitative values in the drawn ROIs in the subtalar and the tuber calcanei of all volunteers showed the highest correlations with the TV-MEDI regularization (compare Figure 4 and Supporting Information Figure S2). In the regularization of the performed MEDI, an important part of the regularizer is a morphological edge mask derived from magnitude information that ensures that susceptibility is piece-wise constant and not artificially smoothed over true discontinuities. Due to magnitude modulations in trabecular bone regions

it is possible that the used edge detection algorithm identifies edges in these regions where susceptibility varies continuously without large discontinuities. The down-weighted regularization in falsely detected edge voxels inside trabecular bone can therefore alter the measured susceptibility. We found that within an order of magnitude of the regularization parameter the chosen number of edge voxels inside the whole imaging volume did not change the resulting susceptibility reconstructions significantly (not shown). The comparison of MEDI to the implemented closed-form solution for dipole inversion, where no edge information is incorporated, shows that the susceptibility contrast is not diminished by the heuristic choice of an edge detection threshold. The same comparison also shows that the chosen data weighting term  $W_d$  in (1) is of less importance as the absence of any data weighting in the closed-form solution also leads to comparable susceptibility contrast. As the susceptibility gradient in trabecularized bone marrow is expected to be smoothly varying, a total generalized variation regularizer could mitigate possible stair-case artefacts of linear susceptibility gradients. However, in this work we limited the class of regularizers under investigation to the more common total variation.

For the nonlinear TV-MEDI we used Nesterov's algorithm (NESTA),<sup>53</sup> which results in fast and accurate reconstruction without the need to define any split variables as in Split-Bregman algorithm. Despite the high resolution and the relatively large FOV the algorithm converged in well under three minutes with a MATLAB implementation on a currently standard lap top machine (4 GHz processor, 16 GB RAM), while similar implementation of Gauss-Newton algorithms can take up to an hour on the same machine.

The numerical simulation in the trabecular bone model of randomly distributed overlapping spherical susceptibility inclusions inside a cubic box confirm the feasibility of QSM to measure changes in the trabecular bone density. Independent of the assumed susceptibility difference between bone inclusions and the outside medium, the susceptibility average over the box could be recovered from the forward simulated field map by only a simple direct solution of to field-to-susceptibility inversion not incorporating any morphological edges or signal weights. Even though inside the ROI the averaged frequency shift from the bone inclusions is small,<sup>6</sup> the bulk effect of the ROI to the surrounding is sufficient for the global dipole inversion step to be sensitive on the distribution of susceptibility sources. In bone literature focusing on  $R_2^*/R_2'$ -mapping in trabecular networks, several other trabecular bone models have been discussed. While an extended treatment of such models is beyond the present work, the more simple approach used here to model a voxel with trabecularized bone marrow was however successful in confirming the sensitivity of QSM on BV/TV.

A concise comparison of the slopes from the regression of susceptibility versus apparent BV/TV in vivo and the corresponding simulation results is not possible at this point. The

direct comparison of the BV/TV-to- $\chi$  slope from the in vivo scans (Figure 4) shows that in the calcaneus the measured  $\chi$  TV-MEDI varies about twice as fast with apparent BV/TV than the steepest simulated BV/TV-to- $\chi$  slope ( $\Delta\chi = -2$  ppm) in Figure 8. While this can suggest that the true susceptibility of trabecular bone might be greater than the values simulated, other properties differ between the simulation and the in vivo measurements that render such interpretations uncertain. In the literature, the range of reported susceptibility values for bone is fairly broad; While several studies from the 1990's based on  $R_2'$ -imaging report values around  $-0.3$  ppm for trabecular bone referenced to water at 0 ppm,<sup>58,59</sup> more recent studies also based on QSM have reported much more diamagnetic values around  $-2$  ppm and lower with respect to water.<sup>5,21</sup> The bone marrow in the calcaneus consist of 100% fat with a reported susceptibility difference to water of  $\sim 0.6$  ppm.<sup>59,63</sup> Assuming a true trabecular susceptibility at the higher end of the reported values and taking the fatty susceptibility source of the inter-trabecular fatty bone marrow into account, one could argue for a steeper in vivo BV/TV-to- $\chi$  slope than in the presented numerical simulation. However, the different dipole inversion methods, the presence of noise, the simplified trabecular network topology in the simulated model and the known over-estimation of the apparent BV/TV in the gradient-echo based measurement together with a low number of in vivo samples are all factors that do not allow a detailed interpretation of the presented results with respect to the true value of trabecular bone susceptibility.

The observed sensitivity of QSM to trabecular bone density in the calcaneus, is however well explained by the strongly simplified trabecular bone model. A detailed comparison of QSM to  $R_2^*$ -mapping is out of the scope of this work, but from Figure 8 one can also appreciate two theoretical advantages of QSM over an  $R_2^*$ .  $R_2^*$  is inherently dependent on the field strength and also on the voxel size, observable in the upper plot in Figure 8 as the nonlinear increase of  $R_2'/f_0$  with BV/TV, whereas QSM algorithms incorporate both properties as input and measured bulk susceptibility can therefore be independent on the field strength and voxel size. While a theoretical investigation complemented with phantom experiments are necessary in future work to further address possible (dis)advantages of QSM over  $R_2^*$ , the study presented here is able to show sensitivity of QSM on trabecular bone density. Further work is necessary in order to investigate whether bone marrow QSM can probe in vivo trabecular density changes induced by pathological bone loss or osteoporosis.

While all implemented regularizations were able to significantly detect BV/TV differences, the current preliminary study has several limitations.

A fundamental issue with QSM is its inability to produce absolute susceptibility values. Starting from MR phase information which is inherently difficult to reference to an

absolute value—particularly in parallel imaging using multiple coils—the QSM processing also shows this limitation. In the solution of the ill-posed dipole inversion deconvolution, the convolution kernel's center singularity is re-normalized by the Lorentz sphere contribution, which results in a zero DC offset of the dipole kernel in k-space.<sup>64</sup> Consequently, the dynamic range of resulting susceptibility maps is centered around the average k-space energy of the local field map before dipole inversion, which is highly dependent on object properties and therefore varying between subjects. Brain QSM studies therefore introduced a referencing procedure, where a specific ROI thought to be relatively homogeneous and of comparable size between subjects is defined and the susceptibility map are centered around the mean susceptibility value inside the ROI. There is an ongoing debate<sup>44</sup> about which reference tissue is best suited for comparing QSM values across different brain subjects in a study.<sup>65</sup> While cerebrospinal fluid or white matter in the internal capsule of the brain can serve well as a reference tissue for QSM, in the body only subcutaneous fat was proposed. In the abdominal region subcutaneous fat is more homogeneous and can be used to reference susceptibility maps between subjects. However as can be seen in bSSFP scans (Figure 4) the subcutaneous tissue is highly inhomogeneous and susceptibility is unlikely to be constant over several voxels. Hence, QSM referencing is difficult in the ankle region.

Another limitation of the current study is the dependence of susceptibility reconstructions on the regularization parameter  $\lambda$  in (1). This parameter was optimized by visual comparison of reconstructions on a wide range of  $\lambda$  values and validated by an L-curve heuristic in only one subjects, shown in Supporting Information Figure S2. The obtained regularization parameter was then used for the QSM dipole inversion in all other datasets. While this procedure followed multi-subject studies in brain QSM, where the size of the cropped out brain in relation to the FOV is not largely varying, for the imaging of the ankle, the ratio of the imaging object to the FOV can vary significantly as with constant FOV, subjects can have different foot sizes. By inspection of Equation (1) one can see that the regularization parameter depends not only on the voxel size (through the gradient operator in the regularizer), and the edge weighting  $W_g$ , but also on precisely the ratio between tissue voxel to background/air voxels in the FOV. Therefore, the optimal regularization parameter in one subject may differ for other subjects with different foot sizes.

A more crucial limitation is the accuracy of the apparent BV/TV measured with the bSSFP sequence. This measurement resembles the high-resolution imaging approach to access trabecular bone density. The formed gradient echoes to image trabeculae are susceptible to chemical shift dispersion and off-resonance effects near the trabeculae–bone marrow interface. Both effects lead to blurring and artificially enlarged trabeculae. The actual BV/TV is therefore

systematically smaller than the apparent BV/TV from the bSSFP measurement.<sup>5</sup> Trabecular bone imaging based on spin-echo sequences does not suffer from the artifactually increased BV/TV, but needs considerably larger repetition times resulting in longer scan time and less motion robustness. From the complementary highly significant correlations of QSM with the direct CT attenuation as well as the indirect measure  $R_2^*$  of trabecularization—both known to have high correlation with actual BV/TV<sup>7</sup> one can deduce that QSM is also sensitive to the trabecular bone density.

In support of reproducible research, source code for the QSM post-processing, ROI analysis, and figure reproduction scripts are available for download at [https://github.com/maxdiefenbach/trabecular\\_bone\\_QSM.git](https://github.com/maxdiefenbach/trabecular_bone_QSM.git) (SHA-1=f0df3fbde928da49c04d91e40c1a6b7c60245696). The git repository also includes an exemplary reconstructed MRI source datasets used in this work.

## 5 | CONCLUSION

In conclusion, the present work developed a methodological framework to simultaneously measure  $R_2^*$  and susceptibility in trabecularized yellow bone marrow, addressing the presence of fat. The presented preliminary results showed a correlation between measured susceptibility values and CT attenuation, apparent BV/TV and  $R_2^*$ <sup>7</sup> demonstrating the sensitivity of QSM on trabecular bone density.

## ACKNOWLEDGMENT

The present work was supported by the European Research Council (grant agreement No 677661—ProFatMRI) and Philips Healthcare. We also acknowledge the use of the MEDI toolbox<sup>52</sup> made freely available at <http://www.weill.cornell.edu/mri/pages/qsm.html> and a NESTA implementation from.<sup>53</sup> The authors gratefully acknowledge the Gauss Centre for Supercomputing e.V. ([www.gauss-centre.eu](http://www.gauss-centre.eu)) for funding this project by providing computing time on the GCS Supercomputer SuperMUC at Leibniz Supercomputing Centre ([www.lrz.de](http://www.lrz.de)).

## CONFLICT OF INTEREST

Dr. Jakob Meineke is an employee of Philips Healthcare.

## REFERENCES

1. Wright NC, Looker AC, Saag KG, et al. The recent prevalence of osteoporosis and low bone mass in the united states based on bone mineral density at the femoral neck or lumbar spine. *J Bone Mineral Res.* 2014;29:2520–2526.
2. Hernlund E, Svedbom A, Ivergård M, et al. Osteoporosis in the european union: medical management, epidemiology and economic burden. *Arch Osteoporosis* 2013;8:136.
3. Kling JM, Clarke BL, Sandhu NP. Osteoporosis prevention, screening, and treatment: a review. *J Women's Health* 2014;23:563–572.
4. Damilakis J, Adams JE, Guglielmi G, Link TM. Radiation exposure in x-ray-based imaging techniques used in osteoporosis. *Eur Radiol.* 2010;20:2707–2714.
5. Wehrli FW, Song HK, Saha PK, Wright AC. Quantitative MRI for the assessment of bone structure and function. *NMR Biomed.* 2006;19:731–764.
6. Yablonskiy DA, Haacke EM. Theory of NMR signal behavior in magnetically inhomogeneous tissues: the static dephasing regime. *Magn Reson Med.* 1994;32:749–763.
7. Song HK, Wehrli FW, Ma J. Field strength and angle dependence of trabecular bone marrow transverse relaxation in the calcaneus. *J Magn Reson Imaging.* 1997;7:382–388.
8. Chung H, Wehrli FW, Williams JL, Kugelmas SD. Relationship between NMR transverse relaxation, trabecular bone architecture, and strength. *Proc Nat Acad Sci.* 1993;90:10250–10254.
9. Wolff J. Das gesetz der transformation der knochen. *DMW-Deutsche Medizinische Wochenschrift* 1893;19:1222–1224.
10. Gibson L. The mechanical behaviour of cancellous bone. *J Biomechan.* 1985;18:317–328.
11. Jensen K, Mosekilde L, Mosekilde L. A model of vertebral trabecular bone architecture and its mechanical properties. *Bone* 1990;11:417–423.
12. Majumdar S, Thomasson D, Shimakawa A, Genant HK. Quantitation of the susceptibility difference between trabecular bone and bone marrow: experimental studies. *Magn Reson Med.* 1991;22:111–127.
13. Yablonskiy DA, Reinius WR, Stark H, Haacke EM. Quantitation of  $t_2'$  anisotropic effects on magnetic resonance bone mineral density measurement. *Magn Reson Med.* 1997;37:214–221.
14. Wang Y, Liu T. Quantitative susceptibility mapping (QSM): decoding MRI data for a tissue magnetic biomarker. *Magn Reson Med.* 2014;73:82–101.
15. Chen W, Gauthier SA, Gupta A, et al. Quantitative susceptibility mapping of multiple sclerosis lesions at various ages. *Radiology* 2014;271:183–192.
16. Langkammer C, Liu T, Khalil M, et al. Quantitative susceptibility mapping in multiple sclerosis. *Radiology* 2013;267:551–559.
17. Chen W, Zhu W, Kovanlikaya I, et al. Intracranial calcifications and hemorrhages: characterization with quantitative susceptibility mapping. *Radiology* 2014;270:496–505.
18. Deistung A, Schäfer A, Schweser F, Biedermann U, Turner R, Reichenbach JR. Toward in vivo histology: A comparison of quantitative susceptibility mapping (qsm) with magnitude-, phase-, and  $T_2^*$ -imaging at ultra-high magnetic field strength. *NeuroImage* 2013;65:299–314.
19. Dimov AV, Liu T, Spincemaille P, et al. Joint estimation of chemical shift and quantitative susceptibility mapping (chemical QSM). *Magn Reson Med.* 2014;73:2100–2110.
20. Sharma SD, Hernando D, Horng DE, Reeder SB. Quantitative susceptibility mapping in the abdomen as an imaging biomarker of hepatic iron overload. *Magn Reson Med.* 2014;74:673–683.
21. Dimov AV, Liu Z, Spincemaille P, Prince MR, Du J, Wang Y. Bone quantitative susceptibility mapping using a chemical

- species-specific  $r_2^*$  signal model with ultrashort and conventional echo data. *Magn Reson Med.* 2018;79:121–128.
22. Du J, Hermida JC, Diaz E, et al. Assessment of cortical bone with clinical and ultrashort echo time sequences. *Magn Reson Med.* 2012;70:697–704.
  23. Kuchel P, Chapman B, Bubb W, Hansen P, Durrant C, Hertzberg M. Magnetic susceptibility: solutions, emulsions, and cells. *Concepts Magn Reson.* 2003;18A:56–71.
  24. Reichenbach JR, Schweser F, Serres B, Deistung A. Quantitative susceptibility mapping: concepts and applications. *Clin Neuroradiol.* 2015;25:225–230.
  25. Schweser F, Deistung A, Lehr BW, Reichenbach JR. Differentiation between diamagnetic and paramagnetic cerebral lesions based on magnetic susceptibility mapping. *Med Phys.* 2010;37:5165–5178.
  26. Wharton S, Schäfer A, Bowtell R. Susceptibility mapping in the human brain using threshold-based k-space division. *Magn Reson Med.* 2010;63:1292–1304.
  27. Liu T, Wisnieff C, Lou M, Chen W, Spincemaille P, Wang Y. Nonlinear formulation of the magnetic field to source relationship for robust quantitative susceptibility mapping. *Magn Reson Med.* 2012;69:467–476.
  28. Yu H, Shimakawa A, McKenzie CA, Brodsky E, Brittain JH, Reeder SB. Multiecho water-fat separation and simultaneous  $r_2^*$  estimation with multifrequency fat spectrum modeling. *Magn Reson Med.* 2008;60:1122–1134.
  29. Ma J. Dixon techniques for water and fat imaging. *J Magn Reson Imaging.* 2008;28:543–558.
  30. Tsao J, Jiang Y. Hierarchical ideal: fast, robust, and multiresolution separation of multiple chemical species from multiple echo times. *Magn Reson Med.* 2012;70:155–159.
  31. Cui C, Wu X, Newell JD, Jacob M. Fat water decomposition using globally optimal surface estimation (goose) algorithm. *Magn Reson Med.* 2014;73:1289–1299.
  32. Zhou D, Liu T, Spincemaille P, Wang Y. Background field removal by solving the laplacian boundary value problem. *NMR Biomed.* 2014;27:312–319.
  33. Schweser F, Deistung A, Lehr BW, Reichenbach JR. Quantitative imaging of intrinsic magnetic tissue properties using mri signal phase: an approach to in vivo brain iron metabolism? *NeuroImage* 2011;54:2789–2807.
  34. Liu T, Khalidov I, de Rochefort L, et al. A novel background field removal method for mri using projection onto dipole fields (pdf). *NMR Biomed.* 2011;24:1129–1136.
  35. de Rochefort L, Liu T, Kressler B, et al. Quantitative susceptibility map reconstruction from mr phase data using bayesian regularization: validation and application to brain imaging. *Magn Reson Med.* 2009;63:NA–NA.
  36. Demoment G. Image reconstruction and restoration: overview of common estimation structures and problems. *IEEE Trans Acoustics, Speech, Signal Process.* 1989;37:2024–2036.
  37. Chambolle A, Caselles V, Novaga M, Cremers D, Pock T. An introduction to total variation for image analysis, Nov 2009.
  38. Kressler B, de Rochefort L, Liu T, Spincemaille P, Jiang Q, Wang Y. Nonlinear regularization for per voxel estimation of magnetic susceptibility distributions from MRI field maps. *IEEE Trans Med Imaging.* 2010;29:273–281.
  39. Liu T, Liu J, de Rochefort L, et al. Morphology enabled dipole inversion (MEDI) from a single-angle acquisition: comparison with cosmos in human brain imaging. *Magn Reson Med.* 2011;66:777–783.
  40. Bilgic B, Chatnuntawech I, Fan AP, et al. Fast image reconstruction with l2-regularization. *J Magn Reson Imaging.* 2013;40:181–191.
  41. Bilgic B, Fan AP, Polimeni JR, et al. Fast quantitative susceptibility mapping with l1-regularization and automatic parameter selection. *Mag Reson Med.* 2013;72:1444–1459.
  42. Langkammer C, Bredies K, Poser BA, et al. Fast quantitative susceptibility mapping using 3d EPI and total generalized variation. *NeuroImage* 2015;111:622–630.
  43. Chatnuntawech I, McDaniel P, Cauley SF, et al. Single-step quantitative susceptibility mapping with variational penalties. *NMR Biomed.* 2016;30:e3570.
  44. Langkammer C, Schweser F, Shmueli K, et al. Quantitative susceptibility mapping: Report from the 2016 reconstruction challenge. *Magn Reson Med.* 2018;79:1661–1673.
  45. Diefenbach MN, Van AT, Meineke J, et al. Quantitative susceptibility mapping of trabecular bone in the distal tibia. Vienna, Austria, 2016. p. 52.
  46. Diefenbach MN, Van AT, Meineke J, et al. On the Feasibility of Quantitative Susceptibility Mapping For Trabecular Bone Volume Density Mapping at 3 T. In Proceedings of the 24th Annual Meeting of ISMRM, Singapore, 2016. p. 0677.
  47. Diefenbach MN, Meineke J, Foehr P, et al. Simultaneous  $R_2^*$  and quantitative Susceptibility Mapping of Trabecularized Yellow Bone Marrow: Initial Results in the Calcaneus. In Proceedings of the 25th Annual Meeting of ISMRM, Honolulu, HI, 2017. p. 0850.
  48. Ruschke S, Eggers H, Kooijman H, et al. Correction of phase errors in quantitative water-fat imaging using a monopolar time-interleaved multi-echo gradient echo sequence. *Magn Reson Med.* 2017;78:984–996.
  49. Gyrotools LLC. Recon frame: mrecon, scanner software patch, pack'n go tool. <http://www.gyrotools.com/products/gt-recon.html>, 2017.
  50. Pruessmann KP, Weiger M, Scheidegger MB, Boesiger P. Sense: sensitivity encoding for fast MRI. *Magn Reson Med.* 1999;42:952–962.
  51. Berglund J, Johansson L, Ahlström H, Kullberg J. Three-point dixon method enables whole-body water and fat imaging of obese subjects. *Magn Reson Med.* 2010;63:1659–1668.
  52. Lab CMR. <http://www.weill.cornell.edu/mri/pages/qsm.html>, 2016.
  53. Becker S, Bobin J, Candès EJ. NESTA: a fast and accurate first-order method for sparse recovery. *SIAM J Imaging Sci.* 2011;4:1–39.
  54. Fedorov A, Beichel R, KalpathyCramer J, et al. 3d slicer as an image computing platform for the quantitative imaging network. *Mag Reson Imaging.* 2012;30:1323–1341.
  55. Yaniv Z, Lowekamp BC, Johnson HJ, Beare R. Simpleitk image-analysis notebooks: a collaborative environment for education and reproducible research. *J Digital Imaging.* 2017;31:290–303.

56. Majumdar S, Genant HK, Grampp S, et al. Correlation of trabecular bone structure with age, bone mineral density, and osteoporotic status: In vivo studies in the distal radius using high resolution magnetic resonance imaging. *J Bone Mineral Res.* 1997;12:111–118.
57. Majumdar S. Quantitative study of the susceptibility difference between trabecular bone and bone marrow: Computer simulations. *Magn Reson Med.* 1991;22:101–110.
58. Ford JC, Wehrli FW, Chung HW. Magnetic field distribution in models of trabecular bone. *Magn Reson Med.* 1993;30:373–379.
59. Hopkins JA, Wehrli FW. Magnetic susceptibility measurement of insoluble solids by NMR: magnetic susceptibility of bone. *Magn Reson Med.* 1997;37:494–500.
60. de Rochefort L, Brown R, Prince MR, Wang Y. Quantitative MR susceptibility mapping using piece-wise constant regularized inversion of the magnetic field. *Magn Reson Med.* 2008;60:1003–1009.
61. Wehrli FW. Magnetic resonance of calcified tissues. *J Magn Reson.* 2013;229:35–48.
62. Buch S, Liu S, Ye Y, Cheng YCN, Neelavalli J, Haacke EM. Susceptibility mapping of air, bone, and calcium in the head. *Magn Reson Med.* 2014;73:2185–2194.
63. Sprinkhuizen SM, Bakker CJG, Ippel JH, Boelens R, Viergever MA, Bartels LW. Temperature dependence of the magnetic volume susceptibility of human breast fat tissue: an NMR study. *Magn Reson Mater Phys Biol Med.* 2011;25:33–39.
64. Marques J, Bowtell R. Application of a fourier-based method for rapid calculation of field inhomogeneity due to spatial variation of magnetic susceptibility. *Concepts Magn Reson Part B: Magn Reson Eng.* 2005;25B:65–78.
65. Straub S, Schneider TM, Emmerich J, et al. Suitable reference tissues for quantitative susceptibility mapping of the brain. *Magn Reson Med.* 2017;78:204–214.
66. Liu T, Xu W, Spincemaille P, Avestimehr AS, Wang Y. Accuracy of the morphology enabled dipole inversion (MEDI) algorithm for quantitative susceptibility mapping in MRI. *IEEE Trans Med Imaging.* 2012;31:816–824.

## SUPPORTING INFORMATION

Additional Supporting Information may be found in the online version of this article.

**FIGURE S1** Water–fat signal model

**FIGURE S2** Top: heuristic L-curve, discrepancy  $\|(F^\dagger DF \chi_{\text{est}}(\lambda) - f_L)\|_2^2$  versus regularization parameter  $\lambda$  (compare to Equation (1)) for all three implemented dipole-inversion schemes. Bottom: susceptibility maps corresponding to different  $\lambda$ 's

**FIGURE S3** Regression analysis of ROI label statics, TIMGRE parameters  $R_2^*$  and susceptibility  $\chi$  versus the apparent BV/TV estimated from the bSSFP scan for the two additional dipole-inversion schemes, the  $\ell_2$ -regularized closed form solution and  $\ell_2$ -MEDI (one outlier removed). Compare to Figure 4 from the main text

**FIGURE S4** Extended version of Figure 5 from the main text showing slices of all main anatomical planes for each patient dataset

**FIGURE S5** Regression analysis of ROI label statics, TIMGRE parameters  $R_2^*$  and susceptibility  $\chi$  versus the CT attenuation for the two additional dipole-inversion schemes, the  $\ell_2$ -regularized closed form solution and  $\ell_2$ -MEDI. Compare to Figure 6 from the main text

**How to cite this article:** Diefenbach M, Meineke J, Ruschke S, et al. On the sensitivity of quantitative susceptibility mapping for measuring trabecular bone density. *Mag Reson Med.* 2018;00:1–16. <https://doi.org/10.1002/mrm.27531>

## 4 Discussion

In the original articles presented in Chapter 3, we developed a complete methodology to estimate trabecular bone density in vivo via QSM in fatty tissues starting from standard multi-gradient-echo MR images. In the following, we contextualize our work in the current literature, discuss advantages and limitations of the developed methodology and give perspectives for future studies.

### 4.1 Review of Existing Literature

The present work for non-invasive MR-based in vivo measurements of trabecular bone density combines two established techniques in MRI parameter estimation—WFI and QSM. First, we give an overview of the state-of-the-art for each field separately and later briefly summarize methods in osteoporosis imaging.

#### 4.1.1 Water–Fat Imaging

In MRI the diagnostically often more valuable signal of water molecules can be shadowed by signal originating from lipid molecules inside the human body. Fat suppression techniques like Short-TI Inversion Recovery (STIR) [86] or SPectral Attenuated Inversion Recovery (SPAIR) [87] therefore aim to null the signal of fat molecules during the MR signal acquisition by introducing dedicated pulses in the pulse sequence building blocks, exploiting different physical properties such as the shorter T1 relaxation time (STIR) or the smaller resonance frequency (SPAIR) of fat protons compared to water protons. Both methods have significant problems if the fat spectrum is broad or susceptibility-induced distortions of the main magnetic field are present.

In contrast to fat suppression, chemical shift-encoded water–fat separation techniques, which form the basis for WFI, do not introduce additional modules to the pulse sequence but rely on algorithmic fitting of a chosen water–fat signal model to a sampled MR signal evolution. Compared to STIR and SPAIR, water–fat separation has the advantage that information of the fat signal is fully estimated and can be used to determine a PDFF of the imaged region.

The accurate estimation of PDFF has been the primary focus of WFI, which is still based on the main idea from the seminal work by Dixon [88] using complex multi-echo MR signals to separate the water and fat signal contribution. To mitigate biases due to model mismatches, the estimation of a robust PDFF per voxel needs a more realistic water–fat signal model compared to the single-fat peak model assuming a constant magnetic field from Dixon’s initial work. A suitable voxel signal model needs to incorporate the spectral

nature of the fat signal [89], MR relaxation effects [90] and the field map parameter [91], all described by the common complex single- $R_2^*$  signal model [36].

The field map in particular is the most important nonlinear parameter in this type of signal models since the parameter estimation problem is non-convex in this dimension and the nonlinearity of the cost function in the field map parameter can lead to the presence of several possible local minima [39]. A poor initial estimation for the field map in the optimization algorithm results to the convergence to such local minima, causing the infamous water–fat swaps, where the water and the fat signal in a voxel are assigned the wrong way, which renders the images limited in their diagnostic value [92]. The initialization of the relaxation parameter, however, does not play an equally important role, as the minimization problem for water–fat separation is convex in this dimension. For a given nonlinear parameters, the problem of water–fat separation simplifies to solving an overdetermined system of linear equations, so the problem effectively reduces to the estimation of the field map, which is further illustrated by the application of the VARPRO method [37] to water–fat separation.

The field map estimation has been previously addressed by primarily imposing constraints on the smoothness of the field map over the whole imaging region instead of separately fitting signal models to the acquired multi-echo data voxelwise. A plethora of algorithms has been developed over the last decade using different methods based on either, region-growing [93, 92], message passing [94, 95], cellular automata [96, 97, 98], or global estimation [99, 41, 44, 42, 43] schemes over all voxels simultaneously. A comprehensive overview of many algorithms can be found in [100] together with their competitive assessment in test datasets. In the public water–fat separation challenge described therein, global minimization techniques based on graph cuts [101] have shown the best performance and graph cut water–fat separation algorithms are still further refined and developed [102, 46].

A fundamentally different approach to sufficiently initialize the field map parameter for water–fat separation has been demonstrated in [103], where inhomogeneities in the main magnetic field caused by the magnetization of the imaging object were simulated separately and incorporated into the initialization. The object-based information was shown to significantly reduce the occurrence of many water–fat swaps, even in challenging anatomies. The work also illustrated the abundance of information contained in the phase of the MR signal and consequently the field map parameter, which includes many sequence-, hardware- and object-dependent physical contributions. Therefore, these contribution to the signal can also confound the water–fat separation through phase errors during the MR acquisition, which propagate into the parameter estimation.

Based on which type of multi-echo acquisition scheme is used, gradient delays, eddy currents, and concomitant fields [104, 29, 105] can necessitate additional considerations or correction methods. In cases where the MR signal phase might be unreliable, the number of echoes is too low or the parameter configuration is unstable, magnitude-based water–fat separation can be used. In magnitude-based algorithms the modulus of the signal model is fitted to the magnitude of the single-echo data points, effectively eliminating the field map parameter from the model, but increasing the number of nonlinear parameters in the cost function [95, 106].

As the magnitude and phase parameters of the chemical species in the model were of major interest in WFI literature, the SNR-optimal echo time selection for such parameter estimation and the noise performance for different parameter constellations was primarily analyzed for those parameters [52, 107], whereas in order to optimally estimate relaxation rates or the field map, it is known that different echo spacings are SNR-optimal for the nonlinear parameters [107]. It has been shown that the PDFF is largely unaffected by the specific choice of the peak locations and amplitudes in an assumed multi-peak fat spectrum as long as multiple peaks are present. While this is true for the linear model parameters—magnitudes and phases or real and imaginary parts of the chemical species in the model—the relaxation rates can be significantly biased by an inaccurate choice of the fat model [108]. Such analysis gains importance as in recent years the active research in WFI expanded its focus from the refinement of PDFF mapping to the accurate estimation of the other available parameters in the single- $R_2^*$  or more complex signal models [109].

Clinical questions in osteoporosis and metabolic diseases challenge WFI techniques to also be adapted to perform reliable quantitative MR relaxometry in the body [110, 111] or estimate more parameters connected to the composition of adipose tissue [112, 113, 114]. The advancement of QSM further pushed WFI for the purpose of field mapping outside the brain.

#### 4.1.2 Quantitative Susceptibility Mapping

As the successor of Susceptibility-Weighted Imaging (SWI), QSM has been an emerging method to quantitatively measure the average magnetic susceptibility per voxel from continuous three-dimensional field map information [34]. Formally, QSM involves three steps, which are described in Section 2.3.2 and usually performed in sequence: field mapping, BFR and DI [115]. For the field mapping step in brain QSM, where typically a tight brain mask is defined as ROI, simple scaling of unwrapped single echo phase images [116], dual echo phase subtraction [117] or voxelwise nonlinear fitting of signal models of only one chemical species to multi-echo data [69] is used to obtain a field map.

In body QSM, the field mapping step needs to account for the presence of fat with its chemical shifts and is therefore analogous to complex-based water–fat separation methods [39]. However, with the field map as the primary parameter of interest, WFI algorithms focusing on mere PDFF mapping that treat the field map as a nuance parameter and often spatially smooth the resulting field maps [99, 44], can therefore only be employed for the initializations of more accurate voxelwise algorithms [91, 118].

For the second background field removal step, several kernel-convolution-based methods were developed such as the LBV method [64] or SHARP [59], showing robust performance in the brain. Conceptually different BFR approaches are minimum-norm methods like the method PDF [62], which also proved to be reliable in the brain [58]. A comprehensive comparison of BFR techniques outside the brain is however yet to be conducted and BFR in the body has not been thoroughly studied.

The most research results were obtained in the development of methods and their evaluation for the last DI step of QSM. The ill-posed, ill-conditioned inverse field-to-

susceptibility problem (Section 2.3.2) is most widely solved by means of regularization [66]. In the Bayesian interpretation of such regularization techniques, the specific regularization terms introduced to the formulated DI minimization problems correspond to different priors about the underlying tissue susceptibility distribution [71]. Many different combinations of regularization terms [2, 72] and optimization algorithms [70, 119] have been applied in the literature, but the most common regularizer used in QSM is total variation (TV) [120, 67] evaluated with the  $\ell_1$  or  $\ell_2$  norm [121, 122] and often combined with morphological edges weightings [123]. Regularizers like TV promote piece-wise constant susceptibility distributions in the QSM reconstructions, whereas the recently proposed Total Generalized Variation (TGV) promotes piece-wise smooth susceptibility maps allowing for more linear spatial variations [124, 72]. The question of which regularization term is best suited for a specific anatomy or QSM application and clinical question is still subject of ongoing research [125].

Being developed for imaging the brain, QSM has been successfully employed in numerous neurological applications, such as the identification of multiple sclerosis lesions [126, 127], the discrimination of cerebral micro-bleeds and intracranial calcifications [128] or the monitoring of iron deposition [129] motivating further applications of QSM outside the brain.

Body QSM has been shown to have applications in breast imaging [130], measuring liver iron content [73], and imaging of cartilage [131], cortical bone [132] and more recently trabecularized bone marrow in the spine [133, 134].

Besides further applications of known QSM algorithms, there is much active development of new QSM methods showing advantages in certain applications. The advancements in machine learning also lead to fruitful applications in QSM reconstruction techniques. When a satisfactory traditional QSM algorithm for a specific application of interest and a significantly large amount of training data is available, deep neural nets of several different architectures have successfully been trained to perform the DI [135] and recently, the Deep Learning approach has also been translated to the BFR step in QSM [136]. The major differences in QSM algorithms using Deep Learning is the training data and the labeling method. Training data either can be generated from randomly oriented objects of arbitrary shapes and susceptibility values [137] simulating the QSM forward model or by acquiring real in vivo data, which is reconstructed by a traditional gold standard QSM technique [138, 75]. Once the network is trained, its use significantly speeds up reconstructions times of the QSM DI step, however, the need for a large training dataset and a traditional labeling method poses the questions about further advantages for Deep-Learning-based QSM other than decreased reconstruction time.

Another major research question in non-machine-learning-based QSM is the development and evaluation of so-called single-step or joint methods. Starting from the estimated (unwrapped) field map, single-step methods perform BFR and DI simulatenously in one joint algorithmic step, which can show some advantages compared to the sequential approach [73, 72, 139, 124]. Traditional BFR techniques need a mask to define imaging regions causing the background field, which often relies on arbitrary choices of ROIs and their manual segmentation. By incorporating the Laplacian operator into the cost-function of the field-to-susceptibility inverse problem, single-step methods intrinsi-

cally remove any harmonic background field contributions without the need for such a background defining mask [140].

A similar QSM approach—also fundamentally changing the treatment of BFR and starting from the raw (total) field map—is TFI [74]. In TFI the total field map is directly inverted through DI without a separate BFR step by using an iterative algorithm that iterates much longer than in standard DI. It has been shown that by such long iterations, iterative algorithms can converge to correct local susceptibility maps, remarkably even without any background field removal. To speed up the convergence of TFI, preconditioning terms can be introduced into the DI formulation by aiding the DI iterations with initializing major susceptibility differences in the imaging regions (e.g. air–tissue interfaces with 9 ppm differences). In a recent public QSM reconstruction challenge (<http://www.listsnu.org/qsm-challenge/>) with a realistic numerical head phantom [78], a TFI algorithm showed the best performance in recovering the susceptibility from a total field map even in the presence of challenging calcifications in the brain.

### 4.1.3 Magnetic Resonance Imaging in Osteoporosis

The most important osteoporosis site is the spine. For osteoporosis screening and monitoring, the measurement of BMD is important for the assessment of bone quality and the associated fracture risk in the spine. The current gold standard techniques to measure BMD are based on Dual-Energy Xray Absorptiometry (DEXA) and Quantitative Computed Tomography (QCT). While with DEXA BMD values can be unreliable and measurement results of healthy and osteoporotic patients overlap, QCT measurements are more accurate and allow simultaneous information gain about the bone microstructure, improving the ability to predict fracture risk. However, QCT is associated with large radiation dose [141]. Early on, the non-invasiveness of MRI made it a candidate for osteoporosis screening [142, 143, 11]. High-resolution MRI to resolve trabeculae is however challenging due to motion artifacts and long scan times. Therefore, osteoporosis imaging using high-resolution MRI is practically limited to the distal skeleton and is not feasible in major osteoporosis sites. Trabecular bone  $R_2^*$ -mapping has been proposed as an indirect measure of trabecular density but was shown to be too dependent on trabecular bone microstructure and orientation to the main magnetic field [144]. Trabecular bone  $R_2^*$ -mapping is based on multi-gradient-echo MRI, which has independently gained clinical interest in the spine as it allows for WFI techniques to quantify changes in bone marrow fat content [145]. Increased bone marrow fat content is highly associated with the progress of osteoporosis [12] and multi-gradient-echo-based spine MRI therefore qualifies for osteoporosis screening/monitoring in terms of PDFF mapping [146]. Furthermore, novel QSM methods show adequate sensitivity on trabecular bone density [147] and the direct susceptibility contrast of QSM shows advantages over  $R_2^*$  [148]. The clinical feasibility of spine QSM was already independently demonstrated [134, 133, 140] with promising potential for QSM applications in the context of osteoporosis.

## 4.2 Present work

This work developed new techniques for the application of QSM in the body and as such, contributed to the field of WFI and QSM. By developing and finally combining methods from both fields, we were able to construct a complete multi-step approach for quantitative parameter estimation of clinical relevant biomarkers for MRI of osteoporosis.

### 4.2.1 Novelty

The field map initialization presented in Section 3.2 demonstrates a way to easily incorporate previously unused information about present magnetic fields to aid the water–fat separation. In addition to the previously used object-based field map generated through magnetization of the imaging object, the proposed field map initialization accounted for the inhomogeneities of the scanner magnet, the shim field, and the susceptibility-induced field from object field sources outside the FOV. Possible extensions to incorporate concomitant fields and gradient delays were also presented. The removal of the considered field map contributions was shown to reliably remove water–fat swaps in standard WFI methods, but also ensures field map results without artificial discontinuities in the imaging region that can be further processed in .

The generalized formulation of the multi-gradient-echo water–fat separation problem proposed in Section 3.3 enabled the development of a complete multi-species MR signal analysis framework, which allows parameter estimation and noise performance assessment over a broad range of signal models. The novel generalized formulation describes different signal models by a corresponding set of so-called constraint matrices introducing model-specific parameter relations. The matrices form an abstraction over the whole class of signal models and become input parameters to a novel algorithmic reformulation of mathematical and computational generality. The generalized parameter estimation algorithm is therefore universally applicable for all signal models of the class. With input matrices describing water–fat signal models the algorithm forms the basis for QSM field mapping outside the brain.

In Section 3.4 we developed a body QSM methodology on top of the field mapping framework established by the two previous journal publications. The work showed the feasibility of the body QSM pipeline in a clinical setting and validated the sensitivity of QSM on trabecular bone density using the gold standard QCT technique. Numerical simulation of simplified trabecular bone models were able to further verify the expected sensitivity of QSM on the trabecular bone volume. Furthermore, the novel implementation of Nesterov’s algorithm for iterative QSM DI was used to compare three different state-of-the-art regularization terms for QSM in trabecularized yellow bone marrow. The developed QSM pipeline for the non-invasive assessment for trabecular bone density combines the susceptibility mapping with the mapping of the quantitative parameters from the WFI-based field mapping step and consequently results in simultaneous  $R_2^*$  and PDFF maps. In vivo results and simulations compared QSM and relaxometry for trabecular bone measurements and confirmed theoretical advantages of QSM.

### 4.2.2 Impact

The field map initialization method presented in Section 3.2 was developed in the context of WFI and showed significant reduction in water–fat swaps compared to previous methods, but the method also has multiple potential applications in experimental MRI scenarios where phase information is important. As the proposed field mapping initialization technique starts from complex source data and scanner output information independent of the MR pulse sequence, it can be translated to many other MRI sequence types. The needed information for the demodulation of most of the largest field contributions is either always intrinsically present in the acquired data or often available from the scanner at no cost of development. The gained information about the estimated field map contributions is potentially valuable in MR applications that use field map estimates for correction purposes such as for example deblurring in Echo Planar Imaging or non-Cartesian imaging. Furthermore, the subsequent demodulations of the major field map contributions effectively separate those large phase contributions from the fine "local" phase differences inside tissues, which results in a local tissue field map with a non-smoothed quantitative field map output valuable for QSM.

The generalized formulation developed in Section 3.3 has several theoretical advantages. The concise formulation of the whole class of signal models allows to generalize many previous single model techniques. As shown, one can follow three simple steps to convert techniques using only one specific signal model of interest to the proposed general form. This generalization then enables the application of the presented parameter estimation and noise performance analysis for all models described by a weighted sum of complex exponentials whose arguments are linear in the time dimension. The developed computer programs for this work are based on the data-structure conventions of the ISMRM fat–water toolbox and are compatible with other routines therein. The implemented software can therefore be considered as an extension allowing the adoption of signal models previously not included in the original ISMRM fat–water toolbox. Thereby, the generalized formulation of the parameter estimation techniques allows for future work in many directions, like semi-automated model selections or a comprehensive model comparison both in theoretical and algorithmic implementations.

The work presented in Section 3.4, for the first time, experimentally validated the sensitivity of body QSM on trabecular bone density and verified in vivo the theoretical advantages of field strength and voxel size independence of QSM over  $R_2^*$  in trabecularized yellow bone marrow. As demonstrated, the developed body QSM pipeline from multi-gradient-echo imaging over fat-corrected field mapping to dipole inversion is fully clinically feasible and therefore poses a potential candidate for osteoporosis imaging without the use of invasive ionizing radiation used in current routine bone density measurements. The work lays a foundation for future research in the direction of QSM for the assessment of bone quality in osteoporosis.

In support of reproducible research, the source code developed for each original journal publication comprised in this thesis was published and made freely available at <https://www.bmrr.de/software> and <https://github.com/maxdiefenbach>.

### 4.2.3 Limitations

Despite the success of the developed trabecular bone QSM methodology with respect to the sensitivity on trabecular bone density, there are several limitations of the presented work and its results.

QSM has an intrinsic inability to produce absolute susceptibility values. The initial phase of the complex MR data is inherently difficult to reference to an absolute value and QSM inherits this limitation. The zero DC offset of the dipole kernel due to the Lorentz sphere correction leaves the absolute mean susceptibility value in the imaging region unchanged. Consequently, the dynamic range of resulting susceptibility maps is centered around the average  $k$ -space energy of the local field map, which is highly dependent on properties of the imaging object. In vivo, this object dependence of the QSM results leads to the challenge of inter-subject comparison. Following the standard procedure in multi-subject studies in brain QSM, the regularization parameter was optimized by visual comparison of QSM reconstructions in only one subject and employed in all other subject datasets. However, the regularization parameter depends on the ratio of the size of the imaging object to the FOV and the imaged anatomy shows a large physical variation from subject to subject. Consequently, the measured subjectwise correlations between average voxel susceptibility and bone-volume-to-total-volume ratio showed a broad distribution from subject to subject. Together with the known over-estimation of the apparent BV/TV in the GRE-based measurements and the low number of in vivo samples, the study did not allow a detailed interpretation of the true value for the proportionality of trabecular bone susceptibility to trabeculae density. The slopes of measured susceptibility versus apparent trabecular bone density were however suggestive that susceptibility values of trabecularized bone marrow might lie on the larger diamagnetic end of reported values from literature. A more concise comparison of the slopes from the regression of susceptibility versus apparent BV/TV with more subjects and refined QSM algorithms was outside the scope of the presented work.

Furthermore, the sensitivity of QSM on trabecular bone density in vivo was demonstrated in a gradient echo sequence with echo times greater than 1 ms, where bone does not exhibit an MR signal due to its fast  $R_2^*$ -relaxation. While differences in trabecular bone density could be detected visually and in quantitative ROI analysis, cortical bone could not be imaged reliably by the developed QSM post-processing, which shows another fundamental limitation of QSM. If the geometries of the MR invisible cortical bone structures do not lead to field distortions in their outside, there is no susceptibility information of the cortical bone structures present in the MR phase data. Especially elongated susceptibility inclusions aligned with the main magnetic field do not create local field contributions outside of the inclusions and therefore remain invisible by the proposed QSM post-processing. For the reliable recovery of QSM values in cortical bone regions—often of clinical importance in osteoporosis—MR phase information in the inside of the bone is necessary. The reliable estimation of cortical bone susceptibility therefore manifests the need for ultra-short echo time (UTE) imaging [149]. For traditional osteoporosis screening, the characterization of trabecular bone loss is however of primary interest and the employed non-UTE QSM method for trabecular bone imaging showed

sufficient sensitivity.

Initial attempts showed that the translation of the developed QSM methodology to the major osteoporosis sites at the lumbar spine and the hip poses additional challenges [140]. In non-UTE based QSM in the body, it is an open question on how to best perform the BFR step when moving from distal locations to the proximal osteoporosis sites. The thicker cortical bone regions inside the imaging volume lead to larger signal voids in the initial field maps, which bears the question on whether to include the voids in the definition of the background in the standard BFR methods. For the application of trabecular bone measurements, one might not define the signal voids from the cortical bone regions in close proximity to the trabeculae as background, although they do not contain information while exerting field distortions inside the trabecularized regions. In contrast to the extremities where volume RF coils are typically employed acquiring the MR signal of the entire anatomy within the coil, in the spine and the hip MRI is typically performed using surface coils (posterior coil elements) that show a strong signal loss as the distance from the coil increases. The definition of the air-tissue interfaces can therefore pose additional problems in the BFR background masking. Preliminary results in QSM of the vertebral column suggest that single-step methods or TFI can however be a solution to the challenges of BFR for osteoporosis QSM as these methods do not require the definition of a background mask [140].

### 4.3 Perspectives

Besides the limitations stated in the last section, the combination of the work presented in the comprising journal publications allows to confirm the central hypothesis of the present thesis. The development of a trabecular bone QSM methodology is possible, clinically feasible and enables the non-invasive assessment of trabecular bone density for osteoporosis imaging.

The complete QSM methodology developed for this work establishes a framework for quantitative parameter estimation from multi-gradient MRI data, combines it with a robust field map initialization technique, and demonstrates its use in QSM for trabecular bone density mapping, which opens new perspectives for future research.

The automatic comparison of many different multi-species signal models in novel model selection and machine learning techniques is an interesting approach to make use of the generalization benefits of the generalized model formulation in the framework (Section 3.3). The fast prototyping capabilities of the developed parameter estimation can also be employed in exploring entirely new multi-species signal models by changing only few input parameters at limited cost in software development. An extension of the generalized formulation from complex-based to magnitude-based parameter estimation schemes to gain robustness against phase errors also presents a possibly fruitful research direction.

With the adequate MR sequences, the developed methodology allows to estimate several quantitative MR parameters simultaneously. In the context of trabecular bone measurement, the parameter estimation is the basis for the field mapping step in the body, but also yields quantitative parameter maps of the transverse reversible relaxation rates,

#### 4 Discussion

fat fractions and possible fatty acid compositions. Currently, this information from the additional quantitative parameter maps is not used in the subsequent QSM steps of BFR and DI. Future studies aiming to translate QSM of trabecular bone to the major osteoporosis sites might try to incorporate fat fraction and relaxation into single-step or TFI QSM methods. The possibility of a detailed uncertainty quantification enabled by the developed previous parameter estimation framework can thereby help to control QSM-inherent noise amplification.

The developed quantitative multi-parameter mapping can find applications in further clinical body MRI research outside of trabecular bone loss in osteoporosis. The methods can for example help in the development of new MR biomarkers for the investigation of (MR) properties of brown adipose tissue or the assessment of fatty acid composition in metabolic diseases.

# Bibliography

- [1] J. R. Reichenbach, F. Schweser, B. Serres, A. Deistung. “Quantitative Susceptibility Mapping: Concepts and Applications”. In: *Clinical Neuroradiology* 25.S2 (July 2015), pp. 225–230. URL: <https://doi.org/10.1007/s00062-015-0432-9>.
- [2] Y. Wang, T. Liu. “Quantitative Susceptibility Mapping (QSM): Decoding MRI Data for a Tissue Magnetic Biomarker”. In: *Magnetic Resonance in Medicine* 73.1 (2014), pp. 82–101. URL: <https://doi.org/10.1002/mrm.25358>.
- [3] J. F. Schenck. “The Role of Magnetic Susceptibility in Magnetic Resonance Imaging: MRI Magnetic Compatibility of the First and Second Kinds”. In: *Medical Physics* 23.6 (1996), pp. 815–850. URL: <https://doi.org/10.1118/1.597854>.
- [4] J. Du, J. C. Hermida, E. Diaz, J. Corbeil, R. Znamirovski, D. D. D’Lima, G. M. Bydder. “Assessment of Cortical Bone With Clinical and Ultrashort Echo Time Sequences”. In: *Magnetic Resonance in Medicine* 70.3 (2012), pp. 697–704. URL: <https://doi.org/10.1002/mrm.24497>.
- [5] P. Kuchel, B. Chapman, W. Bubb, P. Hansen, C. Durrant, M. Hertzberg. “Magnetic Susceptibility: Solutions, Emulsions, and Cells”. In: *Concepts in Magnetic Resonance* 18A.1 (2003), pp. 56–71. URL: <https://doi.org/10.1002/cmr.a.10066>.
- [6] N. C. Wright, A. C. Looker, K. G. Saag, J. R. Curtis, E. S. Delzell, S. Randall, B. Dawson-Hughes. “The Recent Prevalence of Osteoporosis and Low Bone Mass in the United States Based on Bone Mineral Density At the Femoral Neck Or Lumbar Spine”. In: *Journal of Bone and Mineral Research* 29.11 (2014), pp. 2520–2526. URL: <https://doi.org/10.1002/jbmr.2269>.
- [7] E. Hernlund, A. Svedbom, M. Ivergård, J. Compston, C. Cooper, J. Stenmark, E. V. McCloskey, B. Jönsson, J. A. Kanis. “Osteoporosis in the European Union: Medical Management, Epidemiology and Economic Burden”. In: *Archives of Osteoporosis* 8.1-2 (2013), p. 136. URL: <https://doi.org/10.1007/s11657-013-0136-1>.
- [8] E. S. Siris, Y.-T. Chen, T. A. Abbott, E. Barrett-Connor, P. D. Miller, L. E. Wehren, M. L. Berger. “Bone Mineral Density Thresholds for Pharmacological Intervention To Prevent Fractures”. In: *Archives of Internal Medicine* 164.10 (2004), p. 1108. URL: <https://doi.org/10.1001/archinte.164.10.1108>.

## Bibliography

- [9] S. Schuit, M. Klift, A. Weel, C. Laet, H. Burger, E. Seeman, A. Hofman, A. Uitterlinden, J. Leeuwen, H. Pols. “Fracture Incidence and Association With Bone Mineral Density in Elderly Men and Women: the Rotterdam Study”. In: *Bone* 34.1 (2004), pp. 195–202. URL: <https://doi.org/10.1016/j.bone.2003.10.001>.
- [10] T. M. Link. “Radiology of Osteoporosis”. In: *Canadian Association of Radiologists Journal* 67.1 (2016), pp. 28–40. URL: <https://doi.org/10.1016/j.carj.2015.02.002>.
- [11] F. W. Wehrli. “Magnetic Resonance of Calcified Tissues”. In: *Journal of Magnetic Resonance* 229 (2013), pp. 35–48. URL: <https://doi.org/10.1016/j.jmr.2012.12.011>.
- [12] C. J. Rosen, M. L. Bouxsein. “Mechanisms of Disease: Is Osteoporosis the Obesity of Bone?” In: *Nature Clinical Practice Rheumatology* 2.1 (2006), pp. 35–43. URL: <https://doi.org/10.1038/ncprheum0070>.
- [13] T. E. Skinner. “A Complete Solution of the Bloch Equation”. In: *CoRR* (2017). URL: <http://arxiv.org/abs/1704.00826v1>.
- [14] J. D. Jackson. *Classical electrodynamics*. John Wiley & Sons, 2007.
- [15] E. L. Hahn. “Spin Echoes”. In: *Physical Review* 80.4 (1950), pp. 580–594. URL: <https://doi.org/10.1103/physrev.80.580>.
- [16] A. Haase, J. Frahm, D. Matthaei, W. Hanicke, K.-D. Merboldt. “Flash Imaging. Rapid NMR Imaging Using Low Flip-Angle Pulses”. In: *Journal of Magnetic Resonance (1969)* 67.2 (1986), pp. 258–266. URL: [https://doi.org/10.1016/0022-2364\(86\)90433-6](https://doi.org/10.1016/0022-2364(86)90433-6).
- [17] P. Beatty, D. Nishimura, J. Pauly. “Rapid Gridding Reconstruction With a Minimal Oversampling Ratio”. In: *IEEE Transactions on Medical Imaging* 24.6 (2005), pp. 799–808. URL: <https://doi.org/10.1109/tmi.2005.848376>.
- [18] J. A. Fessler. “On Nufft-Based Gridding for Non-Cartesian MRI”. In: *Journal of Magnetic Resonance* 188.2 (2007), pp. 191–195. URL: <https://doi.org/10.1016/j.jmr.2007.06.012>.
- [19] J. W. Cooley, J. W. Tukey. “An Algorithm for the Machine Calculation of Complex Fourier Series”. In: *Mathematics of Computation* 19.90 (1965), pp. 297–297. URL: <https://doi.org/10.1090/s0025-5718-1965-0178586-1>.
- [20] M. Blaimer, F. Breuer, M. Mueller, R. M. Heidemann, M. A. Griswold, P. M. Jakob. “Smash, Sense, Pils, Grappa”. In: *Topics in Magnetic Resonance Imaging* 15.4 (2004), pp. 223–236. URL: <https://doi.org/10.1097/01.rmr.0000136558.09801.dd>.
- [21] M. A. Griswold, P. M. Jakob, R. M. Heidemann, M. Nittka, V. Jellus, J. Wang, B. Kiefer, A. Haase. “Generalized Autocalibrating Partially Parallel Acquisitions (GRAPPA)”. In: *Magnetic Resonance in Medicine* 47.6 (2002), pp. 1202–1210. URL: <https://doi.org/10.1002/mrm.10171>.

## Bibliography

- [22] K. P. Pruessmann, M. Weiger, M. B. Scheidegger, P. Boesiger. “Sense: Sensitivity Encoding for Fast MRI”. In: *Magnetic Resonance in Medicine* 42.5 (1999), pp. 952–962. URL: [https://doi.org/10.1002/\(sici\)1522-2594\(199911\)42:5%3C952::aid-mrm16%3E3.0.co;2-s](https://doi.org/10.1002/(sici)1522-2594(199911)42:5%3C952::aid-mrm16%3E3.0.co;2-s).
- [23] M. Uecker, P. Lai, M. J. Murphy, P. Virtue, M. Elad, J. M. Pauly, S. S. Vasanawala, M. Lustig. “Espirit-An Eigenvalue Approach To Autocalibrating Parallel MRI: Where Sense Meets Grappa”. In: *Magnetic Resonance in Medicine* 71.3 (2013), pp. 990–1001. URL: <https://doi.org/10.1002/mrm.24751>.
- [24] M. Lustig, D. Donoho, J. M. Pauly. “Sparse MRI: The Application of Compressed Sensing for Rapid MR Imaging”. In: *Magnetic Resonance in Medicine* 58.6 (2007), pp. 1182–1195. URL: <https://doi.org/10.1002/mrm.21391>.
- [25] E. Candes, J. Romberg, T. Tao. “Robust Uncertainty Principles: Exact Signal Reconstruction From Highly Incomplete Frequency Information”. In: *IEEE Transactions on Information Theory* 52.2 (2006), pp. 489–509. URL: <https://doi.org/10.1109/tit.2005.862083>.
- [26] D. L. Donoho. “Compressed Sensing”. In: *IEEE Transactions on information theory* 52.4 (2006), pp. 1289–1306.
- [27] E. M. Haacke, R. W. Brown, M. R. Thompson, R. Venkatesan. *Magnetic Resonance Imaging: Physical Principles and Sequence Design*. 1999. URL: <http://books.google.de/books?id=Bn0vQgAACAAJ>.
- [28] D. A. Yablonskiy, E. M. Haacke. “Theory of NMR Signal Behavior in Magnetically Inhomogeneous Tissues: The Static Dephasing Regime”. In: *Magnetic Resonance in Medicine* 32.6 (1994), pp. 749–763. URL: <https://doi.org/10.1002/mrm.1910320610>.
- [29] S. Ruschke, H. Eggers, H. Kooijman, **M. N. Diefenbach**, T. Baum, A. Haase, E. J. Rummeny, H. H. Hu, D. C. Karampinos. “Correction of Phase Errors in Quantitative Water–Fat Imaging Using a Monopolar Time-Interleaved Multi-Echo Gradient Echo Sequence”. In: *Magnetic Resonance in Medicine* 78.3 (2016), pp. 984–996. URL: <https://doi.org/10.1002/mrm.26485>.
- [30] M. H. Levitt. “Demagnetization Field Effects in Two-Dimensional Solution NMR”. In: *Concepts in Magnetic Resonance* 8.2 (1996), pp. 77–103. URL: [https://doi.org/10.1002/\(sici\)1099-0534\(1996\)8:2%3C77::aid-cmr1%3E3.0.co;2-1](https://doi.org/10.1002/(sici)1099-0534(1996)8:2%3C77::aid-cmr1%3E3.0.co;2-1).
- [31] E. Lenz. “Ueber Die Bestimmung Der Richtung Der Durch Elektrodynamische Vertheilung Erregten Galvanischen Ströme”. In: *Annalen der Physik und Chemie* 107.31 (1834), pp. 483–494. URL: <https://doi.org/10.1002/andp.18341073103>.
- [32] M. H. Levitt. “The Signs of Frequencies and Phases in NMR”. In: *Journal of Magnetic Resonance* 126.2 (1997), pp. 164–182. URL: <https://doi.org/10.1006/jmre.1997.1161>.

## Bibliography

- [33] D. J. Griffiths. “Hyperfine Splitting in the Ground State of Hydrogen”. In: *American Journal of Physics* 50.8 (1982), pp. 698–703. URL: <https://doi.org/10.1119/1.12733>.
- [34] F. Schweser, A. Deistung, J. R. Reichenbach. “Foundations of MRI Phase Imaging and Processing for Quantitative Susceptibility Mapping (QSM)”. In: *Zeitschrift für Medizinische Physik* 26.1 (2016), pp. 6–34. URL: <https://doi.org/10.1016/j.zemedi.2015.10.002>.
- [35] H. Yu, A. Shimakawa, C. D. G. Hines, C. A. McKenzie, G. Hamilton, C. B. Sirin, J. H. Brittain, S. B. Reeder. “Combination of Complex-Based and Magnitude-Based Multiecho Water–Fat Separation for Accurate Quantification of Fat-Fraction”. In: *Magnetic Resonance in Medicine* 66.1 (2011), pp. 199–206. URL: <https://doi.org/10.1002/mrm.22840>.
- [36] H. Yu, A. Shimakawa, C. A. McKenzie, E. Brodsky, J. H. Brittain, S. B. Reeder. “Multiecho Water–Fat Separation and Simultaneous R2\* Estimation With Multifrequency Fat Spectrum Modeling”. In: *Magnetic Resonance in Medicine* 60.5 (2008), pp. 1122–1134. URL: <https://doi.org/10.1002/mrm.21737>.
- [37] G. Golub, V. Pereyra. “Separable Nonlinear Least Squares: the Variable Projection Method and Its Applications”. In: *Inverse Problems* 19.2 (2003), R1–R26. URL: <https://doi.org/10.1088/0266-5611/19/2/201>.
- [38] **M. N. Diefenbach**, C. Liu, D. C. Karampinos. “Generalized Parameter Estimation and Optimal Experimental Design in Multi-Echo Gradient-Echo-Based Chemical Species Separation”. In: *Quantitative Imaging in Medicine and Surgery* (2020). Ahead of print.
- [39] J. Ma. “Dixon Techniques for Water and Fat Imaging”. In: *Journal of Magnetic Resonance Imaging* 28.3 (2008), pp. 543–558. URL: <https://doi.org/10.1002/jmri.21492>.
- [40] V. Kolmogorov, C. Rother. “Minimizing Nonsubmodular Functions With Graph Cuts-A Review”. In: *IEEE Transactions on Pattern Analysis and Machine Intelligence* 29.7 (2007), pp. 1274–1279. URL: <https://doi.org/10.1109/tpami.2007.1031>.
- [41] D. Hernando, P. Kellman, J. P. Haldar, Z.-P. Liang. “Robust Water/fat Separation in the Presence of Large Field Inhomogeneities Using a Graph Cut Algorithm”. In: *Magnetic Resonance in Medicine* 63.1 (2009), NA–NA. URL: <https://doi.org/10.1002/mrm.22177>.
- [42] J. Dong, T. Liu, F. Chen, D. Zhou, A. Dimov, A. Raj, Q. Cheng, P. Spincemaille, Y. Wang. “Simultaneous Phase Unwrapping and Removal of Chemical Shift (SPURS) Using Graph Cuts: Application in Quantitative Susceptibility Mapping”. In: *IEEE Transactions on Medical Imaging* 34.2 (2015), pp. 531–540. URL: <https://doi.org/10.1109/tmi.2014.2361764>.

## Bibliography

- [43] J. Berglund, M. Skorpil. “Multi-Scale Graph-Cut Algorithm for Efficient Water–Fat Separation”. In: *Magnetic Resonance in Medicine* 78.3 (2016), pp. 941–949. URL: <https://doi.org/10.1002/mrm.26479>.
- [44] C. Cui, X. Wu, J. D. Newell, M. Jacob. “Fat Water Decomposition Using Globally Optimal Surface Estimation (goose) Algorithm”. In: *Magnetic Resonance in Medicine* 73.3 (2014), pp. 1289–1299. URL: <https://doi.org/10.1002/mrm.25193>.
- [45] C. Böhm, **M. N. Diefenbach**, J. Meineke, A. Haase, D. C. Karampinos. “Improved Body Quantitative Susceptibility Mapping by using a Variable-Layer Single-Min-Cut Graph-Cut Algorithm for Field-Mapping”. In: Seoul, Korea, 2019.
- [46] C. Böhm, **M. N. Diefenbach**, A. Haase, D. C. Karampinos. “Accelerated Single-Min-Cut Graph-Cut Algorithm Using a Variable-Layer Graph Construction Improves Field-Mapping in Water–Fat Regions”. In: *Proceedings 27. Annual Meeting International Society for Magnetic Resonance in Medicine*. Vol. 27. Digital Poster. Montreal, Canada: <https://index.miramart.com/ISMRM2019/PDFfiles/4007.html>, 2019, p. 4007.
- [47] C. Böhm, **M. N. Diefenbach**, J. Meineke, A. Haase, D. C. Karampinos. “Improved Body Quantitative Susceptibility Mapping by Using a Variable-Layer Single-Min-Cut Graph-Cut Algorithm for Field-Mapping”. In: *Proceedings 27. Annual Meeting International Society for Magnetic Resonance in Medicine*. Vol. 27. Power Pitch, Magna Cum Laude Merit Award. Montreal, Canada: <https://index.miramart.com/ISMRM2019/PDFfiles/0693.html>, 2019, p. 0693.
- [48] S. Cavassila, S. Deval, C. Huegen, D. Ormond, D. Graveron-Demilly. “Cramér-Rao Bounds: an Evaluation Tool for Quantitation”. In: *NMR in Biomedicine* 14.4 (2001), pp. 278–283. URL: <https://doi.org/10.1002/nbm.701>.
- [49] A. Bos. “A Cramér-Rao Lower Bound for Complex Parameters”. In: *IEEE Transactions on Signal Processing* 42.10 (1994), p. 2859. URL: <https://doi.org/10.1109/78.324755>.
- [50] C. Jauffret. “Observability and Fisher Information Matrix in Nonlinear Regression”. In: *IEEE Transactions on Aerospace and Electronic Systems* 43.2 (2007), pp. 756–759. URL: <https://doi.org/10.1109/taes.2007.4285368>.
- [51] L. Scharf, L. McWhorter. “Geometry of the Cramer-Rao Bound”. In: *IEEE Sixth SP Workshop on Statistical Signal and Array Processing* (1992), pp. 5–8. URL: <https://doi.org/10.1109/ssap.1992.246835>.
- [52] A. R. Pineda, S. B. Reeder, Z. Wen, N. J. Pelc. “Cramér-Rao Bounds for Three-Point Decomposition of Water and Fat”. In: *Magnetic Resonance in Medicine* 54.3 (2005), pp. 625–635. URL: <https://doi.org/10.1002/mrm.20623>.

## Bibliography

- [53] C.-Y. Liu, C. A. McKenzie, H. Yu, J. H. Brittain, S. B. Reeder. “Fat Quantification With Ideal Gradient Echo Imaging: Correction of Bias From T1 and Noise”. In: *Magnetic Resonance in Medicine* 58.2 (2007), pp. 354–364. URL: <https://doi.org/10.1002/mrm.21301>.
- [54] V. Fortier, I. R. Levesque. “Phase Processing for Quantitative Susceptibility Mapping of Regions With Large Susceptibility and Lack of Signal”. In: *Magnetic Resonance in Medicine* (2017). URL: <https://doi.org/10.1002/mrm.26989>.
- [55] M. A. Schofield, Y. Zhu. “Fast Phase Unwrapping Algorithm for Interferometric Applications”. In: *Optics Letters* 28.14 (2003), p. 1194. URL: <https://doi.org/10.1364/ol.28.001194>.
- [56] W. Li, A. V. Avram, B. Wu, X. Xiao, C. Liu. “Integrated Laplacian-Based Phase Unwrapping and Background Phase Removal for Quantitative Susceptibility Mapping”. In: *NMR in Biomedicine* 27.2 (2013), pp. 219–227. URL: <https://doi.org/10.1002/nbm.3056>.
- [57] **M. N. Diefenbach**, J. Meineke, S. Ruschke, T. Baum, A. Gersing, D. C. Karampinos. “On the Sensitivity of Quantitative Susceptibility Mapping for Measuring Trabecular Bone Density”. In: *Magnetic Resonance in Medicine* (2018). URL: <https://doi.org/10.1002/mrm.27531>.
- [58] F. Schweser, S. D. Robinson, L. Rochefort, W. Li, K. Bredies. “An Illustrated Comparison of Processing Methods for Phase MRI and QSM: Removal of Background Field Contributions From Sources Outside the Region of Interest”. In: *NMR in Biomedicine* 30.4 (2016), e3604. URL: <https://doi.org/10.1002/nbm.3604>.
- [59] F. Schweser, A. Deistung, B. W. Lehr, J. R. Reichenbach. “Quantitative Imaging of Intrinsic Magnetic Tissue Properties Using MRI Signal Phase: An Approach To in Vivo Brain Iron Metabolism?”. In: *NeuroImage* 54.4 (2011), pp. 2789–2807. URL: <https://doi.org/10.1016/j.neuroimage.2010.10.070>.
- [60] H. Sun, A. H. Wilman. “Background Field Removal Using Spherical Mean Value Filtering and Tikhonov Regularization”. In: *Magnetic Resonance in Medicine* 71.3 (2013), pp. 1151–1157. URL: <https://doi.org/10.1002/mrm.24765>.
- [61] B. Wu, W. Li, A. Guidon, C. Liu. “Whole Brain Susceptibility Mapping Using Compressed Sensing”. In: *Magnetic Resonance in Medicine* 67.1 (2011), pp. 137–147. URL: <https://doi.org/10.1002/mrm.23000>.
- [62] T. Liu, I. Khalidov, L. Rochefort, P. Spincemaille, J. Liu, A. J. Tsiouris, Y. Wang. “A Novel Background Field Removal Method for MRI Using Projection Onto Dipole Fields (pdf)”. In: *NMR in Biomedicine* 24.9 (2011), pp. 1129–1136. URL: <https://doi.org/10.1002/nbm.1670>.
- [63] R. Kennedy. *Hilbert space methods in signal processing*. Cambridge: Cambridge University Press, 2013.

## Bibliography

- [64] D. Zhou, T. Liu, P. Spincemaille, Y. Wang. “Background Field Removal By Solving the Laplacian Boundary Value Problem”. In: *NMR in Biomedicine* 27.3 (2014), pp. 312–319. URL: <https://doi.org/10.1002/nbm.3064>.
- [65] W. H. Press, S. A. Teukolsky, W. T. Vetterling, B. P. Flannery. *Numerical recipes 3rd edition: The art of scientific computing*. Cambridge university press, 2007.
- [66] L. Rochefort, T. Liu, B. Kressler, J. Liu, P. Spincemaille, V. Lebon, J. Wu, Y. Wang. “Quantitative Susceptibility Map Reconstruction From MR Phase Data Using Bayesian Regularization: Validation and Application To Brain Imaging”. In: *Magnetic Resonance in Medicine* 63.1 (2009). URL: <https://doi.org/10.1002/mrm.22187>.
- [67] B. Kressler, L. Rochefort, T. Liu, P. Spincemaille, Q. Jiang, Y. Wang. “Non-linear Regularization for Per Voxel Estimation of Magnetic Susceptibility Distributions From MRI Field Maps”. In: *IEEE Transactions on Medical Imaging* 29.2 (2010), pp. 273–281. URL: <https://doi.org/10.1109/tmi.2009.2023787>.
- [68] R. Gonzalez. *Digital image processing*. New York, NY: Pearson, 2018.
- [69] T. Liu, C. Wisnieff, M. Lou, W. Chen, P. Spincemaille, Y. Wang. “Nonlinear Formulation of the Magnetic Field To Source Relationship for Robust Quantitative Susceptibility Mapping”. In: *Magnetic Resonance in Medicine* 69.2 (2012), pp. 467–476. URL: <https://doi.org/10.1002/mrm.24272>.
- [70] C. Milovic, B. Bilgic, B. Zhao, J. Acosta-Cabronero, C. Tejos. “Fast Nonlinear Susceptibility Inversion With Variational Regularization”. In: *Magnetic Resonance in Medicine* 80.2 (2018), pp. 814–821. URL: <https://doi.org/10.1002/mrm.27073>.
- [71] G. Demoment. “Image Reconstruction and Restoration: Overview of Common Estimation Structures and Problems”. In: *IEEE Transactions on Acoustics, Speech, and Signal Processing* 37.12 (1989), pp. 2024–2036. URL: <https://doi.org/10.1109/29.45551>.
- [72] I. Chatnuntaweck, P. McDaniel, S. F. Cauley, B. A. Gagoski, C. Langkammer, A. Martin, P. E. Grant, L. L. Wald, K. Setsompop, E. Adalsteinsson, B. Bilgic. “Single-Step Quantitative Susceptibility Mapping With Variational Penalties”. In: *NMR in Biomedicine* 30.4 (2016), e3570. URL: <https://doi.org/10.1002/nbm.3570>.
- [73] S. D. Sharma, D. Hernando, D. E. Horng, S. B. Reeder. “Quantitative Susceptibility Mapping in the Abdomen As an Imaging Biomarker of Hepatic Iron Overload”. In: *Magnetic Resonance in Medicine* 74.3 (2014), pp. 673–683. URL: <https://doi.org/10.1002/mrm.25448>.
- [74] Z. Liu, Y. Kee, D. Zhou, Y. Wang, P. Spincemaille. “Preconditioned Total Field Inversion (TFI) Method for Quantitative Susceptibility Mapping”. In: *Magnetic Resonance in Medicine* 78.1 (July 2016), pp. 303–315. URL: <https://doi.org/10.1002/mrm.26331>.

## Bibliography

- [75] J. Yoon, E. Gong, I. Chatnuntaweck, B. Bilgic, J. Lee, W. Jung, J. Ko, H. Jung, K. Setsompop, G. Zaharchuk, E. Y. Kim, J. Pauly, J. Lee. “Quantitative Susceptibility Mapping Using Deep Neural Network: QSMnet”. In: *NeuroImage* 179.nil (2018), pp. 199–206. URL: <https://doi.org/10.1016/j.neuroimage.2018.06.030>.
- [76] C. Liu. “Susceptibility Tensor Imaging”. In: *Magnetic Resonance in Medicine* 63.6 (2010), pp. 1471–1477. URL: <https://doi.org/10.1002/mrm.22482>.
- [77] W. Li, C. Liu, T. Q. Duong, P. C. M. Zijl, X. Li. “Susceptibility Tensor Imaging (STI) of the Brain”. In: *NMR in Biomedicine* 30.4 (2016), e3540. URL: <https://doi.org/10.1002/nbm.3540>.
- [78] J. P. Marques, B. Bilgic, J. Meineke, C. Milovic, K.-s. Chan, W. Zwaag, R. Hedouin, C. Langkammer, F. Schweser. “Towards QSM Challenge 2.0: Creation and Evaluation of a Realistic Magnetic Susceptibility Phantom”. In: *Proceedings 27. Annual Meeting International Society for Magnetic Resonance in Medicine*. Vol. 27. Montreal, Canada: <http://archive.ismrm.org/2019/1122.html>, 2019, p. 1122.
- [79] **M. N. Diefenbach**, S. Ruschke, H. Eggers, J. Meineke, E. J. Rummeny, D. C. Karampinos. “Improving Chemical Shift Encoding-Based Water–Fat Separation Based on a Detailed Consideration of Magnetic Field Contributions”. In: *Magnetic Resonance in Medicine* 80.3 (2018), pp. 990–1004. URL: <https://doi.org/10.1002/mrm.27097>.
- [80] **M. N. Diefenbach**, S. Ruschke, H. Kooijman, A. T. Van, E. J. Rummeny, A. Haase, D. C. Karampinos. “Improving Chemical Shift-Encoded Water–Fat Separation Based On A Detailed Consideration Of Magnetic Field Contributions”. In: *Proceedings 24. Annual Meeting International Society for Magnetic Resonance in Medicine*. Vol. 24. Oral presentation, Magna Cum Laude Merit Award. Singapore: <http://archive.ismrm.org/2016/0576.html>, 2016, p. 0576.
- [81] **M. N. Diefenbach**. “Improving chemical shift encoding-based water–fat separation based on a detailed consideration of magnetic field contributions”. In: *Magnetic Resonance in Medicine* 80.3 (Sept. 2018), pp. C1–C1. URL: <https://doi.org/10.1002/mrm.27369>.
- [82] **M. N. Diefenbach**, S. Ruschke, D. C. Karampinos. “A Generalized Formulation for Parameter Estimation in MR Signals of Multiple Chemical Species”. In: *Proceedings 25. Annual Meeting International Society for Magnetic Resonance in Medicine*. Vol. 25. Electronic poster presentation. Honolulu, Hawaii: <http://archive.ismrm.org/2017/5181.html>, 2017, p. 5181.
- [83] **M. N. Diefenbach**, C. Liu, D. C. Karampinos. “Extending the Signal Models of the ISMRM Fat–Water Toolbox: Generalized Parameter Estimation in Multi-Echo Gradient-Echo-Based Chemical Species Separation”. In: Singapore, 2019, p. 18.

## Bibliography

- [84] **M. N. Diefenbach**, A. T. Van, J. Meineke, H. Kooijman, A. Haase, E. J. Rummeny, J. S. Kirschke, T. Baum, D. C. Karampinos. “On the Feasibility of Quantitative Susceptibility Mapping For Trabecular Bone Volume Density Mapping at 3 T”. In: *Proceedings 24. Annual Meeting International Society for Magnetic Resonance in Medicine*. Vol. 24. Oral presentation, Magna Cum Laude Merit Award. Singapore: <http://archive.ismrm.org/2016/0677.html>, 2016, p. 0677.
- [85] **M. N. Diefenbach**, A. Van, J. Meineke, J. S. Kirschke, B. Schwaiger, T. Baum, A. Gersing, D. C. Karampinos. “On the Sensitivity of Bone Marrow Magnetic Susceptibility and R2\* on Trabecular Bone Microstructure”. In: *Proceedings 26. Annual Meeting International Society for Magnetic Resonance in Medicine*. Vol. 26. Power pitch + Electronic poster presentation. Paris, France: <http://archive.ismrm.org/2018/0533.html>, 2018, p. 0533.
- [86] G. Krinsky, N. M. Rofsky, J. C. Weinreb. “Nonspecificity of short inversion time inversion recovery (STIR) as a technique of fat suppression: pitfalls in image interpretation.” In: *AJR. American journal of roentgenology* 166.3 (1996), pp. 523–526.
- [87] E. Kaldoudi, S. C. Williams, G. J. Barker, P. S. Tofts. “A chemical shift selective inversion recovery sequence for fat-suppressed MRI: theory and experimental validation”. In: *Magnetic resonance imaging* 11.3 (1993), pp. 341–355.
- [88] W. T. Dixon. “Simple Proton Spectroscopic Imaging.” In: *Radiology* 153.1 (1984), pp. 189–194. URL: <https://doi.org/10.1148/radiology.153.1.6089263>.
- [89] X. Wang, D. Hernando, S. B. Reeder. “Sensitivity of Chemical Shift-Encoded Fat Quantification To Calibration of Fat MR Spectrum”. In: *Magnetic Resonance in Medicine* 75.2 (2015), pp. 845–851. URL: <https://doi.org/10.1002/mrm.25681>.
- [90] H. Yu, C. A. McKenzie, A. Shimakawa, A. T. Vu, A. C. Brau, P. J. Beatty, A. R. Pineda, J. H. Brittain, S. B. Reeder. “Multiecho Reconstruction for Simultaneous Water–Fat Decomposition and T2\* Estimation”. In: *Journal of Magnetic Resonance Imaging* 26.4 (2007), pp. 1153–1161. URL: <https://doi.org/10.1002/jmri.21090>.
- [91] S. B. Reeder, A. R. Pineda, Z. Wen, A. Shimakawa, H. Yu, J. H. Brittain, G. E. Gold, C. H. Beaulieu, N. J. Pelc. “Iterative Decomposition of Water and Fat With Echo Asymmetry and Least-Squares Estimation (ideal): Application With Fast Spin-Echo Imaging”. In: *Magnetic Resonance in Medicine* 54.3 (2005), pp. 636–644. URL: <https://doi.org/10.1002/mrm.20624>.
- [92] H. Yu, S. B. Reeder, A. Shimakawa, J. H. Brittain, N. J. Pelc. “Field Map Estimation With a Region Growing Scheme for Iterative 3-point Water–Fat Decomposition”. In: *Magnetic Resonance in Medicine* 54.4 (2005), pp. 1032–1039. URL: <https://doi.org/10.1002/mrm.20654>.

## Bibliography

- [93] J. Berglund, L. Johansson, H. Ahlström, J. Kullberg. “Three-Point Dixon Method Enables Whole-Body Water and Fat Imaging of Obese Subjects”. In: *Magnetic Resonance in Medicine* 63.6 (2010), pp. 1659–1668. URL: <https://doi.org/10.1002/mrm.22385>.
- [94] J. Berglund, H. Ahlström, L. Johansson, J. Kullberg. “Two-Point Dixon Method With Flexible Echo Times”. In: *Magnetic Resonance in Medicine* 65.4 (2010), pp. 994–1004. URL: <https://doi.org/10.1002/mrm.22679>.
- [95] H. Eggers, B. Brendel, A. Duijndam, G. Herigault. “Dual-Echo Dixon Imaging With Flexible Choice of Echo Times”. In: *Magnetic Resonance in Medicine* 65.1 (2010), pp. 96–107. URL: <https://doi.org/10.1002/mrm.22578>.
- [96] Q.-S. Xiang. “Two-Point Water–Fat Imaging With Partially-Opposed-Phase (pop) Acquisition: An Asymmetric Dixon Method”. In: *Magnetic Resonance in Medicine* 56.3 (2006), pp. 572–584. URL: <https://doi.org/10.1002/mrm.20984>.
- [97] Q.-S. Xiang, L. An. “Water–Fat Imaging With Direct Phase Encoding”. In: *Journal of Magnetic Resonance Imaging* 7.6 (1997), pp. 1002–1015. URL: <https://doi.org/10.1002/jmri.1880070612>.
- [98] W. Lu, B. A. Hargreaves. “Multiresolution Field Map Estimation Using Golden Section Search for Water–Fat Separation”. In: *Magnetic Resonance in Medicine* 60.1 (2008), pp. 236–244. URL: <https://doi.org/10.1002/mrm.21544>.
- [99] J. Tsao, Y. Jiang. “Hierarchical Ideal: Fast, Robust, and Multiresolution Separation of Multiple Chemical Species From Multiple Echo Times”. In: *Magnetic Resonance in Medicine* 70.1 (2012), pp. 155–159. URL: <https://doi.org/10.1002/mrm.24441>.
- [100] H. H. Hu, P. Börnert, D. Hernando, P. Kellman, J. Ma, S. Reeder, C. Sirin. “Ismrm Workshop on Fat–Water Separation: Insights, Applications and Progress in MRI”. In: *Magnetic Resonance in Medicine* 68.2 (2012), pp. 378–388. URL: <https://doi.org/10.1002/mrm.24369>.
- [101] J. Shen, T. Baum, C. Cordes, B. Ott, T. Skurk, H. Kooijman, E. J. Rummeny, H. Hauner, B. H. Menze, D. C. Karampinos. “Automatic Segmentation of Abdominal Organs and Adipose Tissue Compartments in Water–Fat MRI: Application To Weight-Loss in Obesity”. In: *European Journal of Radiology* 85.9 (2016), pp. 1613–1621. URL: <https://doi.org/10.1016/j.ejrad.2016.06.006>.
- [102] C. Cui, A. Shah, X. Wu, M. Jacob. “A Rapid 3d Fat–Water Decomposition Method Using Globally Optimal Surface Estimation (R-GOOSE)”. In: 79.4 (2017), pp. 2401–2407. URL: <https://doi.org/10.1002/mrm.26843>.
- [103] S. D. Sharma, N. S. Artz, D. Hernando, D. E. Horng, S. B. Reeder. “Improving Chemical Shift Encoded Water–Fat Separation Using Object-Based Information of the Magnetic Field Inhomogeneity”. In: *Magnetic Resonance in Medicine* 73.2 (Feb. 2014), pp. 597–604. URL: <https://doi.org/10.1002/mrm.25163>.

## Bibliography

- [104] P. Peterson, S. Månsson. “Fat Quantification Using Multiecho Sequences With Bipolar Gradients: Investigation of Accuracy and Noise Performance”. In: *Magnetic Resonance in Medicine* 71.1 (2013), pp. 219–229. URL: <https://doi.org/10.1002/mrm.24657>.
- [105] T. J. Colgan, D. Hernando, S. D. Sharma, S. B. Reeder. “The Effects of Concomitant Gradients on Chemical Shift Encoded MRI”. In: *Magnetic Resonance in Medicine* 78.2 (2016), pp. 730–738. URL: <https://doi.org/10.1002/mrm.26461>.
- [106] D. Hernando, C. D. G. Hines, H. Yu, S. Reeder. “Addressing Phase Errors in Fat–Water Imaging Using a Mixed Magnitude/complex Fitting Method”. In: *Magnetic Resonance in Medicine* 67.3 (2011), pp. 638–644. URL: <https://doi.org/10.1002/mrm.23044>.
- [107] S. B. Reeder, E. K. Bice, H. Yu, D. Hernando, A. R. Pineda. “On the Performance of T2\* Correction Methods for Quantification of Hepatic Fat Content”. In: *Magnetic Resonance in Medicine* 67.2 (2011), pp. 389–404. URL: <https://doi.org/10.1002/mrm.23016>.
- [108] D. Franz\*, **M. N. Diefenbach\***, F. Treibel, D. Weidlich, J. Syväri, S. Ruschke, M. Wu, C. Holzapfel, T. Drabsch, T. Baum, H. Eggers, E. J. Rummeny, H. Hauner, D. C. Karampinos. “Differentiating Supraclavicular from Gluteal Adipose Tissue Based on Simultaneous PDFFF and T2\* Mapping Using a 20-echo Gradient-Echo Acquisition”. In: *Journal of Magnetic Resonance Imaging* 50.2 (2019), pp. 424–434. URL: <https://doi.org/10.1002/jmri.26661>.
- [109] H. H. Hu, R. T. Branca, D. Hernando, D. C. Karampinos, J. Machann, C. A. McKenzie, H. H. Wu, T. Yokoo, S. S. Velan. “Magnetic Resonance Imaging of Obesity and Metabolic Disorders: Summary From the 2019 Ismrm Workshop”. In: *Magnetic Resonance in Medicine* nil.nil (2019), mrm.28103. URL: <https://doi.org/10.1002/mrm.28103>.
- [110] D. Hernando, J. H. Kramer, S. B. Reeder. “Multipeak Fat-Corrected Complex R2\* Relaxometry: Theory, Optimization, and Clinical Validation”. In: *Magnetic Resonance in Medicine* 70.5 (2013), pp. 1319–1331. URL: <https://doi.org/10.1002/mrm.24593>.
- [111] B. Henninger, H. Zoller, S. Rauch, A. Finkenstedt, M. Schocke, W. Jaschke, C. Kremser. “R2\* Relaxometry for the Quantification of Hepatic Iron Overload: Biopsy-Based Calibration and Comparison With the Literature”. In: *RöFo - Fortschritte auf dem Gebiet der Röntgenstrahlen und der bildgebenden Verfahren* 187.06 (2015), pp. 472–479. URL: <https://doi.org/10.1055/s-0034-1399318>.
- [112] J. Berglund, H. Ahlström, J. Kullberg. “Model-Based Mapping of Fat Unsaturation and Chain Length By Chemical Shift Imaging-Phantom Validation and in Vivo Feasibility”. In: *Magnetic Resonance in Medicine* 68.6 (2012), pp. 1815–1827. URL: <https://doi.org/10.1002/mrm.24196>.

## Bibliography

- [113] P. Peterson, S. Månsson. “Simultaneous Quantification of Fat Content and Fatty Acid Composition Using MR Imaging”. In: *Magnetic Resonance in Medicine* 69.3 (2012), pp. 688–697. URL: <https://doi.org/10.1002/mrm.24297>.
- [114] M. Schneider, G. Janas, F. Lugauer, E. Hoppe, D. Nickel, B. M. Dale, B. Kiefer, A. Maier, M. R. Bashir. “Accurate Fatty Acid Composition Estimation of Adipose Tissue in the Abdomen Based on Bipolar Multi-Echo MRI”. In: *Magnetic Resonance in Medicine* 81.4 (2018), pp. 2330–2346. URL: <https://doi.org/10.1002/mrm.27557>.
- [115] C. Liu, W. Li, K. A. Tong, K. W. Yeom, S. Kuzminski. “Susceptibility-Weighted Imaging and Quantitative Susceptibility Mapping in the Brain”. In: *Journal of Magnetic Resonance Imaging* 42.1 (2014), pp. 23–41. URL: <https://doi.org/10.1002/jmri.24768>.
- [116] F. Schweser, A. Deistung, B. W. Lehr, J. R. Reichenbach. “Differentiation Between Diamagnetic and Paramagnetic Cerebral Lesions Based on Magnetic Susceptibility Mapping”. In: *Medical Physics* 37.10 (2010), pp. 5165–5178. URL: <https://doi.org/10.1118/1.3481505>.
- [117] S. Wharton, A. Schäfer, R. Bowtell. “Susceptibility Mapping in the Human Brain Using Threshold-Based K-Space Division”. In: *Magnetic Resonance in Medicine* 63.5 (2010), pp. 1292–1304. URL: <https://doi.org/10.1002/mrm.22334>.
- [118] D. Hernando, J. P. Haldar, B. P. Sutton, J. Ma, P. Kellman, Z.-P. Liang. “Joint Estimation of Water/fat Images and Field Inhomogeneity Map”. In: *Magnetic Resonance in Medicine* 59.3 (2008), pp. 571–580. URL: <https://doi.org/10.1002/mrm.21522>.
- [119] Y. Kee, Z. Liu, L. Zhou, A. Dimov, J. Cho, L. Rochefort, J. K. Seo, Y. Wang. “Quantitative Susceptibility Mapping (qsm) Algorithms: Mathematical Rationale and Computational Implementations”. In: *IEEE Transactions on Biomedical Engineering* (2017), pp. 1–1. URL: <https://doi.org/10.1109/tbme.2017.2749298>.
- [120] A. Chambolle, V. Caselles, M. Novaga, D. Cremers, T. Pock. “An introduction to Total Variation for Image Analysis”. Nov. 2009. URL: <https://hal.archives-ouvertes.fr/hal-00437581>.
- [121] B. Bilgic, I. Chatnuntawech, A. P. Fan, K. Setsompop, S. F. Cauley, L. L. Wald, E. Adalsteinsson. “Fast Image Reconstruction With L2-regularization”. In: *Journal of Magnetic Resonance Imaging* 40.1 (2013), pp. 181–191. URL: <https://doi.org/10.1002/jmri.24365>.
- [122] B. Bilgic, A. P. Fan, J. R. Polimeni, S. F. Cauley, M. Bianciardi, E. Adalsteinsson, L. L. Wald, K. Setsompop. “Fast Quantitative Susceptibility Mapping With L1-regularization and Automatic Parameter Selection”. In: *Magnetic Resonance in Medicine* 72.5 (2013), pp. 1444–1459. URL: <https://doi.org/10.1002/mrm.25029>.

## Bibliography

- [123] T. Liu, J. Liu, L. Rochefort, P. Spincemaille, I. Khalidov, J. R. Ledoux, Y. Wang. “Morphology Enabled Dipole Inversion (medi) From a Single-Angle Acquisition: Comparison With Cosmos in Human Brain Imaging”. In: *Magnetic Resonance in Medicine* 66.3 (2011), pp. 777–783. URL: <https://doi.org/10.1002/mrm.22816>.
- [124] C. Langkammer, K. Bredies, B. A. Poser, M. Barth, G. Reishofer, A. P. Fan, B. Bilgic, F. Fazekas, C. Mainero, S. Ropele. “Fast Quantitative Susceptibility Mapping Using 3d Epi and Total Generalized Variation”. In: *NeuroImage* 111 (2015), pp. 622–630. URL: <https://doi.org/10.1016/j.neuroimage.2015.02.041>.
- [125] C. Langkammer, F. Schweser, K. Shmueli, C. Kames, X. Li, L. Guo, C. Milovic, J. Kim, H. Wei, K. Bredies, S. Buch, Y. Guo, Z. Liu, J. Meineke, A. Rauscher, J. P. Marques, B. Bilgic. “Quantitative Susceptibility Mapping: Report From the 2016 Reconstruction Challenge”. In: *Magnetic Resonance in Medicine* 79.3 (2017), pp. 1661–1673. URL: <https://doi.org/10.1002/mrm.26830>.
- [126] W. Chen, S. A. Gauthier, A. Gupta, J. Comunale, T. Liu, S. Wang, M. Pei, D. Pitt, Y. Wang. “Quantitative Susceptibility Mapping of Multiple Sclerosis Lesions At Various Ages”. In: *Radiology* 271.1 (2014), pp. 183–192. URL: <https://doi.org/10.1148/radiol.13130353>.
- [127] C. Langkammer, T. Liu, M. Khalil, C. Enzinger, M. Jehna, S. Fuchs, F. Fazekas, Y. Wang, S. Ropele. “Quantitative Susceptibility Mapping in Multiple Sclerosis”. In: *Radiology* 267.2 (2013), pp. 551–559. URL: <https://doi.org/10.1148/radiol.12120707>.
- [128] W. Chen, W. Zhu, I. Kovanlikaya, A. Kovanlikaya, T. Liu, S. Wang, C. Salustri, Y. Wang. “Intracranial Calcifications and Hemorrhages: Characterization With Quantitative Susceptibility Mapping”. In: *Radiology* 270.2 (2014), pp. 496–505. URL: <https://doi.org/10.1148/radiol.13122640>.
- [129] A. Deistung, A. Schäfer, F. Schweser, U. Biedermann, R. Turner, J. R. Reichenbach. “Toward in Vivo Histology: a Comparison of Quantitative Susceptibility Mapping (QSM) With Magnitude-, Phase-, and R2\*-imaging At Ultra-High Magnetic Field Strength”. In: *NeuroImage* 65 (2013), pp. 299–314. URL: <https://doi.org/10.1016/j.neuroimage.2012.09.055>.
- [130] A. V. Dimov, T. Liu, P. Spincemaille, J. S. Ecanow, H. Tan, R. R. Edelman, Y. Wang. “Joint Estimation of Chemical Shift and Quantitative Susceptibility Mapping (chemical QSM)”. In: *Magnetic Resonance in Medicine* 73.6 (2014), pp. 2100–2110. URL: <https://doi.org/10.1002/mrm.25328>.
- [131] H. Wei, R. Dibb, K. Decker, N. Wang, Y. Zhang, X. Zong, W. Lin, D. B. Nissman, C. Liu. “Investigating Magnetic Susceptibility of Human Knee Joint At 7 Tesla”. In: *Magnetic Resonance in Medicine* 78.5 (2017), pp. 1933–1943. URL: <https://doi.org/10.1002/mrm.26596>.

## Bibliography

- [132] A. V. Dimov, Z. Liu, P. Spincemaille, M. R. Prince, J. Du, Y. Wang. “Bone Quantitative Susceptibility Mapping Using a Chemical Species-Specific  $R_2^*$  Signal Model With Ultrashort and Conventional Echo Data”. In: *Magnetic Resonance in Medicine* 79.1 (2017), pp. 121–128. URL: <https://doi.org/10.1002/mrm.26648>.
- [133] Y. Guo, Y. Chen, X. Zhang, Y. Mei, P. Yi, Y. Wang, Q. Feng, L. L. Tegola, G. Guglielmi, X. Zhang, Y. Feng. “Magnetic Susceptibility and Fat Content in the Lumbar Spine of Postmenopausal Women With Varying Bone Mineral Density”. In: *Journal of Magnetic Resonance Imaging* 49.4 (2018), pp. 1020–1028. URL: <https://doi.org/10.1002/jmri.26279>.
- [134] Y. Chen, Y. Guo, X. Zhang, Y. Mei, Y. Feng, X. Zhang. “Bone Susceptibility Mapping With MRI Is an Alternative and Reliable Biomarker of Osteoporosis in Postmenopausal Women”. In: *European Radiology* 28.12 (2018), pp. 5027–5034. URL: <https://doi.org/10.1007/s00330-018-5419-x>.
- [135] W. Jung, S. Bollmann, J. Lee. “Overview of Quantitative Susceptibility Mapping Using Deep Learning – Current Status, Challenges and Opportunities”. In: *CoRR* (2019). URL: <http://arxiv.org/abs/1912.05410v1>.
- [136] S. Bollmann, M. H. Kristensen, M. S. Larsen, M. V. Olsen, M. J. Pedersen, L. R. Østergaard, K. O’Brien, C. Langkammer, A. Fazlollahi, M. Barth. “Sharqnet - Sophisticated Harmonic Artifact Reduction in Quantitative Susceptibility Mapping Using a Deep Convolutional Neural Network”. In: *Zeitschrift für Medizinische Physik* 29.2 (2019), pp. 139–149. URL: <https://doi.org/10.1016/j.zemedi.2019.01.001>.
- [137] S. Bollmann, K. G. B. Rasmussen, M. Kristensen, R. G. Blendal, L. R. Østergaard, M. Plochanski, K. O’Brien, C. Langkammer, A. Janke, M. Barth. “Deepqsm - Using Deep Learning To Solve the Dipole Inversion for Quantitative Susceptibility Mapping”. In: *NeuroImage* 195.nil (2019), pp. 373–383. URL: <https://doi.org/10.1016/j.neuroimage.2019.03.060>.
- [138] K. G. B. Rasmussen, M. J. Kristensen, R. G. Blendal, L. R. Østergaard, M. Plochanski, K. O’Brien, C. Langkammer, A. Janke, M. Barth, S. Bollmann. “DeepQSM - Using Deep Learning to Solve the Dipole Inversion for MRI Susceptibility Mapping”. In: *bioRxiv* (2018). URL: <https://www.biorxiv.org/content/early/2018/03/07/278036>.
- [139] J. Meineke, F. Wenzel, M. D. Marco, A. Venneri, D. J. Blackburn, K. Teh, I. D. Wilkinson, U. Katscher. “Motion Artifacts in Standard Clinical Setting Obscure Disease-Specific Differences in Quantitative Susceptibility Mapping”. In: *Physics in Medicine & Biology* 63.14 (2018), 14NT01. URL: <https://doi.org/10.1088/1361-6560/aacc52>.

## Bibliography

- [140] **M. N. Diefenbach**, A. Van, J. Meineke, A. Scharr, J. S. Kirschke, A. Gersing, T. Baum, B. Schwaiger, D. C. Karampinos. “Vertebral Column Quantitative Susceptibility Mapping using Joint Background Field Removal and Dipole Inversion”. In: *Proceedings 26. Annual Meeting International Society for Magnetic Resonance in Medicine*. Vol. 26. Oral presentation, Magna Cum Laude Merit Award. Paris, France: <http://archive.ismrm.org/2018/0191.html>, 2018, p. 0191.
- [141] J. Damilakis, J. E. Adams, G. Guglielmi, T. M. Link. “Radiation Exposure in X-Ray-Based Imaging Techniques Used in Osteoporosis”. In: *European Radiology* 20.11 (2010), pp. 2707–2714. URL: <https://doi.org/10.1007/s00330-010-1845-0>.
- [142] F. W. Wehrli, J. C. Ford, M. Attie, H. Y. Kressel, F. S. Kaplan. “Trabecular Structure: Preliminary Application of MR Interferometry.” In: *Radiology* 179.3 (1991), pp. 615–621. URL: <https://doi.org/10.1148/radiology.179.3.2027962>.
- [143] F. W. Wehrli, H. K. Song, P. K. Saha, A. C. Wright. “Quantitative MRI for the Assessment of Bone Structure and Function”. In: *NMR in Biomedicine* 19.7 (2006), pp. 731–764. URL: <https://doi.org/10.1002/nbm.1066>.
- [144] H. K. Song, F. W. Wehrli, J. Ma. “Field Strength and Angle Dependence of Trabecular Bone Marrow Transverse Relaxation in the Calcaneus”. In: *Journal of Magnetic Resonance Imaging* 7.2 (1997), pp. 382–388. URL: <https://doi.org/10.1002/jmri.1880070222>.
- [145] M. E. Schweitzer. “Now Is the Time To Start Routinely Using Chemical Shift Imaging in the Spine”. In: *European Radiology* (2018). URL: <https://doi.org/10.1007/s00330-018-5399-x>.
- [146] D. C. Karampinos, S. Ruschke, M. Dieckmeyer, **M. Diefenbach**, D. Franz, A. S. Gersing, R. Krug, T. Baum. “Quantitative MRI and Spectroscopy of Bone Marrow”. In: *Journal of Magnetic Resonance Imaging* 47.2 (2017), pp. 332–353. URL: <https://doi.org/10.1002/jmri.25769>.
- [147] **M. N. Diefenbach**, J. Meineke, P. Foehr, S. Ruschke, T. Baum, J. S. Kirschke, A. Hock, H. Kooijman, E. J. Rummeny, D. C. Karampinos. “Simultaneous R2\* and Quantitative Susceptibility Mapping of Trabecularized Yellow Bone Marrow: Initial Results in the Calcaneus”. In: *Proceedings 25. Annual Meeting International Society for Magnetic Resonance in Medicine*. Vol. 25. Oral presentation, Magna Cum Laude Merit Award. Honolulu, Hawaii: <http://archive.ismrm.org/2017/0850.html>, 2017, p. 0850.
- [148] Y. Taege, R. Zivadinov, J. Hanspach, J. Hagemeyer, M. G. Dwyer, B. P. Sule, N. Bertolino, D. Shah, D. Jakimovski, N. P. B. B. Weinstock-Guttman, F. Schweser. “Assessing the Cellular Distribution of Iron in Deep Gray Matter based on R2\* and Quantitative Susceptibility Mapping (QSM) - Application to Healthy Controls and Patients with Multiple Sclerosis (MS)”. In: *Proceedings*

## Bibliography

25. *Annual Meeting International Society for Magnetic Resonance in Medicine*. Vol. 25. Honolulu, Hawaii: <http://archive.ismrm.org/2017/1207.html>, 2017, p. 1207.
- [149] S. Kronthaler, **M. N. Diefenbach**, S. Ruschke, J. Meineke, H. Eggers, P. Boerner, D. Karampinos. “Time Interleaved Multi-Gradient-Echo Imaging with UTE and Non-UTE Sampling for Simultaneous PDFFF, T2\* and Magnetic Susceptibility Mapping of Cortical Bone”. In: *Proceedings 26. Annual Meeting International Society for Magnetic Resonance in Medicine*. Vol. 26. Electronic poster presentation. Paris, France: <http://archive.ismrm.org/2018/5157.html>, 2018, p. 5157.

# List of Figures

2.1	Schematic pulse diagram of a basic FID MR experiment. . . . .	25
2.2	Schematic pulse diagram of a basic SE sequence. . . . .	25
2.3	Schematic pulse diagram of a basic GRE sequence. . . . .	26

# List of Acronyms

A2D	Analog-to-Digital
BFR	Background Field Removal
BMD	Bone Mineral Density
BV/TV	Bone-Volume-to-Total-Volume
CRLB	Cramér-Rao Lower Bound
CT	Computed Tomography
DEXA	Dual-Energy Xray Absorptiometry
DFT	Discrete Fourier Transform
DI	Dipole Inversion
ESPIRIT	Eigenvector-based Self-consistent Parallel Imaging Reconstruction from Arbitrary $k$ -Space
FFT	Fast Fourier Transformation
FID	Free Induction Decay
FIM	Fisher Information Matrix
FOV	Field-of-View
GRAPPA	GeneRALized Autocalibrating Partial Parallel Acquisition
GRE	Gradient Echo
IFFT	Inverse Fast Fourier Transformation
ISMRM	International Society for Magnetic Resonance in Medicine
LBV	Laplacian Boundary Value
MEDI	Morphology-Enabled Dipole Inversion
MR	Magnetic Resonance
MRI	Magnetic Resonance Imaging
NUFFT	Nonlinear Fast Fourier Transformation
PDF	Projection onto Dipole Fields
PDFF	Proton Density Fat Fraction
QCT	Quantitative Computed Tomography
qMRI	Quantitative Magnetic Resonance Imaging
QSM	Quantitative Susceptibility Mapping
RESHARP	Regularization-Enabled Sophisticated Harmonic Artifact Reduction for Phase data
RF	Radio Frequency
ROI	Region-of-Interest
SE	Spin Echo

*List of Acronyms*

SENSE	SENSitivity Encoding
SHARP	Sophisticated Harmonic Artifact Reduction for Phase data
SNR	Signal-to-Noise ratio
SPAIR	SPectral Attenuated Inversion Recovery
STIR	Short-TI Inversion Recovery
SWI	Susceptibility-Weighted Imaging
TFI	Total Field Inversion
TGV	Total Generalized Variation
TIMGRE	Time-Interleaved Multi-Gradient-Echo
TV	Total Variation
UTE	Ultra-short echo time
VARPRO	Variable Projection
vSHARP	Variable-kernel Sophisticated Harmonic Artifact Reduction for Phase data
WFI	Water-Fat Imaging

# List of Symbols

$\text{adj } \mathbf{A}$	Adjugate matrix of $\mathbf{A}$
$f * g$	Convolution of functions $f$ and $g$
$\mathbf{B}$	Magnetization field
$B_{\text{bg}}$	Background field
$B_{\text{L}}$	Local field
$\det \mathbf{A}$	Determinant of matrix $\mathbf{A}$
$d(\mathbf{r})$	Dipole kernel in image-space
$D(\mathbf{r})$	Dipole kernel in $k$ -space
$\Delta H$	Inhomogeneities of the main magnetic field along its direction $\hat{\mathbf{z}}$
$\Delta k$	One-dimensional $k$ -space sample size
$\delta_p$	Deshielding constant of chemical species denoted $p$
$\Delta x$	One-dimensional voxel size
$\mathbb{E}[\beta]$	Expectation value of parameter $\beta$
$E_{\pm}$	Zeeman levels of a proton
$F$	Complex signal from protons in lipids
$f_B$	Field map parameter [Hz]
$\mathcal{F}$	Fourier transform
$\phi_{\text{unwr}}$	Unwrapped phase
$\phi_{\text{wr}}$	Wrapped phase
$\gamma$	Gyro-magnetic ratio
$\mathbf{G}(t)$	Gradient waveform
$\mathbf{H}_0$	Main magnetic field
$\hbar$	Reduced Planck constant
$\mathbf{H}$	Total magnetic field
$\mathbf{H}_e$	Effective magnetic field from RF-pulse
$\mathbf{H}_1$	Magnetic field of RF-pulse
$I$	Spin quantum number
$\mathbf{I}$	Fisher Information Matrix
$\mathcal{F}^{-1}$	Inverse Fourier transform
$\mathbf{J}$	Angular momentum
$\mathbf{J}$	Jacobian matrix
$\mathbf{k}$	$k$ -space location vector
$\mathcal{L}$	Laplace transform or Likelihood function
$\nabla^2$	Laplace operator
$\mathbf{M}$	Magnetization vector

*List of Symbols*

$m_I$	Magnetic quantum number
$\boldsymbol{\mu}$	Magnetic dipole moment
$\omega_0$	Lamor frequency
$\Omega$	Angular Frequency of RF-pulse or region-of-interest
$\boldsymbol{\omega}_e$	Precession vector around $\mathbf{H}_e$
$\Pi(x)$	Boxcar function
$\mathbf{r}$	Location vector
$\mathbf{R}$	Rotation matrix $\in SO(3)$
$R_1$	Longitudinal spin-lattice relaxation rate [s <sup>-1</sup> ]
$R_2$	Transverse spin-spin relaxation rate [s <sup>-1</sup> ]
$R_2^*$	Effective transverse relaxation rate [s <sup>-1</sup> ]
$R_2'$	Reversible decay rate [s <sup>-1</sup> ]
Res	Residuum
$\sigma_p$	Shielding constant of chemical species denoted $p$
$S(t)$	MR signal
$\boldsymbol{\tau}$	Torque
TE	Echo time [s]
$\tau_p$	Pulse duration [s]
TR	Repetition time [s]
$t$	Time [s]
$u(x)$	Sampling function
Var $\beta$	Variance of parameter $\beta$
$W$	Complex signal from water protons
$X$	Susceptibility in $k$ -space
$\chi$	Magnetic susceptibility [ppm]
$x$	One-dimensional image-space coordinate

# Acknowledgments

I would like to sincerely thank my first supervisor and group leader, PD Dr. Dimitrios C. Karampinos, who initiated, guided, and supported this research project and helped me on my ongoing path to becoming the researcher I would like to be. He is a true educator and a caring mentor and I will be eternally grateful for the privilege to be part of the Body Magnetic Resonance Research Group (BMRR) he has built at the Klinikum rechts der Isar in Munich.

Thank you also to every single member of BMRR for the friendly and collegial help I could always count on. I can look back on the great times we spent together in lectures, in the office, at lunch, at conferences and at parties!

Many thanks to my secondary supervisor, Prof. Dr. Axel Haase, and part-time secondary supervisor Prof. Dr. Ernst Rummeny. They have been a forthcoming source of support by providing their vast knowledge and experience in MRI in medicine.

My special thanks goes to the senior researchers, Carl Ganter, Jakob Meineke, Thomas Baum, Anh Tu Van and Holger Eggers. Their mentoring and consulting and the exchange of ideas with them made me learn all kinds of useful and interesting things in such a fun way.

I was lucky to have a great time in this thesis project during my research stay at Berkeley University. Many thanks to Prof. Dr. Chunlei Liu for hosting me in his research group and giving me the possibility to experience a different research environment that taught me many new and useful concepts in MRI and beyond.

Thank you also to all my friends from the Bay area, from university, from school, and definitely from Waltrudering. It was incredibly valuable to spend the awesome time with you away from research.

At last and most import, I would like to express my deepest thankfulness to my family, including my partner and true love, Pia Klostermann. I would like to dedicate this work to you all, because this dream of mine would not have been possible without you. Thank you.